THERMOMECHANICAL FATIGUE LIFE PREDICTION OF NOTCHED 304 STAINLESS STEEL

by

JUSTIN OTTO KARL
B. S., A. E., Embry-Riddle Aeronautical University, 2004
B. S., E. P., Embry-Riddle Aeronautical University, 2004
M. S., A.E., Embry-Riddle Aeronautical University, 2006

A dissertation submitted in partial fulfillment of the requirements
for the degree of Doctor of Philosophy in Mechanical Engineering
in the Department of Mechanical and Aerospace Engineering
in the College of Engineering and Computer Science
at the University of Central Florida
Orlando, Florida

Summer Term
2013

Major Professor: Ali P. Gordon

ABSTRACT

The behavior of materials as they are subjected to combined thermal and mechanical fatigue loads is an area of research that carries great significance in a number of engineering applications. Power generation, petrochemical, and aerospace industries operate machinery with expensive components that undergo repeated applications of force while simultaneously being exposed to variable temperature working fluids. A case of considerable importance is found in steam turbines, which subject blades to cyclic loads from rotation as well as the passing of heated gases. The complex strain and temperature histories from this type of operation, combined with the geometric profile of the blades, make accurate prediction of service life for such components challenging. Development of a deterministic life prediction model backed by physical data would allow design and operation of turbines with higher efficiency and greater regard for reliability. The majority of thermomechanical fatigue (TMF) life prediction modeling research attempts to correlate basic material property data with simplistic strain and thermal histories. With the exception of very limited cases, these types of efforts have been insufficient and imprecise in their capabilities. Early researchers did not account for the multiple damage mechanisms that operate and interact within a material during TMF loads, and did not adequately address the extent of the relationship between smooth and notched parts. More recent research that adequately recognizes the multivariate nature of TMF develops models that handle life reduction through summation of constitutive damage terms. It is feasible that a modification to the damage-based approach can sufficiently include cases that involve complex geometry. The focus of this research is to construct an experimentally-backed extension of the damage-based approach that improves handling of geometric discontinuities. Smooth and notched specimens of Type 304 stainless steel were subjected to several types of idealized fatigue conditions to

assemble a clear picture of the types of damage occurring in a steam turbine and similarly-loaded mechanical systems. These results were compared with a number of idealized TMF experiments, and supplemented by numerical simulation and microscopic observation. A non-uniform damage-summation constitutive model was developed primarily based on physical observations. An additional simplistic model was developed based on phenomenological effect. Findings from this study will be applicable to life prediction efforts in other similar material and load cases.

To my parents-
Your love and support have made my endeavors possible.

ACKNOWLEDGMENTS

My continued studies and research would not be feasible without a great deal of assistance from many people. For their personal and professional contributions to my work, I would like to convey my gratitude.

I would like to thank my principal adviser, Professor Ali P. Gordon, for his counsel and encouragement throughout my graduate studies. My proficiency as a researcher, writer, and professional has been greatly enhanced by his indispensable guidance. Dr. Gordon is a model example for academics who wish to simultaneously maintain exceptional levels of productivity in both instruction and research.

My additional thanks must be expressed to my dissertation reading committee. Drs. Yuanli Bai, David Nicholson, and Seetha Raghavan have made significant contributions to my work and improved the contents of this dissertation.

The assistance of my manager at Siemens Energy, Vinay Jonnalagadda, must also be acknowledged, as his understanding and flexibility has enabled me to complete this research. David Kosich and Anthony Gringeri of the Siemens Gas Turbine Laboratory, as well as Tory Jensen of MTS Systems have made significant contributions to my skillfulness regarding practical experimental techniques.

Fellow graduate student Scott Keller has been greatly supportive in both the technical and personal regard. MOMRG researchers Calvin Stewart, Thomas Bouchenot, Darius Hooshmandan, and Francis Tam have made my complex numerical and experimental studies a feasible undertaking. Machinist Tim Lindner, Senior Engineer Abdul Benwali, and Olga Fuentes, and Dr. Jayasuriya Suhada have provided excellent practical advice.

Additionally, I must express that without the support and encouragement of my family this academic pursuit along with all others in the future would not be feasible. My parents James and Pamela, along with my brother Lake, have sent their love and guidance from nearby and far away over many years, and have unquestionably shaped me into the person that I have become. With these lessons gained and a mature understanding of emotion, I was been able to discover love upon meeting my wife, Shannon. In a time of crisis and urgency, my darling has helped me reach levels previously beyond my reach.

TABLE OF CONTENTS

LIST OF FIGURES

LIST OF TABLES

LIST OF NOMENCLATURE

Variables

α	Coefficient of thermal expansion: [°C^{-1}], [°K^{-1}] or [°F^{-1}]
ε_{el}	Uniaxial elastic strain: [mm-mm^{-1}], [in-in^{-1}], or [%]
ε_{pl}, ε'_{pl}	Uniaxial assumed inelastic strain: [mm-mm^{-1}], [in-in^{-1}], or [%]
ε_{m}, ε_{mech}	Uniaxial mechanical strain: [mm-mm^{-1}], [in-in^{-1}], or [%]
ε_{th}	Uniaxial thermal strain: [mm-mm^{-1}], [in-in^{-1}], or [%]
ε_{t}, ε_{tot},	Uniaxial total strain: [mm-mm^{-1}], [in-in^{-1}], or [%]
ε	Uniaxial total strain rate: [mm-mm^{-1} s^{-1}], [in-in^{-1} s^{-1}], or [%-s^{-1}]
ε_{m}	Uniaxial mechanical strain rate: [mm-mm^{-1} s^{-1}], [in-in^{-1} s^{-1}], or [%-s^{-1}]
$\Delta\varepsilon$	Uniaxial total strain range: [mm-mm^{-1} s^{-1}], [in-in^{-1} s^{-1}], or [%-s^{-1}]
$\Delta\varepsilon_{m}$, $\Delta\varepsilon_{mech}$	Uniaxial mechanical strain range: [mm-mm^{-1}], [in-in^{-1}], or [%]
φ	Thermal / mechanical cycle phasing: [°] or [*rad*]
σ	Uniaxial stress: [*MPa*] or [*ksi*]
σ_{avg}	Average tensile stress: [*MPa*] or [*ksi*]
σ^{+}_{max}	Maximum tensile stress: [*MPa*] or [*ksi*]
σ_{max}	Maximum uniaxial stress: [*MPa*] or [*ksi*]
σ_{min}	Minimum uniaxial stress: [*MPa*] or [*ksi*]

σ_y	Yield stress: [*MPa*] or [*ksi*]
σ_{ult}	Ultimate stress: [*MPa*] or [*ksi*]
v	Poisson's ratio
A	Diffusion coefficient: [m^2s^{-1}] or [in^2s^{-1}]
E	Modulus of elasticity (Young's modulus): [*GPa*] or [*Msi*]
k	Reaction rate constant: [s^{-1}]
h_o	Oxide layer thickness: [μm] or [*P*]
h	Oxide penetration depth: [μm] or [*P*]
N	Number of cycles: [*cycles*]
N_i	Number of cycles required for crack initiation: [*cycles*]
N_f	Number of cycles required for specimen failure: [*cycles*]
P	Applied load: [*N*] or [*lbf*]
Q	Activation energy: [$kJ\text{-}mol^{-1}$] or [$ft\text{-}lb\text{-}mol^{-1}\text{-}sec^{-1}$]
R	Universal gas constant: [$Jmol^{-1}\text{-}K^{-1}$] or [$ft\text{-}lb\text{-}slug^{-1}\text{-}R^{-1}$]
T	Temperature: [°*C*], [°*F*], or [°*K*]
T_{min}	Minimum Temperature: [°*C*], [°*F*], or [°*K*]
T_{max}	Maximum Temperature: [°*C*], [°*F*], or [°*K*]
t	Time: [*s*]

t_{cyc}	Cycle duration: [s]
t_{hold}	Hold/dwell duration: [s]
t^{+}	Cycle time in tension: [s]
t_r	Time to rupture: [s]

Abbreviations

304SS	AISI/SAE/UNS Type 304 Stainless Steel
Avg.	Average
Eq. or Eqs.	Equation(s)
Fig. or Figs.	Figure(s)

Acronyms

ASTM	American Society for Testing and Materials
BSE	Backscattered Electron (Microscopy)
C-F	Creep Fatigue
CPM	Cycles per minute
EDS	Energy Dispersive Spectroscopy
ET	Elevated Temperature

IP	In-phase
LCF	Low cycle fatigue
MOMRG	Mechanics of Materials Research Group
MPC(L)	Mechanical Properties Characterization (Laboratory)
OP	Out-of-phase
RT	Room temperature
SEM	Scanning Electron Microscopy
TC	Thermocouple
TMF	Thermomechanical fatigue
UCF	University of Central Florida

CHAPTER 1

INTRODUCTION

Many components in power generation turbines, aero turbines, petrochemical equipment, and other industrial applications are subjected to repeated sets of coupled thermal and mechanical loadings. Especially prevalent in propulsion and power generation are cases where severe mechanical loads and temperatures force materials to work at or near the edge of their performance envelope. This double-faceted process, known collectively as thermomechanical fatigue (TMF), induces several types of damage that alone and in concert impact the lifespan of such parts. TMF life reduction is hence regarded as a consequence of fatigue, creep, and environmentally-driven damage mechanisms. Generally, manufacturers consider these high performance parts to be components that wear and degenerate, and thusly are subject to periodic replacement when service inspections indicate that they have degraded past the limit of acceptable operation.

Correlating the life reduction in parts due to these damage mechanisms with specific TMF load conditions provides a basis for prediction models. The overarching idea behind such models is that they can ultimately lead to more reliable operation of components without the need for conservative service intervals and the associated costs of inspecting or replacing damaged components. As most of the life of these components is spent in the crack initiation stage, life reduction methods which can predict when crack initiation will occur are an important tool for designers, operators, and service personnel. While damage-based TMF lifing efforts have had limited success in smooth specimens, most parts in operation have complex shapes. For example, a cooling hole or a small-radius fillet at the base of a turbine blade causes a significant stress concentration which to date has not been accounted for in previous methods. The addition of geometric dependency to an accurate life model is an important step in bridging the gap between theoretical lab-based efforts and the ultimate application to industry.

1.1 Motivation

The primary goal of this study is characterization of life prior to observable initiation with respect to both load parameters and component shape. Life reduction in steam turbine blades is chosen as the archetypical problem. Such blades, with complex geometry due to their airfoil design, spend the majority of their life cycle in the crack initiation stage. Thusly, the scenario focuses on loads and geometric discontinuities present in these particular components. Crack initiation is most commonly a result of the aggregated effect of the aforementioned TMF damage mechanisms. Figure 1.1 illustrates the three major damage mechanisms that reduce life in TMF cases. Determining the origins of life reduction increases in complexity as varying thermal and mechanical strain histories cause variable proportions of damage to occur. Additionally, certain load conditions instigate interactions between types of damage that may cancel or amplify their influence on crack initiation. Adequate accounting for this convoluted set of circumstances exhibits further difficulty when the consequences of stress concentrations due to geometric discontinuities are realized.

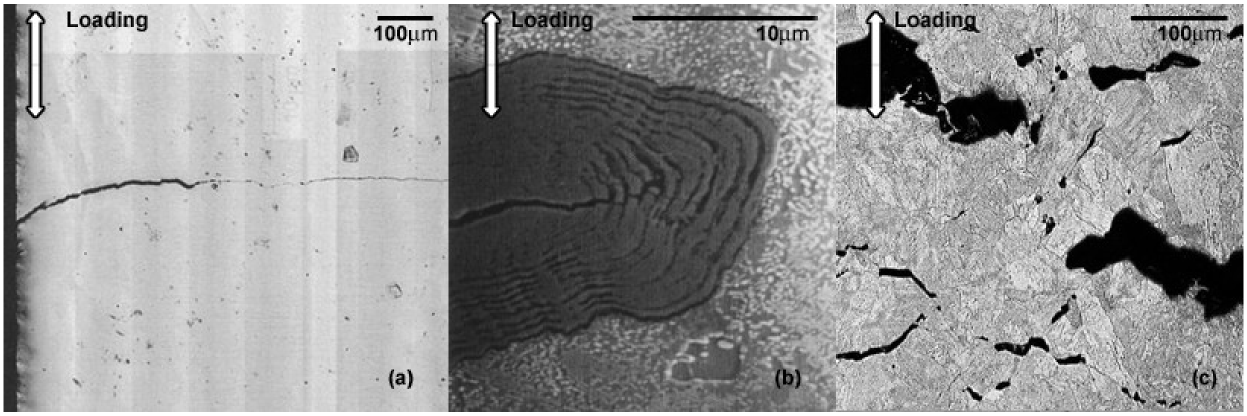

Figure 1.1: Cracks due to mechanical fatigue damage (a), environmental assistance (b), and creep effects (c) in a stainless steel.

To date, life prediction modeling in steam turbine blades has been less than optimal. Previous works that have produced inaccurate or narrowly-scoped TMF lifing models have been subject to a number of major shortcomings. First, the method of extending existing models that were based on simpler cases has reached a useful limit. An example includes the strain range partitioning method developed by Manson et al. in 1971. Though it yielded promising results for isothermal low cycle fatigue (LCF) and extended to creep-fatigue (C-F) cases (Manson, Halford, and Hirschberg, 1971), it ultimately failed to prove useful for non-isothermal cases (Halford and Manson, 1976). Another limitation imposed on research includes the complex nature of TMF experimentation itself. Models which are narrow in scope arise when sample size is restricted, and testing programs must focus on specific strain levels, temperature ranges, or phasing values. It is often that this restriction occurs due to time or resource constraints. A notable instance includes a capable but narrow damage-based TMF lifing model proposed in 1989 (Neu, R., and Sehitoglu, H., 1989) that was based on data from only 20 specimens. This particular model yielded accurate predictions, but only for a select handful of temperature, strain rate, and environmental conditions.

Clearly, with widespread industrial application, the motivation exists to develop a model that maintains its accuracy over a wider range of circumstances. Choosing a load application that mimics idealized steam turbine conditions as a starting point allows for a more comprehensive empirical data set to be applied to model development by virtue of the increased availability of similar steels. This effort aims to develop a model based on empirical results from a wider variety of loading conditions.

1.2 Objectives

This research explores the relationship between notch severity and number of cycles to crack initiation in TMF loadings. A fatigue model is thereby proposed after adequate correlation between load parameters, material properties, stress concentration of the notch, and life is established and verified through analysis of experimental results. Due to the highly multivariate nature of the investigation, the following objectives are outlined in order to clearly quantify progress.

1. **Establish whether damage accumulation type models for TMF life prediction are suitable for extension to include cases that involve geometric discontinuities.** Testing and analysis of variably notched 304SS specimens will be utilized to reveal a relationship between the notch severity and degradation of life for idealized TMF strain histories.
2. **Individual damage mechanisms present in TMF loadings as well as interactions between such mechanisms have predictable effects due to the presence of a notch.** The resulting model, therefore, augments oxidation damage and creep damage terms with appropriately scaled sensitization terms.

3. **Formulate a TMF life model with a predilection towards applied load parameters and other physically measurable quantities.** Numerical data and statistical fits are given consideration secondarily after characterization through empirical findings and microscopic observations.
4. **Offer a first-order variation of the model as an immediately-applicable approximation of the effect of notches in 304SS under TMF.** This theoretical research study will not meet the technical readiness requirements of implementation to industry. A conservative simplified model will be offered which can incorporate more phenomenological effects and statistical design.

While meeting the objectives outlined above, a number of assumptions are made in order to more finely focus the scope of the investigative efforts. The following key assumptions are most important in clearly defining written the parameters and goals of the study.

1. **Mechanical load levels are limited to a regime in which the effect of plasticity has varying degrees of dominance.** In some cases, the plastic zone at the notch tip will remain small when compared to the overall notch size. While large-scale plasticity is generally not encountered in service conditions, some strain levels will be selected such that testing will match with the more severe conditions imposed by industry laboratories.
2. **Experimental strain application in this study is fully-reversed.** As a preliminary investigation, an attempt to minimize the effects of a nonzero mean stress is made.
3. **This study focuses on formulating a model for cycles to crack initiation, N_i, in TMF loadings.** Tests are considered complete when a load drop criterion of 5% from a stable

stress history is met. No efforts are carried out to model crack propagation behavior or cycles to failure or rupture.

1.3 Overview

The lifing model developed by this study is largely based on the outcome of analysis performed on results of a wide-scale mechanical test program. The test plan consists of a large parametric study with several groups of experiments to specimens with both smooth and notched geometries. These groups of similarly designed isothermal and thermomechanical fatigue tests incorporate differences in conditions which are designed to draw out certain types of damage mechanisms or damage mechanism interactions.

Understanding how the conditions that allow each type of damage to be more or less dominant in crack initiation in turn helps reveal the proper proportion of the life degradation effect due to the presence of a notch under such conditions. All tests involve fully-reversed fatigue loadings, at various temperatures, local strain ranges, dwell times, and stress concentration factors. Local strain ranges of 0.7% to 1.4% offer data from low plasticity and high-plasticity cases. Temperature levels are kept primarily between 200°C and 600°C to mimic steam turbine-like conditions. Specimens machined from Type 304 stainless steel vary in geometry from smooth to a stress concentration factor of 3.0, mimicking the most severe discontinuity encountered in turbine blades. (Mazur, Luna-Ramirez, Juarez-Islas and Campos-Amezcua, 2005) Selection of commonly-available stainless steel alloy (Figures 1.2 and 1.3) for the study pair comparable strength and density of more exotic rotor steel alloys with lower costs and the benefits of more easily observable oxidation effects (Ashby, 2005).

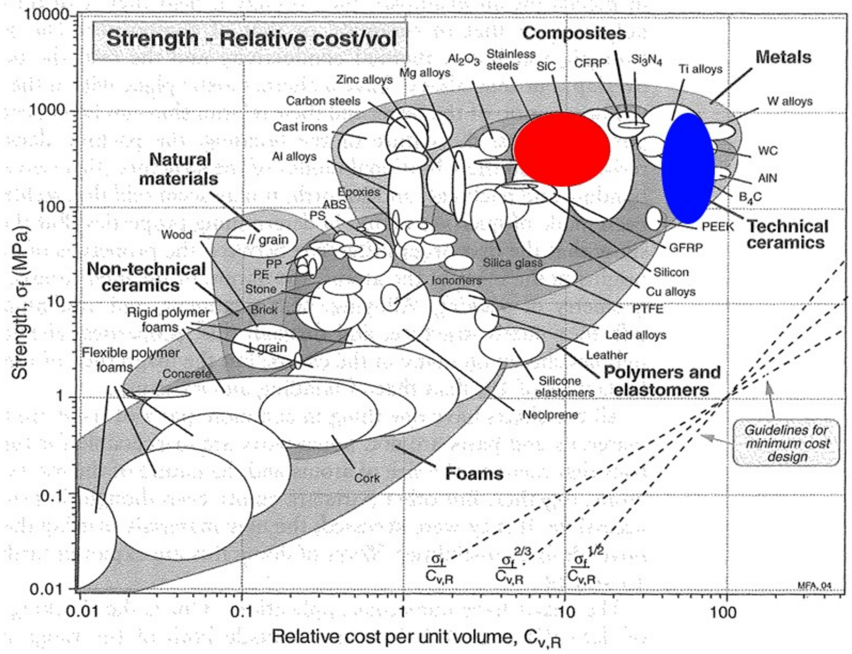

Figure 1.2: Strength vs. cost material selection diagram highlighting superalloys (blue) and stainless steels (red).

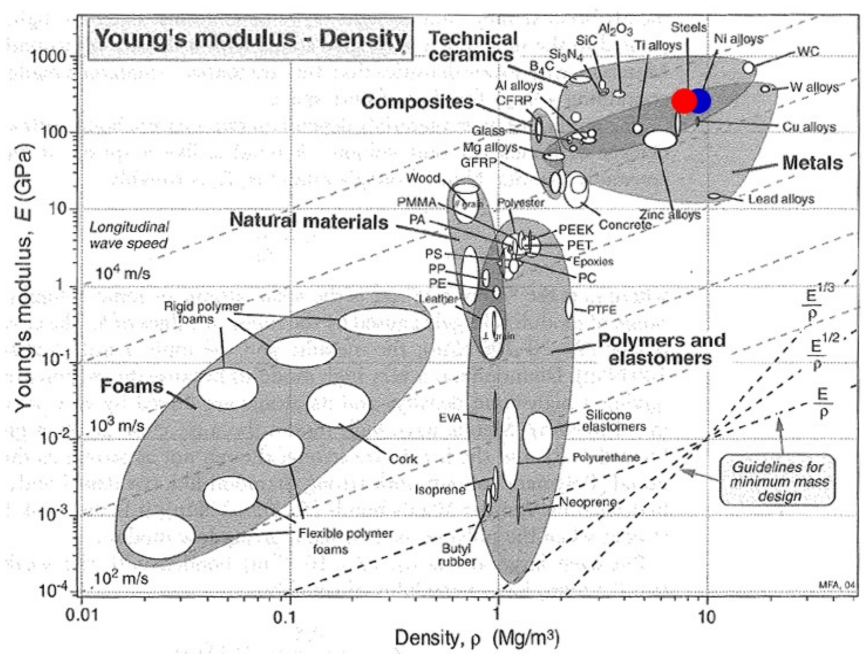

Figure 1.3: Elastic modulus vs. density material selection chart higlighting superalloys (blue) and stainless steels (red).

In addition to the gathering and analysis of empirical data, the study is augmented by use of modern computing packages. Utilizing customized behavioral models and load applications in ANSYS allow for early verification of load parameters in the geometries of notched specimens, where they are otherwise not physically measurable. Additionally, with strong agreement between a numerical model and the observed data, it is useful to interpolate results between two different parameter values computationally. Following the same logic, behavioral modeling can be extended into regimes not tested experimentally with relatively high confidence in the prediction.

Another integral component of the study involves high magnification optical microscopy and Scanning Electron Microscopy (SEM) of fractured specimens. Analysis of the microstructures offers physical measurements to correlate with observed damage effects. Additionally, Energy Dispersal Spectroscopy (EDS) aids in the precise identification of certain oxides and carbides within the material. Post-testing microscopy is hence sourced as a method of increasing the physicality of the resultant model.

CHAPTER 2

LITERATURE REVIEW

This chapter reviews research pertaining to the material, load types, and methodologies which are relevant to the research conducted. These works serve as a baseline of the state-of-the-art in TMF lifing, and a starting point for evaluating the extension that is constructed with the current experiments and modeling.

Stainless steels in power generation applications are subjected to demanding conditions. Steam turbines in particular apply loading conditions that approach the limits of thermal and mechanical service loads for steel. Operating at maximum temperatures of up to 585°C (1085°F, 858°K) with reheating cycles (Siemens Energy, 2013) or at 610°C (1130°F, 883°K) for ultra-super-critical cycle types (GE Energy, 2010), steels in steam turbines must resist damage due to high heat. With loads of up to 400MPa (58ksi) applied through rotational forces of the turbine itself, steels used in steam turbine blades must simultaneously resist damage due to mechanical cycling (Sriraman, M., and Pidaparti, R., 2010). Steam turbines in combined cycle plants can reach these thermal and mechanical load levels in as quickly as 10 minutes from a cool, dead stop when used as a peak demand supplement (Farmer, R., 2010). Peaker turbine operation also means that the loads are cyclic, and turbine components require repair or replacement after several hundred cycles (Ulbrich, A., et al., 2003). This collection of conditions serves as the basis of the test parameters selected by past researchers. Low, medium, and high plasticity mechanical loads have been applied over the course of several minutes in conjunction with temperatures of up to 600°C (1112°F, 873°K). The current research utilizes similar load conditions and extends them to include notched geometries.

2.1 Type 304 Stainless Steel

The material of interest for the study is Type 304 stainless steel. This particular alloy is amongst the most widely used steels in the world, with itself and similar alloys finding many applications within industry, some of which include thermomechanical cycling. The cost to performance ratio of this steel is especially favorable for research, as it is thusly easily obtainable. To date, many studies have been done with a focus on 304SS, which further enhances the value of this material as a selection for experimental work, as its behavioral properties have been well documented.

2.1.1 Applications

Type 304 stainless steel offers enhanced oxidation resistance in comparison to milder steels without a significant cost increase, which makes it an excellent candidate for many types of industrial utilization. Examples from the food industry include processing equipment, cookware, cutlery, and appliances (Smith, 1984). Field-grade military firearms often use 304SS for internal mechanisms and outer casings alike (Wert and DiSabella, 2006). Architectural applications include both load-bearing and decorative uses, as the resistance to corrosion helps buildings and monuments maintain their original appearance over the course of many decades (Xu, 2012). Heavy industrial practices include the manufacturing of 304SS heat exchangers, petrochemical piping, and valving. Higher performance usage still is found in the energy sector, where hydraulic turbine wheels (Simoneau and Roberge, 1981) and gas turbine components such as exhaust recuperators (Fig. 2.1) are manufactured from 304SS (Maziasz, et al., 1999).

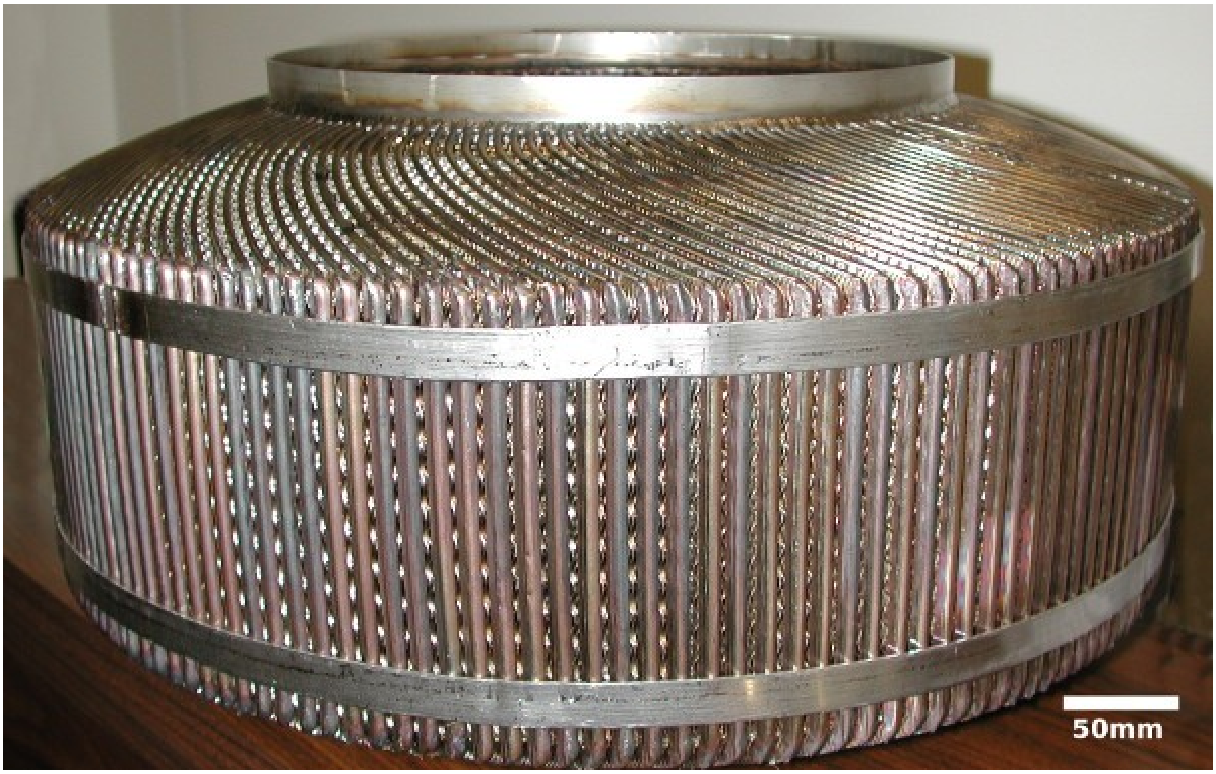

Figure 2.1: Core of a Capstone CS200 gas turbine exhaust recuperator comprised of many interlaced microchannels of 304SS. (Courtesy Capstone Turbine Corporation).

Recently, nuclear and combined cycle power industries have utilized 304SS as a repair material for damaged steam blades, due to their similar material properties (Bhaduri, et al., 2001). As pictured in Figure 2.2, 304SS can be welded directly to rotor steels and hence provides a way of repairing cracks with minimal degradation in material performance.

Figure 2.2: Austenitic stainless steel is deposited onto a steam rotor during welding in a crack repair procedure. (Courtesy GE)

This particular application is amongst the most extreme cases of thermomechanical cycling of 304SS, and thus is of special interest to energy industry-minded researchers attempting to characterize the behavior of the material and geometry.

2.1.2 Composition

The primary alloying agents in Type 304 stainless steel are chromium and nickel. Although the Type 304 designation is given to a wide variety of chromium/nickel mixtures, the most common quantities of 18-20% and 8-10.5%, respectively, offer the reasoning behind why 304SS is often referred to as "18/8" steel. The chromium content in the steel is the primary reason that 304SS offers good oxidation resistance, and the nickel content suppresses the transformation of austenite (γ-Fe) into a ferrite (α-Fe) and cementite (Fe_3C) during cooling from a liquid state during manufacture. In the past two decades, blends of 304 and other austenitic steels have replaced some of the nickel content with less expensive manganese for stabilizing the austenite structure against the carbon diffusion and phase change (Di Schino, 2000). The microstructure of wrought 304SS, shown in Figure 2.3, is dominated by large austenite grains that are outlined darker chromium carbide (Cr_3C_2) heavy boundaries.

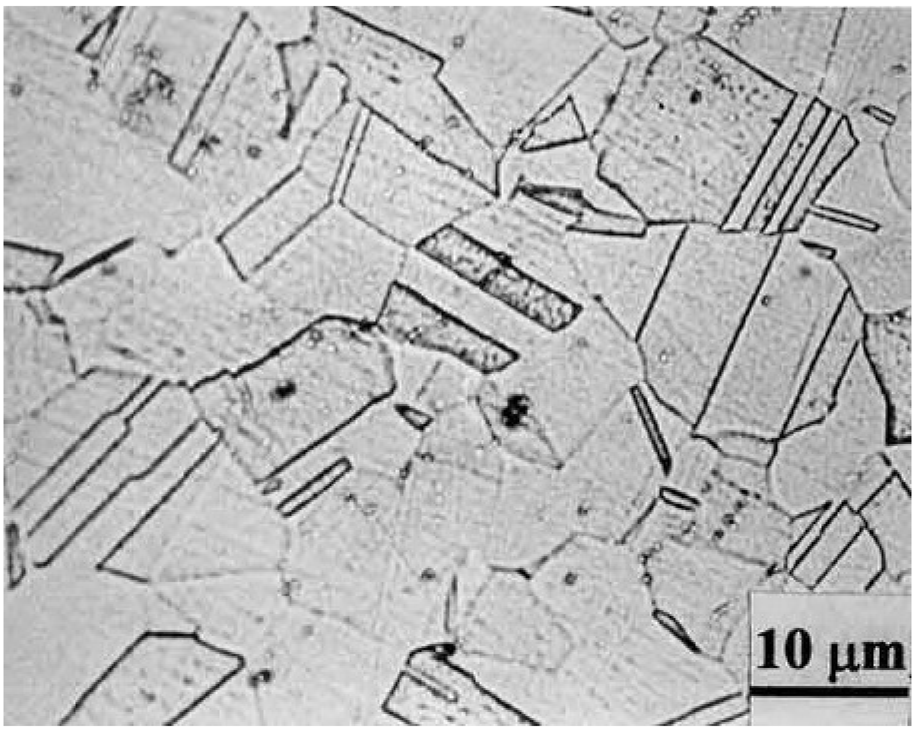

Figure 2.3: Typical microstructure of wrought Type 304 stainless steel (from Skrabski, 2011).

In addition to the primary alloying agents, a number of other constituent elements comprise the chemical makeup of 304SS. Phosphorus and sulfur are added for improvement of machinability, and silicon is often used as an inhibitor to oxidization during the melting process (Harvey, 1982). Carbon is present in low quantities and gives steel the majority of its strength advantage over iron. Copper and cobalt are sometimes found in trace quantities as a result of being present as contaminants in some of the other agents. Table 2-1 shows the range of compositions for 304SS as per the UNS S30400 specification (Lampman and Zorc, 2007).

Table 2-1: Composition of plain Type 304 stainless steel meeting the UNS S30400 designation (from Lampman and Zorc, 2007).

Alloying Agent	% Wt. Composition
Carbon, C	0.04-0.10
Manganese, Mn	up to 2.00
Silicon, Si	1.00
Chromium, Cr	18.0-20.0
Nickel, Ni	8.0-10.5
Phosphorus, P	up to 0.045
Sulfur, S	up to 0.030
Silicon, Si	up to 1.0
Nitrogen, N	up to 0.10

With a range of possible chemical mixtures, different material behaviors can be noted when certain alloying agents are favored. It is important to recognize that with this material system, stochastic tendencies would be evident in material from different suppliers or batches, and that commonly published values for material properties are an averaged value in a scatter band. High percentages of carbon would favor higher strength while lower percentages decrease susceptibility to intergranular corrosion. Increased levels of manganese can increase strength and nitrogen solubility, but lead to faster work-hardening rates and diminished fatigue resistance (Davis, 1994).

2.1.3 Tensile Characteristics

Type 304 stainless steel is strong as wrought, with a tensile strength of 515MPa, and can be conditioned up to a tensile strength of 1035MPa (Garofalo, et al., 1952). Grains are significantly lengthened in worked 304SS, and conditioning can offer a tensile strength increase to 1035MPa with loss of ductility as a trade-off (Iino, 1986). As-wrought, 304SS is capable of up to 55% elongation at failure. Heat treatments can increase the tensile strength without loss of ductility, with 640MPa (93ksi) resulting from the most common annealing treatment (Lampman and Zorc, 2007).

Type 304SS also has favorable elevated temperature characteristics, with elastic modulus gradually softening and ultimate strength at 600°C (1112°F, 873°K) decreasing to approximately 55% of its room temperature value (Peckner and Bernstein, 1977). A collection of tensile properties for 304SS at a range of temperatures is displayed in Table 2-2.

Table 2-2: Tensile properties of plain, wrought Type 304 stainless steel at common service temperatures (from Garofalo, Malencock, and Smith, 1952, and AISI, 2012).

Temperature, *T* (°C) [°F]	**Elastic Modulus, *E* (GPa) [Msi]**	**Yield Strength 0.2% Offset, σ_y (Mpa) [ksi]**	**Ultimate Tensile Strength, σ_{UTS} (MPa) [ksi]**	**Elongation, $\Delta L/L_0$ (%)**
27 [80]	196 [28.5]	290 [42.0]	579 [84.0]	55
149 [300]	187 [27.1]	182 [26.4]	485 [70.3]	50
200 [392]	183 [26.5]	160 [23.2]	472 [68.4]	46
260 [500]	179 [26.0]	151 [21.8]	465 [67.4]	42
371 [700]	170 [24.7]	140 [20.3]	442 [64.1]	38
400 [752]	167 [24.2]	134 [19.3]	427 [61.9]	37
482 [900]	160 [23.2]	125 [18.1]	414 [60.0]	36
593 [1100]	150 [21.8]	113 [16.4]	367 [53.2]	35
600 [1112]	149 [21.6]	110 [16.0]	350 [50.8]	35
704 [1300]	140 [20.3]	95 [13.8]	241 [35.0]	35

The tensile characteristics of Type 304 stainless steel make it such that it remains useful for structural applications up to the 600°C (1112°F, 873°K) mark, which is the upper limit encountered in steam turbine operations. The decline in strength that occurs above 650°C (1202°F, 923°K) is rapid in comparison to the gradual weakening at lower temperatures, but the steel remains useful for low-stress and chemical containment applications up to 1093°C (2000°F, 1366°K) (AISI, 2012).

In addition to predictable strength reduction in high temperature cases, the tensile response of 304SS follows a general monotonic stress-strain curve, without any deviations or nonlinearities from the smooth curve of other metals. Compared against a set of data from tensile tests at different temperatures in Figure 2.4, a multi-stage polynomial can be used to closely represent the curves.

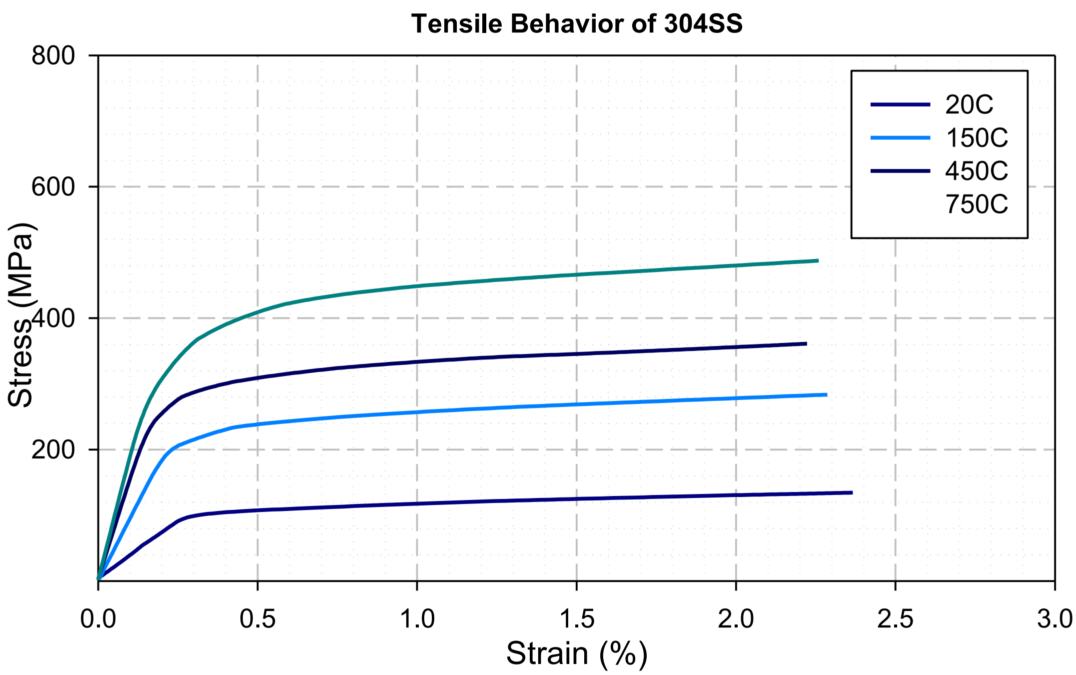

Figure 2.4: Tensile data of type 304 stainless steel at several temperatures (from Abdella, 2012).

A number of more mathematically simplistic equations using a limited number of parameters offer an excellent fit to observed data in cases of low strain. The Ramberg-Osgood relation (Ramberg and Osgood, 1943) is given in terms of elastic and plastic strain terms as:

$$\varepsilon = \varepsilon_{el} + \varepsilon_{pl} + \frac{\sigma}{E} + \left(\frac{\sigma}{K}\right)^{\frac{1}{n}} \tag{2.1}$$

For room temperature 304SS, values of K = 2275MPa (330ksi) and n = 0.334 are commonly used and provide an accurate fit near or below the yield point (Stephens, et al., 2001). This approach can be favored in studies where the strain value is not excessively far into the plastic region. The general accuracy of the Ramberg-Osgood fit is evident in Figure 2.5.

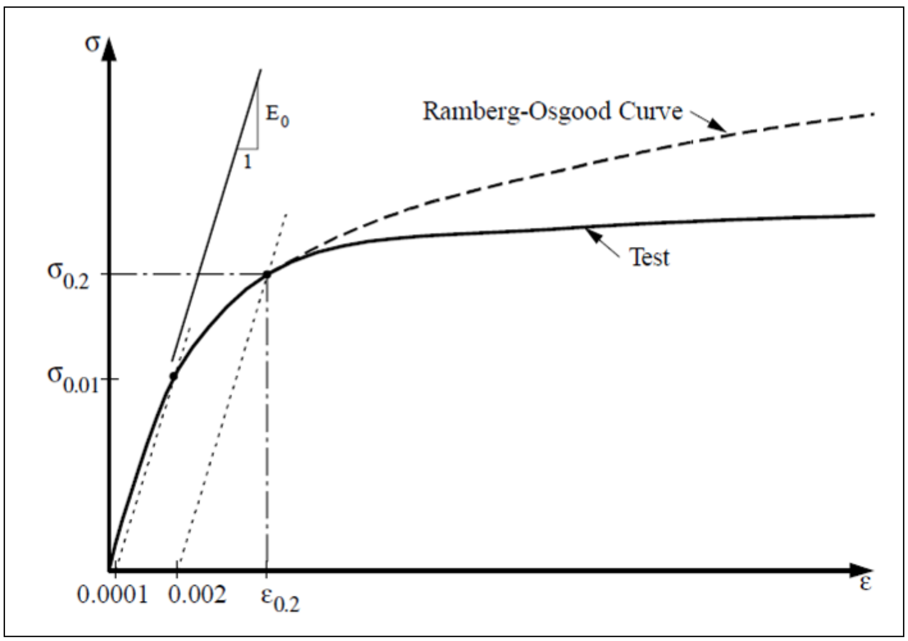

Figure 2.5: A Ramberg-Osgood fit versus empirical room-temperature tensile data in a stainless steel (from Rasmussen, 2006)

Another approach requiring three fit parameters, k_0, R, and b, the Voce equation (Voce, 1948),

$$\sigma = k_0 + R_0\varepsilon_{pl} + R_\infty\left(1 - e^{-be\varepsilon_{pl}}\right) \tag{2.2}$$

provides a stress versus strain interrelation of similar quality, with parameters determined with a secondary fit based on the linear relationship of flow stress to hardening. In the case of all such fits on the response of 304SS, the behavior of different chemical mixtures or performance at elevated temperatures is similarly modeled via redetermination of the parameters for the selected equation (Rasmussen, 2006; Hammond and Sikka, 1977). Furthermore, the majority of these approximation methods can also be extended to fit special load conditions or applications, with studies existing which address methods for determining fit parameters under high-temperature liquid sodium environments (Chopra, and Natesan, 1977) or instances of heavy neutron bombardment (Yoshida, et al., 1977).

2.1.4 Fatigue Behavior

A number of studies have been conducted to characterize the behavior of Type 304 stainless steel under isothermal fatigue conditions. Investigations based on the stress-life and strain-life approaches have been executed, with the majority of historical data being provided by the more precisely controllable and thus more favorable strain-life (and therefore strain-controlled testing) techniques.

Generally, 304SS is considered by designers to exhibit favorable fatigue characteristics at all service temperatures. A generic blend of 304SS characterized by Keisler, Chopra, and Shack found fully-reversed lifetimes at room temperature exceeded 10^6 cycles when stable maximum stresses are less than 42% of the ultimate tensile strength value (Keisler, Chopra, and Shack, 1996). This particular stress condition was met during a strain-controlled test with a strain range of $\Delta\varepsilon$ = 0.44%. Soo and Chow found that mixtures of 304SS better suited for low-stress fatigue can transition to runout-like behavior at larger strain ranges. A strain range of $\Delta\varepsilon$ = 0.56% imparts a stable stress higher than the 42% threshold found by Keisler, Chopra, and Shack, but for the higher chromium 304SS blend studied, this near-yield maximum of 225MPa (32.2ksi) leads to fully-reversed fatigue lives that exceed 10^7 cycles (Soo and Chow, 1981). Strain versus life data from a number of studies conducted on common blends of 304SS at room temperature is plotted in Figure 2.6.

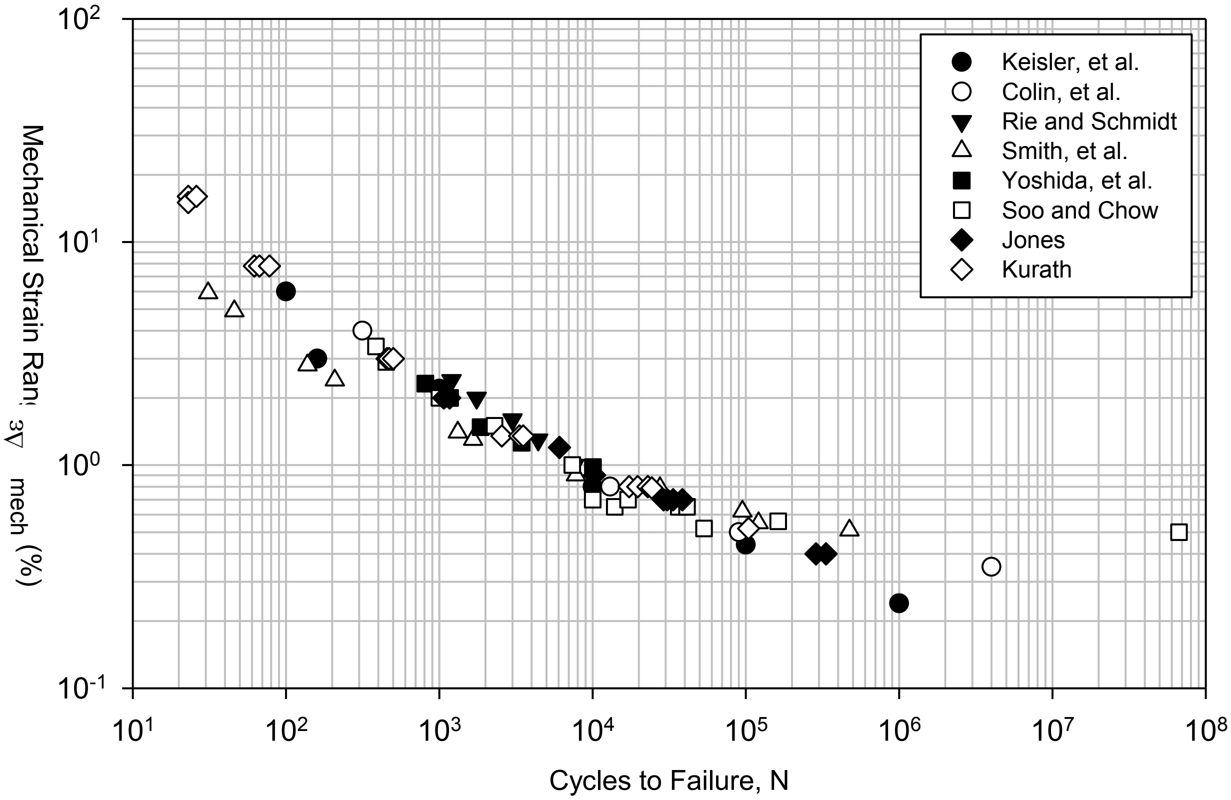

Figure 2.6: Baseline room temperature strain-life data from studies conducted with common 304SS blends (from Keisler et al., 1996, Colin, et al., 2010, Rie and Schmidt, 1984, Smith, et al., 1963, Yoshida, et al., 1977, Soo and Chow, 1981, Jones, 1986, and Kurath, 1987).

Elevation in temperature to the region of 150-300°C (302-572°F, 423-573°K) begins significantly degrading fatigue life at strain ranges of 0.6% and lower, but slightly increases life in strain ranges up to 1.0% due to mild softening of the material (Solomon, et al., 2005). At higher temperatures, fatigue life is degraded further, as strength and toughness are lost while more pervasive chromium carbide growth can contribute to failure in longer cycling times. At 600°C (1112°F, 873°K), Type 304 stainless steel retains approximately half of its original room temperature endurance strength. Studies conducted approaching the maximum service temperature of 850°C (1562°F, 1123°K) indicate further reduction in fatigue life up to an order of magnitude, although the softening of the material can make cycling at very large strain ranges possible for several hundred cycles (Coffin, 1979).

In general, 304SS fatigue data from 427°C (800°F, 600°K) to 150°C (302°F, 423°K) fall within the same scatterband, and data from 427°C (800°F, 600°K) and above fall within another scatterband (Rie and Schmidt, 1984). With the exception of a few instances, the two are separate. The twofold implications are that different mixtures of 304SS can exhibit more favorable or less favorable characteristics, and that regardless of mixture, a shift in behavior can be marked at the 427°C (800°F, 600°K) to 538°C (1000°F, 811°K) range (Soo and Chow, 1981). A number of strain-life curves from research involving elevated temperature fully-reversed fatigue loadings are plotted in Figure 2.7.

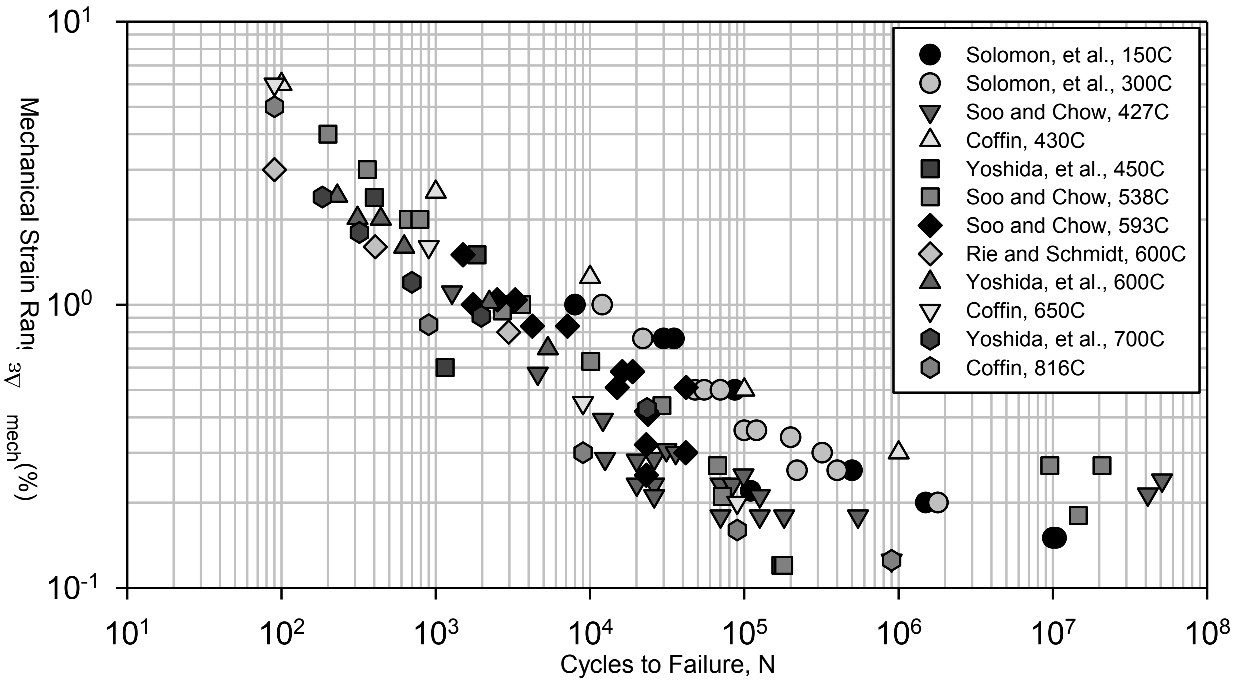

Figure 2.7: Baseline data from elevated temperature strain-life testing of 304SS (from Solomon et al., 2005, Soo and Chow, 1981, Coffin, 1979, Yoshida, et al., 1977, and Rie and Schmidt, 1984).

As is true with the monotonic properties of 304SS, the fatigue characteristics can be fit to functions that closely represent the results obtained from experimentation. The most commonly utilized way of expressing the stable cyclic stress-strain response is via modification of the Ramberg-Osgood formulation to incorporate stress and strain ranges with alternate fit terms:

$$\Delta\varepsilon = \Delta\varepsilon_{el} + \Delta\varepsilon_{pl} + \frac{\Delta\sigma}{E} + \left(\frac{\Delta\sigma}{K'}\right)^{\frac{1}{n'}} \tag{2.3}$$

Additionally, the strain-life behavior of the material can be approximated by the functions based on plastic strain range by Manson or Coffin (Manson, 1954, and Coffin, 1954):

$$\frac{\Delta\varepsilon_{pl}}{2} = \varepsilon'_f\left(2N_f\right)^c \tag{2.4}$$

A similar function which can account for the effects of mean stresses was developed by Morrow with his assumption that a tensile mean stress σ_m reduces fatigue strength σ'_f (Landgraf, Morrow and Endo, 1969):

$$\frac{\Delta\varepsilon_{pl}}{2} = \frac{\sigma'_f - \sigma_m}{E}\left(2N_f\right)^b + \varepsilon'_f\left(2N_f\right)^c \tag{2.5}$$

A table of select fatigue data and fit parameters for room and elevated temperatures of common steel mixtures meeting the Type 304 designation are offered on the following page in Table 2-3.

Table 2-3: Fatigue strain-life curve fitting parameters for common blends of 304SS at different service temperatures (from Rie and Schmidt, 1984, Smith, Hirschberg, and Manson, 1963, Yoshida, et al., 1977, Soo and Chow, 1981, Vehoff and Neumann, 1984, Jones, 1986, Kurath, 1987, and Klee, 1973).

Composition	Trade Name	Temp, T (°C)	Elastic Modulus, E (GPa)	Cyclic Strength Coefficient, K' (MPa)	Strain Hardening Exponent, n'	Fatigue Strength Coefficient, σ'_f(MPa)	Fatigue Ductility Coefficient, ε'_f	Fatigue Strength Exponent, b	Fatigue Ductility Exponent, c
X6CrNi19 9	AISI 304	22	210	6693	0.546	5813	0.194	-0.324	-0.416
X2CrNi18 9	AISI 304	23	192	2807	0.419	1936	0.412	-0.202	-0.483
X3CrNi19 9	AISI 304	23	172.6	2313	0.155	2067	0.301	-0.112	-0.649
X6CrNi19 11	AISI 304	23	183	1628	0.291	986	0.17	-0.117	-0.399
X6CrNi19 11	AISI 304	23	185	1675	0.291	1008	0.171	-0.117	-0.400
X3CrNi19 9	AISI 304 ELC	23	186.4	4634	0.309	2377	0.068	-0.152	-0.428
X10CrNi18 8	Remanit 1880	23	204	2397	0.331	2032	0.3249	-0.183	-0.441
X5CrNi18 9	SUS 304-B	23	210	3331	0.455	1470	0.161	-0.179	-0.389
X5CrNi18 9	SUS 304-B	23	210	3001	0.434	1268	0.134	-0.16	-0.366
X6CrNi19 9	AISI 304	427	179	2795	0.435	1942	0.1352	-0.222	-0.394
X5CrNi18 9	SUS 304-B	450	170.5	4497	0.514	2528	0.325	-0.247	-0.481
X5CrNi18 9	SUS 304-B	450	170.5	2363	0.375	1700	0.386	-0.202	-0.529
X5CrNi18 9	SUS 304-B	450	170.5	2193	0.34	1890	0.653	-0.212	-0.627
X6CrNi19 9	AISI 304	538	193	954	0.226	1315	1.0389	-0.186	-0.650
X6CrNi19 9	AISI 304	593	171	797	0.223	360	0.023	-0.036	-0.261
X2CrNi18 9	AISI 304	600	149	1022	0.272	635	0.177	-0.121	-0.446
X2CrNi18 9	AISI 304	600	149	836	0.249	576	0.226	-0.138	-0.557
X2CrNi18 9	AISI 304	600	149	861	0.248	530	0.141	-0.112	-0.452
X2CrNi18 9	AISI 304	600	149	1080	0.282	625	0.145	-0.119	-0.422
X6CrNi18 11	AISI 304/316	600	143.2	1074	0.319	677	0.234	-0.146	-0.459
X5CrNi18 9	SUS 304-B	600	158	1544	0.316	1009	0.268	-0.156	-0.499
X5CrNi18 9	SUS 304-B	600	158	1031	0.236	728	0.224	-0.118	-0.499
X5CrNi18 9	SUS 304-B	600	158	437	0.074	394	0.262	-0.041	-0.564
X5CrNi18 9	SUS 304-B	700	152	473	0.147	382	0.255	-0.075	-0.523
X5CrNi18 9	SUS 304-B	700	152	587	0.212	389	0.138	-0.094	-0.439
X5CrNi18 9	SUS 304-B	700	152	372	0.154	286	0.182	-0.076	-0.493

Despite the appreciable differences in mixtures, the austenitic steel grades that meet the Type 304 designation have fatigue properties that are generally similar, with the differences well documented. Historically, industries that develop Type 304 stainless steels for specialized purposes do so with heavy experimentation and support from researchers during the process (AISI, 2012). Thus, the fully-reversed isothermal fatigue life of many subtypes of 304SS is backed by a wealth of testing data, which serves as a benchmark and starting point for this particular course of study.

2.1.5 Time-Dependent Behaviors

Two major behavioral considerations must be taken into account when Type 304 stainless steel is in service at elevated temperatures for extended periods of time. Firstly, with high chromium and carbon content, 304SS is likely to form chromium carbides at grain interfaces, resulting in a significant loss of ductility. The other serious consideration is that of stress relaxation and the ultimate transition to creep or creep-like response. This section addresses both of these two time-dependent behaviors in turn.

Type 304 stainless steel can become "sensitized" or susceptible to embrittlement when exposed to temperatures above 475°C (752°F, 673°K) for extended periods of time (Boyer and Gall, 1985). At temperatures between 475°C (752°F, 673°K) and 815°C (1500°F, 1089°K) chromium and carbon have a tendency to diffuse outward from the austenite lattice in proportions that foster the growth of small chromium carbide regions already present at the grain boundaries. Chromium can form several different metallic carbides with carbon, but the type present in austenitic steels is $Cr_{23}C_6$, which carries similar proportions of chromium and carbon as the overall steel mixture itself (Rashid et al., 2012). The carbide's mechanical properties differ significantly from that of the austenite, with a hardness and elastic modulus an order of magnitude higher (Freyd and Suprunov, 1970). This combination at the interface causes a tendency toward voids opening at the interface due to shear stresses, or for existing cracks to quickly propagate through the carbide.

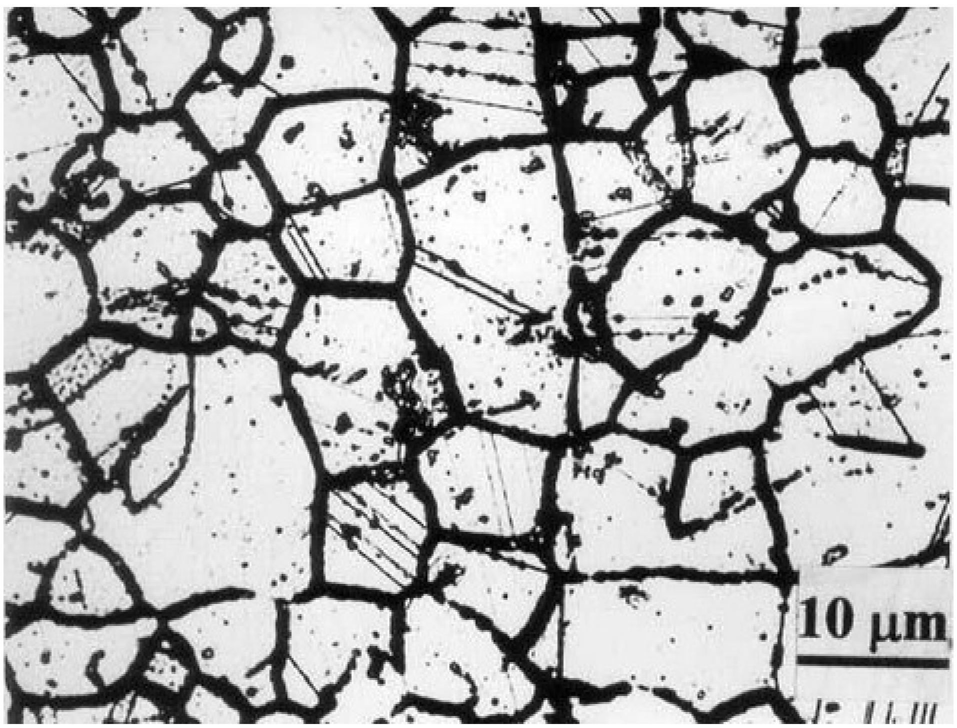

Figure 2.8: Microstructure of sensitized Type 304 stainless steel (from Skrabski, 2011).

This carbide growth is easily identifiable in micrographs, as evidenced by the dark carbide regions in Figure 2.8. The growth of the carbides is exacerbated by mechanical loading, but can be reversed by re-diffusion with exposure to much higher temperatures (Hansen and Puyear, 1996). Sigma-phase embrittlement is a mechanism which has a similar outward appearance as carbide embrittlement, and occurs at temperatures between 565-925°C (1050-1700°F, 839-1200°K). Sigma phase is an intermetallic iron-chromium mixture as well, but this compound builds up very slowly over the course of many years, even in stainless steels like 304SS which do not include stabilizing agents (Al-Kawaie and Kermad, 2011).

Microstructural changes due to heat exposure and oxide formation are not the only evolutionary mechanisms that are time-dependent in 304SS. A number of time-dependent creep and creep-like phenomena are observable in the alloy when also exposed to static or dynamic mechanical loadings while at elevated temperatures for extended periods of time. Creep is generally defined as a change in the crystalline structure that occurs due to mechanical stress application while under high thermal loading. Creep manifests itself in a number of ways, with the most prominent types being due to grain boundary sliding, dislocation, and diffusion (Collins, 1993). In standard mixtures of 304SS, the former two occur at temperatures well below the maximum service temperature of the material, whilst diffusion creep generally only occurs in 304L blends with very little carbon content (Marshall, 1994).

Grain boundary sliding is a deformation mechanism in which individual grains slide against each other on an atomic scale. While usually due to dislocation motion via glide and climb, it is not grouped with dislocation creep, as it only favors the movement of edge dislocations at the grain interfaces. In 304SS, grain boundary sliding is observed at relatively low stresses of less than 13MPa (1.88ksi) when exposed to constant temperatures in the 650-850°C (1202-1562°F, 922-1123°K) range (Ruano and Sherby, 1982).

As dislocation creep is the single mechanism possible at the maximum temperatures and testing times encountered in this study, it is deductively the only creep damage which could contribute to crack initiation. In 304SS, dislocation creep effects are most pronounced at low strain ranges and extremely long dwell periods, even when considered in concert with fatigue (Goswami, and Hanninen, 2001). With the majority of dwell periods in this study very short in duration, the onset of this type of creep is the focus for damage contribution from that type of mechanism.

Dislocation creep occurs through a number of different mechanisms in austenitic stainless steels, but 304SS exhibits preferential disposition to a combination of glide and lattice diffusion at the grain boundaries (Deleury, Donati, and Strudel, 1981). This mechanism occurs at higher stress levels of 76-110MPa (11-16ksi), but at a lower temperature range of 600-700°C (1112-1292°F, 873-973°K). Dislocation creep is evident and identifiable via imaging early in the lifetimes of specimens and structures that eventually fail due to creep or creep-assisted mechanisms (Ohtani, Ogi, and Hirao, 2011). When studied via metallograph or electron microscope, the areas of dislocation buildup are visually conspicuous as coalescing dislocations begin to form voids at the boundaries and triple points of the grain structure. An example of microstructural damage due to dislocation creep can be compared against the virgin microstructure of a 304SS specimen early in its usable life in Figure 2.9.

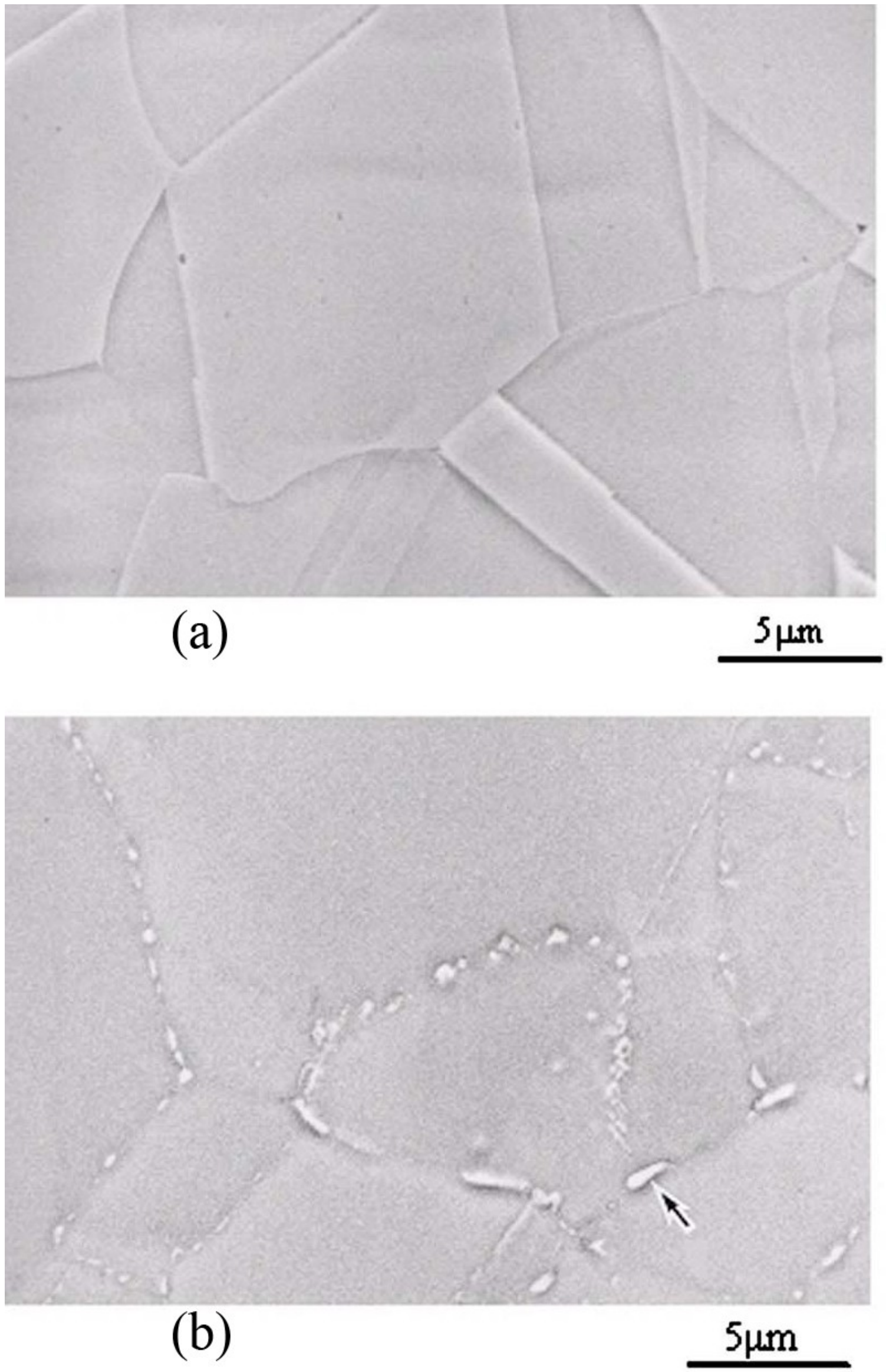

Figure 2.9: An SEM image of the undamaged microstructure (a) of 304SS is compared against the damaged microstructure (b) of a 304SS specimen at 40% of its usable life while subjected to a stress of 100MPa at 700°C (973°K) [from Ohtani, Ogi, and Hirao, 2011].

While both grain boundary sliding and dislocation creep in 304SS contribute to a gradual straining of the material, dislocation creep is more damaging, as more edge dislocations eventually lock in the same regions, build up, and larger microvoids form (Aghajani, et al., 2009). Such microvoids would initially be homogeneous in their distribution throughout the austenite interfaces, but additional stress concentration at grain boundary triple points due to mechanical loading will cause coalescence to more quickly transition to more macroscopic defects in these regions (Chen and Argon, 1981).

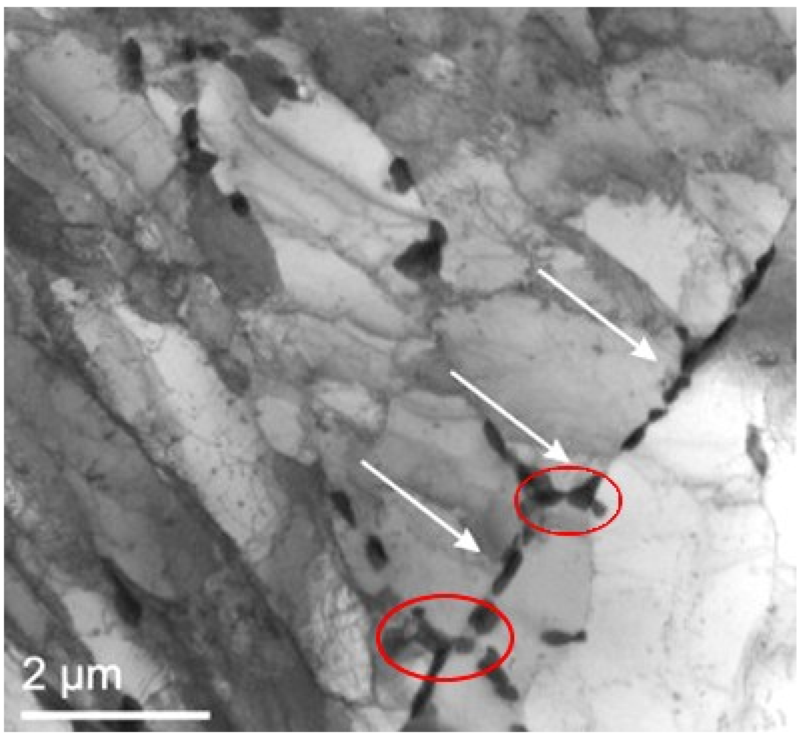

Figure 2.10: Cavitation along grain boundaries (white arrows) favors nucleation near triple points (red highlighted regions) in a steel (modified from Aghajani, et al., 2009).

Coalesced voids which grow into larger optically-observable cavities indicate significant creep damage, whose growth and nucleation can ultimately contribute greatly to the ultimate rupture of the material.

Several models for behavior under the effects of dislocation creep have been developed, yet the initial formulation developed from the general creep equation (Frost and Ashby, 1982) is robust in its application, and remains widely favored to date (Kassner and Perez-Prado, 2004). In its original form, the general creep equation,

$$\frac{d\varepsilon}{dt} = \frac{A\sigma^m}{d^b} e^{-Q/kT} \tag{2.6}$$

can be used to describe the strain rate of any generic creep mechanism in terms of grain size *d*, activation energy *Q*, and applied stress *σ* with *A, m,* and *b* as fitting constants. When considering only the relatively high stresses and low temperatures of dislocation creep, the function can undergo simplification:

$$\frac{d\varepsilon}{dt} = A(\sigma - \sigma_{min}) e^{-Q/kT} \tag{2.7}$$

This results in a power law function independent of grain size and requiring two less fitting constants. This equation more closely follows the form of the Arrhenius Equation, with the strain rate analogous to the reaction rate in this case (Laidler, 1993). Because dislocation mechanisms require certain stress thresholds to be met for any kinetics to occur, the term σ_{min} is introduced to represent the stress level at which no creep could be observed.

2.1.6 Environmental Exposure

The effect of exposure to varying environments has been extensively studied with regard to 304SS, as stainless steels by definition were developed to resist oxidation and corrosion. The ultimate result of material development efforts in austenitic stainless steels is a chromium content which allows for a protective layer of chromium oxide to form on the surface of 304SS

(Callister, 1996). However, several different oxide and carbide types are formed under a number of varying conditions.

At temperatures near 20°C (68°F, 273°K), Type 304 stainless steel is commonly utilized for structural purposes, cutlery, and sheathing of work tables or food handling equipment. Under normal use, 304SS maintains a thin layer of chromium(III) oxide (Cr_2O_3) on the order of 10Å thick (Langevoort, Sutherland, Hanekamp, and Gellings, 1987). This passivation layer is what protects the steel substrate from oxidation and corrosion. If the oxide layer is penetrated or scraped away, a new layer forms instantly as the underlying chromium bonds with oxygen in the air (Qiu, 2001).

When service temperatures of 100°C (212°F, 373°K) or higher are met in an air environment, the chromium oxide layer begins to allow iron to diffuse outward. The iron reacts with atmospheric oxygen as well, producing a thin layer of iron(II) oxide (FeO). Initially, both oxide layers grow at approximately the same rate (Huntz, et al., 2007) with iron(II) oxide forming over the chromium(III) oxide. At higher temperatures, growth of the chromium(III) oxide layer arrests, and the iron(II) oxide continues to expand. This further expansion of the iron(II) oxide causes a thin-film effect known to industry as “bluing”, wherein different spectral colors are reflected as the layer depth correspond to varying visible light wavelengths (Sabioni, et al., 2012). This phenomena is strongly temperature-dependent and weakly time-dependent, so parts with varying temperature distribution appear to reflect several colors, as pictured in the unevenly heated sheet of steel in Figure 2.11.

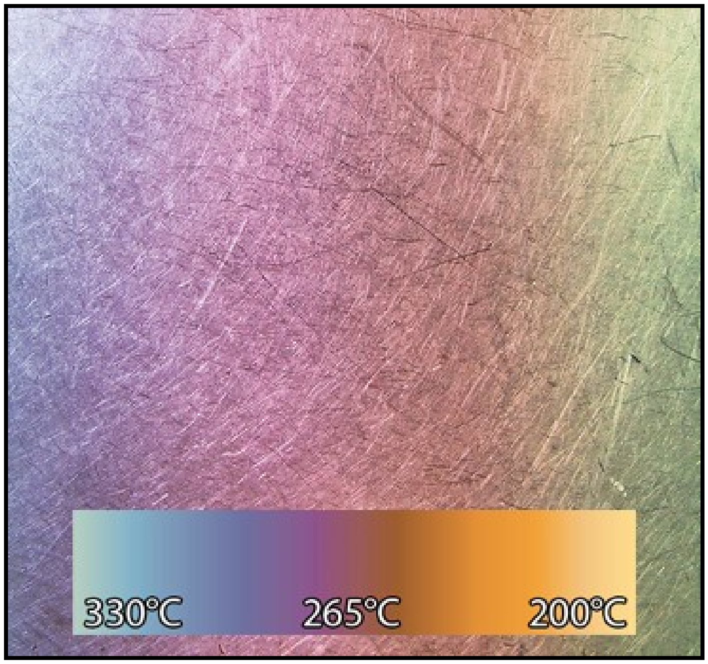

Figure 2.11: Varying spectral reflection of 304SS subjected to asymmetric heat application (resistance furnace enveloping the left side of the specimen only, with inlaid scale).

With increased temperature, the iron(II) oxide layer grows beyond the thin-film stage and becomes more easily recognizable as its natural dark-gray to black color (Alpha Chemicals MSDS, 2006). At this stage, some of the cubic structure of iron(II) oxide can oxidize into tetrahedral or rhombohedral iron(II,II) (Fe_2O_3) and iron(III) (Fe_3O_4) oxides. As the crystals have different structures, the combined layer is rough and weakly adhered to layers of oxides which are closer to the base metal (Smolik, et al., 1987). This outer layer is dark, rough in appearance, and flakes away easily, as evident in the macroscopic photo of Figure 2.12.

Figure 2.12: Heavy layers of brown and black oxides are present on a steel chain (Wong, 2008).

If subjected to an environment with high hydrogen content, the iron(III) oxides will become hydrated, forming Fe_2O_3-n(H_2O), which is the most common form of rust. In high-moisture environments, rust becomes the dominant oxide on the surface of 304SS (Ishida, et al., 1986). Chemically pure rust is produced in powder form as a pigment and oxidizing agent, and appears red or brown in color. Rust observed in steels which have been subjected to service conditions will be tinted red or brown due to high quantities of rust, but may not appear as chromatically intense due to impurities. Figure 2.13 depicts hydrated ferric oxide in its pure form.


Figure 2.13: Hydrated iron oxide powder appears as red or brown in color.

Under conditions where tensile stress being is applied in addition to thermal loading, exacerbated iron oxide layer growth occurs. The mechanical action allows for additional diffusion of iron, coupled with deeper oxygen penetration. Thicker layers will exhibit macroscopic crack propagation on the outer surface of the oxide, which subsequently provides a path for corrosion mechanisms. Oxides begin intrusion into the substrate in the form of intergranular microcracks (Lozano-Perez, S., et al., 2012). As mechanical loading at high temperature continues, the brittle outer oxide layers will crack, and then begin to break off from the underlying layers in the form of flakes (Picqué, et al., 2006).

The cracking and flaking of these layers of scale are due to a number of different mechanisms that occur during fully-reversed cycling. Such mechanisms are attributed to the mismatch of the material properties of the steel and oxide scale manifesting itself in multiple ways (Schütze, 1995). Regardless of temperature, the oxide layer will have an elastic modulus that exceeds that of the steel by near ten percent, is approximately four times harder, and exhibits more brittle behavior with a much lower failure strain (Nagl, et al., 1994). With good bonding between the scale and the substrate, this mismatch first promotes large transverse fissures in the scale, viewable in the Figure 2.14.

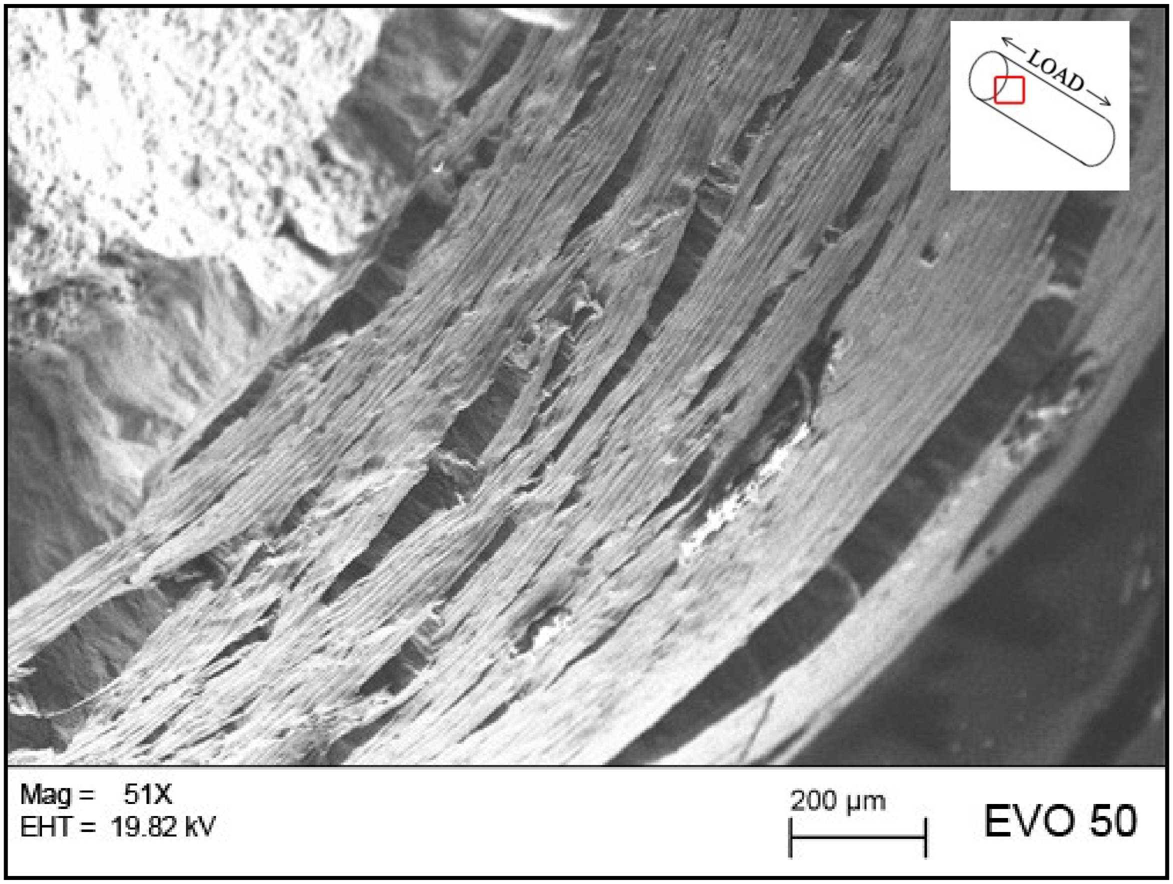

Figure 2.14: Severe fissuring in the outer oxide layer of a cylindrical section of 304SS.

As cycling continues, the layers of oxide can delaminate from the steel surface due to condition-specific mechanisms. When in tension, the opening of transverse cracks coupled with the high longitudinal strain can allow oxide flakes to disbond and fall away from the scale layer. When in compression, similar disbonding occurs due to buckling of the stiffer oxide layer (Picqué, et al., 2006). In both load directions, a difference in moduli can lead to significant shear stresses at the interface. In common mixtures of type 304, thermal expansion rates of the steel are relatively high, leading to exacerbation of the shear at the oxide/base interface (Outo Kumpu, 2012). The diagram in Figure 2.15 shows an example of each type of spallation mechanism.

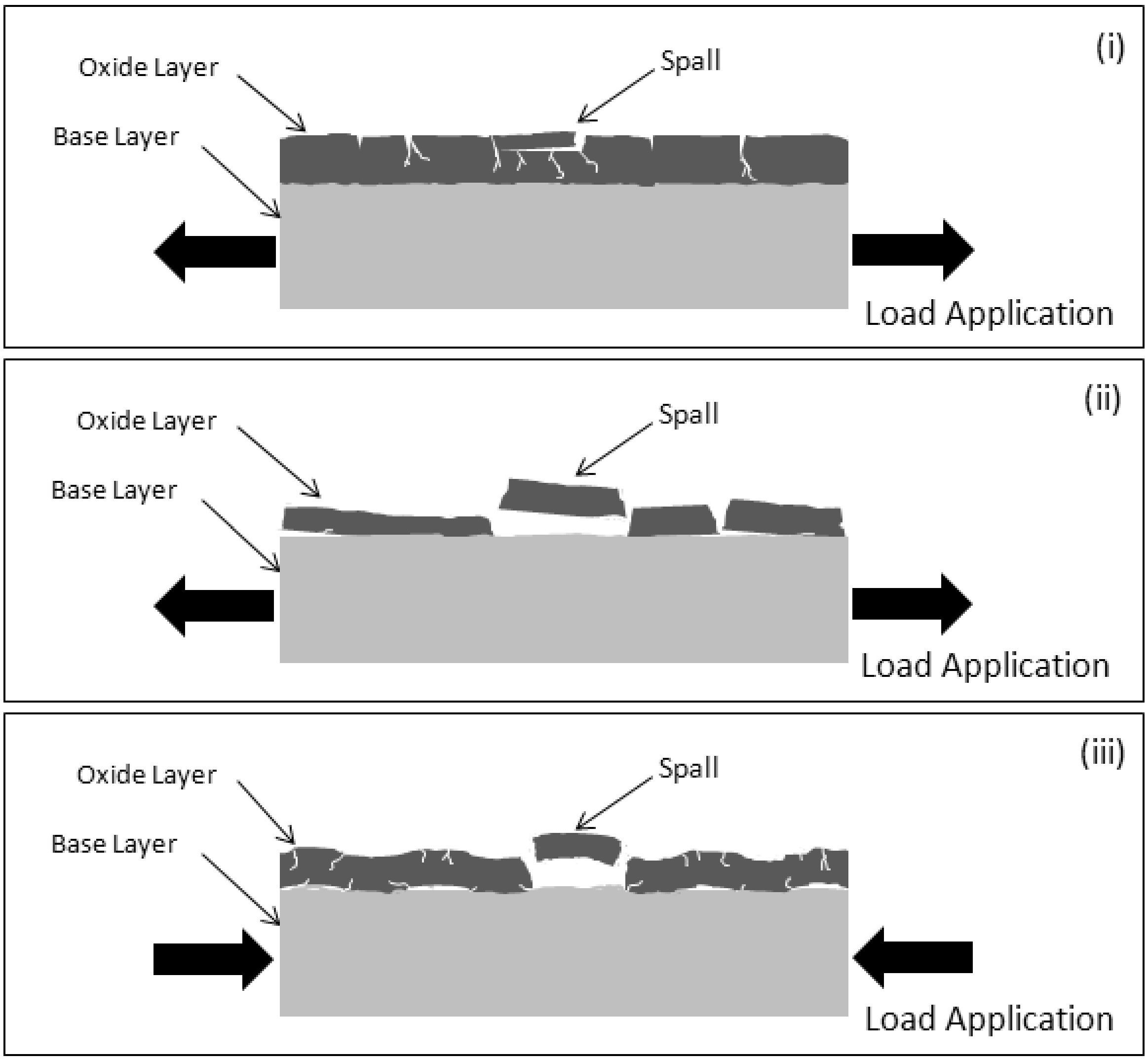

Figure 2.15: Oxide spalling due to: (i) Tensile load with transverse cracking and strong bonding, (ii) Tensile load with high interface shear stress, (iii) Compressive load with buckling and poor bonding.

These oxide spallation mechanisms allow for continual oxide growth and thus removal of iron and chromium from the parent material (Langevoort, J., Hanekamp, L., Gellings, P., 1987). This action could eventually contribute to chemical weakening of the 304SS, but other mechanisms which are more dominant often obscure the effects (Vesel, et al., 2008). While spallation of the outer layers of oxide may appear more visually compelling, it is important to note that this is a secondary effect of the oxidation kinetics (Qing-xin, 2009), with the part or specimen oxide intrusion depth being the important factor in life reduction under fatigue conditions (Nishino and Yamada, 1994).

Identification of intruding cracks will reveal two subtypes of oxide crack mechanisms that can affect fatigue life through offering an initiation point for the primary crack. Both of these methods can lead to intergranular or transgranular propogation, based on the material and presence of other damage due to load type (Sehitoglu, 1992a). A fissure which intrudes into the base material without losing significant portions of the oxide is identified as "Type I". These cracks therefore retain oxide build-up at the crack tip, which under different circumstances can either reinforce/protect the base material or provide a brittle point for failure to occur (Remy, et al., 1995). "Type II" cracks are identified by some loss of material coupled with significant oxide growth in multiple layers in the loading direction. Cracks of this nature penetrate level by level, each time leaving an oxide stratum behind as they advance into the grain structure of the parent material. Depending on the load, the stratum layers may partially or totally delaminate from those beneath them, which in turn causes spalling at the crack mouth. The two subtypes of oxide-assisted crack are illustrated in Figure 2.16.

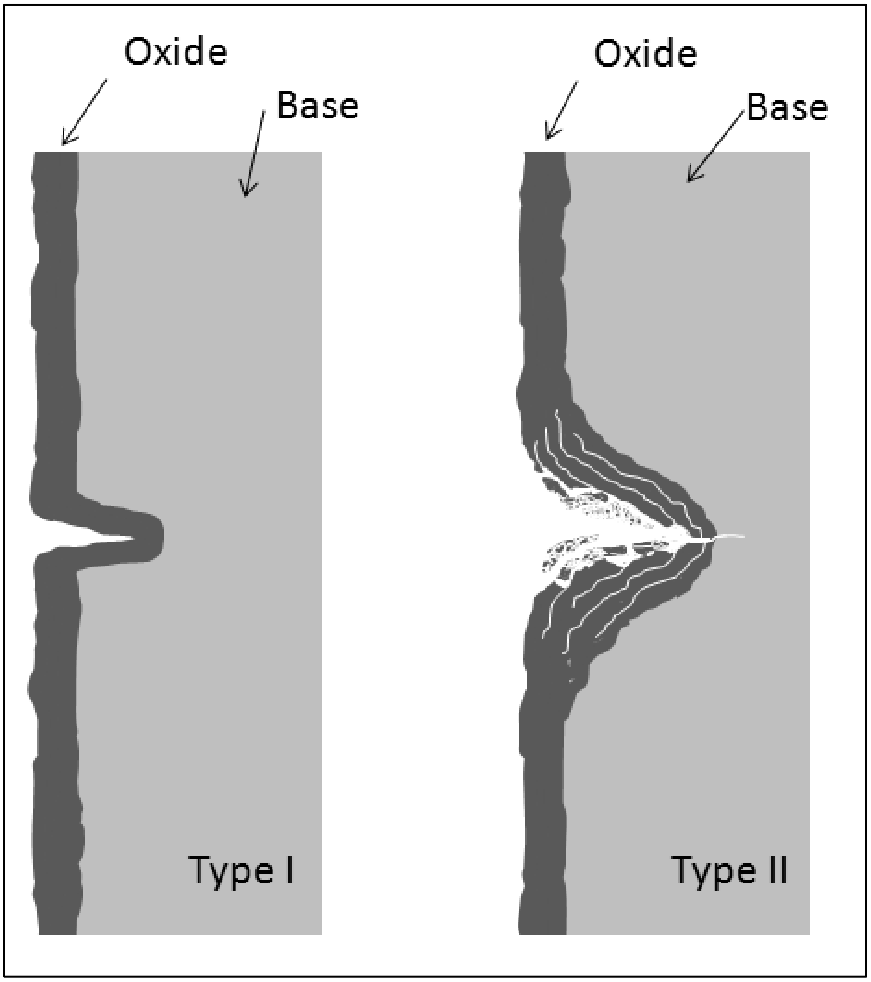

Figure 2.16: Type I and Type II intruding oxidation-assisted cracks.

An important indicator of crack intrusion potential can be inferred from the oxide layer thickness (Kunio, et al., 1984), thus substantiating the necessity to model oxide growth accurately. In many materials, including austenitic stainless steel, the favored method of modeling this growth is the parabolic rate law (Visscher, 2006). The model is simplistic in its final form, and can offer information about both the rate of oxidation and the depth of the oxide layer. In austenitic stainless steels, the transfer of Fe^{+} ions through the outer perimeter of the oxide layer from the base metal is the enabling factor for continued oxidation. The Fe^{+} cation flux through the existing oxide layer is governed by the concentration of Fe left in the steel and the layer depth. In expressing this as a rate, the ion velocity through the scale layer dx_{Fe}/dt is proportional to the mobility B_{Fe}, temperature T, and concentration gradient dc_{Fe}/dx:

$$\frac{dx_{Fe}}{dt} \propto (B_{Fe})kT\frac{dc_{Fe}}{dx} \tag{2.8}$$

With the introduction of a fitting constant *C* and the parabolic rate constant *k'*, the expression takes the form

$$k' = C(B_{Fe})kT\frac{dc_{Fe}}{dx} \tag{2.9}$$

that can then be recombined with the previous and integrated to arrive at

$$x^2 = 2k't \tag{2.10a}$$

which in more recent literature (McGuire, 2008) often takes the form:

$$h = \sqrt{k_p t} \tag{2.10b}$$

Where *h* has been substituted for *x* in describing oxide depth, and the parabolic fit constant k_p further simplifies the use. In some cases with Type 304 steels, a single constant *k* is not sufficient to describe the oxide growth rate or thickness. Some austenitic stainless steels display rates that change at the point where spalling begins, thus necessitating a piecewise parabolic fit. Variations in trace elements, especially silicon and aluminum in the case of 304SS, can retard or expedite the oxidation process in a highly nonlinear fashion (Lacombe, et al., 1993). Nickel content variation also has a strong effect on the oxide rates at different temperatures (Lacombe, et al., 1993). However, in even in those cases, the constant k can be replaced with an effective term k_{eff} that more adequately describes the behavior with some dependency on other variables, thus providing a clear indicator of oxide damage in a mathematically concise format.

2.2 Thermomechanical Fatigue

Thermomechanical fatigue is a term used to describe load cases that include both mechanical and thermal cycling. The complex nature of TMF cycling imparts fatigue, oxidation, and creep damage, which vary in proportion depending on the conditions of the loading and the susceptibility of the material to each mechanism (Sehitoglu, 1996). TMF life prediction is a difficult multivariate problem, but necessitated by a wide range of applicability to modern high performance engineering systems.

2.2.1 About TMF and its Applications

The type of TMF cycle is defined by the relative timing of the mechanical and thermal load application. A specimen in a TMF cycle which is entirely in phase (IP) would experience the highest temperatures during maximum mechanical strain application. An out-of-phase (OP) TMF cycle applies the greatest mechanical strain during the lowest temperature. While these loadings incorporate elements of thermal fatigue and isothermal low cycle fatigue, the behavior of specimens and parts under TMF conditions differ from what is encountered in the less complex load types (Engler-Pinto and Rézaï-Aria, 2000).

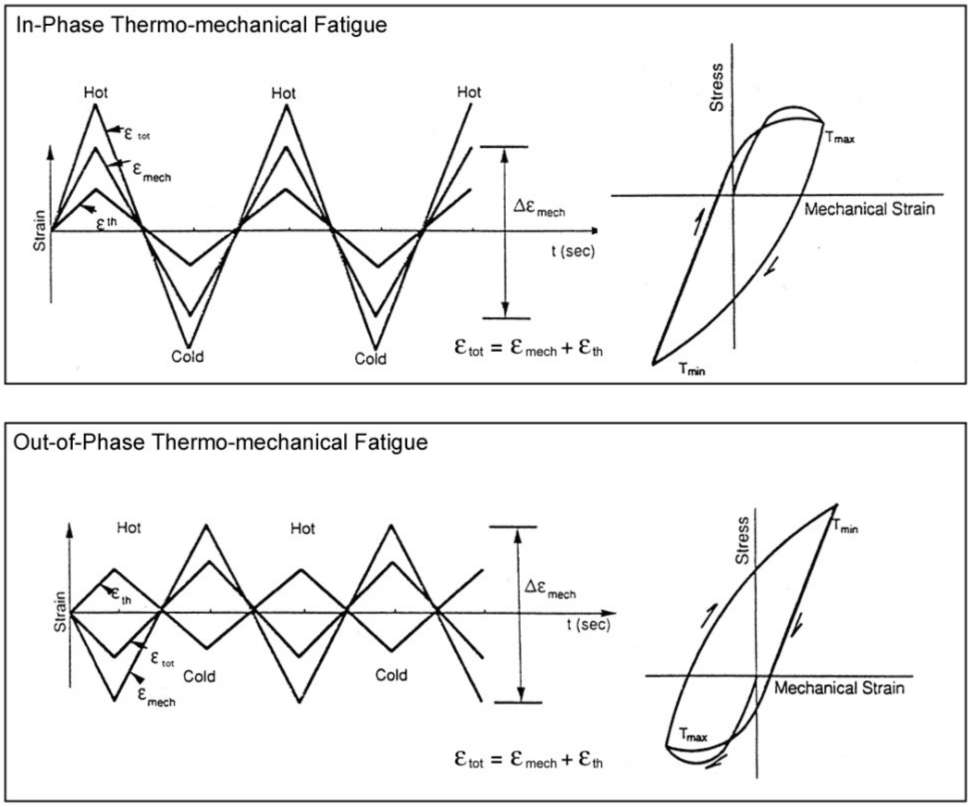

Figure 2.17: In-phase (upper) and out-of-phase (lower) fully-reversed strain-controlled TMF cycles (modified from Cai, 1999).

Simplistic strain-controlled TMF load cycles, like those shown in Figure 2.17, include idealized in-phase and out-of-phase configurations. While TMF cycle types could be infinitely variable, in practice the load schemes correlate to the types of applications that induce them. Common examples include diamond phasing, nonlinear cycling, and TMF with dwell periods. A typical rotor steel specimen loaded to simulate steam turbine conditions, for instance, would incorporate an out-of-phase condition that has mechanical strain levels at a maximum of 1.0%, low strain rates ($\sim 10^{-5}$/s) and temperatures varying between 300°C (572°F, 573°K) and 550°C (1022°F, 823°K) (Holdsworth, Mazza, and Jung, 2003).

Referencing isothermal fatigue as a touchstone, damage on a part or specimen due to intrinsically more complex TMF cycle types is inherently difficult to quantify. Common damage mechanisms that are present in isothermal cycling can be found to be either proportionally or qualitatively different when considered under TMF conditions (Kuwabara, and Nitta, 1976). Oxide growth and subsequent intrusion mechanics can vary significantly with respect to TMF cycle type (Esmaeili, et al., 1995). Creep effects can be much more or much less severe than in isothermal counterparts with TMF phase differences, especially in the presence of a cycle with dwell periods (Skelton, 1987).

While multiple standalone damage mechanisms are induced by TMF, certain strain and phasing conditions can cause interactions between damage mechanisms that may cancel or amplify their effects (Kuwabara and Nitta, 1977). Compared against corresponding LCF strain and temperature levels, TMF lifetimes can be reduced, extended, or remain unchanged based on the specifics of the load and phasing (Wahi, et al., 1997). With many parallel variables of varying influence and complexity, lifing data from TMF does not correlate well with analogous data from IF situations. Consequently, methods traditionally useful in life prediction for isothermal fatigue cases cannot be readily extended into TMF cases. Some materials, with an example found in AISI 1010 steel, are reduced in all non-isothermal phasing types, hence serving as an argument that TMF lifing is an important issue that should be handled independently of LCF lifing (Jaske, C., 1976).

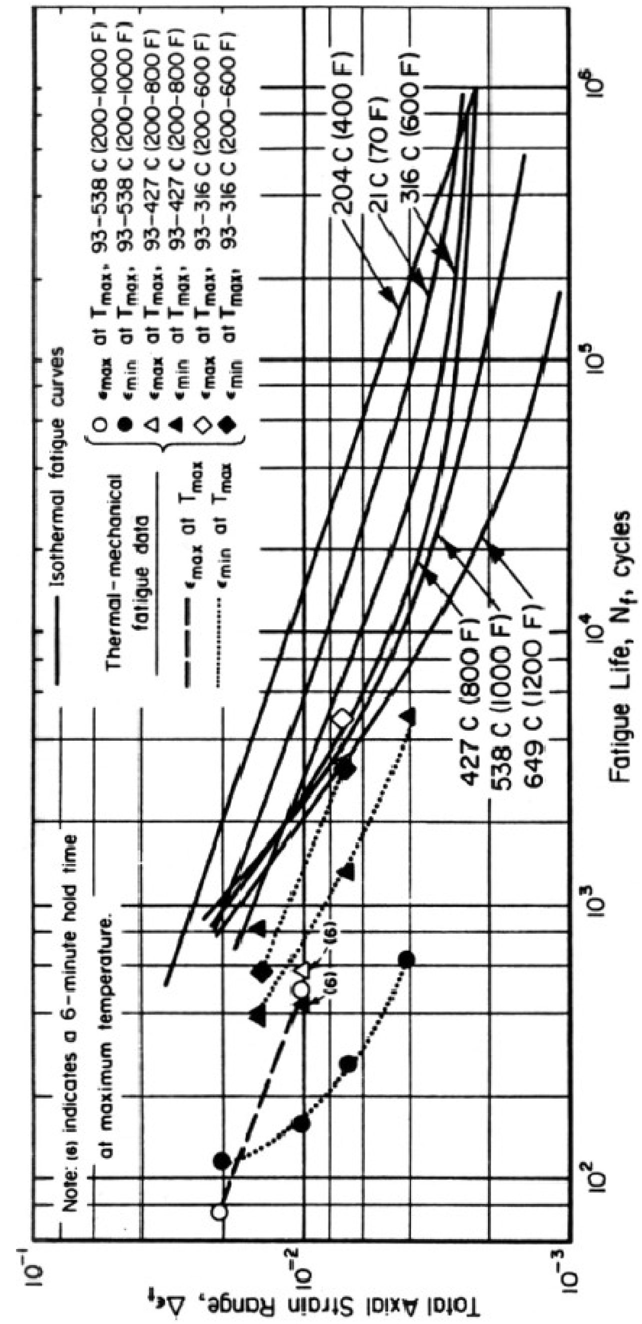

Figure 2.18: Comparison of LCF and TMF lifetimes for AISI 1010 steel (from Jaske, 1976).

As evident from the strain-life curves in Figure 2.18, TMF reduces cases by an order of magnitude in some circumstances when compared with LCF. Hence, a great deal of motivation exists for accurate life prediction. To date, many modeling efforts focused purely on TMF have been made via a broad array of approaches, but a widely-accepted life prediction framework for TMF has remained elusive (Cai, et al., 1999).

2.2.2 TMF in Type 304 Stainless Steel

In the case of TMF, the non-isothermal loadings not only influence variance in the temperature-dependent properties of the material, but also greatly affect the damage mechanics. The severity levels of individual damage mechanisms are variably influenced by strain, temperature, time, and phasing (Kuwabara and Nitta, 1976). Additionally, processes that strengthen or inhibit interaction between multiple mechanisms are similarly influenced, thus further complicating the intricate set of interconnected physical effects (Kuwabara and Nitta, 1979). These mechanistic behaviors in 304SS have historically been studied through comparisons between IF, IP, and OP cycle types (Kuwabara and Nitta, 1977), with most testing coming from fully-reversed experimentation. While individual behaviors for specific load parameters can be identified as major contributors to the ultimate failure of the specimen after the fact, there is still difficulty in determining the behavior due to applied conditions in advance of fracture.

Though TMF of 304SS promotes complex behavior that defies a comprehensive set of rules, a few general trends in data have become identifiable. When temperature differences are low and consequential thermal strain is kept minimal in comparison to the mechanical strain, austenitic steels behave much like they do in high-temperature fatigue cases (Shi, 1993). Viewable as a group of closely-grouped data points in the strain-life curve of Figure 2.19, it is difficult to determine the impact of IP or OP TMF phasing on the fully-reversed test specimens.

However, the most obvious broad trend is that in most load cases, both OP TMF and IP TMF have a life reduction effect when compared to isothermal fatigue (Lampman and Zorc, 2007).

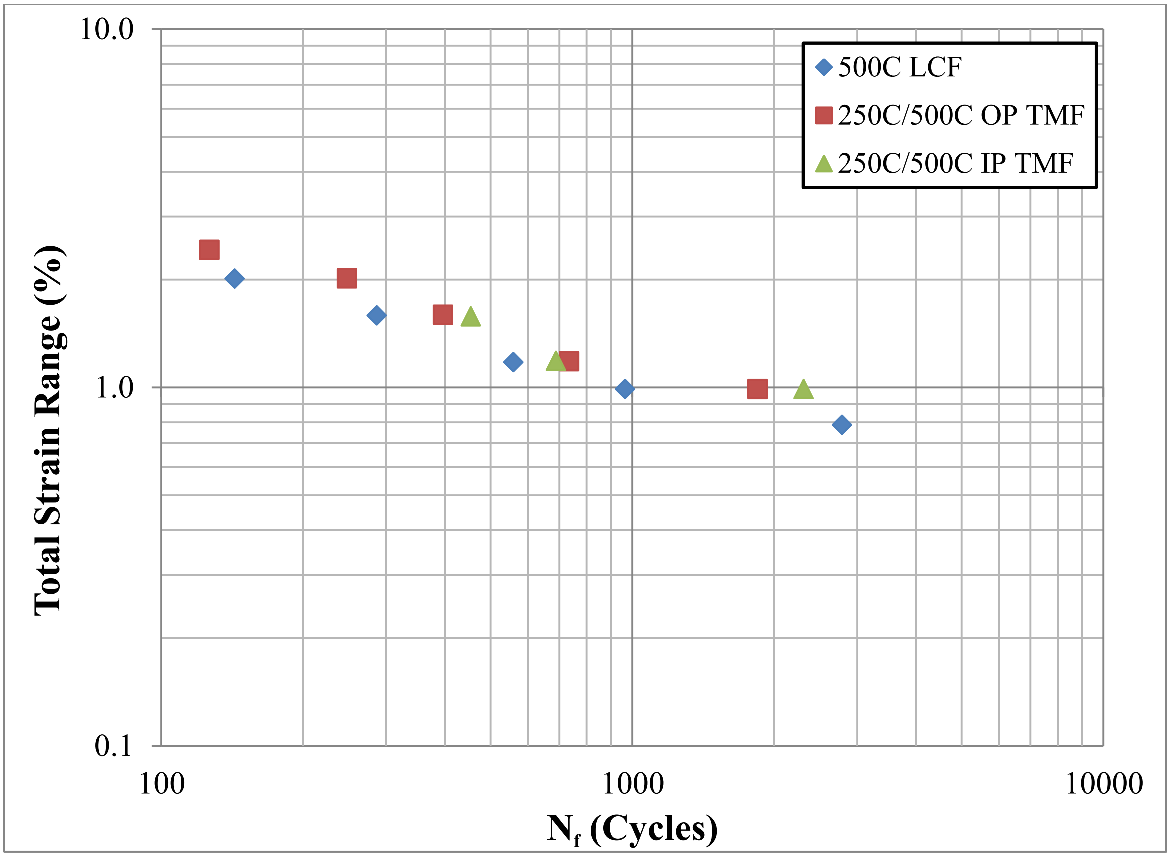

Figure 2.19: TMF and IF data within the same scatterband in the case of low thermal strains and maximum temperatures of 500°C (from Shi, et al., 1993).

When compared against one another, IP TMF is generally shown to have a more damaging effect versus OP TMF, assuming that the thermal strain is sufficiently high (Coffin, 1979). This particular trend is better identifiable in even the limited strain-life data from Coffin's work, shown in Figure 2.20, and serves as the basis of several qualitative assertions made in the industry-accepted ASM International references (Lampman and Zorc, 2007).

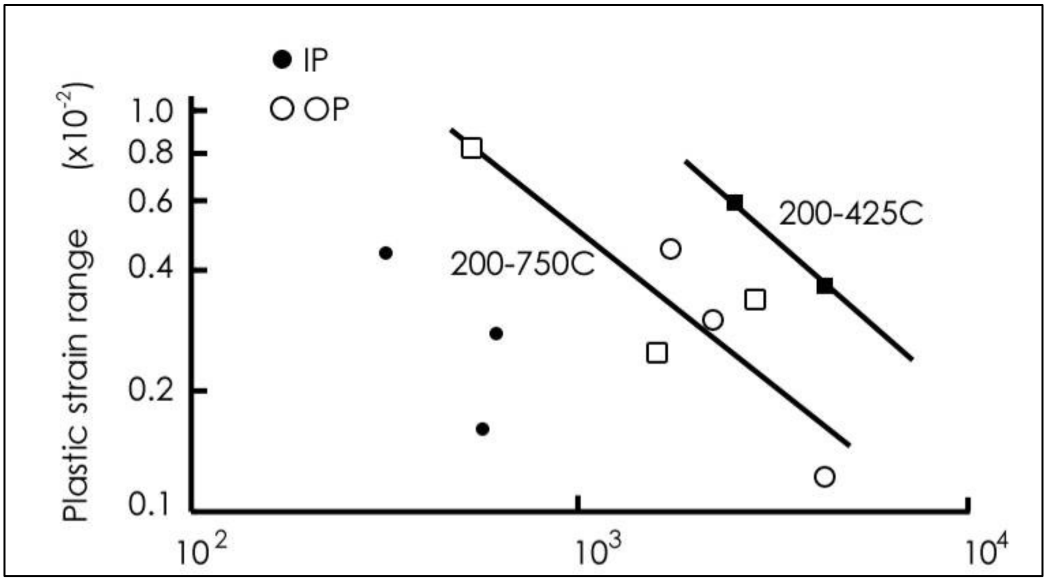

Figure 2.20: Data of Coffin, IP and OP TMF in 304SS (from Lampman and Zorc, 2007).

TMF cycling which incorporates hold times in tension or compression that are sufficiently long lead to observation of another important effect. While hold times less than one hour in duration are severely detrimental to life in IF, OP TMF, and IP TMF cases (Skelton, 1987), microstructural ageing that occurs in longer hold periods can inhibit cavitational damage processes and thus provide an extension effect (Westwood, 1979). The trends in Westwood's data are evidenced in Figure 2.21 and a significant recovery effect is noted, especially at large strain ranges.

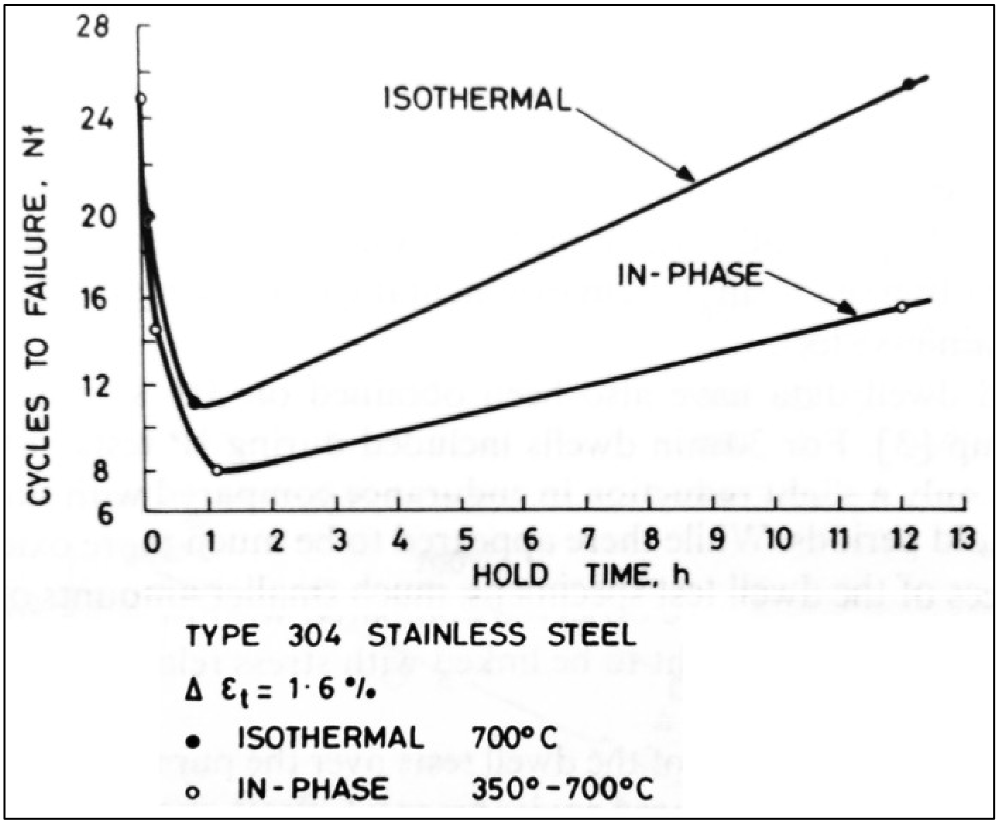

Figure 2.21: Effect of long duration holds on IF and IPTMF life (from Westwood, 1979).

An additional line of TMF research in 304SS has strongly correlated life reduction with intergranular crack initiation. The work of Kuwabara and Nitta in 1979 as well as the work of Westwood and Lee in 1982 was revisited by Shi, et al. while developing a model for behavior (Mitchell and Landgraf, 1993). The conclusions of all of the researchers involved suggested that intergranular cracking and the mechanisms that support it are a prime cause of failure in 304SS when regarding both IF and TMF cases. This idea underpins the observations in that previously published research where a number of grain-boundary centric mechanisms resulting from certain load conditions that were established to correlate with life reduction in 304SS.

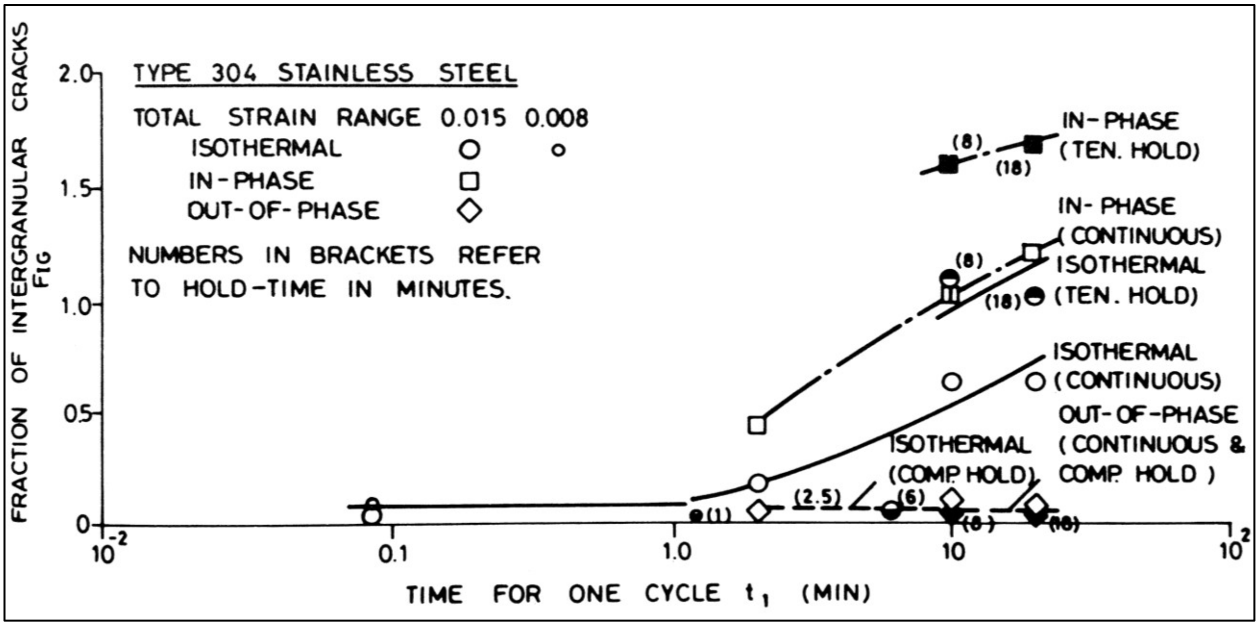

Figure 2.22: Correlations between the presence of intergranular surface cracks with cycle time for IF and TMF cases with and without holds, with minimum/maximum temperatures of 300°C/ 600°C (from Mitchell and Landgraf, 1993).

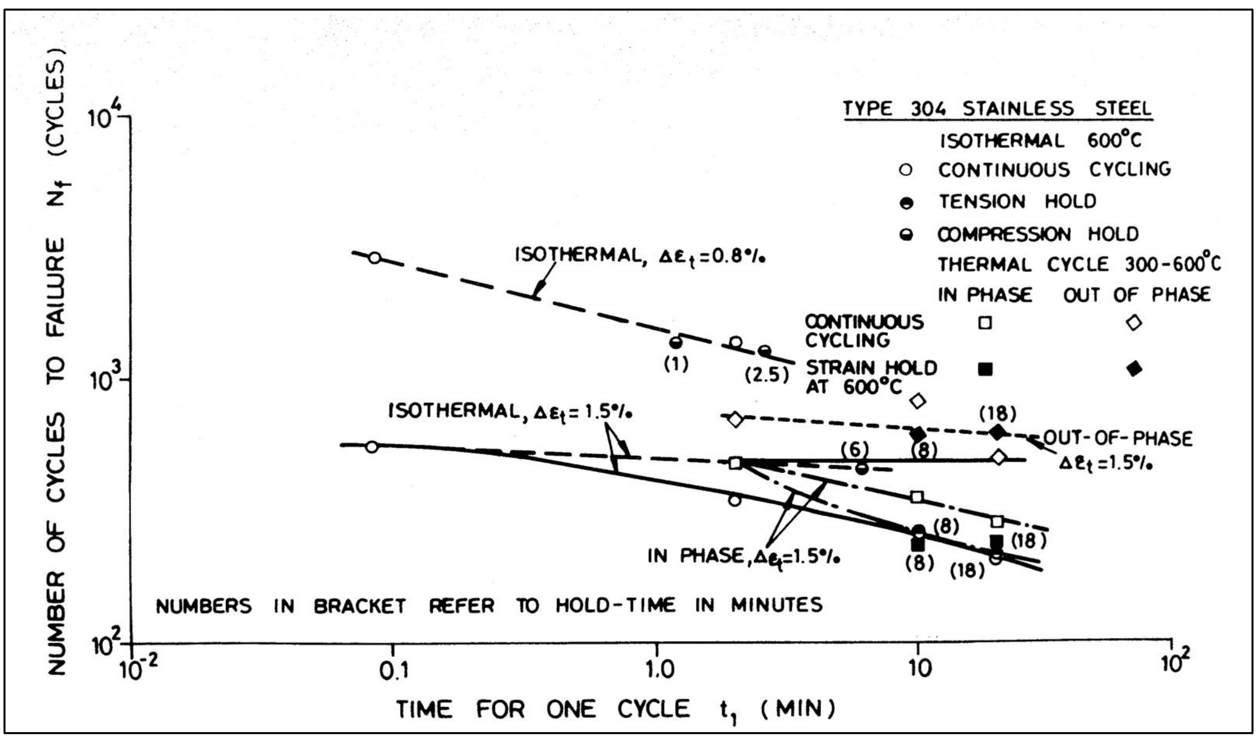

Figure 2.23: Cycle length effect on life reduction in IF and TMF tests cited in plots of Figure 2.22 (from Mitchell and Landgraf, 1993).

Aside from the simplistic cycle frequency effect identifiable in Figures 2.22 and 2.23, the data more importantly indicates dependency on the presence of grain structure-related damage. In 304SS, many load conditions and different phasings contribute to dominant and less dominant grain-damaging mechanisms in a complex manner. Under both IP and OP TMF, higher dislocation density with more mixing of dislocation types is observed (Taira, 1973), increasing the strain-aging effect of cycling with respect to IF cases (Fujino and Taira, 1979). In-phase loadings exhibit grain boundary sliding in tension versus compression (Taira, Fujino, and Ohtani, 1979), which can cause some observable micro-ratcheting. Type 304SS under IP TMF also has a higher density of intergranular cracks (Taira, Fujino, and Marayuma, 1974), and at grain boundaries cavity nucleation can be facilitated by relaxing of residual stresses at high temperature (Sheffler, 1976). In OP TMF cases, the lowest amount of intergranular crack formation is observed (Westwood, 1978). Additionally, cavity nucleation is effectively suppressed by high-temperature compressive strain states (Miller and Priest, 1983). Together, these findings account for why OP TMF loadings can exceed those of IF in terms of life under some circumstances (Zauter, et al., 1993). The consideration of these many trends in parallel constructs a framework of expected behavior when 304SS undergoes different mechanical loadings.

2.2.3 TMF Life Prediction Approaches and Limitations

An accurate model for TMF life prediction is desirable due to its wide applicability in modern machines. Crack initiation and early propagation due to TMF are the primary life-limiting factor for many parts in high-performance service conditions. Thus, research is driven directly by technical viability for industry, in power generation turbines (Embley and Russell, 1984), aircraft turbines (Coppola, et al., 2010) automotive powerplants (Riedler, et al., 2007) passenger trains (Wetenkamp, Sidebottom, and Schrader, 1950), and petrochemical processing equipment (Majumdar, 1987). A viable TMF lifing model is sought in order to allow for more efficient design and optimized service schedules that would increase both output and reliability of such systems.

Development of TMF life prediction models follows a process that, in the generalized sense, is not unlike life prediction modeling in more simplistic IF load types (Sehitoglu, 2006). In most cases, peak or timed strain, stress, temperature, and cycle count data is obtained from a series of standardized laboratory tests. Idealized loadings are applied to simple specimens in an effort to approximate service conditions of parts (Taira and Ohnami, 1963). Data is then analyzed, reduced, and fitted for use in any number of approaches that have the common goal of analytically describing the behavior of the material under TMF during its lifetime (ASTM, 2004).

While a simplistically-defined model that can correlate the number of cycles to initiation (N_i) or failure (N_f) with common mechanical or average stress (σ_m, σ_a, etc.) or mechanical, average, or ranges of strain terms (ε_m, ε_a, $\Delta\varepsilon_{pl}$, etc.) in addition to maximum and minimum service temperatures (T_{max}, T_{min}) is decidedly advantageous (Sehitoglu, 1996), the complex nature of the loadings and temperature-dependent material response necessitates the incorporation of additional variables into consideration (Sehitoglu and Boismier, 1990). Stress and strain ranges (divisible into thermal, elastic mechanical, and plastic mechanical components), thermal-mechanical phasing, hold times, and material response at high and low temperatures in the applied thermal range have been candidates for the most simplistic approaches. More involved prediction methods that have initially shown promise include strain range partitioning (Halford and Manson, 1976), damage rate (Miller, McDowell, and Oehmke, 1993) and damage accumulation (Kadioglu and Sehitoglu, 1993).

In the case of strain range partitioning (SRP), TMF is treated as a load case in which creep and fatigue interact synergistically, with the splitting of the cycle hysteretic response into constituent fundamental parts giving the method its namesake. These inelastic cycle types are shown in Figure 2.24 and there are four possible modal configurations that are labeled based on the assumed plasticity in the tensile/compressive parts of the cycle (plastic/plastic, plastic/creep, creep/creep, and creep/plastic). The modes are handled independently and give the flexibility of addressing dependencies on each individual strain (and thus microstructural damage) type (Manson, Halford, and Hirschberg, 1971).

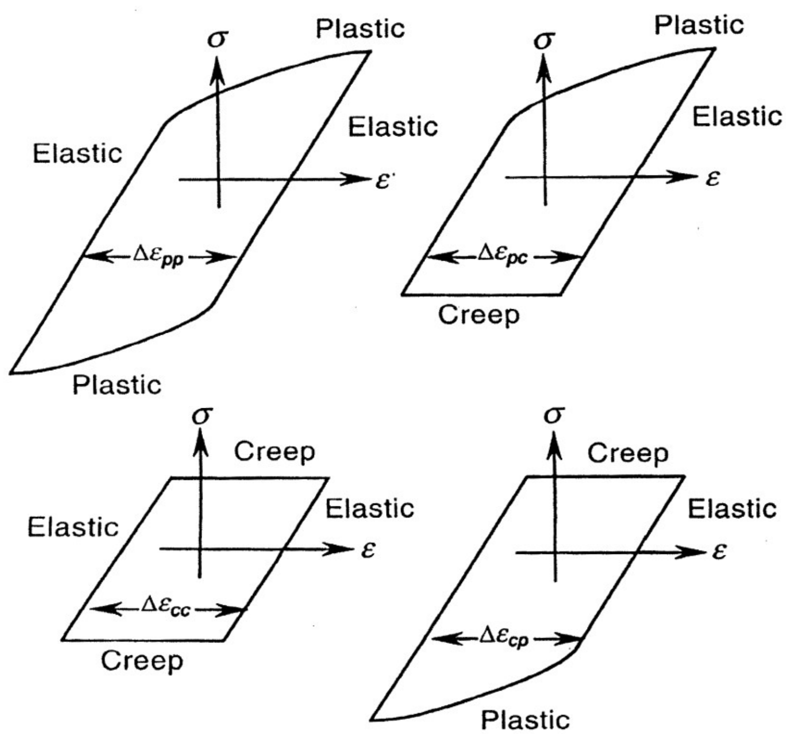

Figure 2.24: Types of decomposed fundamental cycles used in the SRP method in TMF cases (from Stephens, et al., 2001).

With the assumption that inelastic strain is the primary contributor to each constituent cycle's effect on life, individual relations can be built the power law form

$$\Delta\varepsilon_{ij} = A_{ij}\left(N_{ij}\right)^{b_{ij}} \tag{2.11}$$

in which *A* and *b* fitting constants are found for each mode. Therefore, a total reduction in life is dependent on all the specific fits for the pp, cp, pc, and cc modes. A linear summation rule can then be stated as

$$\frac{1}{N_f} = \frac{F_{pp}}{N_{pp}} + \frac{F_{cp}}{N_{cp}} + \frac{F_{pc}}{N_{pc}} + \frac{F_{cc}}{N_{cc}} \tag{2.12}$$

where *F* denotes the relative fraction of any one type of inelastic strain present. Issues with this particular method have not rendered it completely without use, but the inherent shortcomings are significant. The shape of non-idealized TMF hysteretic responses make the SRP process difficult to apply, as the transition from one type of strain to another is not apparent. Additionally, the method has the effect of masking effects due to dwell periods and small strains dues to its graphic nature. Lastly, the effects of any environmental processes are not addressed, which can lead to lack of conservatism in the model (Cai, 1999).

The damage rate method of Miller, McDowell, and Oehmke explicitly accounts for the contribution of fatigue, creep, and oxidation. The method proposed in 1993 uses a physical measurement of crack length in order to quantify the damage occurring as cracks progress. The general form of the model is a linear combination of terms, but instead of inelastic strain contributions to life reduction, a summation of crack propagation rates is utilized to balance the damage. Thus, the model provides an overall damage rate-based on the fractional share of each mechanism as

$$\frac{da}{dN} = \left.\frac{da}{dN}\right|_{fatigue} + \left.\frac{da}{dN}\right|_{oxidation} + \left.\frac{da}{dN}\right|_{creep} \tag{2.13}$$

where *da/dn* is the measurement of crack length *a* per cycle *N*. The growth rate due to fatigue is based on the ΔJ parameter,

$$\left.\frac{da}{dN}\right|_{fatigue} = C_f \Delta J^{m_f} \tag{2.14}$$

with C_f and m_f representing fitted constants, and ΔJ calculated based on the geometric factor *Y,* cyclic hardening exponent *n'*, measured crack length *a,* and the stress and strain ranges $\Delta\sigma$, $\Delta\varepsilon_e$, and $\Delta\varepsilon_p$. This relation, given as

$$\Delta J = 2\pi Y^2 \left[\frac{\Delta\sigma\Delta\varepsilon_e}{2} + \frac{f(\frac{1}{n'})\Delta\sigma\Delta\varepsilon_p}{2\pi}\right] a \tag{2.15}$$

also incorporates an additional experimentally-determined function *f* . Oxidation damage rate is handled by incorporating time and temperature dependence into the ΔJ approach. Equation 2.16 shows the addition of fitting constants φ and m_o, as well as the coefficient C_o:

$$\left.\frac{da}{dN}\right|_{oxidation} = C_o \Delta J^{m_o} \Delta t^{\varphi} \tag{2.16}$$

The coefficient C_o is formulated based on oxidation activation energy Q_{ox}, minimum effective temperature T_{eff}, minimum effective stress σ' and the universal gas constant R, but is further reliant on empirically-determined B, k, and C_o' terms:

$$C_o = C_o' exp\left[\frac{-(Q_{ox} - (B\sigma')^k)}{RT_{eff}}\right] \tag{2.17}$$

The final term, which accounts for the creep damage as the crack progresses, is of a similar form

$$\left.\frac{da}{dN}\right|_{creep} = C_c(C')^{m_c} \tag{2.18}$$

requiring fitting exponent m_c and coefficient C_c, determined as:

$$C' = \left\langle a\left[\frac{1}{t_t}\int_0^t \sigma\varepsilon'_e dt - \frac{1}{t_c}\int_0^t \sigma\varepsilon'_e dt\right]\right\rangle \tag{2.19}$$

with t_t and t_c denoting time in tension and compression. Significant complexity is added at this stage, where the Macaulay brackets denote a piecewise function that is determined by an additional constitutive model built for the specific material system. Thus, while this particular model was found to anticipate critical crack lengths within a factor of 2 for most conditions, it is extremely complex, proven only to work on 247-series nickel alloys, and relies on several fitting methods that require a complete set of failed specimen data and physical measurements in advance of having any predictive capability. Additionally, this method requires initiation of cracking to be useful- it cannot be used to imply when initiation of a primary crack has occurred (Cai, 1999 and Mitchell and Landgraf, 1993).

Recent TMF life modeling studies have improved prediction capability in comprehensiveness and depth. Utilization of a greater number of load parameters, as well as introduction of pertinent phenomenological observations (Seifert, et al., 2010), has led to large, non-unified approaches that are sometimes highly nonlinear in nature (Chataigner and Remy, 1996). These approaches, while more mathematically intensive, offer a more comprehensive basis for future model development (Seifert and Riedel, 2010). The recent maturation of modern computing packages have provided compensation with continually increasing numerical processing capability (Howe, et al., 2012).

Additional models have accurately correlated life to directly observable effects. These include some which follow techniques based on empirical/phenomenological mixes (Miller, 1976), and fracture mechanics-based models (Nissley, 1995). The accuracy in such models is promising, yet these approaches require additional inputs and assumptions (Evans, Jones, and Williams, 2005), including but not limited to explicit physical measurements, phenomenological terms, and unknown TMF characterization parameters (Neu, R., and Sehitoglu, H., 1989). If the model lacks robustness, many parts or specimens may need to be consumed and analyzed before it would be useful. At present, TMF life prediction models for a single material system have been considered successful if observed life lies within the order of magnitude of the predicted life (Halford, et al., 1992).

2.2.4 Recent Damage-Centric TMF Lifing Methods

In an effort to improve upon the predictive consistency of behavioral models, a number of techniques have evolved in recent decades and persisted to be presented as the forefront of research. Large and computationally intensive constitutive models have gained favor over more compact analytical approaches in the pursuit of increased accuracy (Lemaitre and Chaboche, 1974). Specifically, damage-based models have gained wide popularity, rapidly evolving from the simplistic linear models first applied to TMF (Taira, 1962). Incorporation of elements from predictive modeling of individual mechanisms (Hayhurst, 1976) has led to development of constitutive models of increased complexity that include nonlinearly proportioned terms and summations (Leckie and Hayhurst, 1977). Though computationally vigorous, more adequate handling of the balancing and overlap of damage from different mechanisms increases suitability for application to complex TMF behaviors. A line of research which utilizes such methods (Remy, et al., 1993) proposes a model for crack initiation and growth that separately and explicitly handles interaction between damage mechanisms through sub-models based on physical observation (Reuchet, and Remy, 1983). Accurate predictions have also been obtained by recent energy-based models (Zamrik, Davis, and Firth, 1996), which modify previous damage (Ostergren, 1976) and interaction handling (Ostergren and Krempl, 1979) to include changes due to temperature and time in calculating hysteretic energy.

Most recently, researchers in TMF lifing have begun to plainly state that several unified models types are attempted and abandoned during a line of research in favor of a non-unified approach that offers better agreement with empirical data (Rosa, Nagode, and Fajdiga, 2007). In these types of studies, different damage types are sub-modeled via statistical lifing approaches, energy methods, physical measurements, chemical reaction kinetics, or other models according to their level of accuracy and compatibility with the others. The successful use of non-unified constitutive approaches reinforces the notion that simplicity may not be key in developing a good TMF model. A line of non-unified, constitutive lifing methods (Slavik and Sehitoglu, 1986) draw terms from physical observation of phenomena, as well as energy and traditional strain-life approaches in order to become more generally applicable yet continue to maintain significant accuracy (Slavik and Sehitoglu, 1987). A number of recent researchers also posit that still additional parameters and terms may either merit consideration or have yet to be developed in the bulk of current techniques (Gordon, Williams, and Schulist, 2008)

As non-unified constitutive approaches, by definition, handle contributing damage mechanisms separately, it is important to identify which of types of model structures would be amenable to the incorporation of notch sensitivity modifications. Such a structure, in which individual notch sensitivity terms tailored to the mechanisms could be assigned, is found in simple damage accumulation approaches (Sehitoglu, 2006). More specifically, the deconstruction of a TMF lifing model which has been used in both steel (Neu, and Sehitoglu, 1989) and Nickel-based alloy (Sehitoglu and Boismier, 1990) applications is exmplary in illustrating such a point. The model is of the cumulative damage type, broken into relations suitable for describing the effect of each mechanism. This simple extension of the Palmgren-Miner type rule for damage (Palmgren, 1924; Miner, 1945) is generally expressed as the sum of the inverse of the life terms:

$$\frac{1}{N_f} = \frac{1}{N_f^{fat}} + \frac{1}{N_f^{ox}} + \frac{1}{N_f^{cr}} \tag{2.20}$$

Each of the damage terms are independently determined with a method that offers as much physical backing as feasible balanced with a good fit with empirical data. The fatigue damage survivability term N_f^{fat} is represented by a power-law strain-life relation based only on fitting constant and exponent C and d:

$$\frac{\Delta\varepsilon_{mech}}{2} = C\left(2N_f^{fat}\right)^d \tag{2.21}$$

which mirrors the Coffin-Manson formulation (Manson, 1953; Coffin, 1954) with the exception of using a mechanical strain term $\Delta\varepsilon_{mech}$ in place of the plastic strain term used in the original relation. The oxidation damage term N_f^{ox} is based largely on physical elements,

$$\frac{1}{N_f^{ox}} = \left[\frac{h_{cr}\delta_0}{B\Phi^{ox}\left(K_{peff}^{ox} + K_{peff}^{\gamma'}\right)}\right]^{-1/\beta} \frac{2(\Delta\varepsilon_{mech})^{(2/\beta)+1}}{\dot{\varepsilon}_{mech}{}^{1-(b/\beta)}} \tag{2.22}$$

where h_{cr} represents the length of an environmentally-assisted crack, and δ represents ductility of the surrounding depleted zone. The phasing coefficient Φ^{ox} handles distribution of damaging effects that differ with IP, OP, and LCF phasing types. Constants B, K, b, and β assist in mapping the function to a form that parallels existing oxide formation models, as well as scaling the effect to be dependent on mechanical stain levels and rate. The model's creep term N_f^{cr} is developed and fitted in a likewise fashion. While largely based on stress components, this formulation remains dependent on the strain levels and rates as well:

$$\frac{1}{N_f^{cr}} = \frac{1}{t_c}\int_0^{t_c} exp\left[-\frac{1}{2}\left(\frac{\left(\frac{\dot{\varepsilon_{th}}}{\dot{\varepsilon_m}}\right) - 1}{\xi^{cr}}\right)^2\right] Ae^{\left(-\frac{\Delta H}{RT}\right)}\left(\frac{\alpha_1\bar{\sigma} + \alpha_2\sigma_H}{K}\right)^m dt \tag{2.23}$$

In this case, ΔH is the activation energy for the primary creep mechanism, while σ and σ_H represent the average and the hydrostatic stresses. The accompanying terms α_1 and α_2 appropriately scale the stresses during different parts of the cycle, as creep damage predominantly accrues only during the tensile loading (Argon, Chen, and Lau, 1980). This particular model is favorable because the complex piecewise nature offers flexibility in adapting it to multiple materials while maintaining accuracy. It is surmised that a similar approach could allow for additional considerations, including that of geometric discontinuities.

2.3 Notched Geometries

The term "notch" refers to a localized discontinuity in a smoothly-contoured geometry (Peterson, 1953). Industrial machinery incorporate parts with sharp bends or holes which create such discontinuities. In laboratory tests, geometric discontinuities are created by incising a notch in the gage section of an otherwise smooth specimen. Upon loading the part or specimen, the inconsistency in shape causes changes in local stresses not only because of the reduced area, but also because of the increased density of load paths and high stress gradient near the notch (Peterson, 1959). Beginning with root cause analyses on early rail disasters, it has long been recognized that this concentration of stress increases the susceptibility of components to damage and ultimately, rupture (Stephens, et al., 2000).

2.3.1 Stress and Strain Effects

With notches as an unavoidable consequence of modern machine design, the studies of stress gradients and stress intensities due to notches, as well as their effects on fatigue, have been important subjects of interest to researchers for many years (Neuber, 1937). Generally, the effect on notched components is quantified by relating the ratio between the local stress σ (or local strain, ε) at a notch and the remote stress S (or remote strain, e) condition. In elastic cases, both stress and strain ratios are identical and either is identified as the theoretical Stress Concentration

Factor (SCF), commonly denoted by K_t (Peterson, 1974) with the local-remote dependency relation is given as:

$$\sigma = K_t S \quad or \quad \varepsilon = K_t e \tag{2.24}$$

In many cases, loads on notched geometries are high enough that plasticity occurs at the notch, and as such, the stress and strain concentration factors must be handled independently,

$$K_\sigma = \frac{\sigma}{S} \tag{2.25}$$

for the stress case, or

$$K_\varepsilon = \frac{\varepsilon}{e} \tag{2.26}$$

for the case of strain, with K_σ and K_ε representing the individual stress and strain intensities. With increasing plasticity these factors diverge in a nonlinear fashion based on the material's stress-strain behavior. Dependent on temperature and load history, this additional complexity can make determination of true local stresses and strains exceedingly difficult (Seeger and Heuler, 1980).

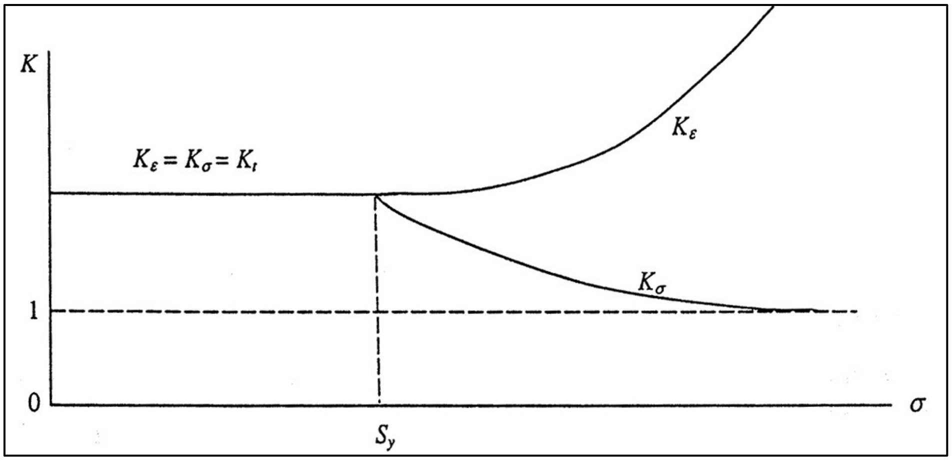

Figure 2.25: Divergence of stress and strain concentration factors during plasticity. [from Stephens, R., Fatemi, A., Stephens, R., and Fuchs, H., 2000]

Turbine blades in particular offer an excellent example when considering parts with notches. Not only does the overall shape of a combustion turbine airfoil possess a complex shape itself, but a number of features on modern turbine blades have geometries that carry a small radius of curvature (Endo, Kondo, and Kadoya, 1995). Dovetail joints used to affix individual blades to rotor assemblies have sharp curvatures and often carry intensified loadings, but cooling holes and channels are the most severe case of geometric discontinuity on the blades, commonly exhibiting a K_t value of nearly 3.0. This causes the immediate area surrounding a cooling hole in a turbine blade to experience stresses approximately three times (Rao, 2000) larger than that of the overall loadbearing cross-section.

Other types of parts with overall high degrees of curvature, such as lower-pressure steam turbine blades (which are often referred to as "buckets" due to their concave shape), experience varying and complex loads throughout their bodies that are not always governed by the presence of a notch (Yates, Kiew, and Goldthorpe, 1993). The most extreme effects of geometry in such a blade are clearly due to notches, however. This is viewable by examining the contrast between loadings in the nominal (region 6) and most severely stressed (region 1) areas in the cross section depicted in Figure 2.26.

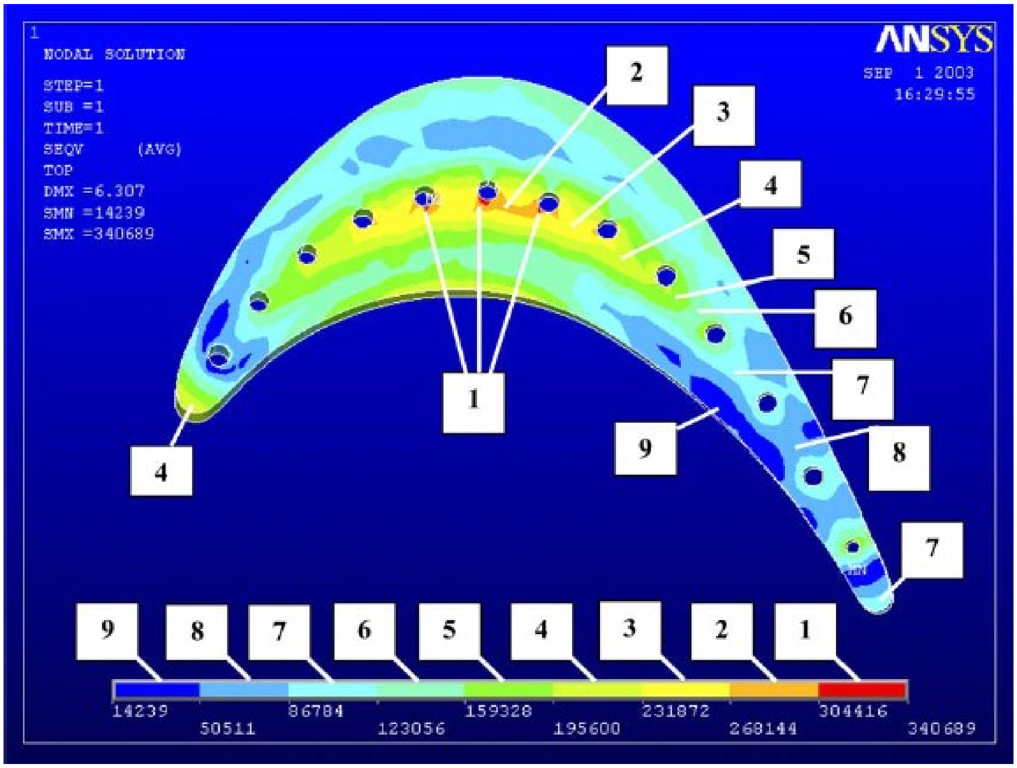

Figure 2.26: Color-mapped ANSYS simulation results denoting stress regions in a turbine blade.

2.3.2 Effect on Fatigue Life

A considerable portion of engineering failures involve fatigue, which always start at a localized concentration when excessive plastic flow leads to crack initiation. Notches provide an obvious starting point for this type of behavior, and thereby notched fatigue life methodologies become of paramount importance (Miller, 2005). Many works have attempted to establish a method for dependable extension of strain-life approaches to notched parts (Sehitoglu, 2006). Two prominent challenges to consider in notched fatigue are as follows: actual stress and strain values at a notch are difficult to reliably determine (Hyde, Sabesan, and Leen, 2004), and the factors and methods used to estimate notch behavior are often insufficient for fatigue prediction or for use in TMF situations (Ahmad, de los Rios, and Yates, 1994).

Mathematical shakedown methods that make use of theoretical stress and strain concentration values have been developed, with Neuber's rule (Neuber, 1961) using a phenomenological approach, and Glinka's method (Glinka, 1985a) which applies a strain energy balance that involves both elastic and plastic deformation energy, and has been extended to include fatigue cases with some limited success (Glinka, 1985b). Note that the resultant equation from Neuber's rule,

$$\frac{\sigma^2}{E} + \sigma\left(\frac{\sigma}{K}\right)^{\frac{1}{n}} = \frac{(K_t\, S)^2}{E} \tag{2.27}$$

has many terms in agreement with the more recent approach by Glinka:

$$\frac{(K_t\, S)^2}{E} = \frac{\sigma^2}{E} + \frac{2\sigma}{n+1}\left(\frac{\sigma}{K}\right)^{\frac{1}{n}} \tag{2.28}$$

Both the Neuber and Glinka methods provide accurate estimates of notch conditions for monotonic loadings, but as of yet lack sufficient precision for most fatigue cases. Attempts to handle the problem via substitution of stress ranges $\Delta\sigma$ and ΔS in place of the monotonic stress in the formulation have not yielded accurate results (Knop, et al., 2000).

Current predictive models that utilize FEA or shakedown approaches do not incorporate changes in the material or stress-strain field near the notch during cyclic loading. This evolution makes a significant difference in the notch condition estimates after the initial cycle, and accounts for some of the inaccuracies of previous works. Several decades ago, early studies conducted by Frost and Dugdale determined that the direct use of theoretical stress concentration factors (K_t) only showed limited viability (Frost, 1955a; Frost, 1955b). Drastic changes in the stress field of a notch during cyclic loading made it difficult to pinpoint the conditions for crack initiation (Frost, and Dugdale, 1956). If initiation did occur, it was also difficult to determine whether the crack would become dominant in the presence of secondary cracks, grow, or self-arrest (Frost, 1959). It was clear that LEFM-based solutions were unable to account for the complexities of the plasticity and gradients at a notch tip. This assertion against LEFM approaches is understandable when considering that crack initiation and growth are observed at load applications below the fatigue limit in some studies (Kitagawa and Takahashi, 1976).

A limited solution in the form of stress concentration factors fitted specifically for fatigue ($K_{fatigue}$) were realized (Smith, 1975), which provide additional compensation for material evolution due to the Bauschinger and other property-changing effects brought on by cyclic load conditions. Successive works have deemed this type of factor to be viable, coupled the approach with FEA investigations (Hammouda, 1978) and then evaluated as applied to life prediction situations (Hammouda and Miller, 1980). The $K_{fatigue}$ factor is notably different from K_f, dependent only on notch depth D and notch radius ρ, with development based on empirical data from differing materials. The resulting $K_{fatigue}$ expression is given as a piecewise equation:

$$K_{fatigue} = \begin{cases} \left(1 + 7.69\sqrt{D/\rho}\right)^{0.5} & \text{Cyclic hardening} \\ \left(1 + 5\sqrt{D/\rho}\right)^{0.5} & \text{Cyclic soften ing} \end{cases} \tag{2.29}$$

With a piecewise approach, the values are calculated differently for materials which undergo cyclic softening or hardening without reconciling the coincident case. Considering previous attempts at modeling with intent to closely fit empirical findings, Equation 2.29 appears exceedingly simplistic. The heuristic development of this formulation has led to it not being favored for inclusion in any major predictive models to date, but has continued to be acknowledged as an alternative to more complex practices requiring higher computing power (Ahmad and Yates, 1994). Given its proven usefulness, it is clear that it and other concise frameworks should not be discounted, and simple adjustments to K_t or $K_{fatigue}$-like terms provide positive adjustments to approaches that otherwise remain inaccurate.

2.3.3 Local Strain Measurement

Inability to measure the actual notch behavior is largely due to physical size and environmental susceptibility limitations on current transducer technology. Some attempts have paired diametral and linear extensometers in estimating notch strains, but oxide buildup obscures the actual outer dimension made by sensitive diametral extensometers. This consequence inherently makes this approach unsatisfactory for high temperature conditions, including TMF (Mazza, et al., 2004). Recent attempts to measure local strain via optical means through the use of painted speckle-patterns and image correlation software have met with some success, allowing for precision observations in cases where traditional sensors could not be applied (Kraft, and Gordon, 2012). Additional encouragement for this approach is supported by application to strain measurement in notched fatigue cases (Algarni, et al., 2013). High temperature applications remain difficult to handle due to the inevitable loss of the patterned coating due to char or discoloration, or optical aberration caused by the surrounding heated air. Very high performance computing power would also be required to provide real-time results for use as feedback for control in experimental testing, highlighting another shortcoming.

Continuing advances in computing power have made FEA a viable approach at closely estimating some notch conditions (Yates, 1991), but full-scale fatigue simulations have not yet been able to adequately describe the evolutionary effects of notch plasticity during cyclic loadings (Yates, and Lüsebrink, 1994). Augmentation of lifing model research by FEA are currently limited to determining conditions during initial loadings or at a given stable cycle (Karl, and Gordon, 2012a) and generally must be limited to individual material systems. However, constitutive models with wider applicability can be utilized when proper fitting of constants for the material in question is feasible without prohibitive increases in computation (DeMarco, et al., 2010). An excellent example of the evolution of a particularly accommodating constitutive model is found when examining the work of Miller. First introduced in 1976, this complex constitutive model was built to accurately simulate many of the mechanistic features of fatigue modeling in Type 304 stainless steel (Miller, 1976). Cyclic, temperature, and strain rate dependencies are handled accurately by the model, and stress/strain conditions at any time can be extracted from the calculations. The behavioral relations in Miller's model are based on computation of the characteristic drag stress, *D*, which regulates isotropic hardening, and the rest stress (also known as 'back stress'), *R*, which governs kinematic hardening. Material constants A_1, A_2, B, C_2, H_1, H_2, n, and Q used in the model are computed based on the results of empirical data. A summary of the parameters used in the application of Miller's model is available in Table 2-4.

Table 2-4: Fitting and material constants from Miller's fatigue-capable constitutive model.

Parameter	Description
A_1	Material hardening constant
A_2	Material hardening constant
B	Temperature dependence constant
C_2	Cyclic fit constant
H_1	Kinematic hardening coefficient
H_2	Isotropic hardening coefficient
n	Creep exponent
Q	Plastic flow activation energy
Θ'	Arrhenius diffusion term
D	Drag stress tensor
R	Rest (back) stress tensor

Simulations of stress-controlled tests can be made by calculating incremental values of stress and strain terms. Inclusion of the sign function *sgn*() allows both positive and negative values of stress and strain. In the numerical routine, the governing equations would be nested in a loop. The first equation calculates the rate change in inelastic strain (noted as plastic in the original paper, as all loadings were isothermal and thus mechanical),

$$\dot{\varepsilon}_{inel} = B\theta' \left\{ sinh\left[\left(\frac{|\sigma - R|}{D} \right)^{1.5} \right] \right\}^{n} sgn\,(\sigma - R)\,, \tag{2.30}$$

which can then be applied as a major component of the time derivative of the rest stress,

$$\dot{R} = H_1 \dot{\varepsilon}_{inel} - H_1 B\theta' [sinh(A_1|R|)]^n sgn\,(R). \tag{2.31}$$

Known material constants are combined with the previous two steps to derive an expression for the resultant drag stress:

$$\dot{D} = H_2|\dot{\varepsilon}_{inel}|\left[C_2 + |R| - \left(\frac{A_2}{A_1}\right)D^3\right] - H_2C_2B\theta'[sinh(A_2D^3)]^n \quad (2.32)$$

which closes the computational loop with only a relationship between stress and strain remaining. A simple stress-strain relationship that defines mechanical strain as the sum of elastic and inelastic strain components can be added to the beginning of the loop to allow for the start conditions of each loop to be constrained via mechanical strain,

$$\varepsilon_{mech} = \varepsilon_{inel} + \frac{\sigma}{E} \quad (2.33)$$

thus provides a formulation in terms of the control parameter often used in modern strain-life fatigue experimentation. The capability of Miller's original model maintaining relevancy has been demonstrated by success in efforts to extend it to include multiaxial (Kagawa and Asada, 1983) cases, more severe thermal fatigue (James, et al., 1987), and creep cases of different steels (Tahami, Daei-Sorkhabi, and Biglari, 2010). While the original applications of Miller's model did not include non-isothermal cases, recent efforts by a number of Mechanics of Materials Research Group (MOMRG) researchers have shown that TMF cases can be modeled in numerical routines that update the *D* and *R* tensors based on not only strain increments, but temperature increments as well, incorporating associated changes in behavior due to thermal effects with higher accuracy (Karl and Gordon, 2012b).

The major implication of updating Miller's 1976 model and verifying applicability to TMF cases offers the possibility of pseudo- notch strain control. In an experimental study, use of the Miller model in an FEA program can offer measures of stress and strain at local and remote points in a loaded notched specimen. This information, when cross-checked with simpler geometries, can be utilized in the creation of a correction algorithm for local control based on remotely-measured response.

CHAPTER 3

EXPERIMENTAL METHODOLOGY

A parametric study was conducted on multiple specimen geometries in order to separate the characteristics of damaging effects to smooth and discontinuous shapes. Fatigue, creep-fatigue, and thermomechanical fatigue experiments were run under varying temperatures, phasings, and strain ranges to create conditions which would favor dominance of certain damage mechanisms. A summary of the parameters varied in this study are available in Table 3-1.

Table 3-1: Experimental parameters varied in the study.

Parameter	Experimental Values	Description
$\Delta\varepsilon_{mech}$	0.7, 1.0, 1.4	Local mechanical strain range (%)
T	200, 600	Isothermal test temperature (°C)
T_{min}/T_{max}	200 / 600	Minimum/maximum TMF temperature (°C)
t_{hold}	0, 60	Tensile hold time (s)
K_t	1.0, 1.73, 3.0	Theoretical stress concentration factor
φ	0, 1, -1	Thermal / mechanical strain phasing

These experiments, conducted via uniaxial test frame, provided stress and strain data in real time for analysis purposes. A large percentage of the test specimens were also selected for metallographic imaging after testing, which further assisted understanding of microstructural mechanism evolution in regards to crack initiation. The following chapter details the specimens, equipment, and procedures utilized during the course of the study.

3.1 Test Specimen Design

The nature of the study requires that data must be obtained from specimens of several geometries. The chosen values of theoretical stress concentration factor for each of these specimen types are K_t = 1.0, 1.73, and 3.0. Values of K_t = 3.0 and 1.73 denote sharply notched and bluntly notched geometries, respectively. Notch dimensions were determined via high-degree polynomials recently developed for stress concentration determination in round bars, which were found to be in better empirical agreement than previously published SCF formulas (Noda, N., and Takase, Y., 2006). The upper limit of K_t = 3.0 is based on the most severe stress concentration found in steam turbine blades. The value of K_t = 1.73 is the geometric mean of 3.0 and 1.0. A concentration value of K_t = 1.0 indicates a smooth geometry, for which a standard round "dogbone"-shaped fatigue specimen with a gage length of 25.4 mm (1.0 inches) and a diameter of 6.53 mm (0.25 inches) is utilized.

The corresponding specimen geometry for K_t = 3.0 specimens also has a gage length of 25.4 mm (1.0 inches) and a minimum diameter of 6.53 mm (0.25 inches), yet has an increased outer diameter of 7.62 mm (0.30 inches) to accommodate the additional depth of the notch while maintaining the same minimum cross-sectional area of the smooth specimens. The third type of specimen geometry with a less severe notch providing a K_t value of 1.73 is similarly shaped, with identical gage length, inner radii, and outer radii. The dimensions of this less severely notched fatigue specimen are otherwise similar to the sharply notched specimen.

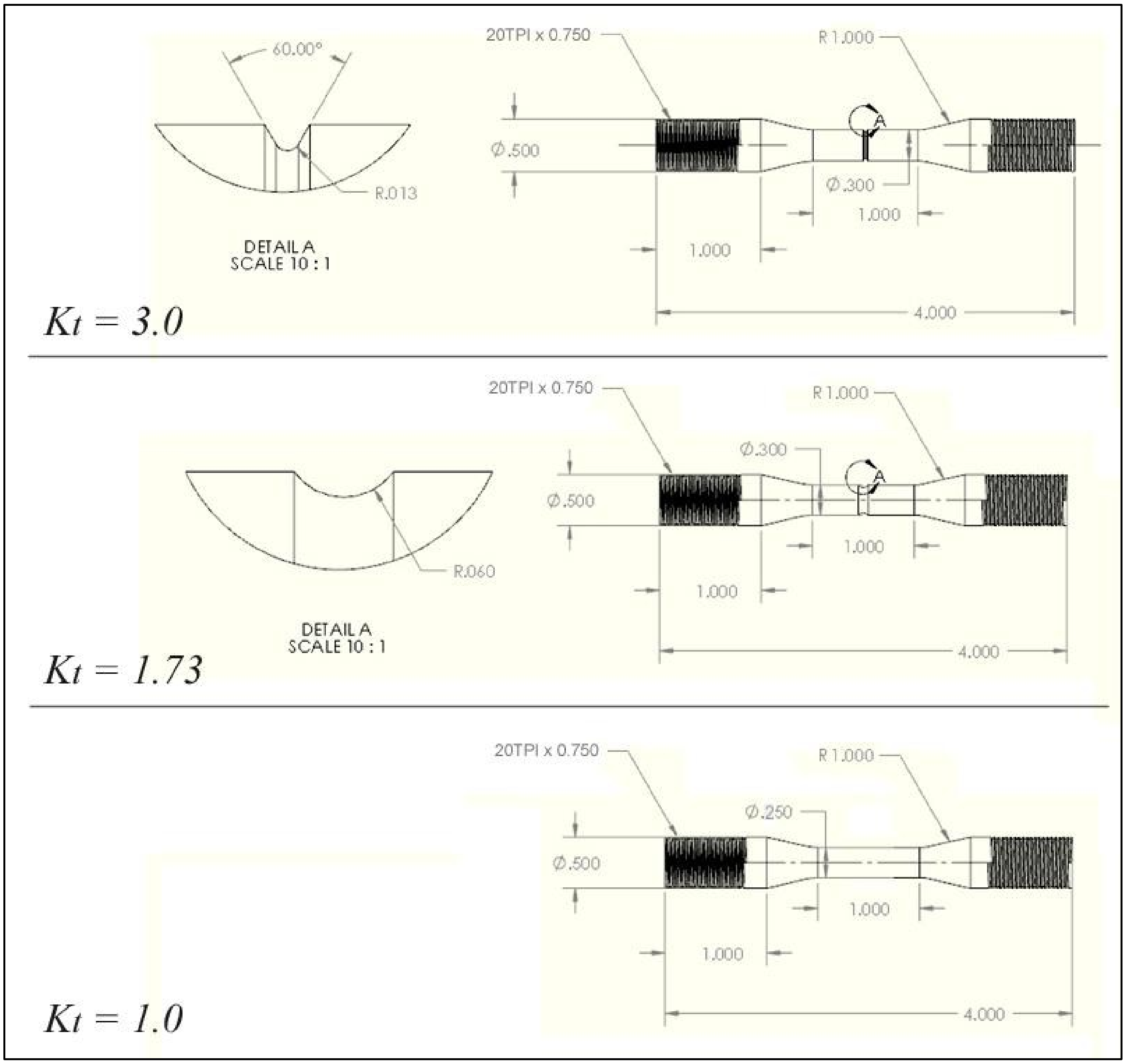

Figure 3.1: Dimensions of notched (upper) and smooth (lower) specimens.

Figure 3.1 details the dimensions of the smooth and notched modified dogbone-type specimens. In all cases, 19.0 mm (0.75 inches) from the ends of the specimen were tapped with ½"x20tpi threads, which allowed the specimens to be fitted into hydraulic grips. All specimens were provided by a machine shop following ISO 9001 standard procedures, and were finished with a 0.5micron polish as per recommended in ASTM E-8 (ASTM, 2008). Post-finished specimens were kept in air-tight tubular containers for storage and transport. Before initiating a test, specimens were fit-checked and additional thread cutting was performed by a manual tap for some cases. Next, specimens were inspected for surface flaws in the gage section and additional finishing on a polishing lathe was performed where necessary. Test articles were then cleaned with acetone to remove any contamination from handling or additional polishing. Because acetone can leave a film after evaporation, methanol was used as a secondary cleaning agent before the specimen was mounted into the hydraulic grips for testing.

3.2 Overview of Test Apparatus

The equipment setup required to perform TMF experiments which conform to ASTM standard E-2368 (ATM, 2004) is a unique configuration which is built around an MTS Systems servohydraulic load frame. The particular load frame in use at the Material Property Characterization Lab (MPCL) at the University of Central Florida is equipped with a load capacity of 100 kN (22kip) and a single 19.0LPM (5GPM) servovalve-controlled hydraulic actuator capable of displacement rates in excess of 50 mm/s (1.97in/s), which exceed load application capability required for the study. The manufacturer's performance data for this type of system is available in Figure 3.2.

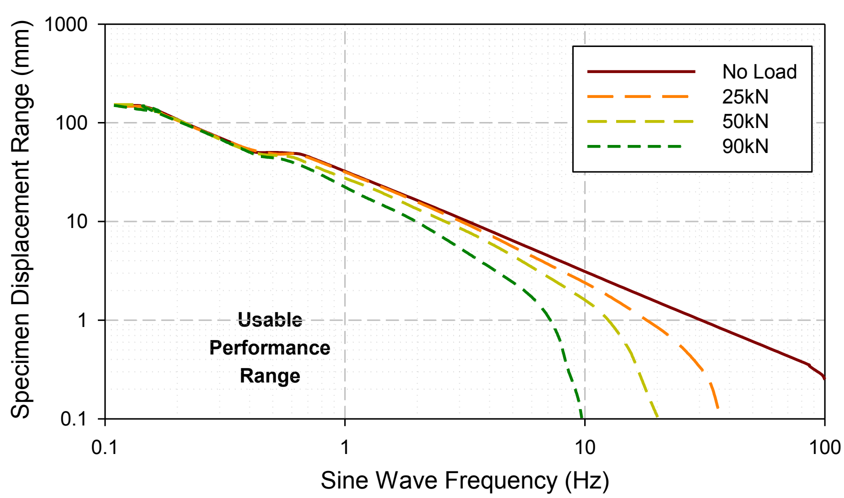

Figure 3.2: Load frame performance curve. (Courtesy of MTS Systems)

Additionally, this particular load frame has been augmented with a number of hardware improvements to qualify it for thermomechanical fatigue. A high-temperature MTS model 632.53 extensometer fitted with ceramic contacts and active cooling is used to report strain in the specimen gage section through all temperature ranges. Specimens are affixed to the test frame via MTS type 646 hydraulic collet grips, which are also actively cooled. Specifications of MTS Systems hardware comprising the testing setup are available in Table 3-2.

Table 3-2: Load frame measurement and control specifications.

Loadframe	
Servovalve maximum flow rate	19.0LPM (5.0 GPM)
Load frame maximum dynamic force	100kN (22kip)
Actuator static force	100kN (22kip)
Actuator dynamic stroke	150mm (6in)
LVDT sensitivity	0.1mm (0.0039in)
Extensometer	
Extensometer model	632.53
Gage length	12.7mm (0.5in)
Measurement range	+/- 2.0mm (0.08in)
Measurement sensitivity	0.001mm (0.000039in)
Excitation	10VDC
Bridge resistance	1000Ω
Maximum service temperature	1200°C (2200°F)
Contact type	Ceramic vee-chisel rods
Contact force	< 3N (300g)
Force Transducer	
Transducer (load cell) model	661.20F-03
Measurement capacity	100kN (22kip)
Overload capacity	150kN (33kip)
Measurement sensitivity	1N (0.22lbf)
Excitation	20VDC
Bridge resistance	300Ω
Collet Grips	
Grip model	646.10
Method	Hydraulic end-loading
Force capacity	100kN (22kip)
Maximum service temperature	65°C (150°F)
Cooling method	Open-loop water
Control and Software	
Control system model	493.01 (TestStar IIs)
PC control interface software	493 (Station Manager) 4.0
PC testing software	Multipurpose Testware
Analog inputs	0-10VDC process control (x6)
Analog outputs	0-10VDC readout channels (x2)

In strain-controlled testing, actuator movement is controlled by feedback from the extensometer, which is directly read by the TestStar IIs controller. During TMF testing, specimen cooling is rendered constantly through a dehumidified compressed air system regulated to 25psi with multiple directional rake-style nozzles delivering the flow. Heat is applied to the specimen internally via eddy currents in the gage length induced by the magnetic field of an Ameritherm HOTShot 3500W radio frequency induction furnace, with the final transformer coil around the test article. Figure 3.3 shows an overhead schematic of the heating and cooling systems around the test specimen.

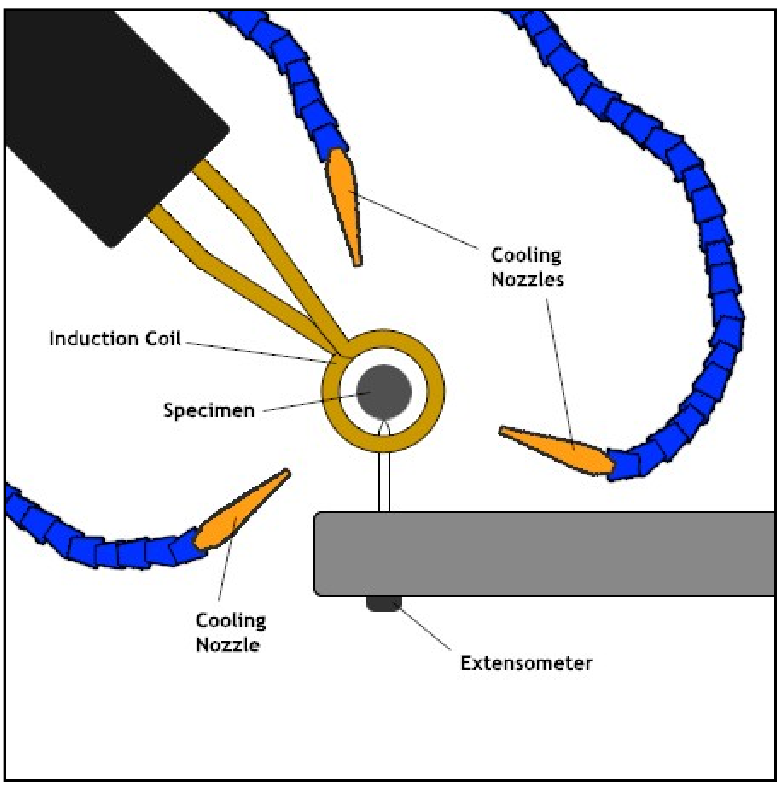

Figure 3.3: Overhead schematic of heating and cooling component arrangement.

During increasing temperature ramps, the induction heating system overpowers the effects of the cooling air. During cooling ramps, the induction furnace operates near idle, adding only enough heat to keep cooling from happening at a rate more rapid than the heating ramps. The coil type utilized in this study is of the 2-1-2 configuration. The difficulty of thermal gradient management in the gage section is minimized with concentrated heat application at the ends of the gage length coupled with conduction into the gage section where some additional heat is created with the center coil. The coils are also spaced such that the extensometer rods can contact the gage section of the specimen without interfering with the coils. This configuration is viewable in the photograph of Figure 3.4.

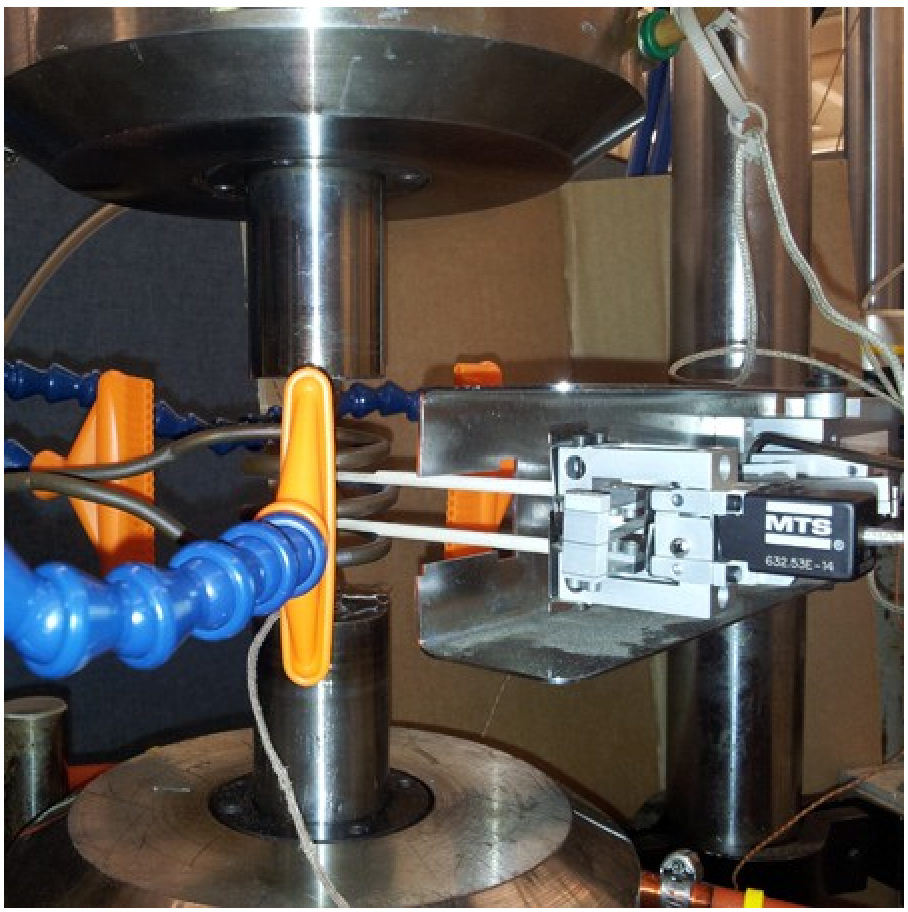

Figure 3.4: Close-up side view of coil (center), coolant nozzles (foreground and background), and extensometer (right foreground) placement.

Temperature feedback during heating and cooling processes is provided by a separate Watlow 989A temperature controller. The temperature controller reads a millivolt-scale signal from a type K thermocouple welded to the gage section of the specimen, conditions the signal, and then scales it to a higher DC process control voltage range before retransmitting it via analog input to the TestStar IIs control unit. A full set of specifications for the heating subsystem equipment is available in Table 3-3.

Table 3-3: Thermal control equipment specifications.

Induction Furnace	
Manufacturer	Ameritherm
Model	HOTShot
Maximum power	3500W
Induction field operational frequency	140-400kHz
Power control resolution	25W
Process control input	0-10V or 4-20mA
Cooling method	Closed-loop water
Temperature Controller	
Manufacturer	Watlow
Model	989A
Measurement range	0-2316°C (0-3300°F)
Thermocouple types	J, K, T, N, R, S, B, E, C, D
Sampling rate	10Hz
Retransmit rate	1Hz
Restransmit resolution	0.1°C
Retransmit output	0-10VDC

Temperature control and other individual subsystems utilized in the testing equipment configuration for the study are ultimately managed by the MTS TestStar IIs control and acquisition unit. This piece of hardware is a UNIX computer-based multiplexing controller that allows simultaneous monitoring and output of many signals at once. Sensor excitation, voltage monitoring, servo drive, and process control input and output are handled by a series of daughter boards which report conditions and get commands from the primary controller motherboard at a rate of 2048Hz.

A schematic of the overall setup including sensor and control signals is shown in Figure 3.5.

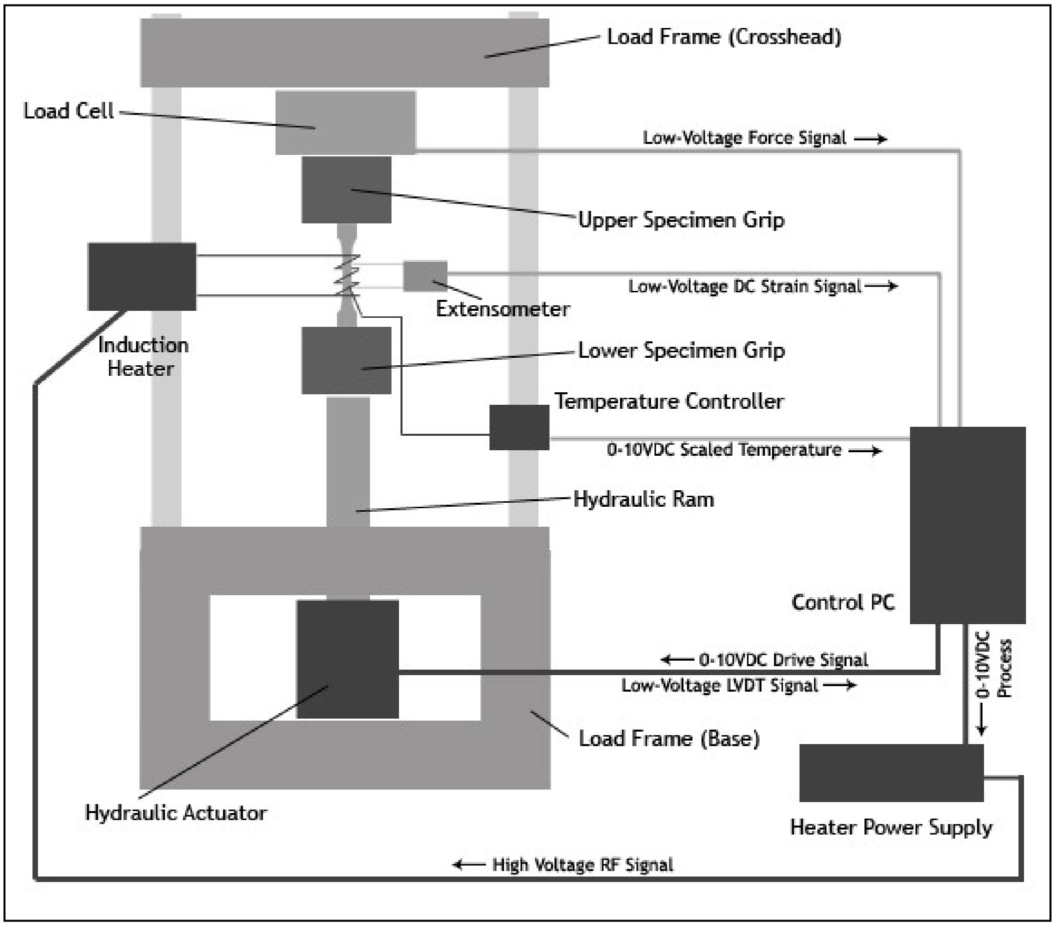

Figure 3.5: Diagram of TMF test apparatus connections and signals.

The TestStar IIs is thus in direct communication with the test frame sensors to acquire data while controlling load application via the force, strain, or displacement channel feedback. Heating commands are sent to the Ameritherm HOTShot induction furnace power supply via an analog process control signal from one of the 0-10V TestStar IIs analog readout ports, with voltage adjusted up or down to apply or decrease heat based on PID control settings within the 493 management software and the difference between commanded temperature and the actual temperature. Test programming and operator interfacing are handled by a PC networked with the primary controller motherboard. This PC utilizes the MTS Multipurpose Testware software package to program complex cyclic loadings and collect data in a user-friendly manner.

Prior to testing, a number of additional hardware checks and calibrations are performed in order to maintain compliance with ASTM standards. The MTS type 464 hydraulic collet grips are used to grip specimens through end-loading them with a piston and platen assembly, while automatically maintaining frame alignment in accordance with ASTM E-1012 (ASTM, 2005). While the hydraulic grips are actively cooled from an open loop water source, custom – made Inconel type 718 collet extensions further insure that high temperatures did not interfere with load frame control compliance. When heat is applied from the induction furnace, a thermal gradient with less than 1% deviation in the gage section (Locations 2,3,4, and 6 in Table 3-4) is required by standards E-21, E-606, and E-2368 (ASTM, 2009; ASTM, 2004; ASTM, 2004). This temperature distribution is established by careful adjustment and qualification of the induction furnace coil during which a dummy specimen with multiple thermocouples is loaded. Gage section temperature gradient worst-case deviance values are available in Table 3-4.

Table 3-4: Specimen thermal gradient worst-case error values.

Location			Command Temperature (°C)							
Map	TC #	Description	20°C	100°C	200°C	300°C	400°C	500°C	600°C	
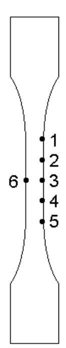	1	Upper shoulder	0.4	1.4	2.2	3.2	2.1	1.0	3.8	Error (°C)
	2	Top of gage section	0.4	0.9	1.5	2.7	1.6	4.3	2.1	
	3	Center	0.0	0.0	0.0	0.0	0.0	0.0	0.0	
	4	Bottom of gage section	0.1	0.2	0.3	2.1	0.9	2.7	3.6	
	5	Lower shoulder	0.5	2.5	3.9	4.0	4.0	6.1	3.2	
	6	Rear center (offset 180°)	0.2	0.6	1.0	0.9	-0.3	1.5	-0.5	

Following the establishment of a satisfactory temperature gradient, trials to evaluate the control viability of heating and cooling rates were performed. Similar to those which would be conducted for measuring specimen thermal expansion, these trials heated and cooled the coil qualification specimen through the 200-600°C (392-1112°F, 473-873°K) range in order to determine the maximum rate at which the applied temperature did not appreciably deviate from the command temperature during heating and cooling processes. Trials at 2°Cs^{-1} and 3.333°Cs^{-1} yielded small errors, with 3.333°Cs^{-1} being selected for the study. This rate this corresponds to a ½ΔT = 200°C ramp time of 60 seconds for non-isothermal tests. Trial heating and cooling ramp responses are shown in the graph in Figure 3.6.

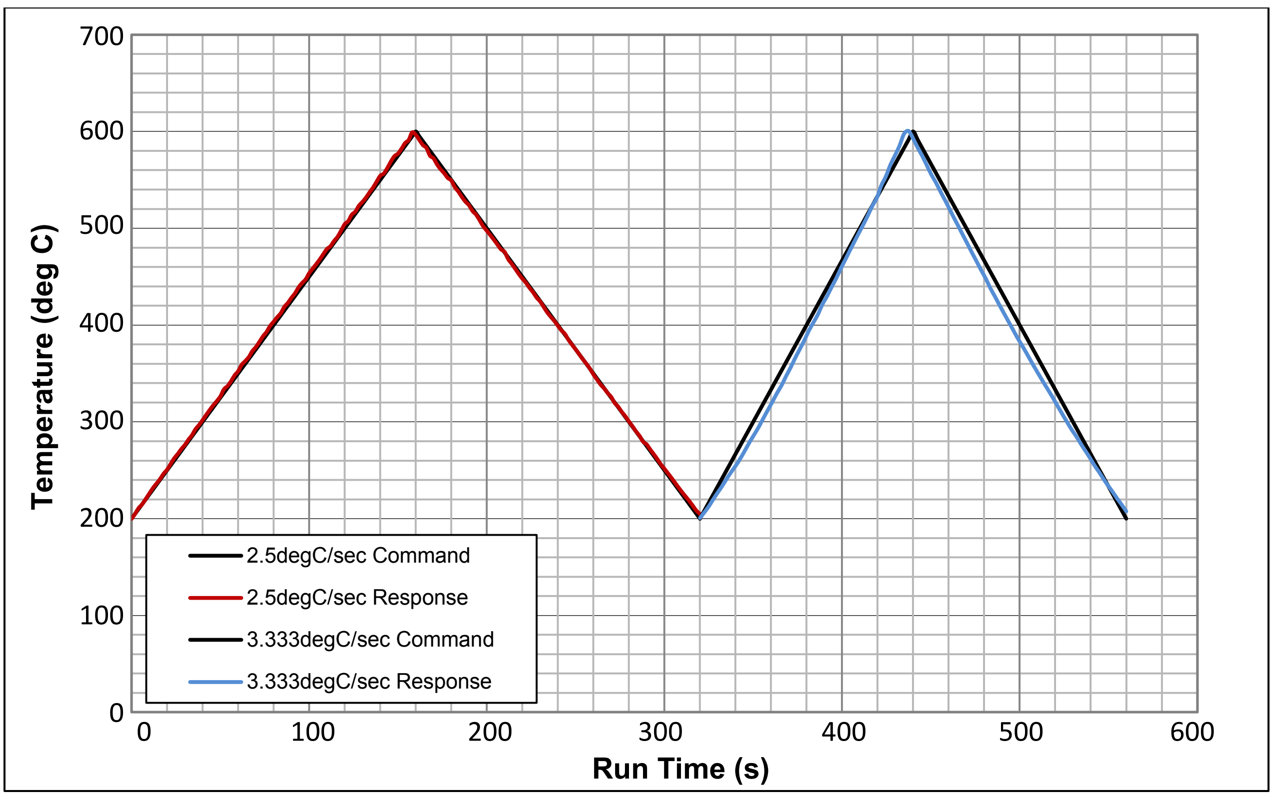

Figure 3.6: Results of trial to determine stable heating and cooling rates for non-isothermal tests.

In TMF cases, 2 thermal pre-cycles were conducted before mechanical loads were applied, as recommended by ASTM E-2368 (ASTM, 2004). Before LCF tests were initiated, specimens were held stress-free at the target temperature for 15 minutes.

When an experiment had completed, the mechanical load was fully relaxed and the specimen was allowed to cool to room temperature. Post-tested specimens which were fractured for microscopy were done so in displacement control at the highest possible rate so that during and after-test surfaces would be clearly differentiable. At this time, the hydraulic grips were depressurized, while fractured and unfractured specimens alike were removed from the load frame, to be stored in a sealed protective container.

3.3 Low Cycle Fatigue Testing of Smooth Specimens

A significant number of isothermal strain-controlled fatigue tests conducted at 200°C (392°F, 473°K) and 600°C (1112°F, 873°K) provide data for this study. Utilizing the hardware and pre-trial methods outlined in the previous section, fully-reversed experimental trials on smooth geometries were conducted in accordance with ASTM E-606 (ASTM, 2004). Testing parameters for the smooth LCF tests are given in Table 3-5.

Table 3-5: Summary of smooth LCF test parameters

Parameter	**Values**
Mechanical strain range, $\Delta\varepsilon_{mech}$	0.7%, 1.0%, 1.4%
Mechanical strain rate, $\Delta\dot{\varepsilon}_{mech}$	6.0% / min
Cycle time, t_{cyc}	14s, 20s, 28s
Test temperature, T	200°C (473°K), 600°C

Feedback for control via strain levels in smooth specimens was extracted directly from the extensometer signal. Mechanical strain ranges of $\Delta\varepsilon_{mech}$ = 0.7%, 1.0%, and 1.4% corresponding to low, medium, and high plasticity cases were studied. All LCF testing was conducted at a mechanical strain rate of $\Delta\dot{\varepsilon}_{mech}$ = 6.0%min^{-1} ($\Delta\dot{\varepsilon}_{mech}$ = 0.001sec^{-1}) in an effort to match industry-standard test practices. This strain rate produces total cycle times of 14, 20, and 28 seconds per cycle for the mechanical strain ranges of 0.7%, 1.0%, and 1.4%, respectively. Stress and strain level samples were recorded by the acquisition system at a rate of 100Hz, to be used in the construction of hysteresis and stress history plots during the analysis process. A typical hysteretic response from a low cycle fatigue test is shown in Figure 3.7, while complete results from the isothermal low cycle fatigue tests are available in Appendix A.

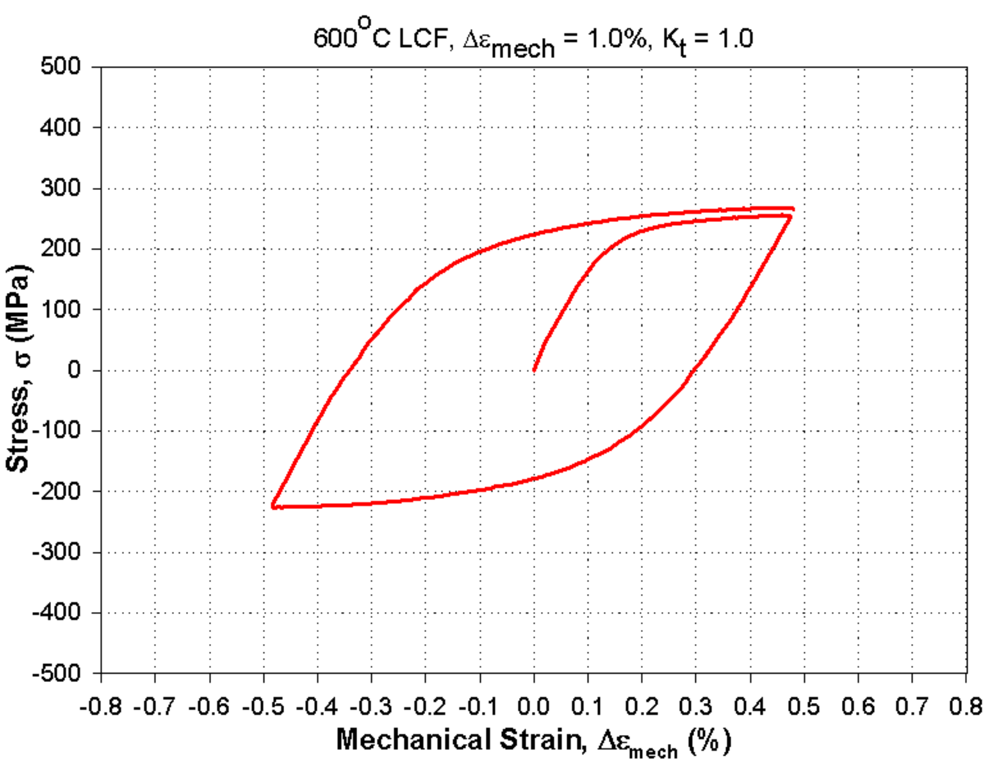

Figure 3.7: First-cycle hysteretic response of a 600°C (1112°F, 873°K) LCF test conducted with a mechanical strain range of 1.0%.

3.4 Low Cycle Creep-Fatigue Testing of Smooth Specimens

Additional isothermal, strain-controlled low cycle fatigue tests are conducted with a 60-second hold introduced at the maximum tensile strain level. Equipment and control methods described in the previous sections are used to apply the same fully-reversed strain ranges (0.7%, 1.0%, and 1.4%) while following the principles outlined by ASTM standard E-2714 (ASTM, 2009). The implication of similar loadings with the exception of the tensile hold is intended to clearly illustrate the effect of the hold by comparison of this dataset with that obtained by the tests outlined in section 3.3. A list of parameters for the creep-fatigue tests is given in Table 3-6.

Table 3-6: Summary of smooth C-F test parameters

Parameter	**Values**
Mechanical strain range, $\Delta\varepsilon_{mech}$	0.7%, 1.0%, 1.4%
Mechanical strain rate, $\Delta\dot{\varepsilon}_{mech}$	6.0% / min
Cycle time, t_{cyc}	74s, 80s, 108s
Test temperature, T	200°C (473°K), 600°C

A 60-second hold, while exceedingly short compared to some creep cycles, has been chosen for use in this laboratory setting. This one-minute hold time provides a dwell period whose length is on the same order of magnitude as the strain ramp in the cycle, and has been demonstrated to allow a significant portion of the stress relaxation that would occur during an indefinite hold. The most easily observable effect of the hold is an overall negative shift in peak stresses, as the tensile stresses begin relaxing on the first cycle, while higher compressive stresses are required to reach the compressive strain target levels.

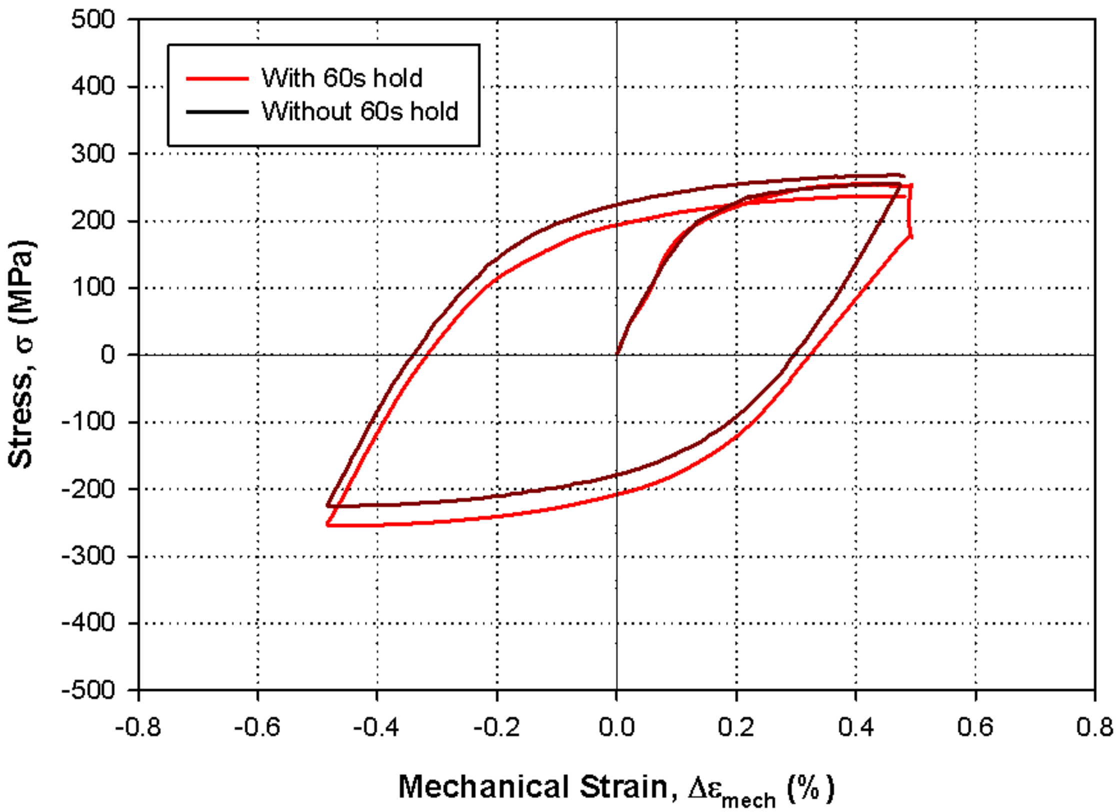

Figure 3.8: First-cycle hysteretic responses from an LCF test conducted at 600°C (1112°F, 873°K) with a mechanical strain range of 1.0% (dark plot) versus the same type test with a 60 second tensile hold (red plot).

The stress relaxation effect is evident in the hysteresis loop depicted in Figure 3.8. Additionally, the hold period extends the overall duration of the test such that additional creep and oxidation effects can be noted where present. A complete set of results from the creep-fatigue tests conducted in this study are found in Appendix B.

3.5 Thermomechanical Fatigue Testing of Smooth Specimens

The most complex type of specimen loadings were incurred during strain-controlled thermomechanical fatigue tests, conducted in compliance with ASTM E-2368 (ASTM, 2004). Mechanical load parameters match the previous sets of tests, with fully-reversed mechanical strain ranges of $\Delta\varepsilon_{mech}$ = 0.7%, 1.0%, and 1.4% applied to the specimens. In addition to strain loading, an additional thermal fatigue load is superimposed. During in-phase (IP) tests, the non-isothermal heating is timed such that the highest and lowest temperatures occur at the highest and lowest mechanical strain values. Out-of-phase (OP) tests had heat applied such that the highest and lowest strain values are met with the lowest and highest thermal loadings. A variable φ equal to the ratio between the normalized mechanical and thermal strains is assigned to describe the phasing cases. In-phase TMF cases have a $\varphi = 1$, while out-of-phase cases have a $\varphi = -1$. This variable can also be used in isothermal LCF cases, where $\varphi = 0$. Tests were conducted at the highest temperature rates possible while maintaining good control of the wave shape. This temperature rate of 3.333°Cs^{-1} (~6.53°Fs^{-1}) matches strain rates of 0.58E-4s^{-1}, 0.83E-5s^{-1}, and 1.16E-5s^{-1} of the mechanical strain ranges in the study. In select cases, a tensile hold period like those described in the tests of section 3.5 was added to IP TMF tests. A summary of the test parameters for the TMF loadings is available in Table 3-7.

Table 3-7: Summary of smooth TMF test parameters

Parameter	Values
Mechanical strain range, $\Delta\varepsilon_{mech}$	0.7%, 1.0%, 1.4%
Mechanical strain rate, $\Delta\dot{\varepsilon}_{mech}$	0.58E-4s^{-1}, 0.83E-5s^{-1}, 1.16E-5s^{-1}
Minimum test temperature, T_{min}	200°C
Maximum test temperature, T_{max}	600°C
Thermal/mechanical phasing, φ	1 (IP), -1 (OP)
Tensile dwell time, t_{hold}	0s, 60s
Cycle time, t_{cyc}	240s, 300s

With temperature-dependent material properties, the stress-strain curves captured during TMF tests are unlike those exhibited in the isothermal fatigue tests. Qualitatively different hysteretic response is expected with each phasing type, as material response is not the same at minimum and maximum strain levels.

This effect is illustrated in Figure 3.9, which provides overlaid graphs of two TMF tests conducted at like parameters with different phase values.

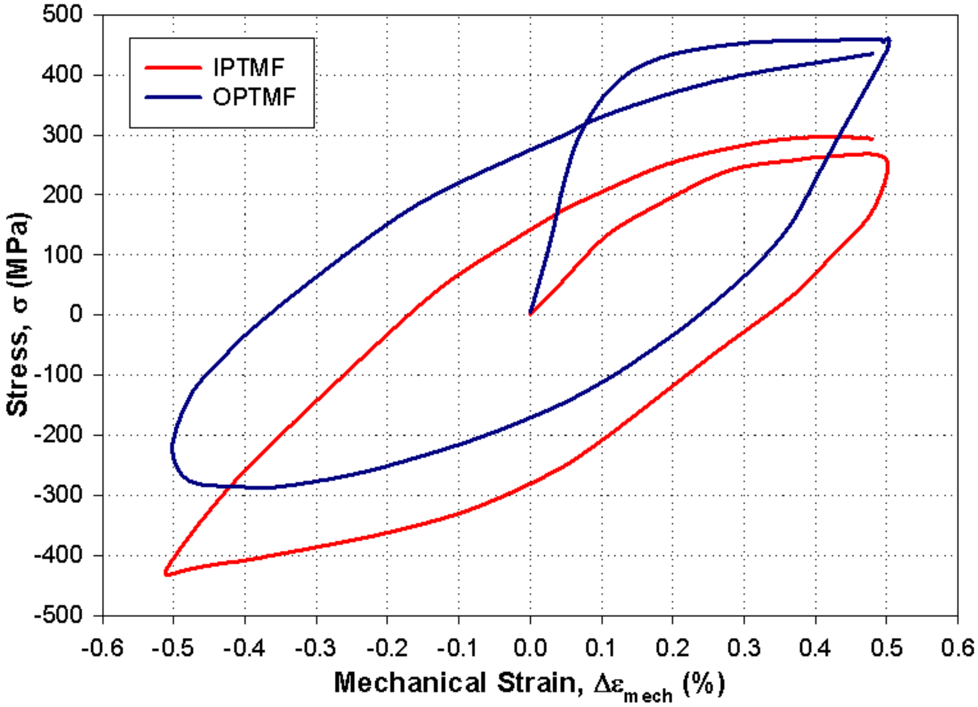

Figure 3.9: IP (red) and OP (blue) TMF hysteresis loops from cycle 1 of 200°C/600°C (473°K/873°K) fully-reversed tests conducted with a strain range of 1.0%.

In-phase test specimens are softer on the tensile side, where out-of-phase specimens maintain their stiffest elastic modulus value. This alone has the effect of shifting maximum stress values with respect to each case, as well as shaping the hysteresis curve itself. TMF tests are directly compared with sections 3.3 and 3.4 as well as one another in order to highlight the effects of non-isothermal phasing. Complete results from the TMF tests are found in Appendix C.

3.6 Testing of Specimens with Notched Geometries

The study incorporates low cycle fatigue, creep fatigue, and thermomechanical fatigue testing of specimens with geometric discontinuities. Blunt and sharp notches in the gage section of the specimens create theoretical stress concentration factors of K_t = 1.73 and K_t = 3.0, respectively. Because the ability to measure the strain condition at the notch tip is limited by the specimen geometry itself, feedback for control via strain levels in the notched cases incorporated correction factors approximating the relationship between the local strain at the notch tip and the remote strain measured by the extensometer. This pseudo-local control method is derived from a two-step approach, elicited from the findings of smooth specimen testing and preliminary numerical studies. While this method is limited in its capability to precisely control notch response, it provides a simple and viable technique for applying a close estimate, the effects of which can be compared against smooth specimens.

3.6.1 Low Cycle Fatigue Testing of Notched Specimens

The first experiments conducted in the presence of a notch incorporated fully-reversed isothermal fatigue loadings. The majority of specimen lifetimes are spent in a stable condition between the beginning of the test and the load drop that indicates crack initiation. Because of this, stress histories of previously-tested smooth specimens at the desired strain range and temperature were inspected in order to determine the number of cycles required for the material response to stabilize. Where the stable region begins, stress-strain responses are utilized to identify material properties which in some cases had appreciably changed with work.

Figure 3.10 annotates a stress history plot from an LCF test to indicate the stable region and regions with transient material response.

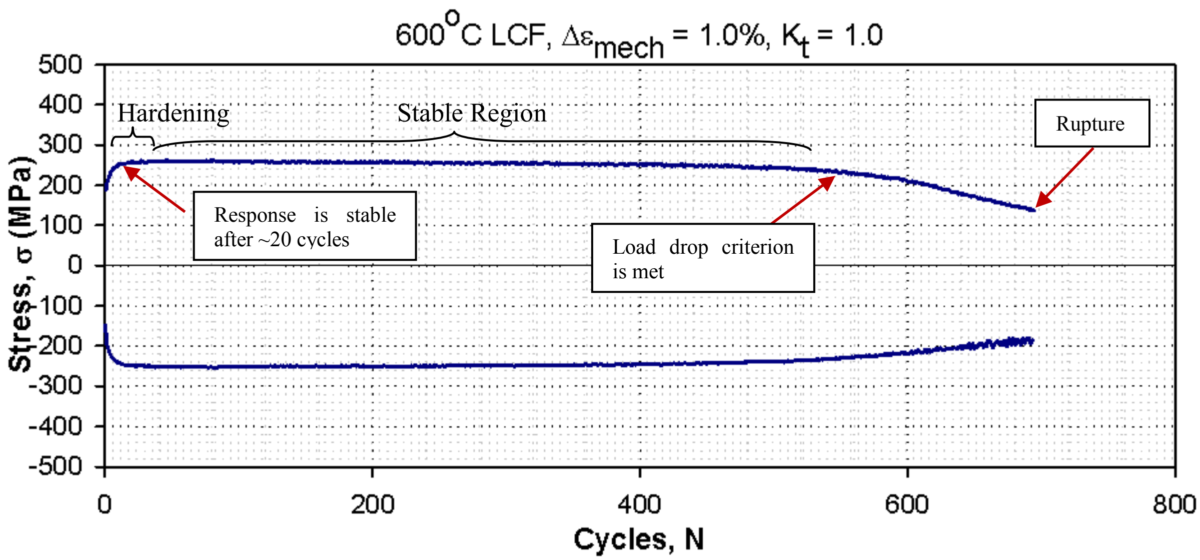

Figure 3.10: Stress history of a smooth LCF specimen tested at 600°C (873°K) with a mechanical strain range of 1.0%

With material properties, strain, and temperature parameters known, implementation of numerical simulations could then be used to determine the remote strain levels necessary to create the desired local strains at the notch root. Customized ANSYS input decks were utilized to build a notched geometry identical to the physical specimens, create and refine a mesh, and apply the appropriate properties and load conditions. The input decks for construction and testing of K_t = 1.73, and K_t = 3.0 specimen geometries are available in Appendix D. Repeated simulation runs were performed with incrementally increasing positive and negative remote strains along the longitudinal axis of the specimen. Each simulation set was concluded when the local strain at the notch root matched that of the desired strain levels for the test. Analysis of multiple steps along the finalized strain ramp shows that the strain response at the notch closely follows that of the remotely applied strain while elasticity is dominant. As the strain ramp continues, local strain diverges from remote strain quickly as the plastic zone in front of the notch increases. To accurately account for this behavioral transition, the remotely applied strain would have to decrease in rate such that the local strain rate remains constant. However, limitations in the current test frame control software make it impossible to apply dynamic rates. Ultimately, the local-to-remote strain ratios for tensile and compressive cases were used as linear scaling factors so that the test frame could apply simpler ramps and still produce the desired local strain end levels. With average local strain rates kept at the previously-utilized 6.0%/min, strain application was done slow enough that effects from the rate transition could be minimized. Complete results from this series of tests are available with their smooth geometry counterparts in Appendix A.

During analysis, the scaling between local strain and remote strain causes a few changes in the way the hysteresis loops are presented. Because the strain is being reported by the remotely-located extensometer and then scaled to the appropriate value, the stress-strain graphs become skewed. With increasing K_t values, the elastic modulus appears to decrease, and the plastic strain range presents itself as artificially low. These effects are apparent in the graph of Figure 3.11.

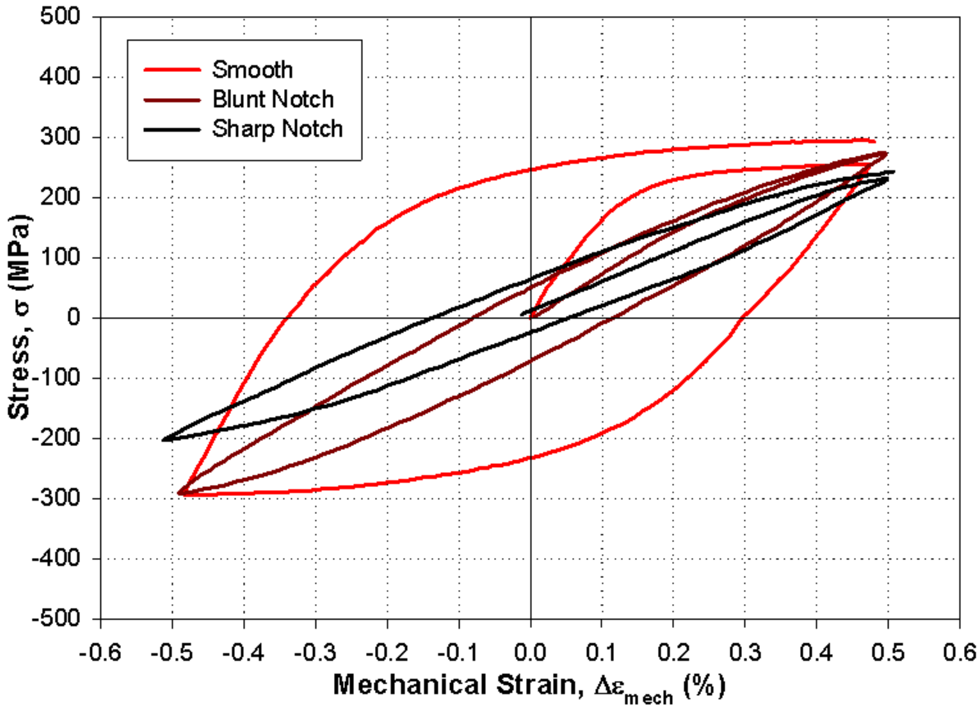

Figure 3.11: LCF specimens tested at 600°C and a local mechanical strain range of 1.0% have varying response due to the severity of the geometry.

For analysis purposes, the elastic moduli values are known with respect to the temperature, and the true elastic modulus of each test is used. Where strain values are used for computation, a correction is not made to the artificially low plastic strain range. Instead, the term "assumed maximum plastic strain range" represented by the variable $\Delta\varepsilon'_{pl}$ is introduced. In the case of smooth specimens, $\Delta\varepsilon'_{pl}$ and $\Delta\varepsilon_{pl}$ are equal and interchangeable, so thusly the $\Delta\varepsilon'_{pl}$ variable can be used seamlessly throughout the study.

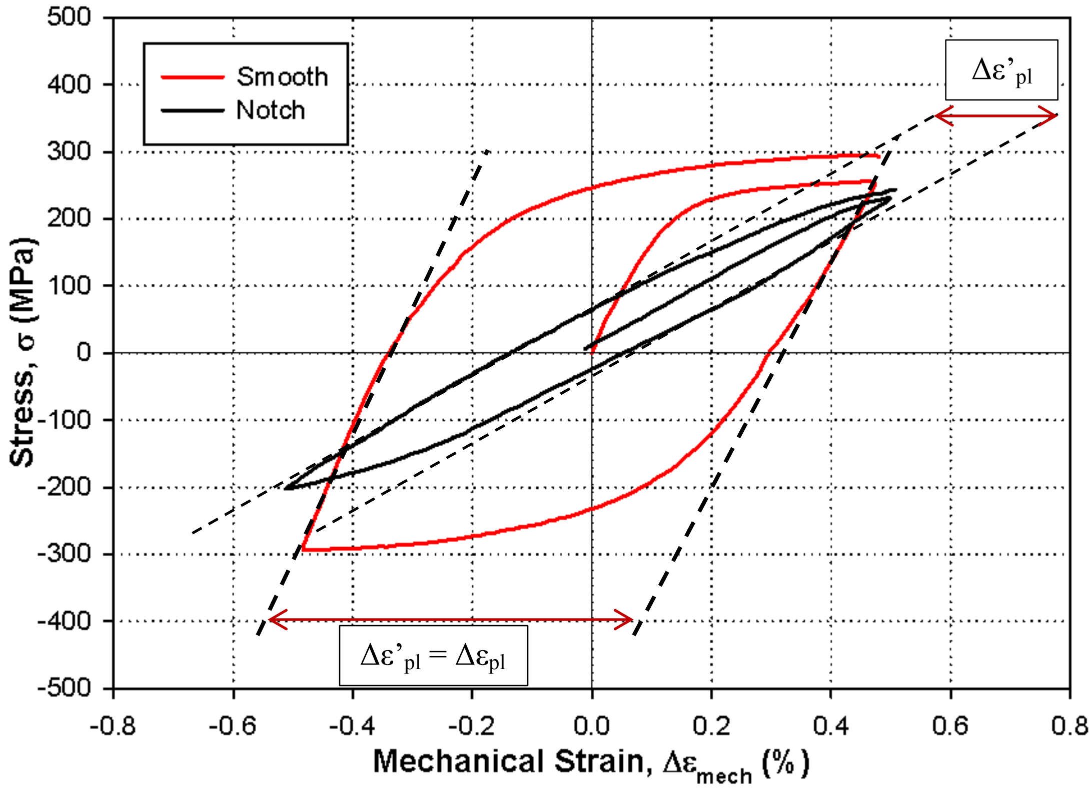

Figure 3.12: Measurement of assumed plastic strain values in a sharply notched versus smooth LCF specimen tested at 600°C (873°K) with $\Delta\varepsilon_{mech}$=1.0%.

While it is not a measure of the actual plastic strain at the notch tip, the term is still indicative of the levels of damage being done to the specimen when properly augmented by the prediction model. Figure 3.12 offers a graphical depiction of how the assumed maximum plastic strain range is measured in a smooth versus sharply notched specimen.

3.6.2 Creep-Fatigue Testing of Notched Specimens

Creep-fatigue tests on blunt and notched geometry were performed with the addition of a 60 second tensile dwell period identical to those applied during the tests described in section 3.4. The shape of the hysteretic response is changed in the same fashion as with the smooth creep-fatigue tests, with tensile stresses relaxing out during the hold. Thus, this second set of experiments performed with discontinuous specimen geometries are controlled and analyzed in the same manner as those tests outlined in section 3.6.1, with additional apparent plastic strain present due to the widening of the stress-strain loop. Results from creep-fatigue tests conducted on notched specimens are available along with those of their smooth specimen counterparts in Appendix B.

3.6.3 Thermomechanical Fatigue Testing of Notched Specimens

In the case of thermomechanical fatigue testing of specimens that incorporate a notch, experiments again were performed identically to those in section 3.5, with the applied local strain levels controlled in the manner discussed in section 3.6.1. In the case of determining plastic strain levels, the assumed maximum plastic strain in the more complex TMF hysteresis curves was derived from the widest part of the loop. Results from the notched TMF experiments are available in Appendix C.

3.7 Metallography

In order to properly characterize the contribution of certain damage mechanisms to the life reduction of the specimen, microscopic analyses of the structures and properties of the material pre- and post-experimentation were necessary. Observations and measurements of various effects were taken at several magnification levels and necessitated the use of both optical and scanning electron microscopes (SEM's). Areas of interest for microscopic analysis were selected from outer surfaces, fracture surfaces, and cross-sections cut from the specimen material.

Low-magnification optical microscopy of up to 200X was conducted with the use of a Dino-Lite Premier high resolution PC-based optical microscope. These magnification levels were suitable for identification of macro cracks, secondary cracks, pitting, and the buildup of oxides on the material surface. Test articles consisting of post-experiment specimens were removed from their protective containers and temporarily attached to the microscope stage with inert mineral-tack mounting putty. Lighting, brightness, and contrast were adjusted as necessary to provide the optimum conditions for feature recognition before a high resolution image was captured via host computer. A photograph of the imaging setup is available in Figure 3.13.

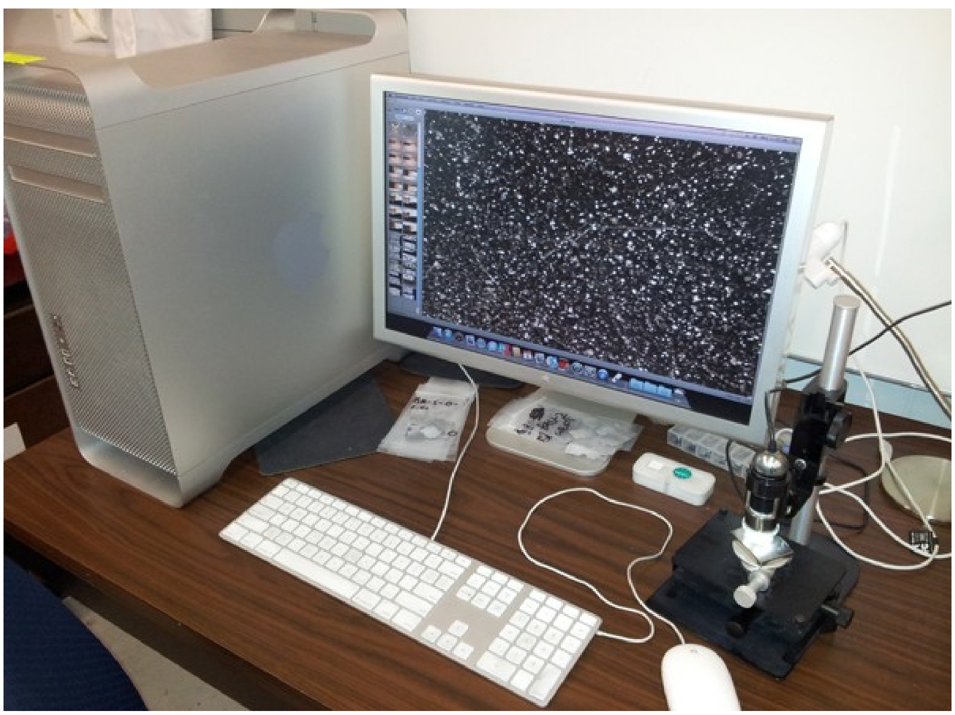

Figure 3.13: Dino-Lite Premier PC-based digital microscope.

Optical microscopy at higher magnifications utilized a Keyence VHX-600 multi-wavelength super-resolution microscope. The optics in this equipment create a composite image constructed from multiple wavelengths at multiple independent focus depths, allowing for more detailed imaging at magnifications up to 500X. This level of magnification is appropriate for closer inspection of surface features, but primarily was used for pre-SEM analysis of fractured specimens. Multiple specimens mounted in a single epoxy puck were placed on the microscope stage, and the microscope optics were articulated to accommodate imaging from normal and non-normal directions. This piece of equipment is pictured in Figure 3.14.

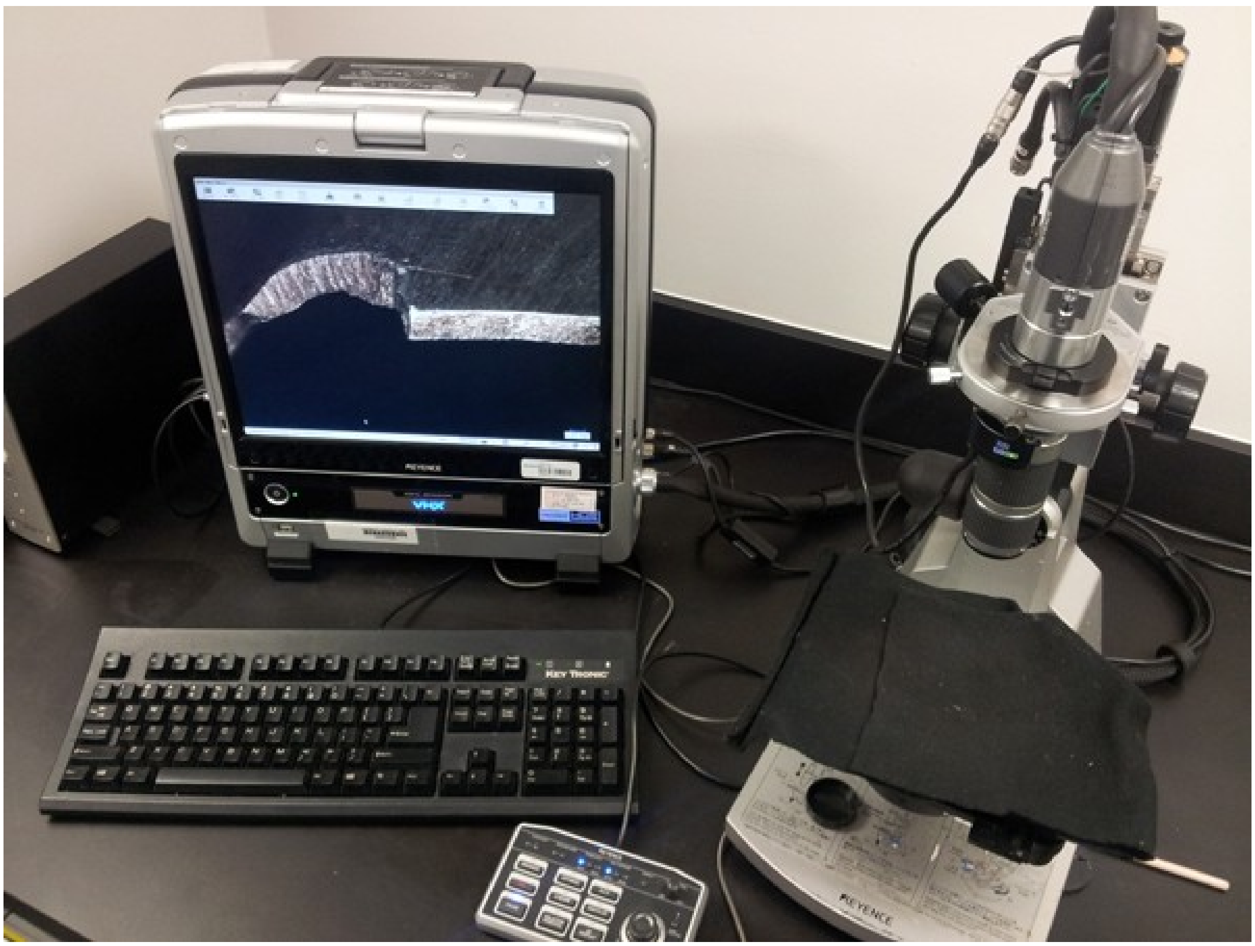

Figure 3.14: Keyence VHX multi-wavelength digital microscope system.

Microstructural features including grain size, carbide boundary growth, oxide penetration depth, microcrack depth, and void identification were studied via images of samples sectioned from the gage length of specimens. These sampled sections were cut from the gage length of test articles with a Struers Minitom diamond abrasive saw. Cuts in the longitudinal and transverse directions were performed, in order to produce a sample which included edges from the fracture surface, outer diameter, and notch where applicable. Photos of the saw and resultant sample are viewable in Figures 3.15a and 3.15b.

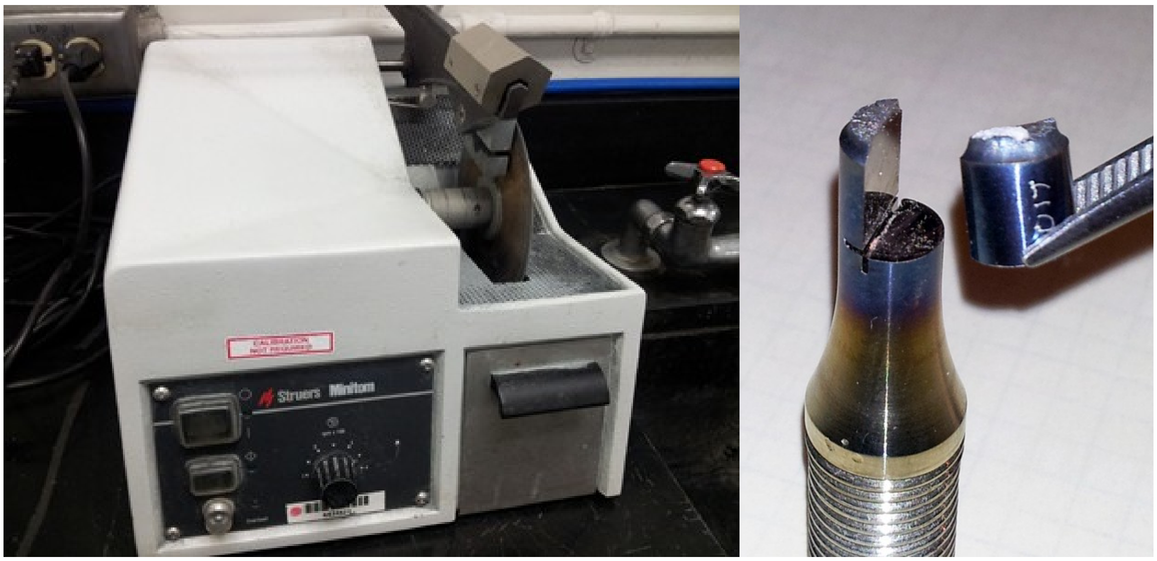

Figure 3.15: (a) Struers Minitom saw [left] and (b) resultant metallography sample [right].

After the sectioning process, the samples are mounted in epoxy prior to polishing. Dried epoxy pucks containing the metallography sample are processed in order to produce a very fine surface finish on the metal. A Struers Tegramin-30 rotary polishing machine is used to sand and polish the samples in a multistage process. Figure 3.16 depicts this piece of equipment with a sample wheel and polishing surface mounted, with bottles of different types of dosing suspensions connected via the system of hoses.

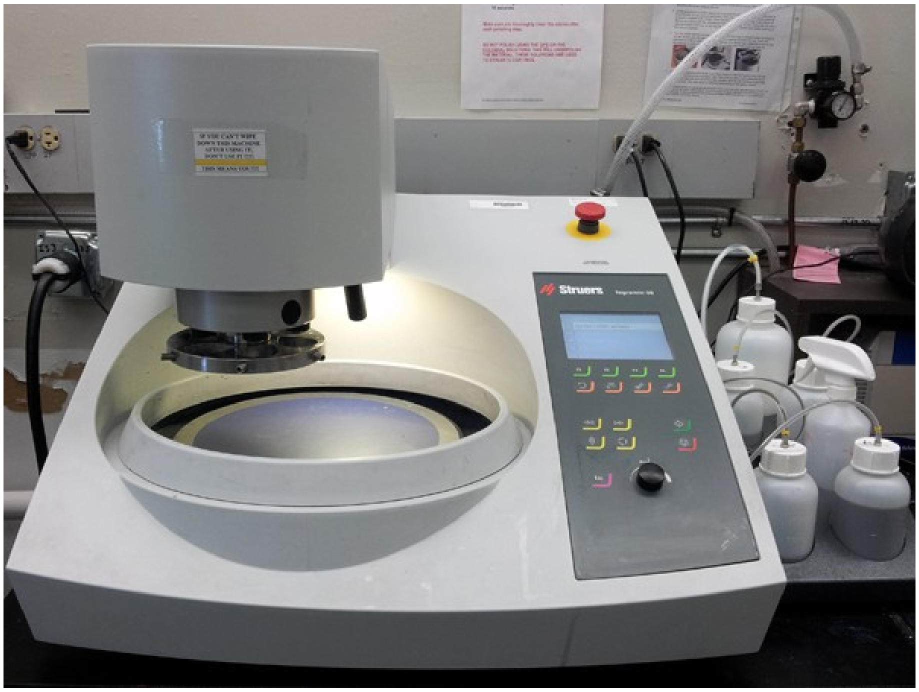

Figure 3.16: Struers Tegramin-30 automatic polishing machine.

The polishing machine reduces the coarse cutting surface from the abrasive blade to a mirror-finish suitable for microscopy over the course of five different steps. Each step rotates the samples and rotary table at 150rpm and applies a contact force of 200N, but requires a different rotary disc surface and dosing. Details of these steps are outlined in Table 3-6.

Table 3-8: Polishing details for metallographic specimens.

Step	Surface	Dosing	Duration
1	220grit SiC sandpaper	Water	1 minute
2	MD-Allegro composite grinding surface	DiaDuo 9μm suspension	4 minutes
3	MD-Dac woven acetate cloth	DiaDuo 3μm suspension	3 minutes
4	MD-Nap final polishing cloth	DiaDuo 1μm suspension	2 minutes
5	MD-Chem finishing cloth	OP-S suspension	1 minute

After the polishing process is complete, methanol is used to remove any surface contamination. When drying is complete, a swab of waterless Kalling's reagent is applied to lightly etch the surface of the steel. After 60 seconds, another methanol cleansing removes the excess etchant. Table 3-7 details the composition of waterless Kalling's reagent.

Table 3-9: Chemical composition of waterless Kalling's reagent.

Amount	Compound	Chemical Formula
5g	Copper(II) Chloride	$CuCl_2$
100ml	Hydrochloric acid	HCl
100ml	Ethanol	C_2H_6O

Metallography samples after completion of the finishing process appear like that in Figure 3.17.

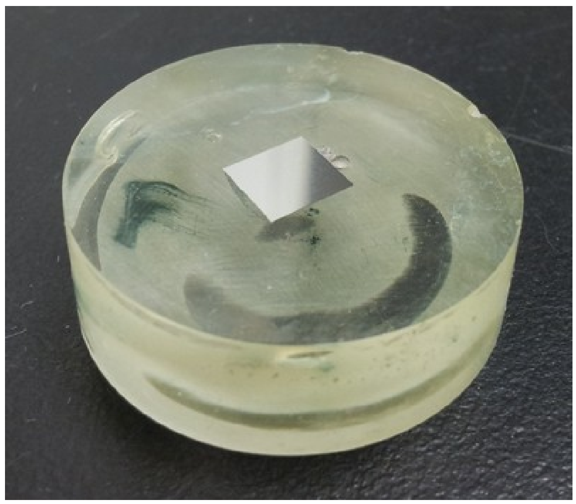

Figure 3.17: A metallography specimen ready for imaging.

The Zeiss Axio Observer metallograph is specifically designed for imaging of polished, encapsulated specimen sections. Samples are placed face-down on the microscope stage and an optical viewfinder is used to find microstructural features, then control is transferred to a PC for image capture. This inverted digital optical microscope is capable of obtaining sharp images up to 1000X magnification, which in addition to reducing the workload for SEM imaging, also returns images in true color. Figure 3.18 shows the piece of equipment utilized for detailed metallographic analyses in this study.

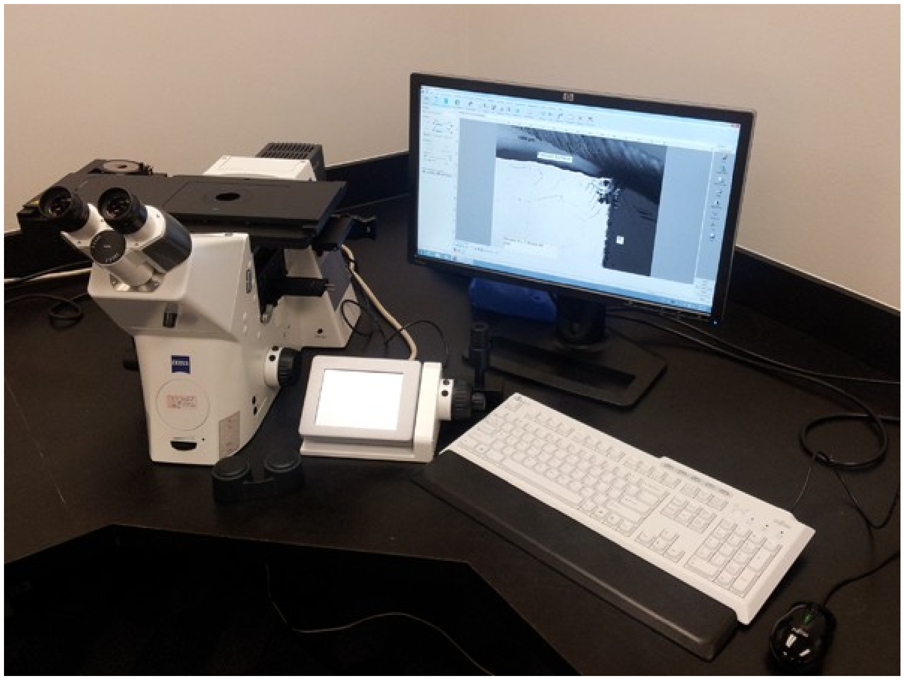
Figure 3.18: Zeiss Axio Observer workstation with control PC.

When additional image detail, contrast, or material composition measurements were necessary, imaging of up to 2000X was performed with a Zeiss EVO 50 desktop SEM. Specimens were mounted directly to the microscope stage via electrically-conductive carbon tape, and then stabilized with mineral putty before imaging. SEM images were captured at acceleration voltages between 8.0 and 20.0keV, depending on angle and composition of the material. All SEM imaging utilized an emitter filament current of 2.8A. A photo of this microscope is available in Figure 3.19, with spectral analysis counter visible on the right side of the frame. The additional spectral analysis hardware was utilized to identify the composition of the specimens, as well as certain oxides, carbides, and inclusions.

Figure 3.19: Zeiss EVO 50 scanning electron microscope workstation.

This particular system is manufactured by iXRF, and is a model 550i X-ray-based energy-dispersion spectroscopy (EDS) system. High-energy emissions from the SEM probe stimulate small amounts of X-ray emission from the specimen, which are counted by the X-ray detector.

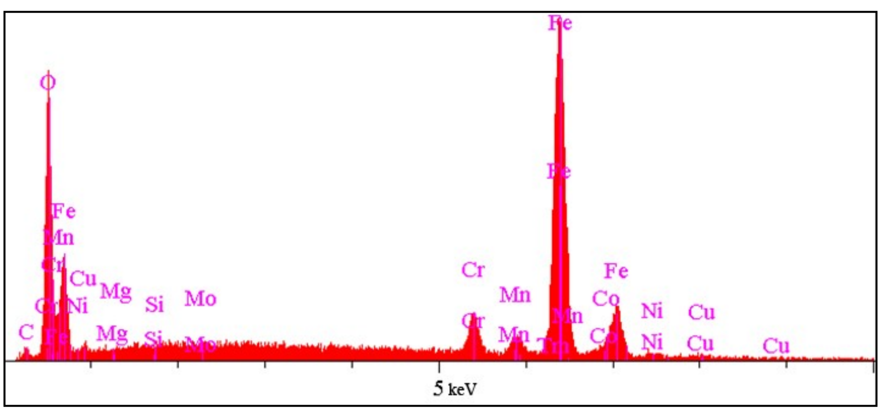

Figure 3.20: EDS spectral analysis of oxides inside the fracture path of a K_t = 3.0 200°C/600°C (473°K/873°K) IPTMF specimen tested at a mechanical strain range of 1.0%.

Because unique atomic structures release X-rays with different energy levels, spectra of the X-ray emission from a particular focal point can be analyzed for its elemental makeup. For instance, iron, chromium, nickel, and manganese are expected in certain quantities in this type and grade of steel. High carbon areas, which indicate the presence of carbides, or areas that are high in silicon from the metal casting process are also clearly identifiable. The detection of significant amounts of oxygen indicates oxidation, and the ratio between the oxygen content and iron content identifies the type of iron oxide present. An EDS spectrum obtained from a ferric oxide is shown in Figure 3.20.

CHAPTER 4

EXPERIMENTAL RESULTS

The computer system responsible for controlling the mechanical tests also simultaneously collects data regarding stress, displacement, and temperature. Assessment of the material in terms of stress response to the applied strain can be performed. Historically, strain-controlled fatigue tests are analyzed via a focus on two quantification methods- the stress history, and analysis of the stress-strain hysteretic response. In addition to determining when a fatigue test has met the initiation criterion, stress histories provided an overarching view of average load-carrying capacity across the minimum cross section, as well as any transient hardening or softening characteristics in the tested specimens. Inspection of individual hysteretic responses provided additional information about energy dissipation via plastic work, and also any considerable progressive or ratcheting-like changes in material response.

4.1 Examination of Stress Histories

Broad trends are immediately evident whenever comparison of stress history plots in similar cycle types was performed. As intuitively expected in the 200°C (473°K) LCF cases, increasing applied mechanical strain results in higher magnitudes of the stresses in all instances, with a 96MPa difference in peak stresses between the 0.7% and 1.4% mechanical strain ranges for smooth specimens. The presence of a notch influences the maximum and minimum stress values less dramatically, with only a 19MPa decrease in initial tensile stresses from the smooth to the sharply notched cases. In all tests, the cycle count to initiation lowered with increased strain application and/or increased notch sharpness. All specimen failures in the 200°C (473°K) LCF category

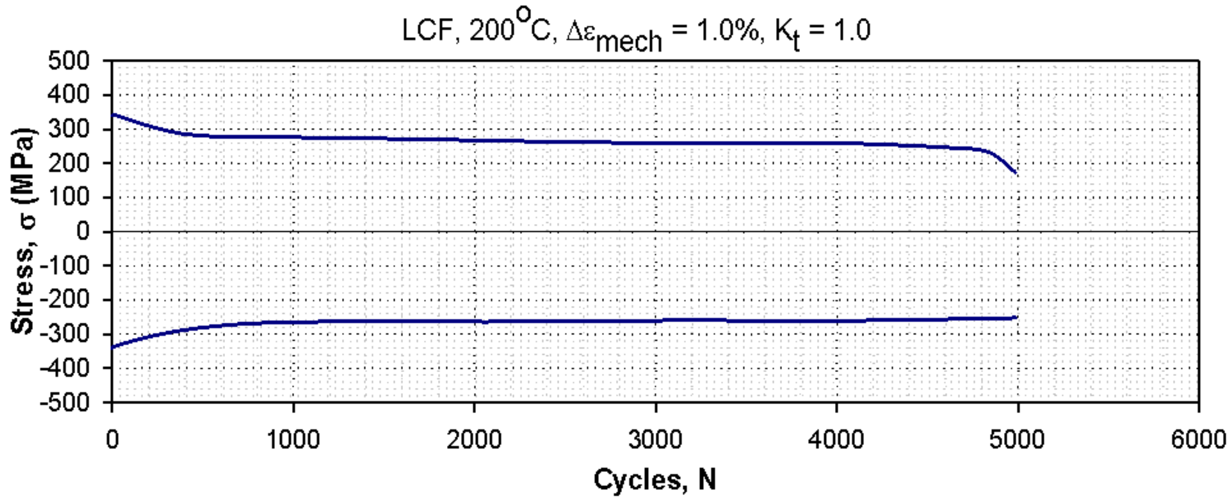

Figure 4.1: Stress history response of smooth 200°C (473°K) LCF specimen cycled at $\Delta\varepsilon_{mech}$ = 1.0%.

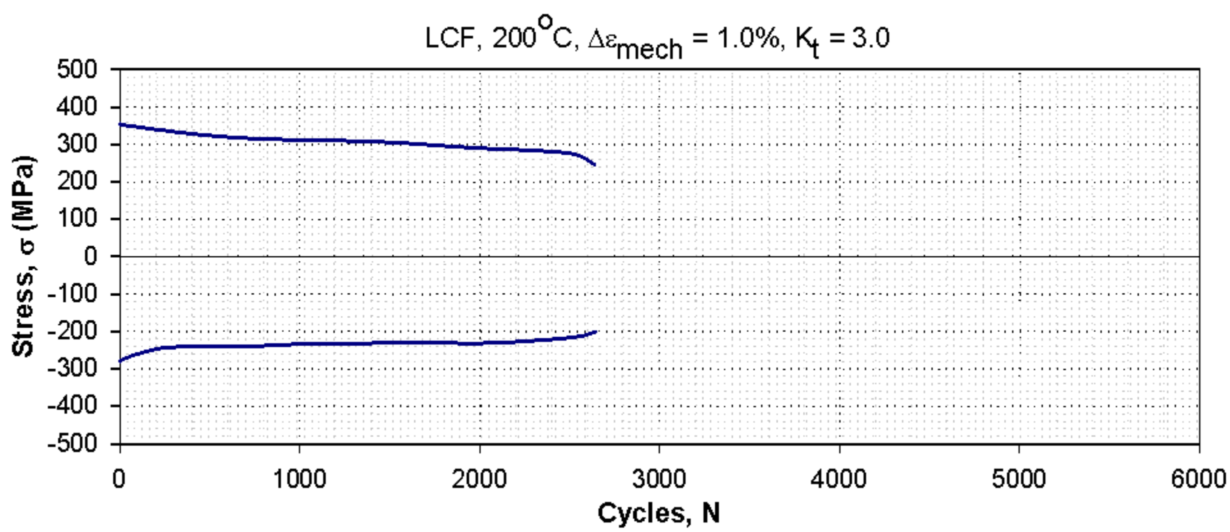

Figure 4.2: Stress history response of notched 200°C (473°K) LCF specimen cycled at $\Delta\varepsilon_{mech}$ = 1.0% with K_t = 3.0.

were relatively abrupt, with ability to carry the loading decreasing rapidly after crack initiation. Stress histories additionally reveal that each test initially shows a transient softening behavior in the first cycles. In smooth geometries, this softening lasts for approximately the first 10% of the specimen lifetime, except in the case of a tensile hold, which extends the softening portion of the plot to up to one-third of the entire stress history after facilitating higher initial peak stresses. During the majority of the lifetime, stress peaks remain in a stable state, where it can be shown

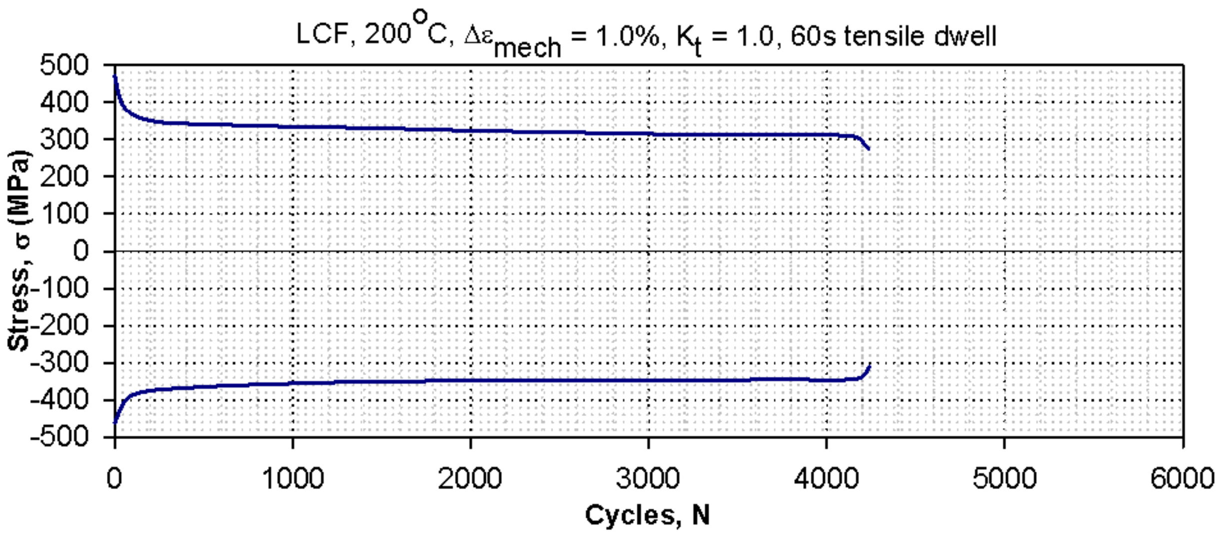

Figure 4.3: Stress history response of a smooth 200°C (473°K) LCF specimen cycled at $\Delta\varepsilon_{mech}$ = 1.0% with a 60s tensile dwell.

that smooth specimens carry a mean stress at or very close to zero. Notched specimens have a low tensile mean stress, implying asymmetric stiffness in the tensile and compressive directions regardless of softening behavior, as well as maintain a stable region of unchanging maxima for a shorter time than their smooth counterparts. Relevant data and parameters from all experimental cases is summarized at the end of the section in Table 4-1.

When considering the 600°C (873°K) LCF cases, the qualitative behavior of the stress responses appears similar for a significant percentage of specimen life. In particular, smooth specimens have a long region of constant stress peak/valley levels, while notched specimens continually decrease the minimum and maximum stresses in the stable region. Unlike the stiffer 200°C (473°K) LCF cases, the higher strain range 600°C specimens had a tendency to harden for the first few cycles, though softening begins afterward and the softer material exhibits an overall reduction in stress levels compared to 200°C (473°K) LCF specimens. Initial maximum stresses decreased by 20% and 28% from the 200°C levels for smooth and sharply notched cases to 261MPa and 243MPa, respectively. Midlife stress peaks are likewise reduced, which decreased maximum stress levels by 4% and 14% in the respective smooth and notched cases. With this elevated temperature condition, only the sharply notched (K_t = 3.0) cases show a small tensile mean stress. All of the

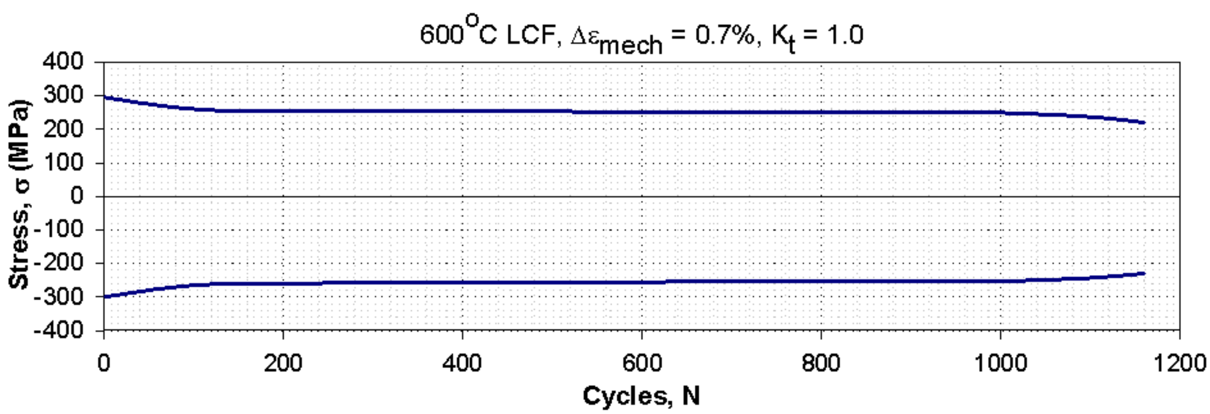

Figure 4.4: Stress history response of smooth 600°C (873°K) LCF specimen cycled at $\Delta\varepsilon_{mech}$ = 0.7%.

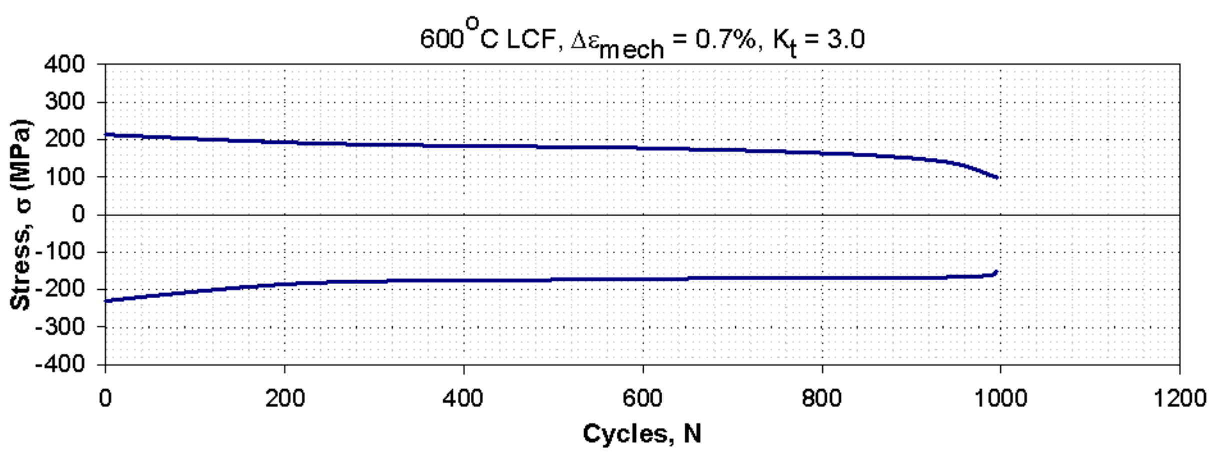

Figure 4.5: Stress history response of notched 600°C (873°K) LCF specimen cycled at $\Delta\varepsilon_{mech}$ = 0.7% with K_t = 3.0.

failures in the 600°C (873°K) LCF tests were gradual, with specimen load-carrying capacity decreasing slowly between initiation and failure cycles. Cycles which included a tensile dwell significantly decreased life as well as the overall load capacity of the specimens, with a difference of 18% noted for tensile peaks in smooth specimens with a strain range of $\Delta\varepsilon_{mech}$ = 1.0%. A comparison of representative cases is available in the plots of Figures 4.6 and 4.7, with data and parameter summary of all cases available in Table 4-1 at the end of this section.

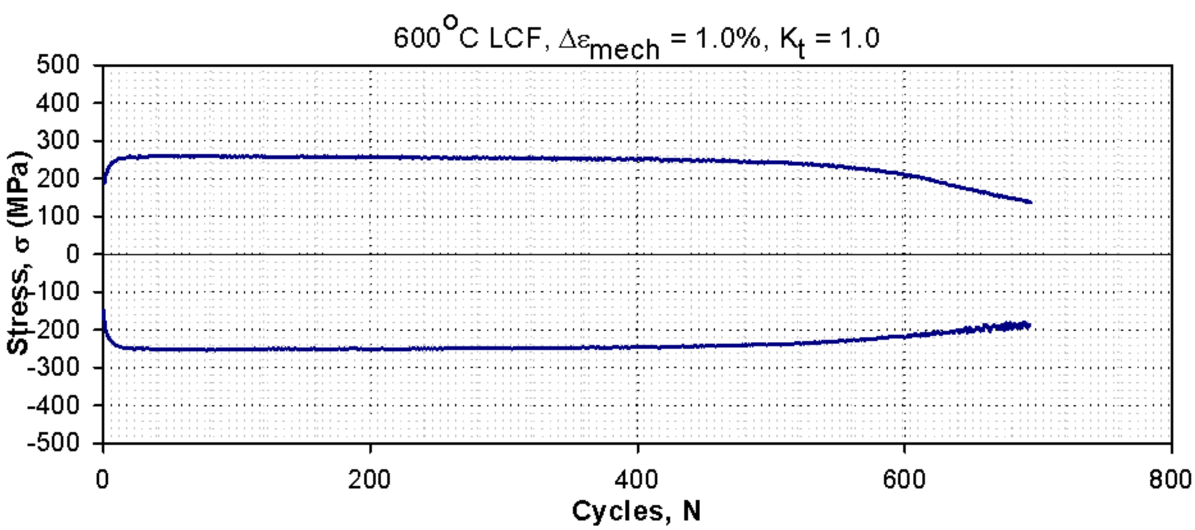

Figure 4.6: Stress history response of smooth LCF specimen at 600°C (873°K), cycled at $\Delta\varepsilon_{mech}$=1.0%

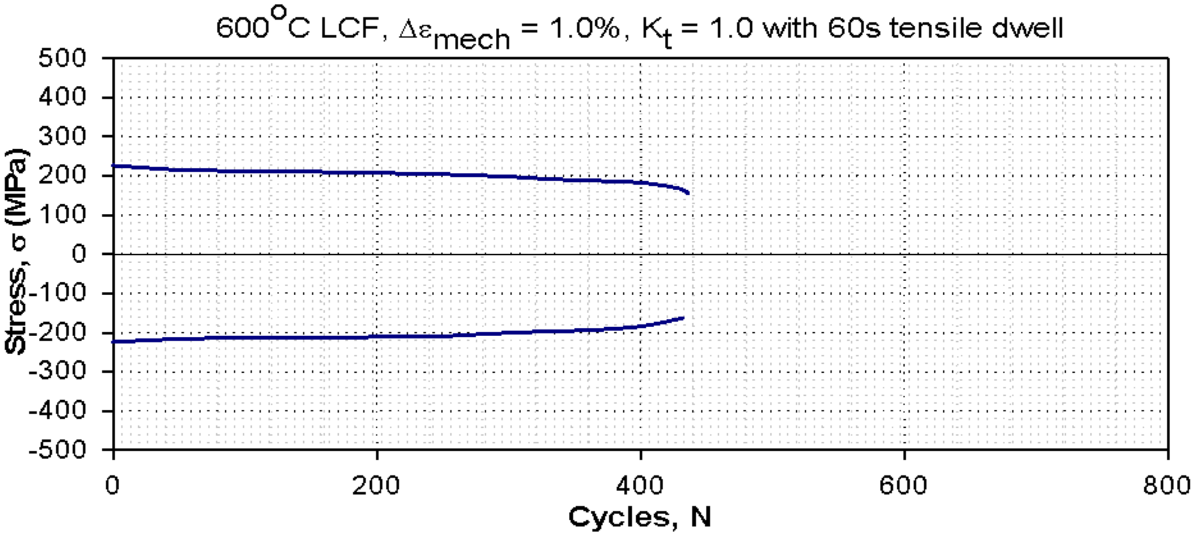

Figure 4.7: Stress history response of smooth LCF specimen at 600°C (873°K), cycled at $\Delta\varepsilon_{mech}$=1.0% incorporating a 60s tensile dwell.

For non-isothermal cases, the most striking difference in the stress histories with those of isothermal testing is the presence of a significant mean stress. In IPTMF, stiffness is lowest when strain is tensile, generally leading to a shift in the compressive direction.

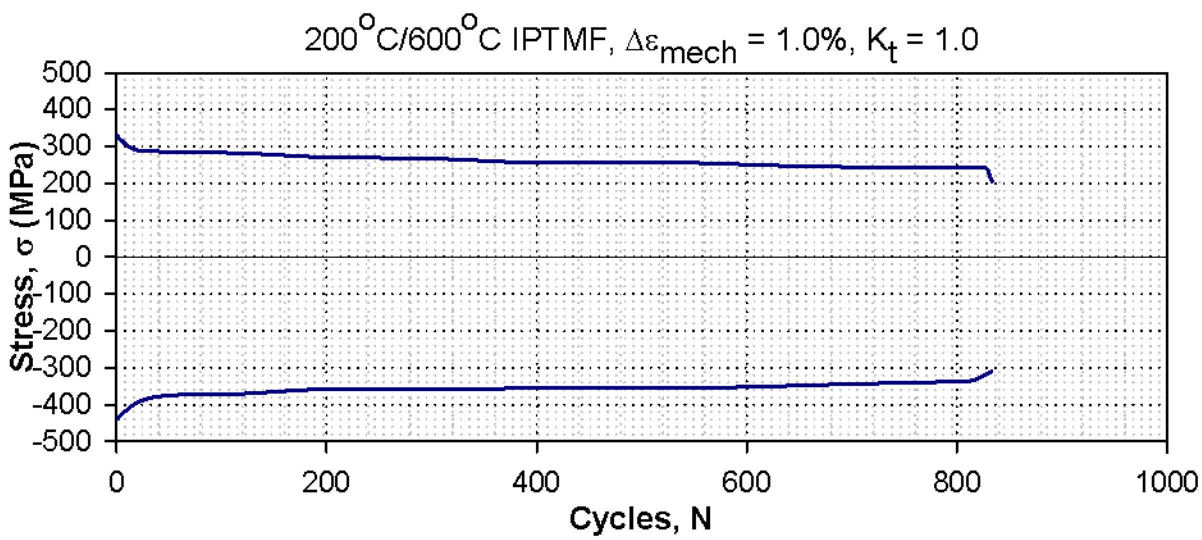

Figure 4.8: Stress history response of a smooth 200°C/600°C (473°K/873°K) IPTMF specimen cycled at $\Delta\varepsilon_{mech}$ = 1.0%.

In OPTMF, stiffness is highest when strain is tensile, which causes the mean stress to shift to the tensile side. Compared with other cycle types, this asymmetric material stiffness effect causes

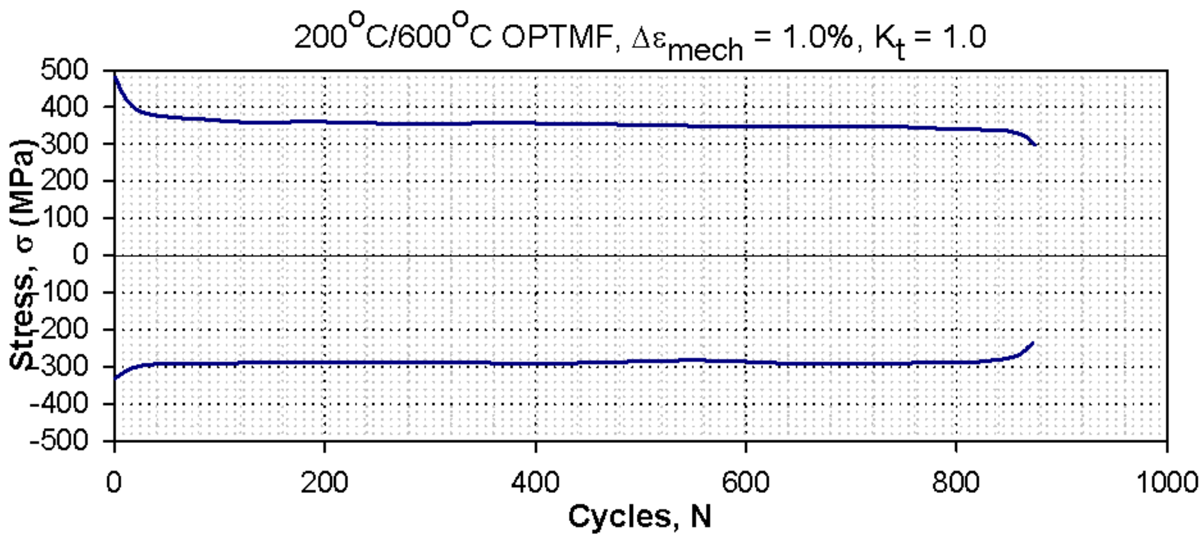

Figure 4.9: Stress history response of a smooth 200°C/600°C (473°K/873°K) OPTMF specimen cycled at $\Delta\varepsilon_{mech}$ = 1.0%.

IPTMF cases to have the greatest compressive stresses in the study. With $\Delta\varepsilon_{mech}$ = 1.0%, IPTMF initial compressive stresses are 49-81% greater than those in LCF counterparts with similar conditions for smooth cases, and 53% greater in the presence of a sharp notch. OPTMF conversely has the highest tensile stresses in the study- in smooth specimens, OPTMF maximum tensile stresses for $\Delta\varepsilon_{mech}$ = 1.0% exceed the 600°C (873°K) LCF case by 60-66%, and notched cases by

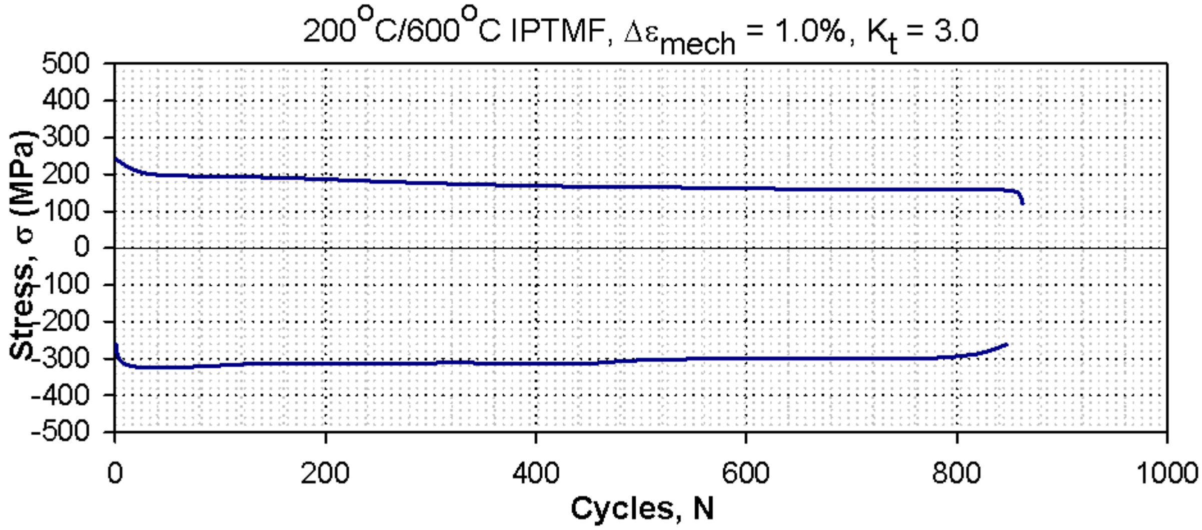

Figure 4.10: Stress history response of a notched 200°C/600°C (473°K/873°K) IPTMF specimen with $\Delta\varepsilon_{mech}$ = 1.0% and K_t = 3.0.

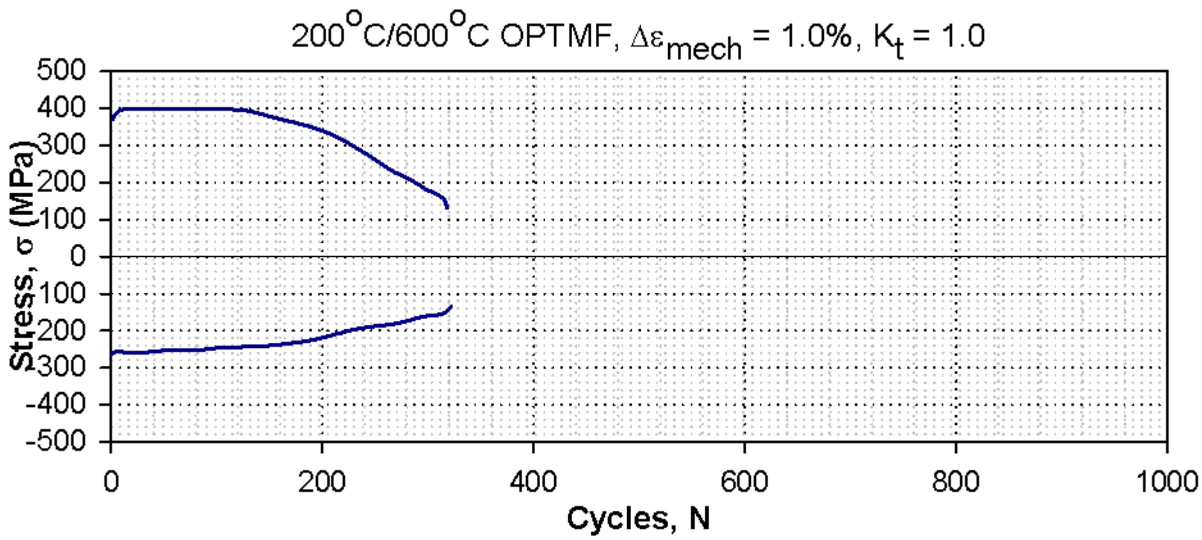

Figure 4.11: Stress history response of a notched 200°C/600°C (473°K/873°K) OPTMF specimen with $\Delta\varepsilon_{mech}$ = 1.0% and K_t = 3.0

55%-73%. This high tensile stress discrepancy indicates a likely cause of the significant life reduction in OPTMF versus IPTMF in the notched specimens for this strain range. Like the LCF cases, the TMF cases are more prone to transient hardening in the first 5%-10% of life when either in the presence of a notch, or incorporating a tensile dwell. Otherwise, the initial behavior is a softening of the response, followed by a long constant stress period. In IPTMF, the stability

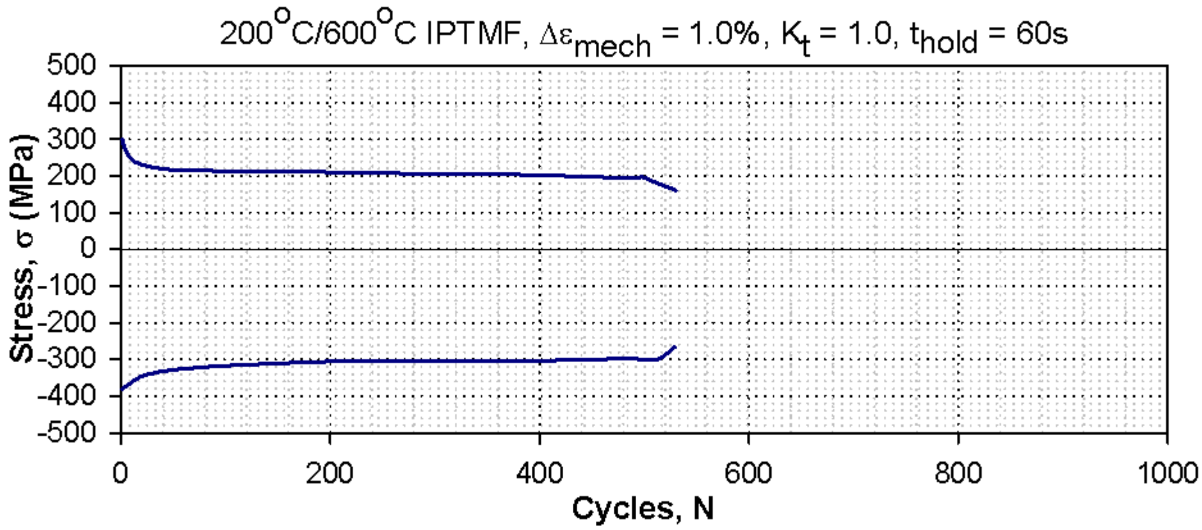

Figure 4.12: Stress history response of a smooth 200°C/600°C (473°K/873°K) IPTMF specimen with $\Delta\varepsilon_{mech}$ = 1.0%, incorporating a tensile dwell of 60s.

remains until just before an abrupt failure, but in OPTMF a small amount of additional softening occurs before crack initiation and a more gradual failure. Figures 4.8 to 4.12 compare IPTMF and OPTMF stress histories for conditions representing the range of behaviors. Data and parameter summaries of all tests are available in Table 4-1.

Table 4-1: Summary of stress history responses

Cycle Type	Mechanical Strain Range, $\Delta\varepsilon_{mech}$ (%)	Theoretical Stress Concentration Factor, K_t	Initial Transient Behavior	Description of Stable Behavior	Description of Stable Mean Stress Condition	Initial Maximum Stress, σ_{max} (MPa)	Initial Minimum Stress, σ_{min} (MPa)	Stable Maximum Stress, σ_{max} (MPa)	Stable Minimum Stress, σ_{min} (MPa)	Initiation Cycle, N_i	Failure Type
200C LCF	0.7	1.0	Softening	Constant	None	324	-287	254	-250	7607	Abrupt
	0.7	3.0	Softening	Continuous softening	Slightly tensile	269	-257	251	-219	4580	Abrupt
	1.0	1.0	Softening	Constant	None	328	-317	265	-260	4624	Abrupt
	1.0	1.73	Softening	Continuous softening	Slightly tensile	353	-418	311	-365	3428	Abrupt
	1.0	3.0	Softening	Continuous softening	Slightly tensile	334	-250	246	-240	2576	Abrupt
	1.4	1.0	Softening	Constant	None	458	-420	350	-347	2290	Abrupt
200C LCF, 60s Tensile Hold	1.0	1.0	Softening	Constant after additional softening	None	435	-420	327	-338	4151	Abrupt
	1.4	1.0	Softening	Constant after additional softening	None	456	-435	353	-362	1075	Abrupt
600C LCF	0.7	1.0	Softening	Continuous softening	None	291	-291	243	-245	1105	Gradual
	0.7	3.0	Softening	Continuous softening	Slightly tensile	192	-191	181	-172	945	Gradual
	1.0	1.0	Slight hardening	Constant	None	261	-248	258	-250	574	Gradual
	1.0	1.73	Slight hardening	Continuous softening	None	270	-292	262	-266	489	Gradual
	1.0	3.0	Slight hardening	Continuous softening	Slightly tensile	243	-203	212	-183	421	Gradual
	1.4	1.0	Slight softening	Constant	None	290	-284	225	-220	260	Gradual
600C LCF, 60s Tensile Hold	1.0	1.0	Slight hardening	Constant	None	213	-210	203	-205	410	Gradual
	1.0	3.0	Slight hardening	Constant	None	368	-254	285	-245	580	Gradual
	1.4	1.0	Slight softening	Constant	None	341	-337	312	-310	338	Gradual
200/600C IPTMF	0.7	1.0	Slight hardening	Constant	Compressive	231	-316	219	-318	1010	Abrupt
	1.0	1.0	Softening	Constant	Compressive	301	-431	268	-349	840	Abrupt
	1.0	3.0	Slight hardening	Constant	Compressive	222	-310	185	-303	694	Abrupt
	1.4	1.0	Slight hardening	Continuous softening	Compressive	311	-422	292	-385	74	Abrupt
200/600C IPTMF, 60s Tensile Hold	1.0	1.0	Softening	Constant	Compressive	318	-366	191	-299	498	Abrupt
	1.0	1.73	Slight hardening	Constant	Compressive	316	-327	240	-337	719	Abrupt
	1.0	3.0	Slight hardening	Constant	Compressive	429	-317	145	-309	298	Abrupt
200/600C OPTMF	1.0	1.0	Slight softening	Constant	Tensile	480	-282	350	-285	1655	Gradual
	1.0	1.73	Slight softening	Continuous softening	Tensile	490	-320	418	-300	566	Gradual
	1.0	3.0	Slight hardening	Continuous softening	Tensile	386	-246	384	-229	201	Gradual
	1.4	1.0	Slight softening	Constant	Tensile	478	-305	449	-318	23	Gradual

4.2 Examination of Hysteresis Curves

Hysteretic response, or a loci plot of the strain loading versus stress response points throughout a cycle, contain additional information about the behavior that cannot be gathered from minimum and maximum stress conditions alone. Specifically, cycle plasticity, relaxation behavior, and energy dissipation can be useful in determining the damage to the specimen during cyclic load application. The stress-strain response gathered during the first, midlife, and initiation cycles of each test provides this data. For each cycle type, a smooth specimen test at a low mechanical strain range is shown as the archetypical case, and compared against corresponding instances where strain, severity of geometry, or hold time has been increased. Additionally, comparisons are draw against similar conditions with different temperature and phasing conditions.

Under 200°C (473°K) LCF, a smooth specimen cycled with a mechanical strain range of $\Delta\varepsilon$ = 0.7% initially experiences stresses of +/-300MPa, and has measurable plasticity, with a maximum plastic strain range of $\Delta\varepsilon_{pl}$ = 0.28%. As mechanical strain application is increased, plasticity increases greatly with smaller corresponding increases in stress range. This denotes that load carrying capacity is saturating as plasticity grows, as expected in fatigue where plastic effects are appreciable. While the test progresses, in all applied mechanical strain range cases, the plastic strain range continues to grow as the stress range decreases. These effects are illustrated in Figures 4.13 and 4.14, where increased strain ranges grow the hysteretic energy inside the curve, and then as energy levels decrease and the curve shape flattens with test progression.

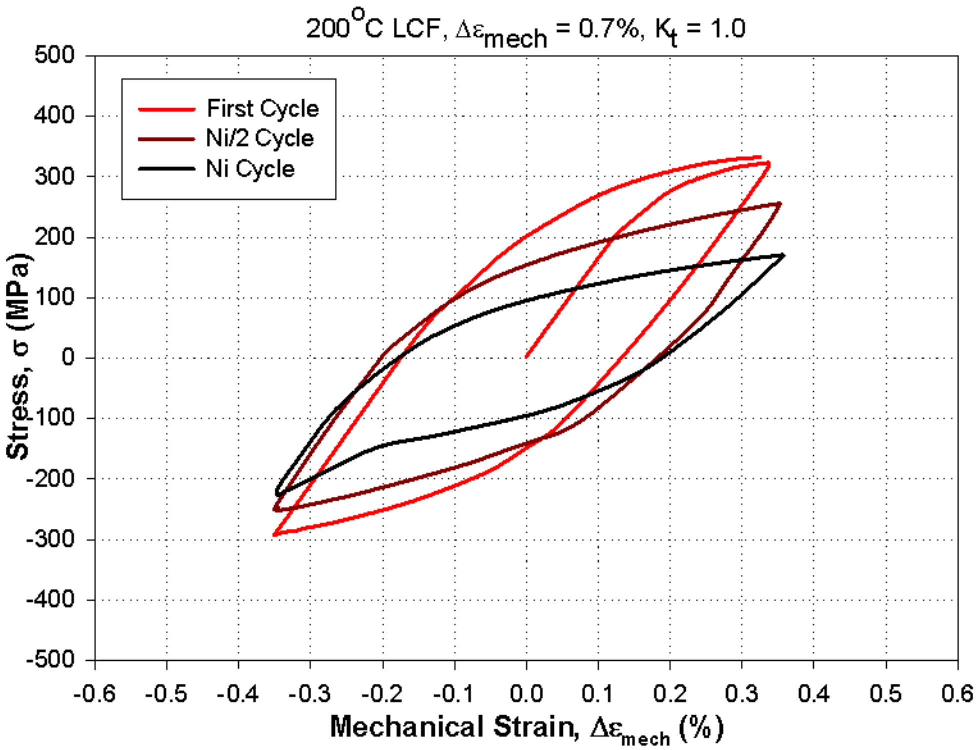

Figure 4.13: Comparison of hysteresis curves from initial, stable, and final cycles of a smooth 200°C (473°K) LCF specimen subjected to $\Delta\varepsilon_{mech}$=0.7%.

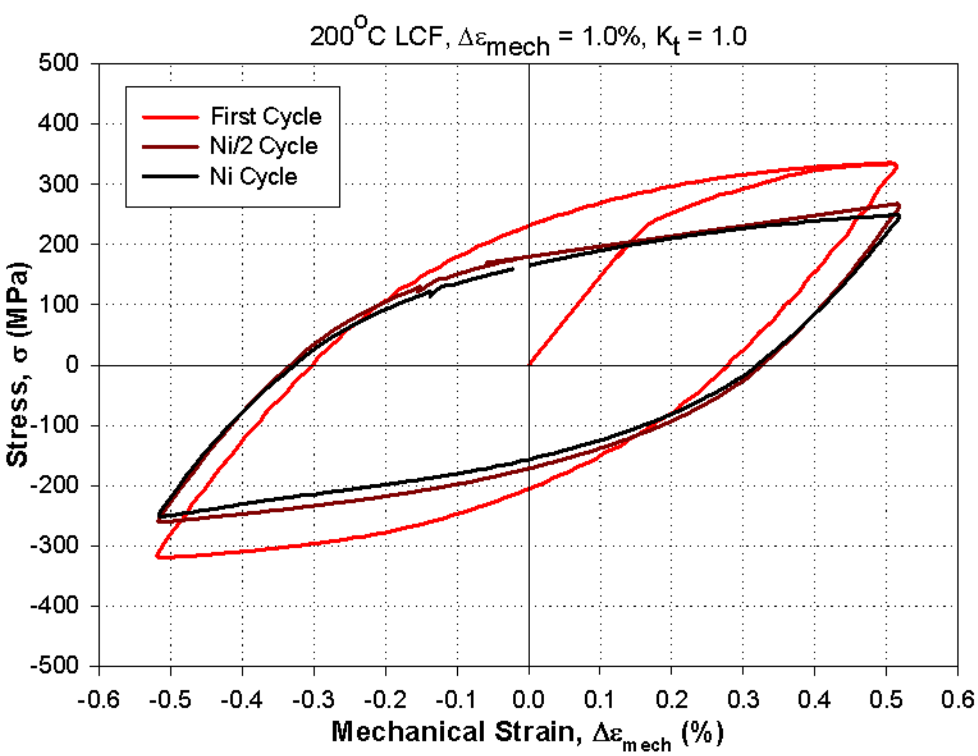

Figure 4.14: Comparison of hysteresis curves from initial, stable, and final cycles of a smooth 200°C (473°K) LCF specimen subjected to $\Delta\varepsilon_{mech}$=1.0%.

When the geometry is notched, the ability to carry stress is decreased, with a smaller stress range as the result in all applied strain range cases. The plastic strain range, (denoted as the "apparent" plastic strain range $\Delta\varepsilon'_{pl}$, to accommodate the slight skewing of the hysteresis curve by correction for the notched geometry, as addressed in the previous chapter) decreases slightly with respect to the smooth geometry $\Delta\varepsilon_{pl}$ value. As strain range application increases, the discrepancy in plastic strain range value between smooth and notched specimens is exacerbated. The effect of a notch on the hysteresis curve of a 200°C (473°K) LCF specimen is shown in Figure 4.15. In the case

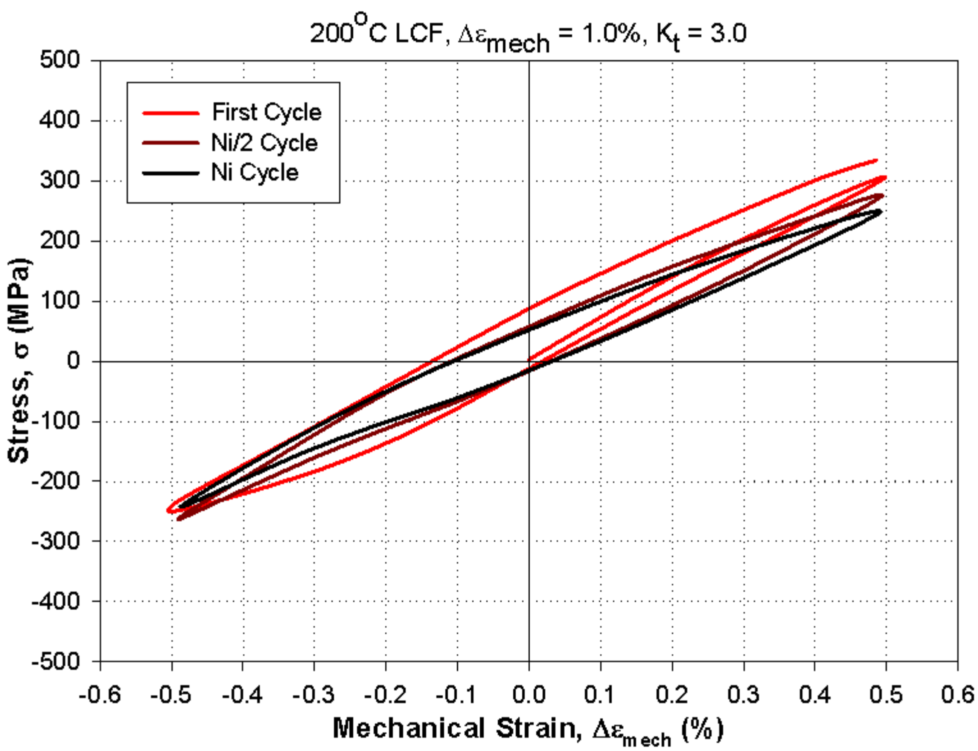

Figure 4.15: Comparison of hysteresis curves from initial, stable, and final cycles of a notched 200°C (473°K) LCF specimen subjected to $\Delta\varepsilon_{mech}$=1.0% and K_t=3.0.

of a dwell period, stress range and hysteretic energy increase without a noticeable change in plastic strain. This consequence of the tensile dwell is apparent in the plots of Figure 4.16. All relevant hysteresis curve parameters and responses are available in Table 4-2 at the end of this section.

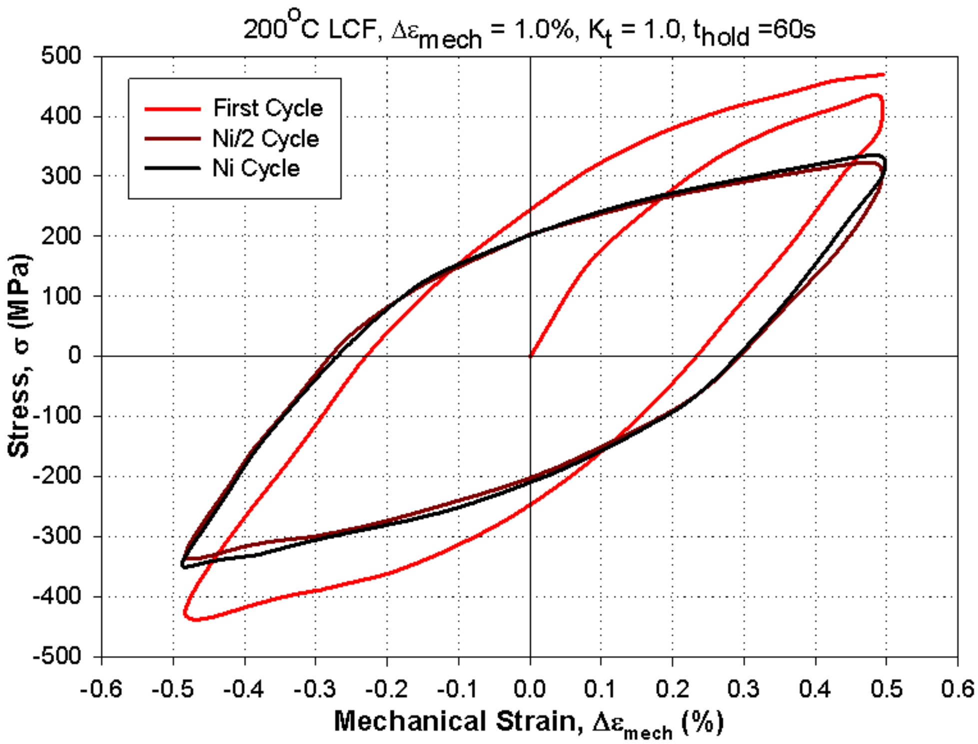

Figure 4.16: Comparison of hysteresis curves from initial, stable, and final cycles of a smooth 200°C (473°K) LCF specimen subjected to $\Delta\varepsilon_{mech}$=1.0% with 60s tensile dwell.

When considering 600°C (873°K) LCF behavior against the 200°C (473°K) LCF results, initial cycles show a softer response to strain commensurate with increased temperature, but with the hysteresis loop having a similar plastic strain range. This lower stress capacity is not decreased further as applied mechanical strain range $\Delta\varepsilon_{mech}$ is increased, unlike the plastic strain $\Delta\varepsilon'_{pl}$ which continues to grow up to $\Delta\varepsilon'_{pl}$ = 0.97% in high strain range cases. Lowered stress capacity is noted however, in the notched cases, where $\Delta\sigma$ and $\Delta\varepsilon'_{pl}$ both decrease significantly. These comparisons are visible in the plots of Figures 4.17 and 4.18. As notched testing proceeds beyond the initial cycles, the 600°C (873°K) LCF cases rapidly lose additional stress capacity as

$\Delta\varepsilon'_{pl}$ slightly increases to near 1.0% for high strain range cases. A tensile dwell in the cycle decreases the overall stress range for smooth cases with lower strain ranges, but the stress relaxation of up

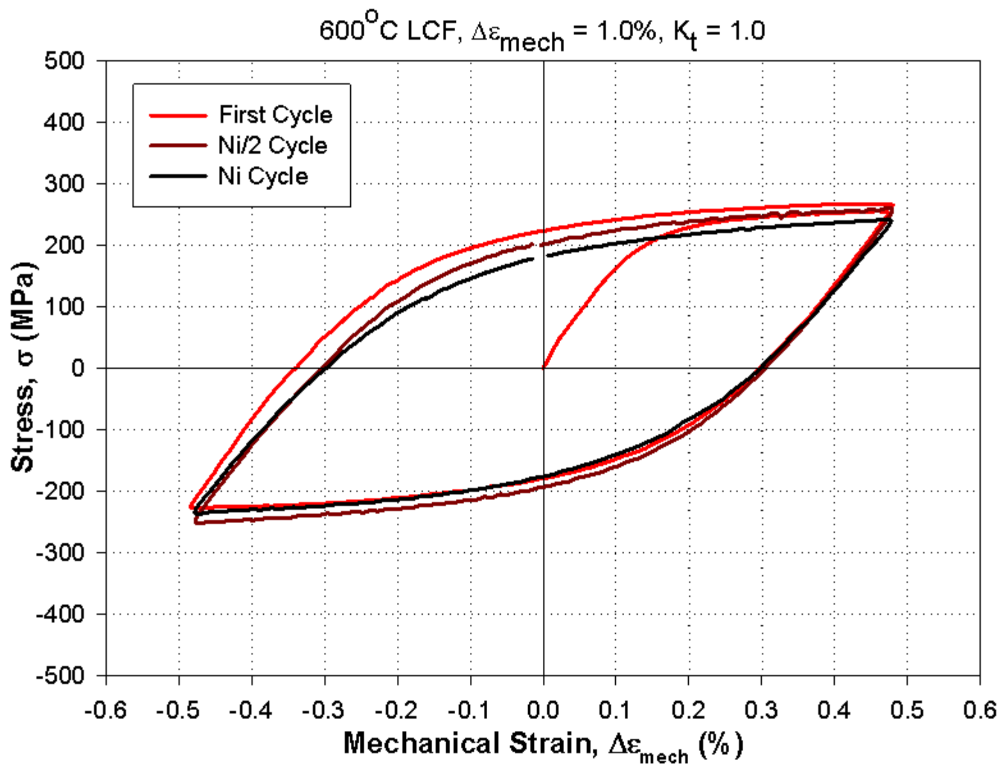

Figure 4.17: Comparison of hysteresis curves from initial, stable, and final cycles of a smooth 200°C (473°K) LCF specimen subjected to $\Delta\varepsilon_{mech}$=1.0%.

to 40% (368MPa to 233MPa in 60sec) with discontinuous geometries resulted in a reinforcement effect with noticeable increase in stress capacity for both the tensile and compressive regions of the load application. This effect is shown in the plots of Figures 4.18 and 4.19, with a summary of load cases and results available in Table 4-2 at the end of this section.

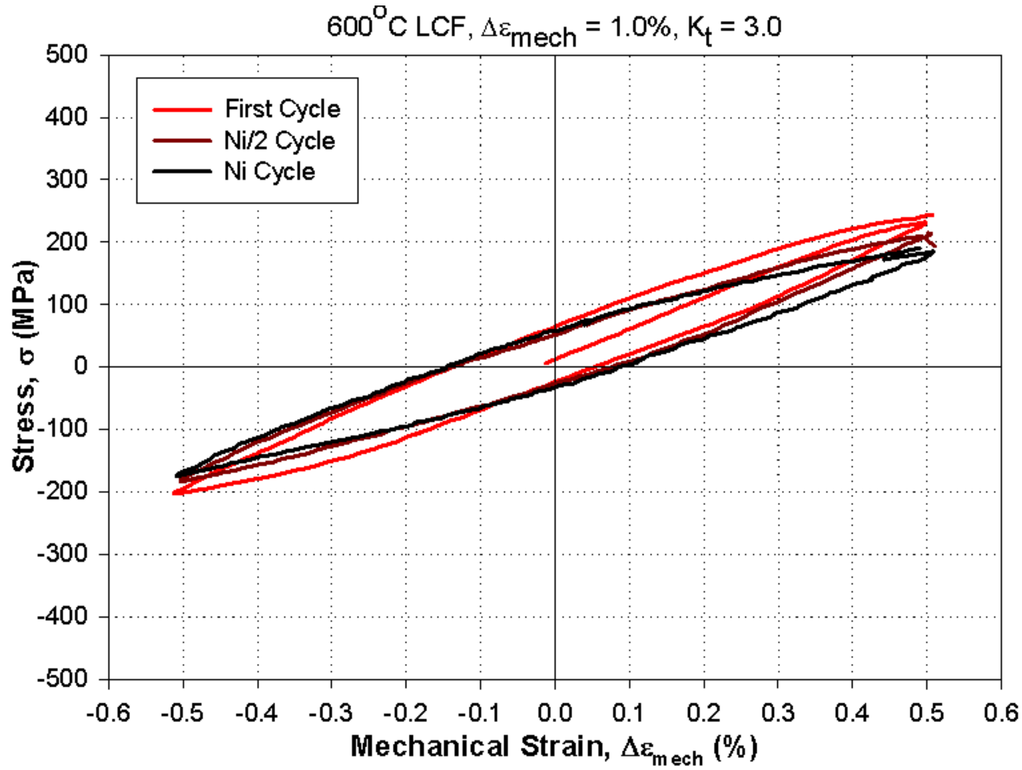

Figure 4.18: Comparison of hysteresis curves from initial, stable, and final cycles of a smooth 200°C (473°K) LCF specimen subjected to $\Delta\varepsilon_{mech}$=1.0%.

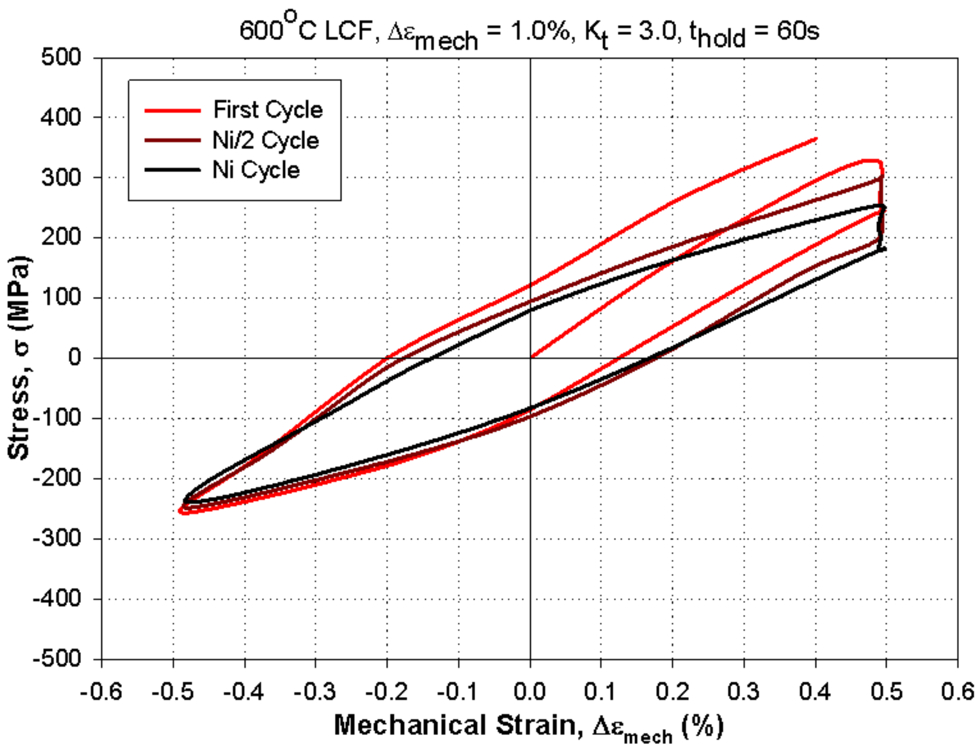

Figure 4.19: Comparison of hysteresis curves from initial, stable, and final cycles of a notched 600°C (873°K) LCF specimen subjected to $\Delta\varepsilon_{mech}$=1.0, with K_t=3.0 and a 60s tensile dwell.

Similar to the previous analyses involving stress histories, many of the behavioral effects noticeable in the stress-strain response under TMF are related to the inherent stiffness/thermal mismatch and resulting mean stress effects. Considering the IPTMF case first, in-phase tests with a maximum temperature of T_{max} = 600°C initially have maximum tensile stresses similar to those of their 600°C (873°K) LCF counterparts with identical $\Delta\varepsilon_{mech}$ values. However, as 200°C/600°C (473°K/873°K) IPTMF cycles cool during compressive strain application, the stiffer material at lower temperature leads to more significant compressive stresses. In the case of smooth specimens at $\Delta\varepsilon_{mech}$ = 1.0%, IPTMF minimum first cycle stresses were measured as σ_{min} = -431MPa while the LCF counterpart had a value of σ_{min} = -248MPa, amounting to a 74% increase, which is also in excess of the 200°C minimum stress value, owing to the soft ramp to maximum temperature before the first load reversal.

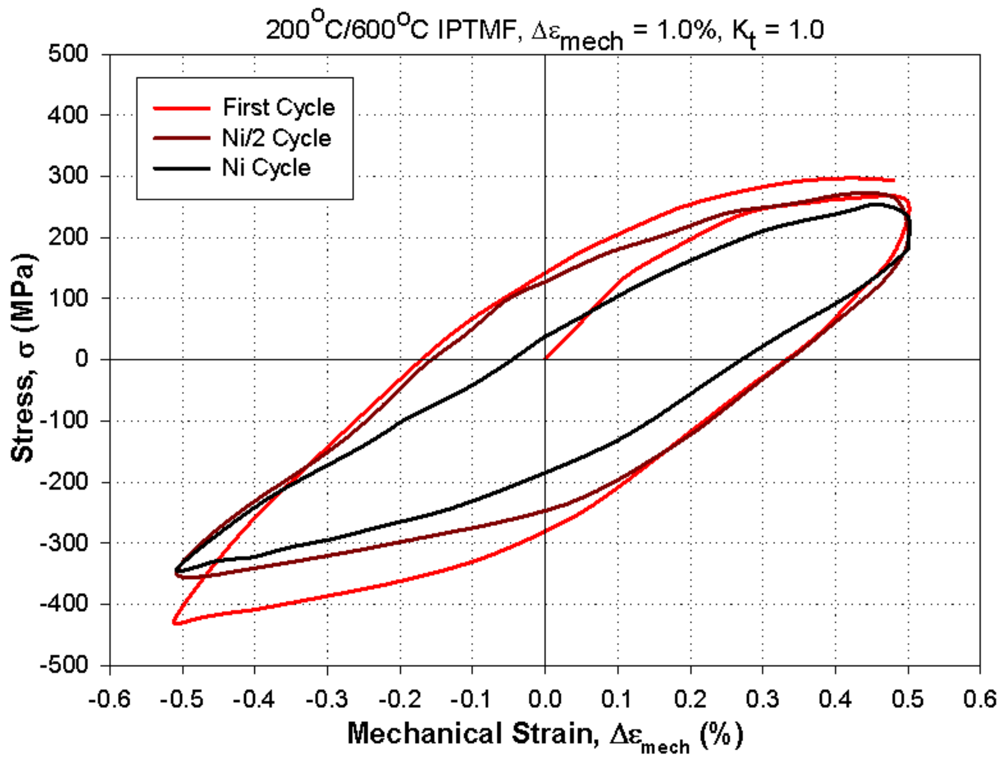

Figure 4.20: Comparison of hysteresis curves from initial, stable, and final cycles of a smooth 200°C/600°C (473°K/873°K) IPTMF specimen subjected to $\Delta\varepsilon_{mech}$=1.0%.

As higher mechanical strain range $\Delta\varepsilon_{mech}$ values are applied, the initial cycles increase the plastic strain range $\Delta\varepsilon'_{pl}$ accordingly, while also slightly increasing the stress range $\Delta\sigma$, albeit almost completely a consequence of increased compressive stresses. With the progression of cycling, IPTMF cases slowly decrease their stress ranges while $\Delta\varepsilon'_{pl}$ values remain similar. If a notched geometry is cycled in IPTMF, both the stress range $\Delta\sigma$ and plastic strain range $\Delta\varepsilon'_{pl}$ decrease as the hysteresis loop takes on a characteristic deflated areal appearance. In the case of a tensile dwell for IPTMF loadings, $\Delta\varepsilon'_{pl}$ is increased in all cases, while detrimental to the stress capacity. Figures 4.22 and 4.23 detail the effects notched and hold effect on IPTMF strain-based cycling.

Table 4-2 at the end of this section contains a summary of all relevant load parameters and stress-strain responses.

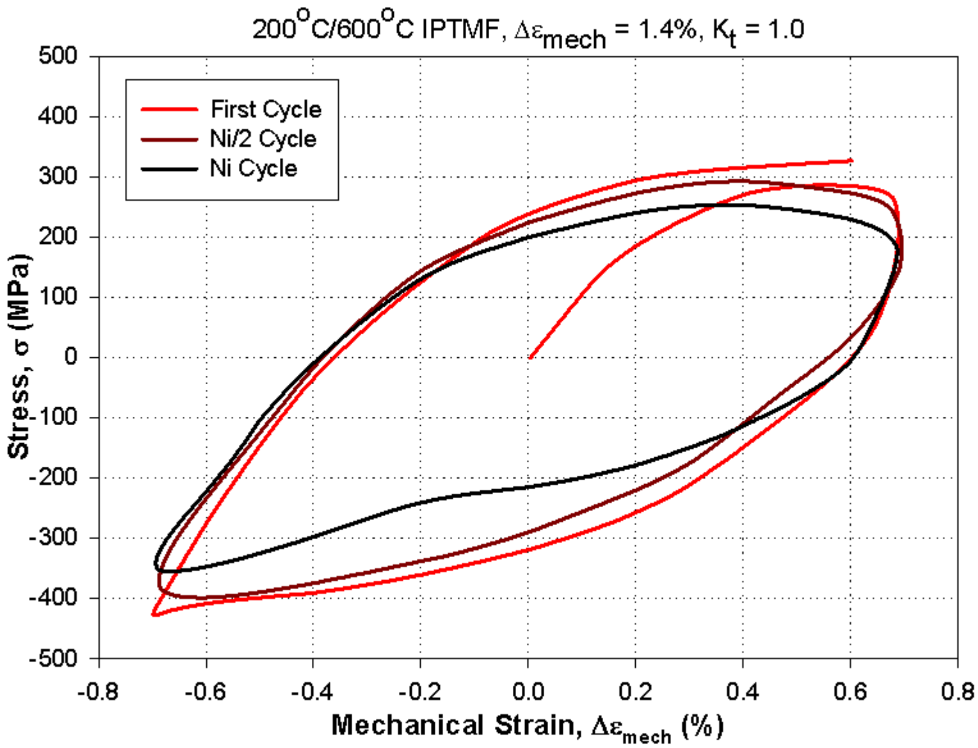

Figure 4.21: Comparison of hysteresis curves from initial, stable, and final cycles of a smooth 200°C/600°C (473°K/873°K) IPTMF specimen subjected to $\Delta\varepsilon_{mech}$=1.4%.

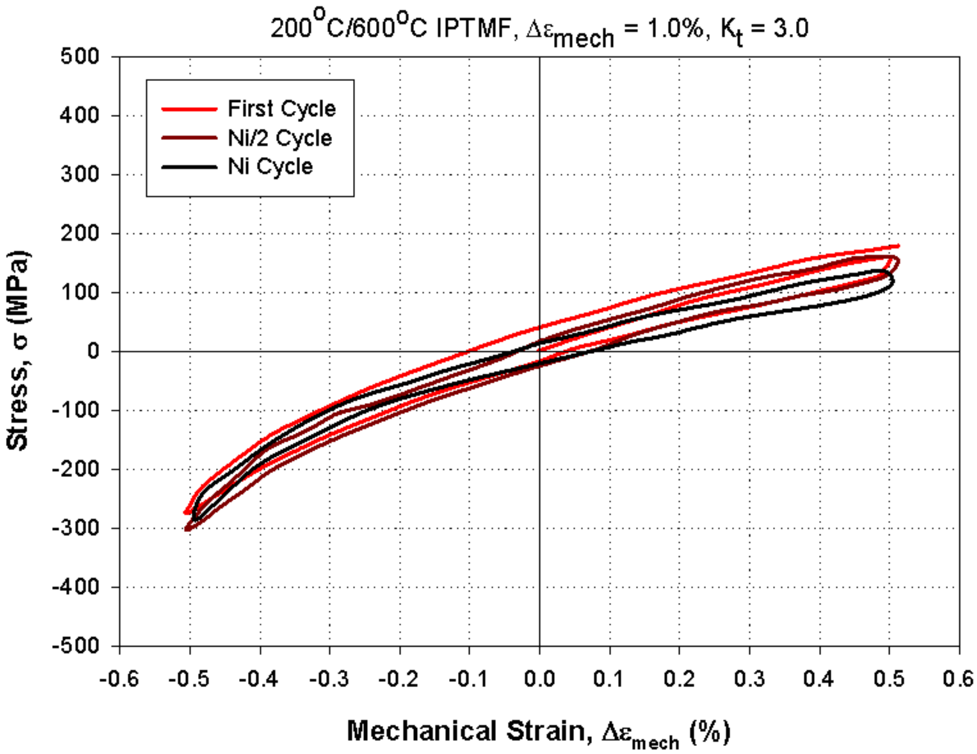

Figure 4.22: Comparison of hysteresis curves from initial, stable, and final cycles of a notched 200°C/600°C (473°K/873°K) IPTMF specimen with K_t=3.0 when subjected to $\Delta\varepsilon_{mech}$=1.0%.

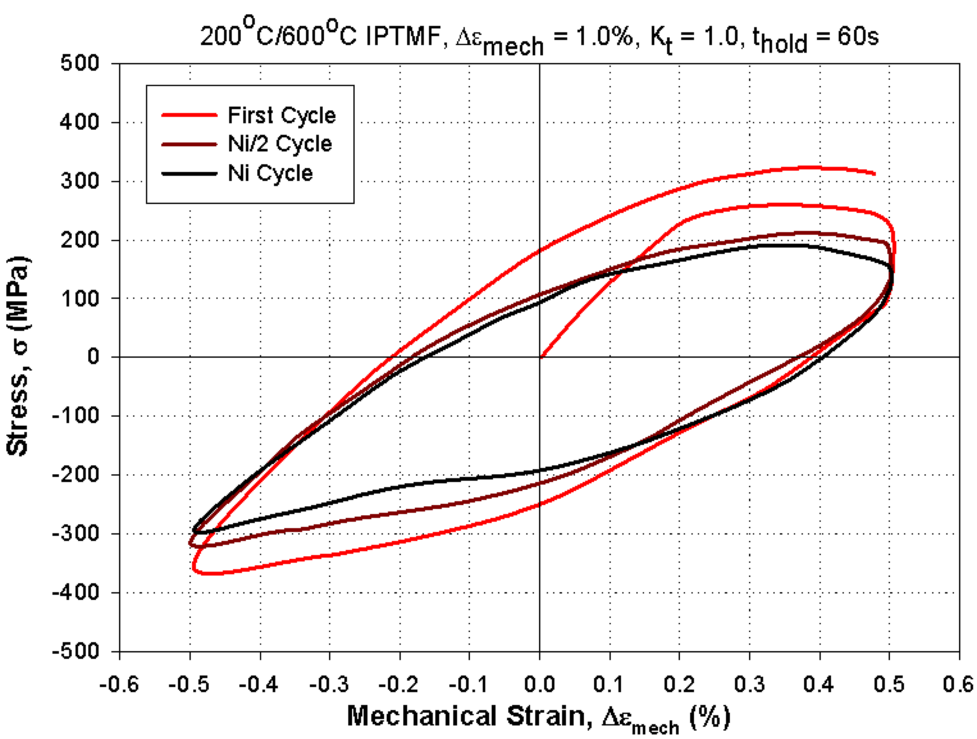

Figure 4.23: Comparison of hysteresis curves from initial, stable, and final cycles of a smooth 200°C/600°C (473°K/873°K) IPTMF specimen subjected to $\Delta\varepsilon_{mech}$=1.0% with the addition of a 60s tensile dwell.

While IPTMF cases increased their compressive stiffness in comparison to 600°C (873°K) LCF, 200°C/600°C out-of-phase loadings increase their tensile stiffness in comparison. Thus, a stress response effect opposite to that of IPTMF is realized, with stress range increases in OPTMF primarily due to tensile stresses that are nearly double that of 600°C (873°K) LCF loadings with similar conditions. OPTMF cases explored in the study did not have significant changes in $\Delta\varepsilon'_{pl}$ as cycling continues, but the overall stress range decreased as tensile stress values $\Delta\sigma$ dropped due to decreases in σ_{max}, which lowered by approximately 100MPa in smooth cases but with less impactful result in severely notched cases. The results of OPTMF testing with varied notch geometry are highlighted in the plots of Figures 4.24 to 4.26. All available TMF hysteresis load parameters and responses are catalogued in Table 4-2.

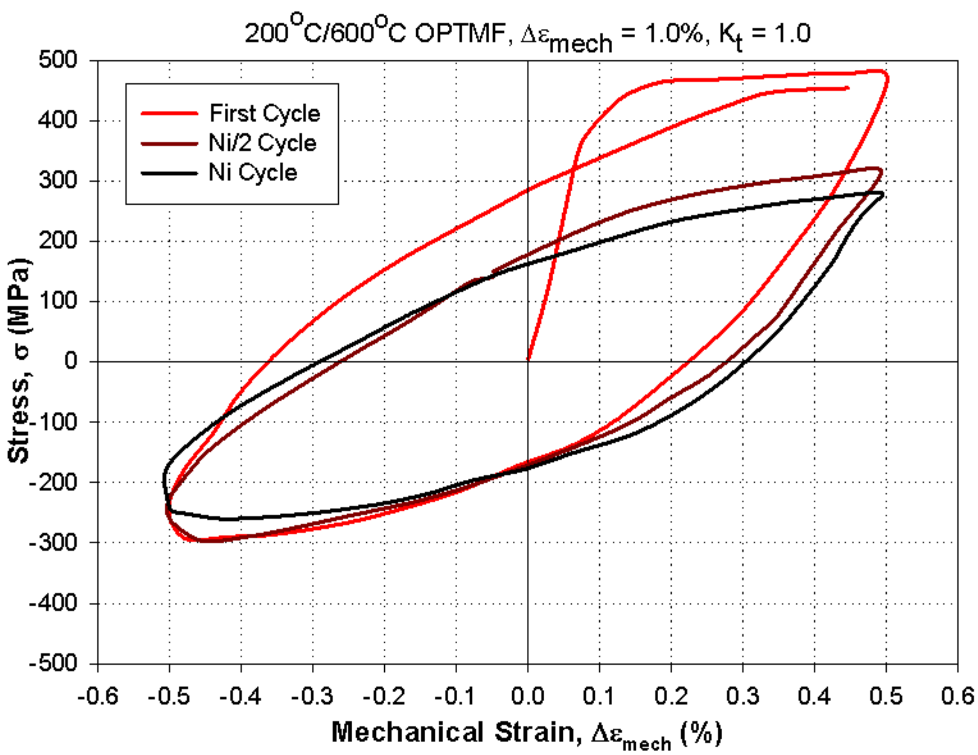

Figure 4.24: Comparison of hysteresis curves from initial, stable, and final cycles of a smooth 200°C/600°C (473°K/873°K) OPTMF specimen subjected to $\Delta\varepsilon_{mech}$=1.0%.

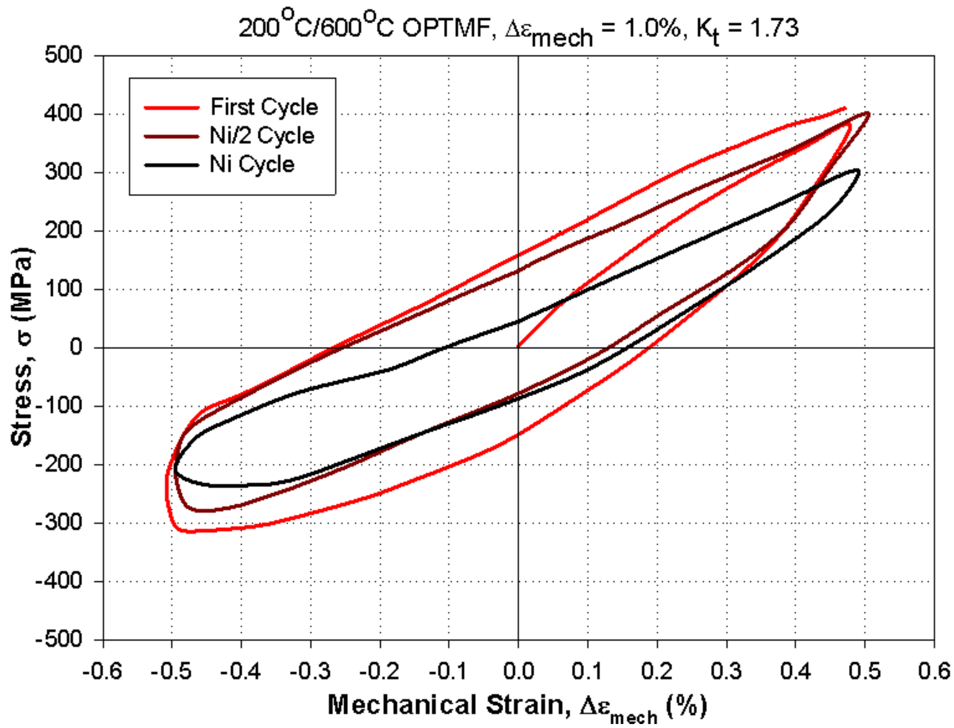

Figure 4.25: Comparison of hysteresis curves from initial, stable, and final cycles of a notched 200°C/600°C (473°K/873°K) OPTMF specimen subjected to $\Delta\varepsilon_{mech}$=1.0%, with K_t=1.73.

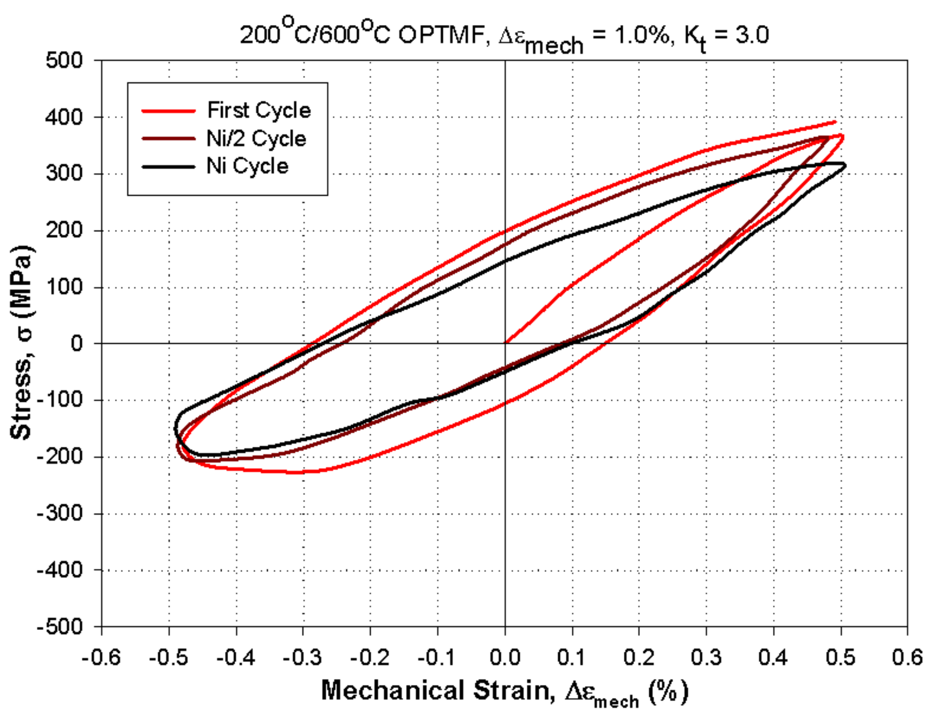

Figure 4.26: Comparison of hysteresis curves from initial, stable, and final cycles of a notched 200°C/600°C (473°K/873°K) OPTMF specimen subjected to $\Delta\varepsilon_{mech}$=1.0%, with K_t=3.0.

Table 4-2: Summary of hysteretic response characteristics

Cycles to Initiaion, Ni	1010	840	694	74	498	719	298	7607	4580	4624	3428	2576	2290	1105	945	574	489	421	260	4151	1075	410	580	338	1655	566	201	23
Stable Cycle Hold Stress Relaxation, Δσ (MPa)	0	0	0	0	58	17	40	0	0	0	0	0	0	0	0	0	0	0	0	9	57	56	104	42	0	0	0	0
Stable Maximum Plastic Strain Range $\Delta\varepsilon_{pl}$ (%)	0.27	0.52	0.05	0.9	0.57	0.06	0.06	0.37	0.27	0.66	0.12	0.13	0.95	0.36	0.12	0.6	0.29	0.22	1.03	0.57	0.93	0.51	0.31	1.03	0.54	0.33	0.31	0.97
Stable Cycle Minimum Stress, σ_{min} (MPa)	-318	-349	-303	-385	-299	-337	-309	-250	-219	-260	-365	-240	-347	-245	-172	-250	-266	-183	-220	-338	-362	-205	-245	-310	-285	-300	-229	-318
Stable Cycle Maximum Stress, σ_{max} (MPa)	219	268	185	292	191	240	145	254	251	265	311	246	350	243	181	258	262	212	225	327	353	203	306	312	350	418	384	449
Initial Hold Stress Relaxation, $\Delta\sigma_{hold}$ (MPa)	0	0	0	0	180	25	191	0	0	0	0	0	0	0	0	0	0	0	0	18	80	107	135	46	0	0	0	0
Initial Maximum Plastic Strain Range, $\Delta\varepsilon_{pl}$ (%)	0.16	0.48	0.08	0.95	0.59	0.12	0.24	0.37	0.23	0.58	0.11	0.14	0.84	0.37	0.07	0.64	0.19	0.19	0.97	0.45	0.83	0.61	0.32	0.96	0.48	0.37	0.39	1.02
Initial Minimum Stress, σ_{min} (MPa)	-316	-431	-310	-422	-366	-327	-317	-287	-257	-317	-418	-250	-420	-291	-191	-248	-292	-203	-284	-420	-435	-210	-254	-337	-282	-320	-246	-305
Initial Maximum Stress, σ_{max} (MPa)	231	301	222	311	318	316	429	324	269	328	353	334	458	291	192	261	270	243	290	435	456	213	368	341	480	490	386	478
Average Temperature, Tavg (K)	673	673	673	673	713	713	713	473	473	473	473	473	473	873	473	873	873	873	873	473	473	873	873	873	673	673	673	673
Average Elastic Modulus, E (GPa)	168	168	168	168	163	163	163	183	183	183	183	183	183	148	148	148	148	148	148	183	183	148	148	148	168	168	168	168
Tensile Dwell Period, thold (sec)	0	0	0	0	60	60	60	0	0	0	0	0	0	0	0	0	0	0	0	60	60	60	60	60	0	0	0	0
Cycle Time, tcyc (sec)	240	240	240	240	300	300	300	14	14	20	20	20	28	14	14	20	20	20	28	80	88	80	80	88	240	240	240	240
Minimum Cycle Temperature, Tmin (K)	473	473	473	473	473	473	473	473	473	473	473	473	473	873	873	873	873	873	873	473	473	873	873	873	473	473	473	473
Maximum Cycle Temperature, Tmax (K)	873	873	873	873	873	873	873	473	473	473	473	473	473	873	873	873	873	873	873	473	473	873	873	873	873	873	873	873
Theoretical Stress Concentration Factor, Kt	1	1	3	1	1	1.73	3	1	3	1	1.73	3	1	1	3	1	1.73	3	1	1	1	1	3	1	1	1.73	3	1
Mechanical Strain Range, $\Delta\varepsilon_{mech}$ (%)	0.7	1	1	1.4	1	1	1	0.7	0.7	1	1	1	1.4	0.7	0.7	1	1	1	1.4	1	1.4	1	1	1.4	1	1	1	1.4
Phasing, φ	1	1	1	1	1	1	1	0	0	0	0	0	0	0	0	0	0	0	0	0	0	0	0	0	-1	-1	-1	-1
Specimen Designation	K-025	K-007	K-016	K-003	K-009	K-015	K-020	K-021	K-023	K-004	K-013	K-011	K-11N	K-022	K-024	K-005	K-014	K-012	K-11O	K-010	K-001	K-006	K-019	K-002	K-008	K-017	K-018	K-11P

4.3 Baseline Comparison of Strain–Life Plots

As the experimental test program progressed, the most simplistic measure of methodology and result viability can be given by plotting the resultant number of cycles to crack initiation based on strain range application and comparing the data with that of previous studies. Although initiation and failure criterion may vary, the differences in the data due to the original experimenters' preferences are small in comparison to the lifetimes encountered in LCF and TMF testing. This method of verification requires no analysis other than the test's resulting cycle count. A summary of smooth LCF tests is offered first, which provides a cursory glance at LCF data quality. As pictured in the figure, the tests conducted in the current study fall within the bounds of the data which has been historically gathered on 304SS in fully-reversed strain testing. Accounting for the lower grade blend of steel in use, the 600°C (873°K) LCF tests appear to be within the scatter band which includes tests at temperatures between 427°C and 816°C.

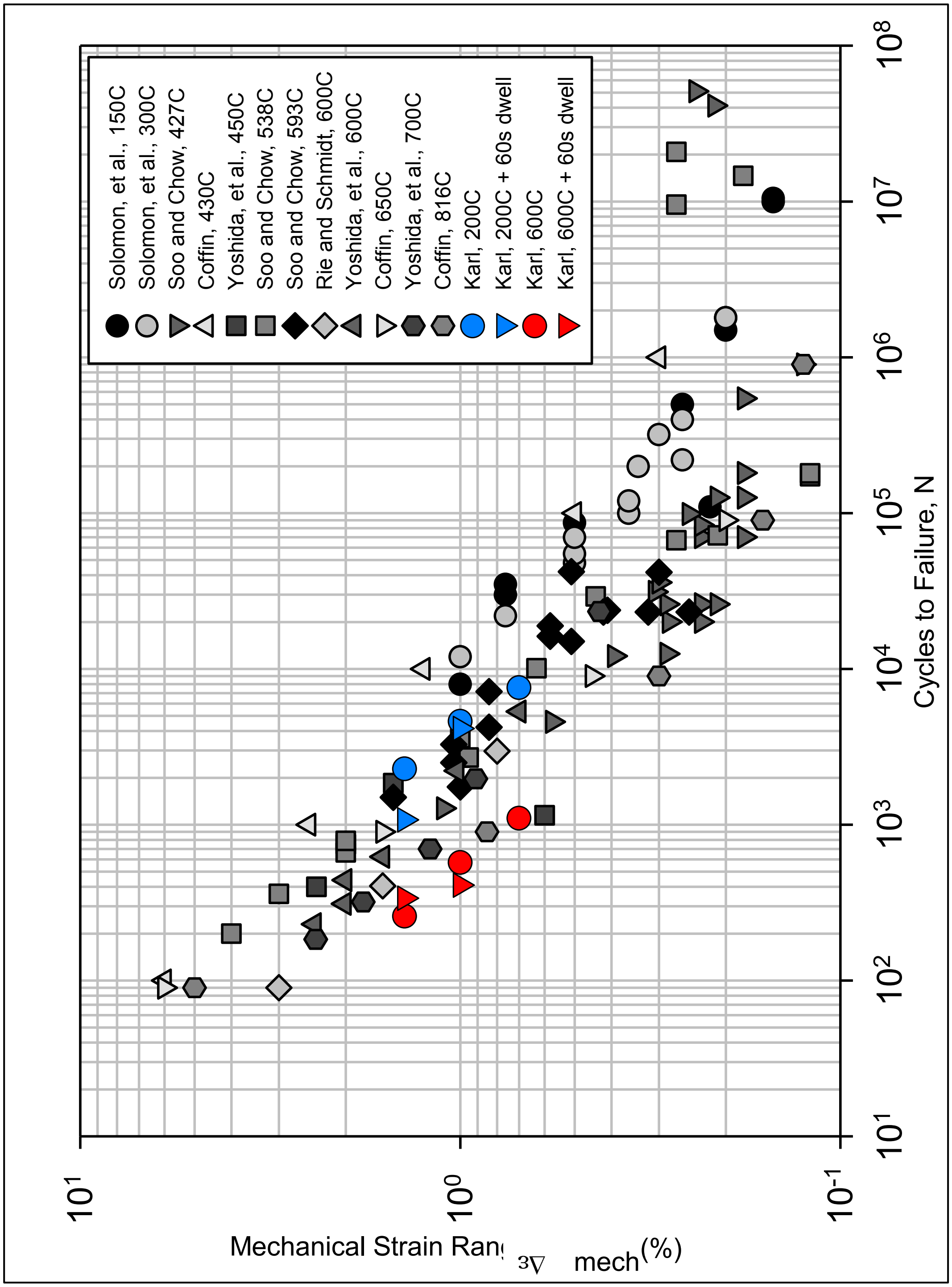

Figure 4.27: Smooth specimen LCF data is compared against elevated temperature data from Solomon, et al., Soo and Chow, Coffin, Yoshida, et al., and Rie and Schmidt.

In addition to smooth specimen LCF data, limited TMF data was available that was comparable against the conditions of the study. Several studies are compared with the current data, with clustering evident between historical data and that of this study.

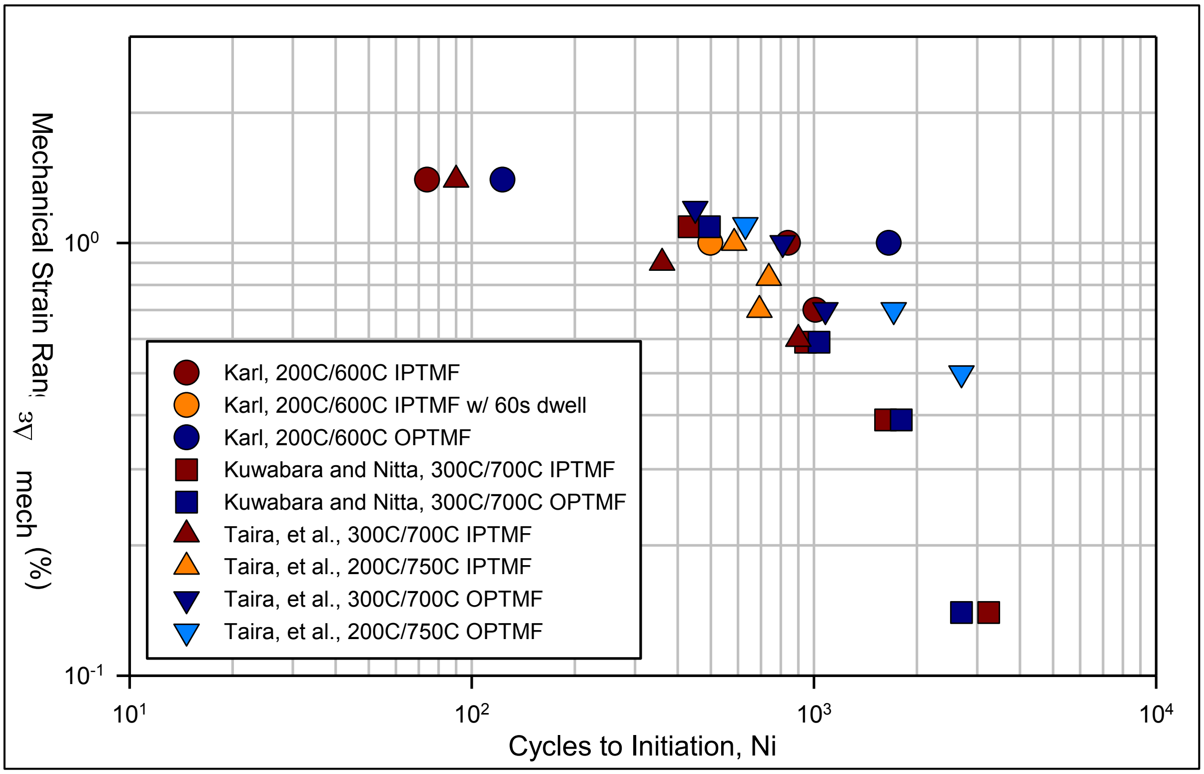

Figure 4.28: Current study data from smooth TMF specimens compared against studies from Kuwabara and Nitta, and Taira, et al.

CHAPTER 5

MICROSCOPIC OBSERVATIONS

To supplement the information gleaned from stress history and hysteresis data gathered during mechanical testing, a number of microscopic observation techniques were employed to gain insight into the microstructural changes in the material itself. Several specimens representative of differing load conditions were subjected to low-power optical microscopy, multi-wave optical microscopy, metallography, and scanning electron microscopy. For the purposes of quantifying damage for modeling, these types of observations have proven crucial, providing a basis for determining the methods of action that lead to the response and degradation in load-carrying capacity of the materials which are tested.

5.1 Low-Power Microscopy

Preliminary inspection of specimens was conducted using a low-power computer-linked optical microscope. These initial observations yielded information about the type and depth of the oxide layer present, as well as suggestions of the types of primary and secondary cracking. Images of the gage section indicated various stages of tempering and coloring corresponding to the different layer thicknesses of an outer coating of iron(II) oxide. LCF tests conducted in air at 200°C consistently exhibited a uniform straw-yellow color. This thin film interference effect serves as an indicator of an oxide coating a few microns thick. The overall oxide thickness in the 200°C cases did not appear dependent on strain range application. Both bluntly- and sharply-notched specimens had identical coloring inside and outside the notch. In the case of specimens subjected to a 60-second tensile hold period, the oxide layer appeared as a slightly darker bronze color, which would denote the presence of an oxide layer on the order of ~10 microns. Figure 5.1 illustrates this type of oxide coating and offers a comparison of multiple LCF specimen types tested at 200°C.

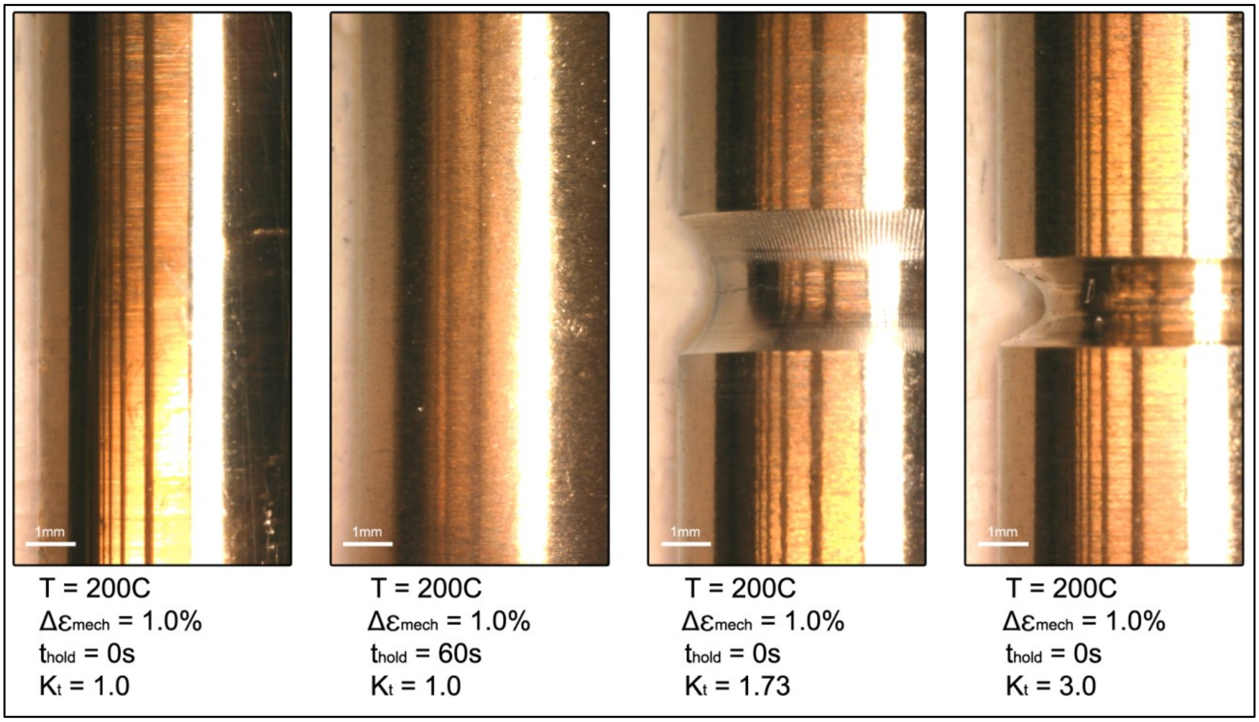

Figure 5.1: Photos of the gage section of specimens subjected to LCF at 200°C.

Optical analyses of LCF tests conducted in air at 600°C also revealed a near-uniform coating of iron(II) oxide, with the layer thickness increased to the point where the thin-film effect exhibits a deep blue color. Heavier deposits of ferric oxide were noted in tests which were longer in overall duration, with smaller strain ranges and the addition of tensile holds promoting the growth of a thicker opaque layer. In higher strain ranges, transverse cracks in the oxide layer were prevalent throughout regions where the oxide had reached considerable thickness. Many tests additionally showed evidence of pitting as well as large regions of hydrated iron oxides, with a darker brown color. A comparison of multiple LCF specimens tested at 600°C is offered in Fig 5.2.

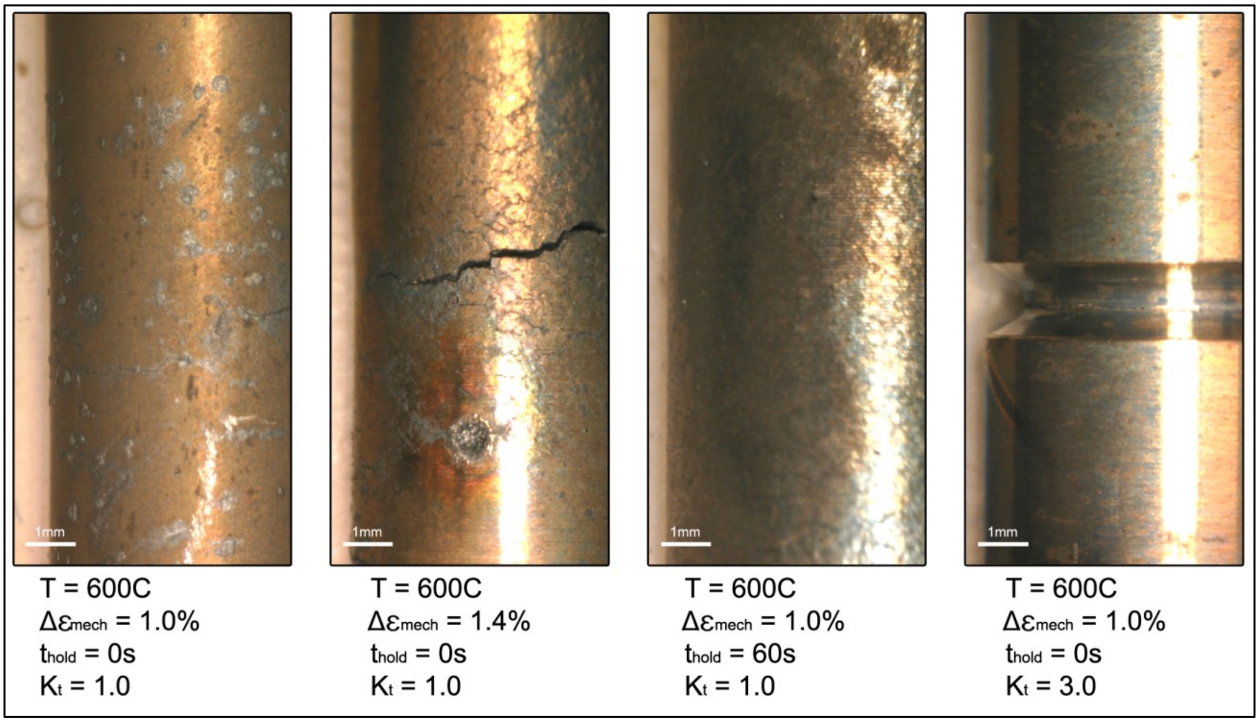

Figure 5.2: Photos of the gage sections of specimens subjected to LCF at 600°C.

Samples which were exposed to 200°C/600°C thermomechanical fatigue conditions in air shared many visual aspects with those of long duration LCF tests conducted at 600°C (873°K), with heavier opaque oxide layers formed unevenly over a blue temper. TMF-cycled test articles displayed prominent cracking in the outer oxide layer as pictured in Figure 5.3. Generally, OPTMF loadings caused a flake-like oxide layer prone to spalling, while IPTMF oxide layers were better adhered to the parent material, and displayed transverse cracking. Both IP and OP TMF cases alike resulted in the least amount of hydrated oxide formation in all of the tests conducted.

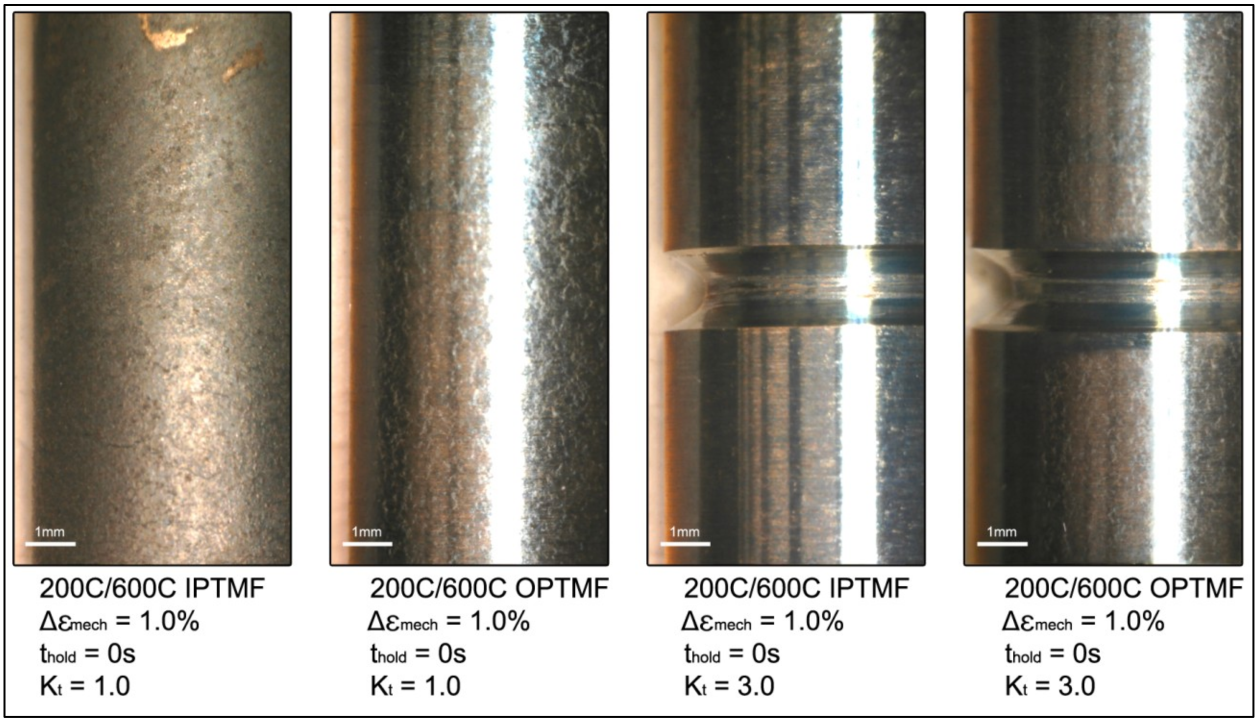

Figure 5.3: Macro photos of the gage sections of specimens subjected to 200°C/600°C (473°K/873°K) IP and OP TMF.

A final mechanical effect is readily observable in the more severe notch cases. Plastic deformation at the notch tip is not evenly distributed, resulting in an asymmetric notch shape in specimens after mechanical cycling. The deformed notch geometry results in a complex shape with multiple local radii of curvature, but crack initiation sites do not favor any local geometries. Figure 5.4 exhibits an example of the change in notch profile of a K_t = 3.0 specimen.

Figure 5.4: Example of a sharply-notched specimen cycled in 200°C (473°K) LCF with $\Delta\varepsilon_{mech}$ = 1.0% exhibiting asymmetric deformation.

5.2 Multi-Wave Optical Microscopy

A number of specimens were pulled apart in tension after the completion of a test, in order to expose their fracture surfaces. As some primary crack growth occurs before the initiation cycle load drop criteria is met, information about the direction of growth as well as the propensity of the oxide to penetrate all the way to the crack front can be obtained, even in specimens which have been cycled beyond the initiation cycle. A multi-wave microscope with a high focus depth range was employed to measure and catalog these qualitative results.

When considering specimens subjected to 200°C (473°K) LCF, the color change of light oxidation is evident along the crack path, but is not present at the crack front. Smooth specimen primary cracks travel directly through the cross section, while bluntly and sharply notched specimens steer the primary crack along the circumference of the specimen before inward propagation leads to failure. Figure 5.5 illustrates this comparison between two specimens tested under 200°C (473°K) LCF conditions. If temperatures of 600°C are considered, more oxidation is observable at the front of the crack, but crack propagation directions are unaffected. Figure 5.6 offers a comparison of LCF specimen fracture surfaces when the cycling temperature is increased to 600°C.

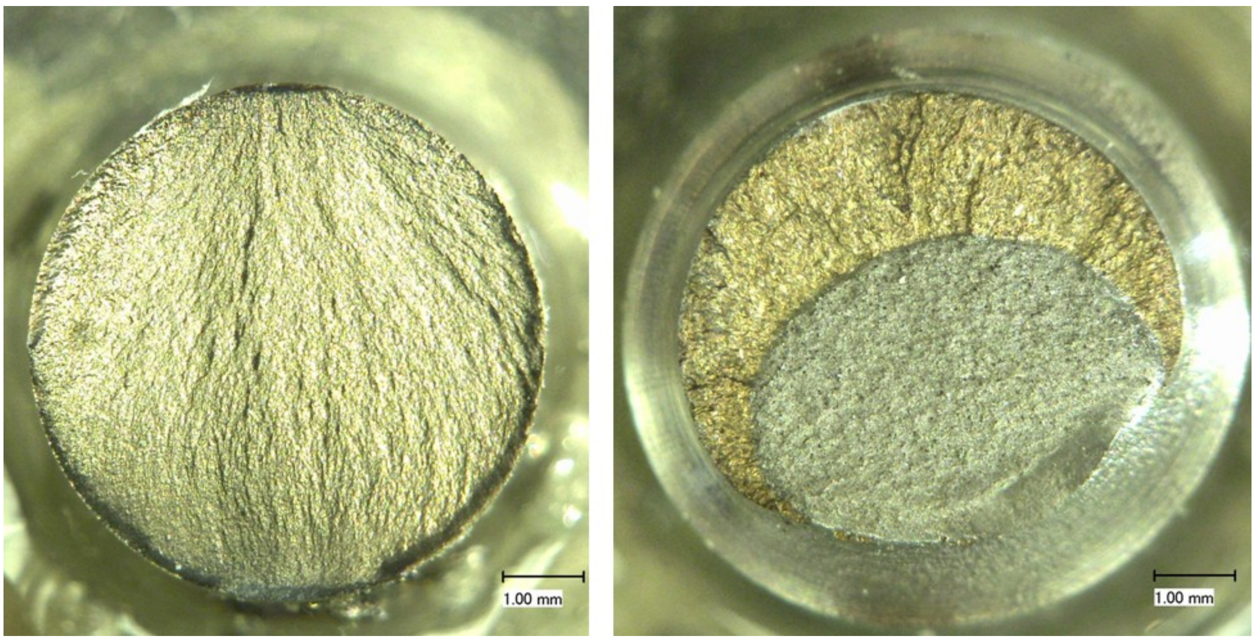

Figure 5.5: Fracture surface comparison of 200°C (473°K) LCF specimens with smooth geometry cycling at $\Delta\varepsilon_{mech}$ = 0.7% (left) and a bluntly notched (Kt= 1.73) geometry cycling with $\Delta\varepsilon_{mech}$ = 1.0% (right).

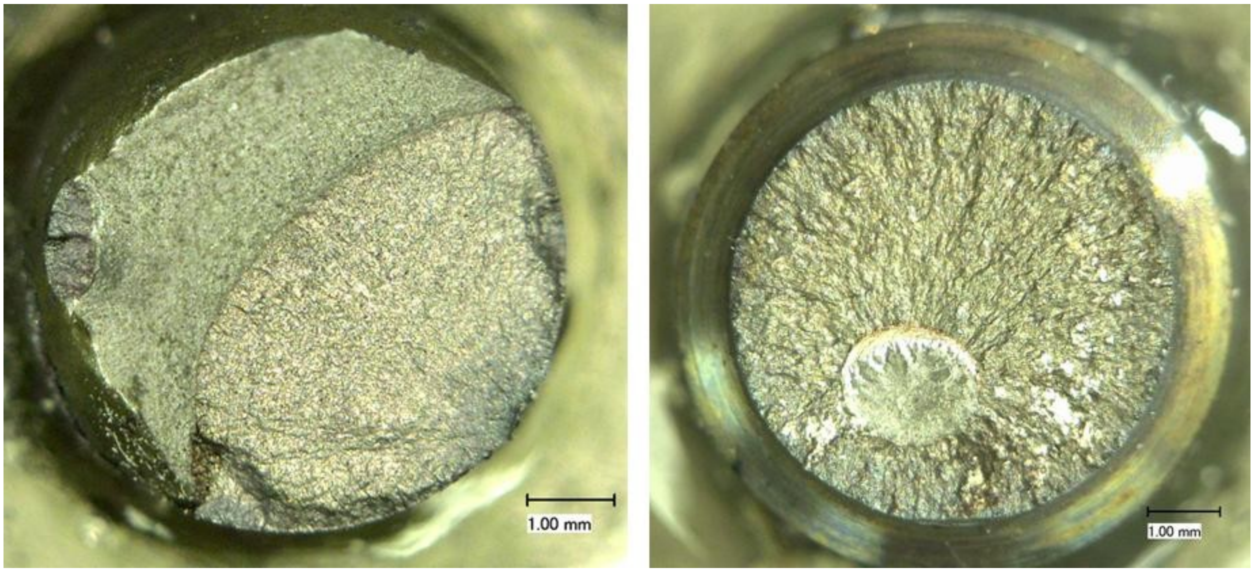

Figure 5.6: Comparison of fracture surfaces from smooth (left) and sharply notched (K_t = 3.0) (right) specimens cycled under LCF conditions at 600°C (873°K) with a strain range $\Delta\varepsilon_{mech}$=1.0%.

Under TMF conditions, imagery was obtained of notched cases only. These particular cases do, however, offer evidence of the effects of a few notable behaviors. Firstly, whereas LCF and OPTMF specimens with notches propagate primary cracks circumferentially at first, they do not do so around the entire cross-section, and bias deeper penetration to favor the side where the initiation point is located. In IPTMF the primary cracks propagated evenly in the circumferential direction, with the penetration depth on the opposite side of the initiation point being nearly equal with that at the crack initiation site itself. Additionally, the crack surface itself on each of the TMF specimens differ in appearance. The OPTMF cases appear to show greater amounts of secondary cracking and cleavage near the outer surface of the specimens, with relatively steady and featureless propagation as the crack moves to the interior. The IPTMF specimens show less features on the outside, and the remaining ligaments show more fragmentation and cleavage over the tensile-fractured surface than the OPTMF cases. This

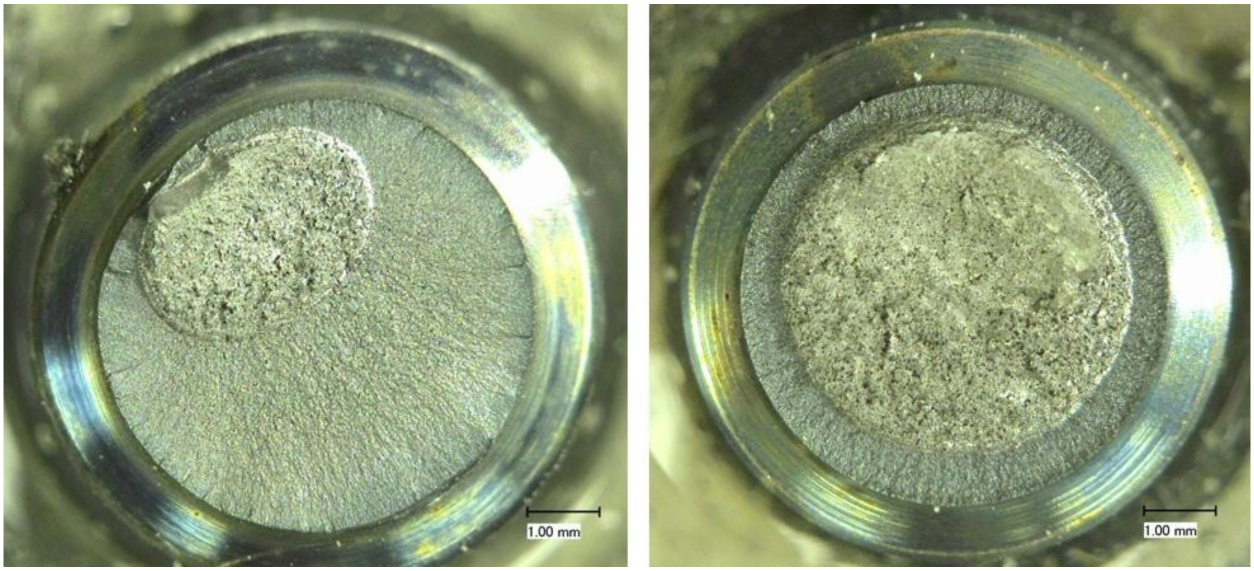

Figure 5.7: Comparison of 200°C/600°C (473°K/873°K) OPTMF (left) and IPTMF (right) sharply notched (K_t = 3.0) specimens cycled at $\Delta\varepsilon_{mech}$ = 1.0%

difference in appearance indicates, at least in notched cases, that crack propagation in OPTMF is dissipating more energy in the beginning, while IPTMF retains more elastic energy at failure. This observation reinforces data that indicates larger differences in initiation and failure cycle count in IPTMF than in OPTMF, with out-of-phase lifetimes being shorter in general.

5.3 Metallography

Use of an optical metallograph allowed for closer inspection of microstructures in sectioned specimens, with the plane of interest lying tangent to the longitudinal and transverse axes. All metallography sections were removed from the gage section of the specimens, and subjected to the same mounting, polishing, and etching procedure. Micrographs from this method were at much higher optical zoom levels and revealed fine detail. Oxide intrusion measurements from this data set were used as the foundation for the oxidation damage model.

Imaging of the general microstructure of the untested material shows austenitic grains between 50μm and 100μm in width. Larger grains show less preference, but many small grains are oriented lengthwise in the longitudinal direction. With the specimens being sourced from 304SS rod stock, this orientation corresponds to the extrusion direction. In addition to the austenite grains, some thin carbide layers are observable at grain boundaries, as well as manufacturing defects that also are aligned with the longitudinal axis. Small voids and inclusions are evident throughout the structure, but in very low quantities. When compared against specimens that have been tested under different conditions, it is found that the general grain structure remains essentially the same, with very little effects discernible between the micrographs from differing load conditions. Shown in Figures 5.8 and 5.9, this serves to indicate that the conditions are not causing significantly different microstructural changes to the interior

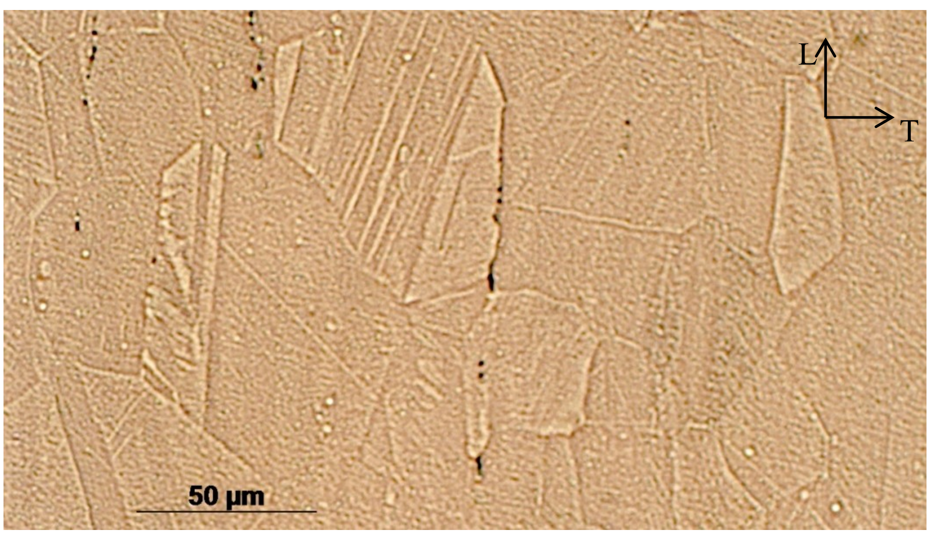

Figure 5.8: Representative microstructure of an untested 304SS specimen.

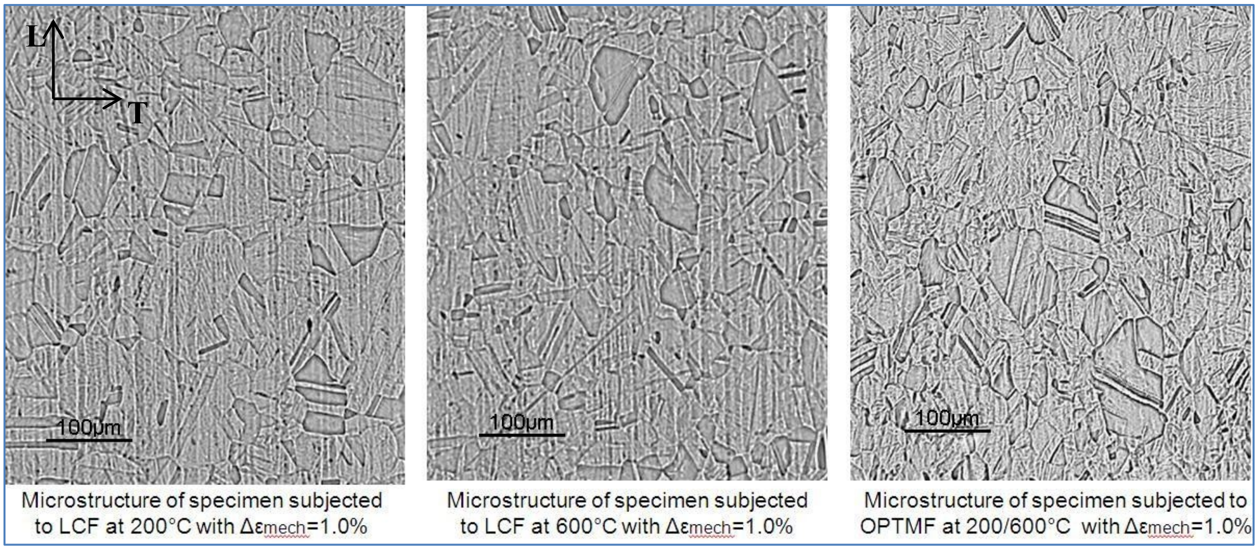

Figure 5.9: Comparison of microstructures from the gage section of smooth specimens subjected to 200°C (473°K) LCF (left), 600°C (873°K) LCF (center), and 200°C/600°C (473°K/873°K) OPTMF (right) with $\Delta\varepsilon_{mech}$ = 1.0%.

of the specimen. While higher temperatures lead to some additional carbide growth, the mechanical action of the cycling seems to impart nearly the same damage to the microstructure. It can be inferred that the pure fatigue effects are nearly identical on a strain range basis, as the conditions do not appear to work or age the microstructure in ways that are readily apparent through microscopic observation.

Several processing- and manufacturing-induced flaws are common in commercial 304SS, and instances of such flaws are noted in the material used for testing. Metallurgical quality assurance methods effectively keep the presence of defects to a minimum. In the specimens inspected after testing, no imperfections in the material makeup appeared to contribute to any significant life reduction or extension mechanisms. The most prevalent undesirable features in the microstructure are carbide inclusions and microvoids. The elongated carbides create hard, brittle regions that exist between austenite grains and are preferentially oriented in the longitudinal direction. These carbides are 20-30μm long on average, and can be 5μm wide in some cases. Voids in the material are smaller in size, with the largest

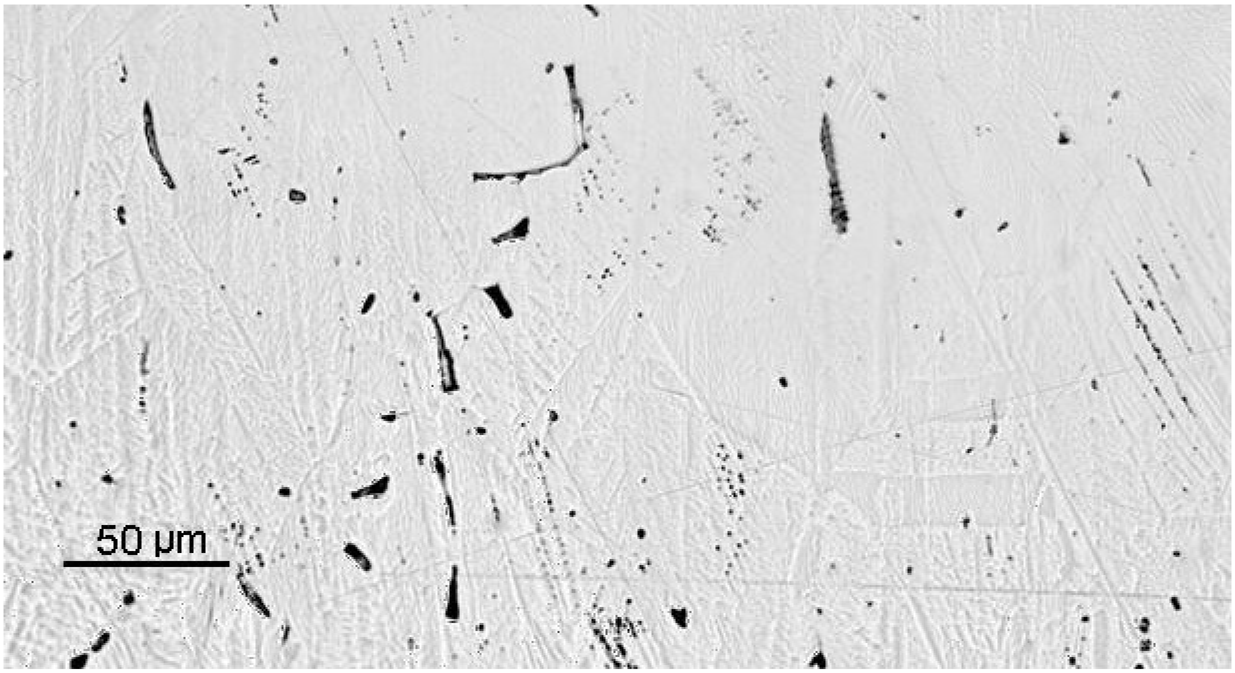

Figure 5.10: A worst-case example of carbide inclusions and microvoids in the grain structure (contrast enhanced).

having a diameter of ~1μm. Voids are found in clusters as well as in lines that follow grain boundaries and dendritic tendrils in the structure. Figure 5.10 contains examples of both types of feature. Less common features are notable in localized areas. Figure 5.11 shows an instance of un-alloyed grains of silicon. Figure 5.12 highlights a nick in the notch of a specimen that occurred during transport and handling. The underlying grain structure has been deformed, but the primary crack initiation site remains sufficiently remote from the defect.

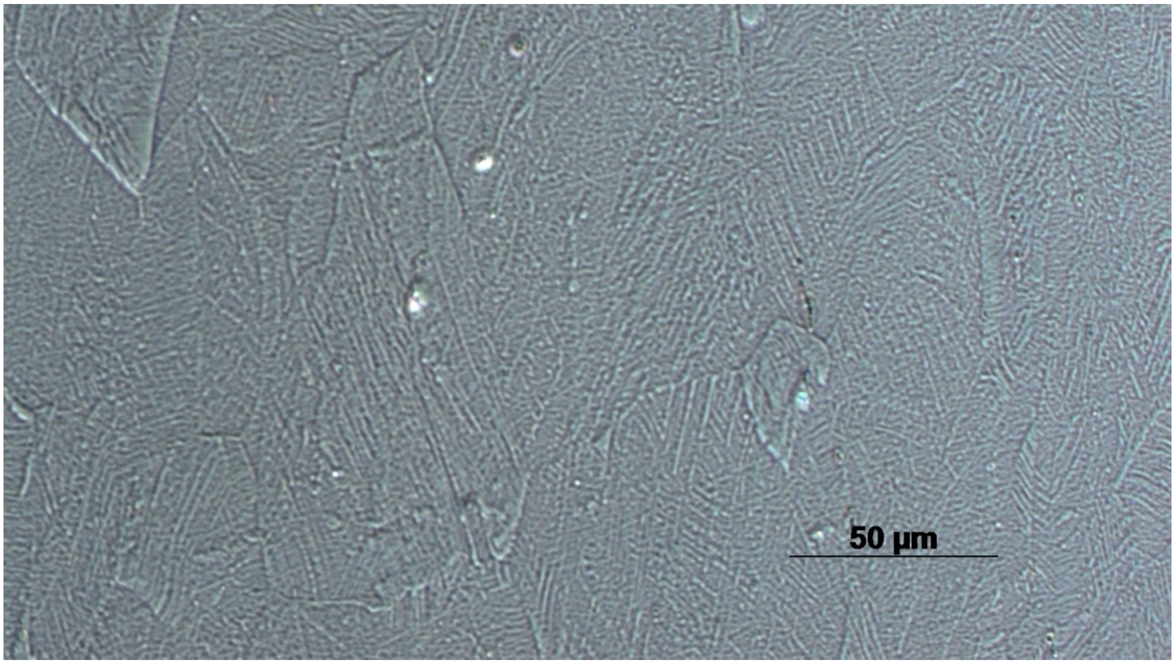

Figure 5.11: Several silicon spherules are found in a specimen subjected to 200°C/600°C (473°K/873°K) IPTMF with $\Delta\varepsilon_{mech}$ = 0.7%.

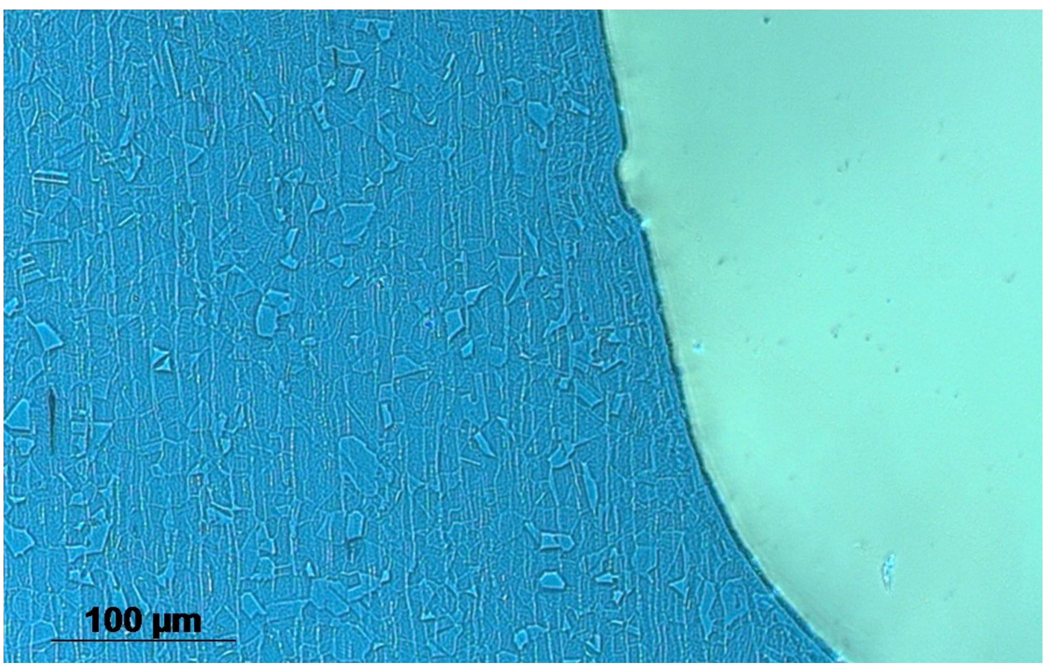

Figure 5.12: Handling damage to a specimen with a blunt notch (K_t = 1.73) resulted in a nick that deforms the grains below the surface.

A number of defects become apparent as specimens are exposed to higher temperatures for longer durations. In the case of 600°C (873°K) LCF specimens, some carbide precipitation is evident in tests where the strain range is slow. Shown in Figure 5.13, these local regions of carbon chromium mixtures eventually coalesce into thicker grain outlines like those of the OPTMF specimen viewable in Figure 5.14, which signals the onset of sensitization of the steel. Another effect noticeable under long durations is the opening of small voids between some grains. Viewable in Figure 5.15, some TMF specimens that incorporated hold periods revealed such voids, and the onset of creep can be implied from their presence.

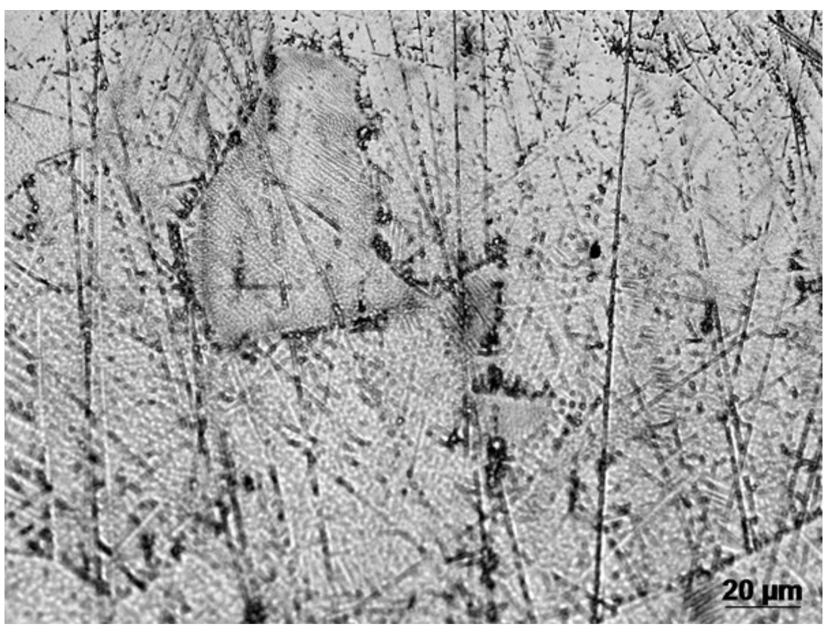

Figure 5.13: Carbide precipitation begins in a 600°C (873°K) LCF specimen subjected to a strain range of $\Delta\varepsilon_{mech}$ = 0.7%.

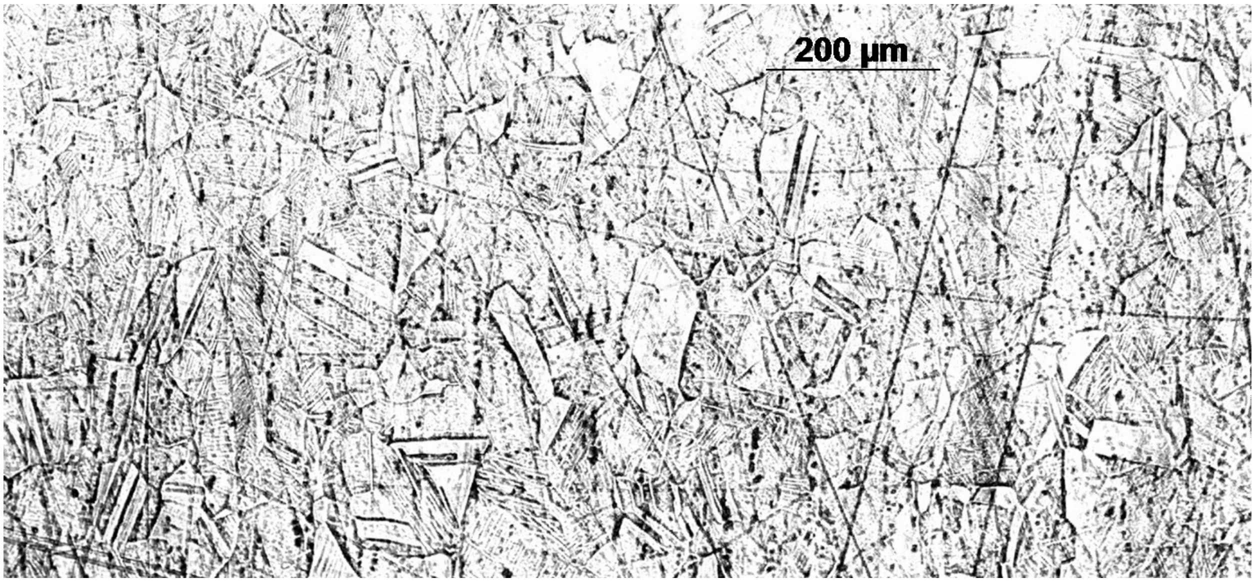

Figure 5.14: The onset of sensitization is visible in a specimen subjected to 200°C/600°C (473°K/873°K) OPTMF with $\Delta\varepsilon_{mech}$ = 0.7%.

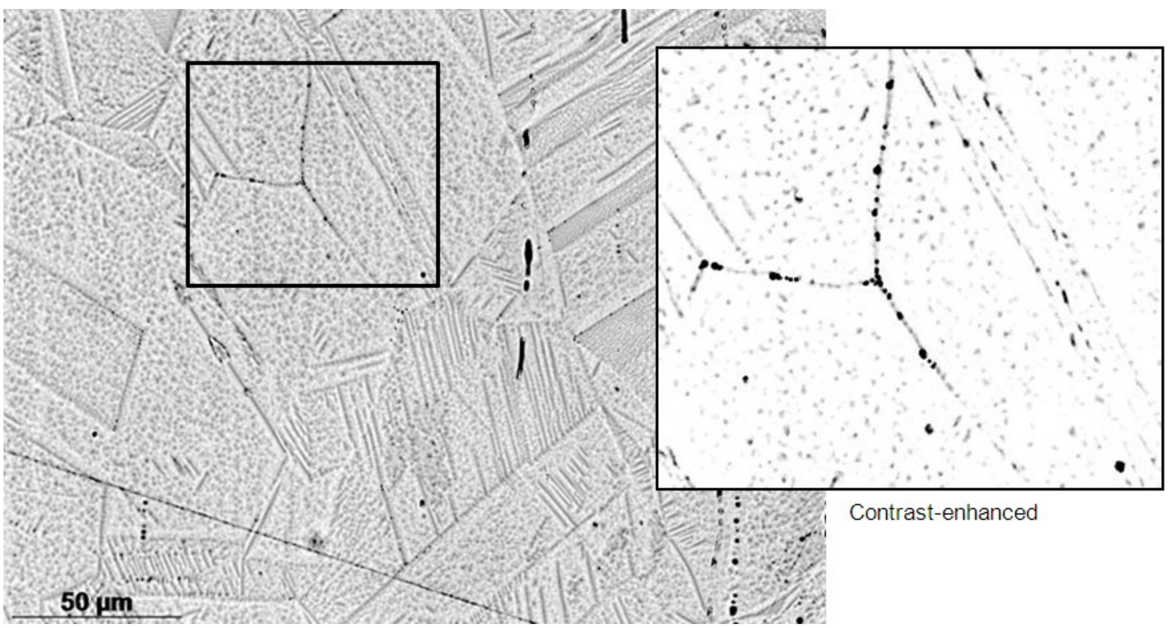

Figure 5.15: The onset of creep cavitation is visible in a specimen subjected to 200°C/600°C (473°K/873°K) IPTMF at Δεmech = 1.0% with a 60s tensile dwell.

The most conspicuous features in all of the metallographic examinations occurred on the surface of the specimen sections. Oxide layers, secondary cracks, and oxide intrusion within these cracks provided large, measurable features that were clearly representative of damage. At low temperatures, LCF specimens revealed long, tortuous cracks with secondary branches. These transgranular cracks, like the example in Figure 5.16, required branching to release the additional strain energy encountered through cycling specimens while retaining a higher elastic modulus. At higher temperatures, the cracks remain transgranular, indicating large release of strain energy, but little or no effect of creep. Thick oxide layers are present at higher temperatures, and oxide intrusion occurs as the oxidation assists the cracks. Both LCF and TMF cycle types exhibit small cracks in high numbers within the gage section, which is common in conditions where oxidation plays a key role. In the case of IPTMF and LCF, heavy layers on the exterior of the specimen are readily identifiable, and are comprised of iron(II) and iron(III) oxides that slowly intrude into the substrate as the iron and chromium compete to diffuse outward.

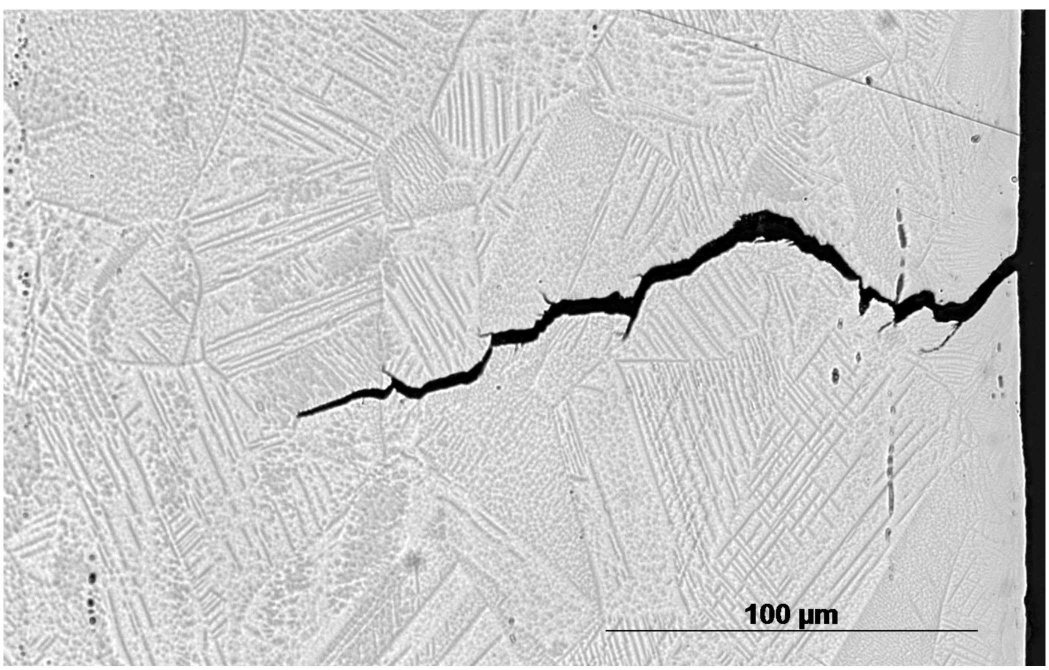

Figure 5.16: A transgranular fatigue crack in a specimen subjected to LCF conditions at 200°C (473°K) with $\Delta\varepsilon_{mech}$ = 1.0%.

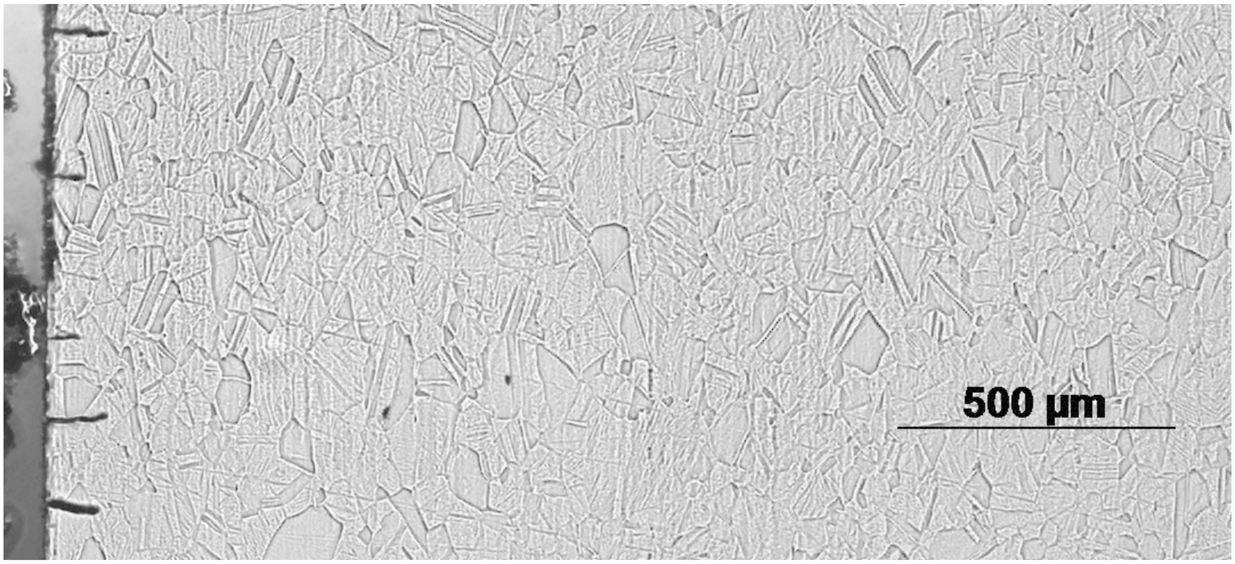

Figure 5.17: Multiple oxide-assisted cracks are visible on a specimen subjected to 600°C (873°K) LCF with $\Delta\varepsilon_{mech} = 0.7\%$.

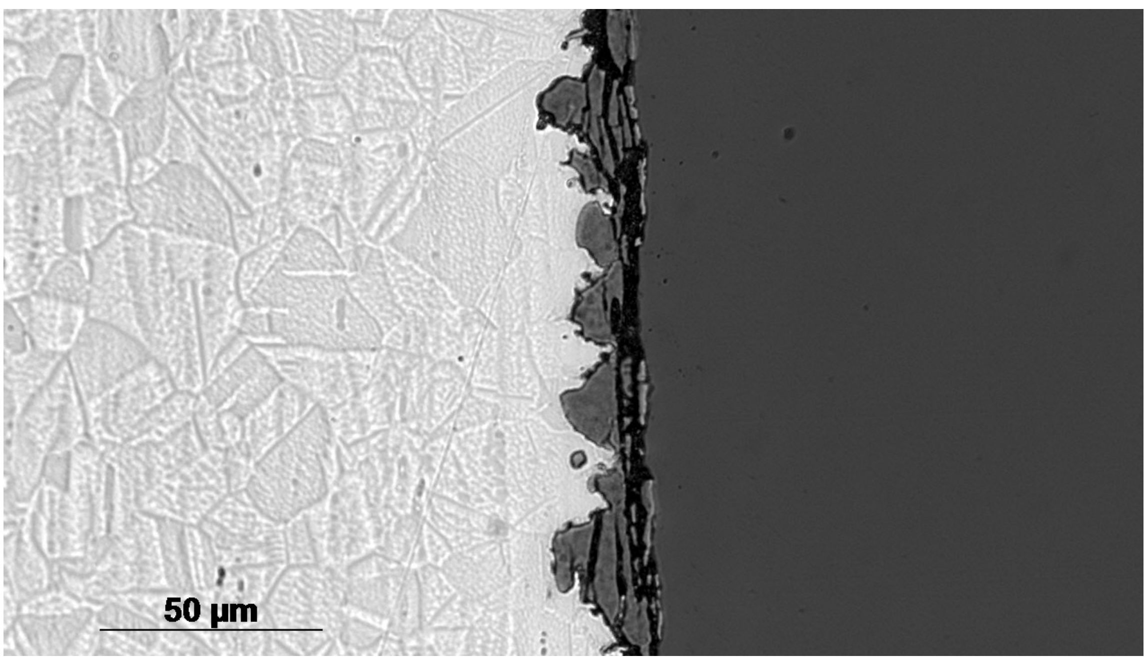

Figure 5.18: Multiple oxide types grow on the exterior of a specimen subjected to 600°C (873°K) LCF with $\Delta\varepsilon_{mech} = 1.0\%$ and a 60s tensile dwell.

Growth of the outer oxide layer is exacerbated by the presence of a hold. Deeper penetration of the oxide into the material in IPTMF and LCF cases occurs through intrusion via Type I cracks. In OPTMF cases, oxide layers are more likely to buckle and spall, with the material removal allowing Type II cracks as the worst case. Figures 5.19 and 5.20 detail cracks in IPTMF and OPTMF situations, respectively. Due to the combination of oxide depth and penetration level of oxide-laden cracks appearing to be a good combined indicator of oxide damage level, measurements of the worst-case oxide depth were recorded from secondary cracking in the gage sections of all specimens inspected via metallograph. Geometric effects did not impact the worst-case secondary crack depths, though it is indicated that primary cracks in notched specimens carried a propensity to initiate with less observable secondary crack intrusion present. The results are available in Table 6-1 for all crack and layer types.

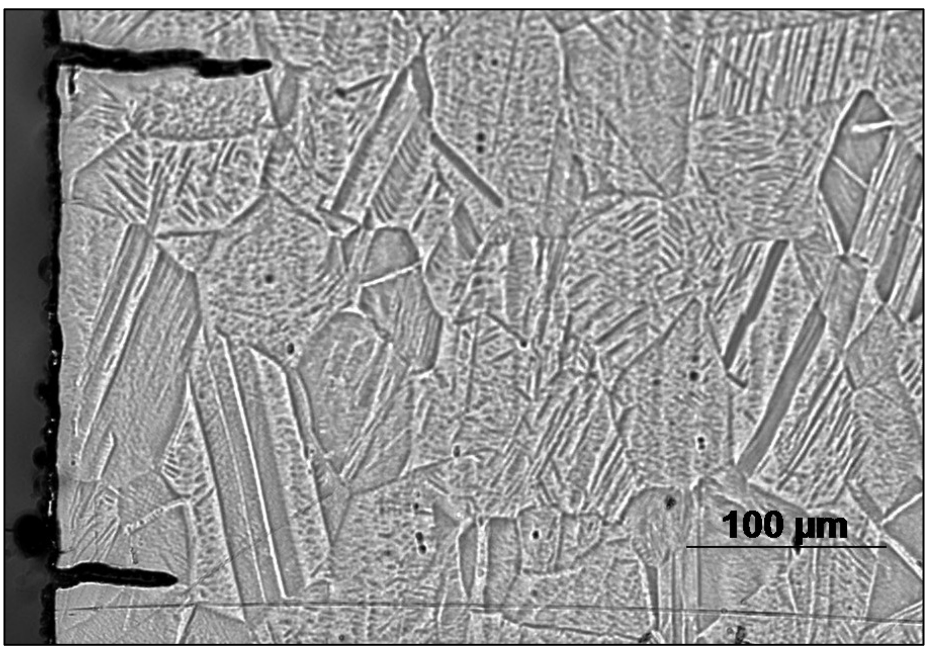

Figure 5.19: Type I cracks in a 200°C/600°C (473°K/873°K) IPTMF specimen cycled with $\Delta\varepsilon_{mech}$ = 0.7%.

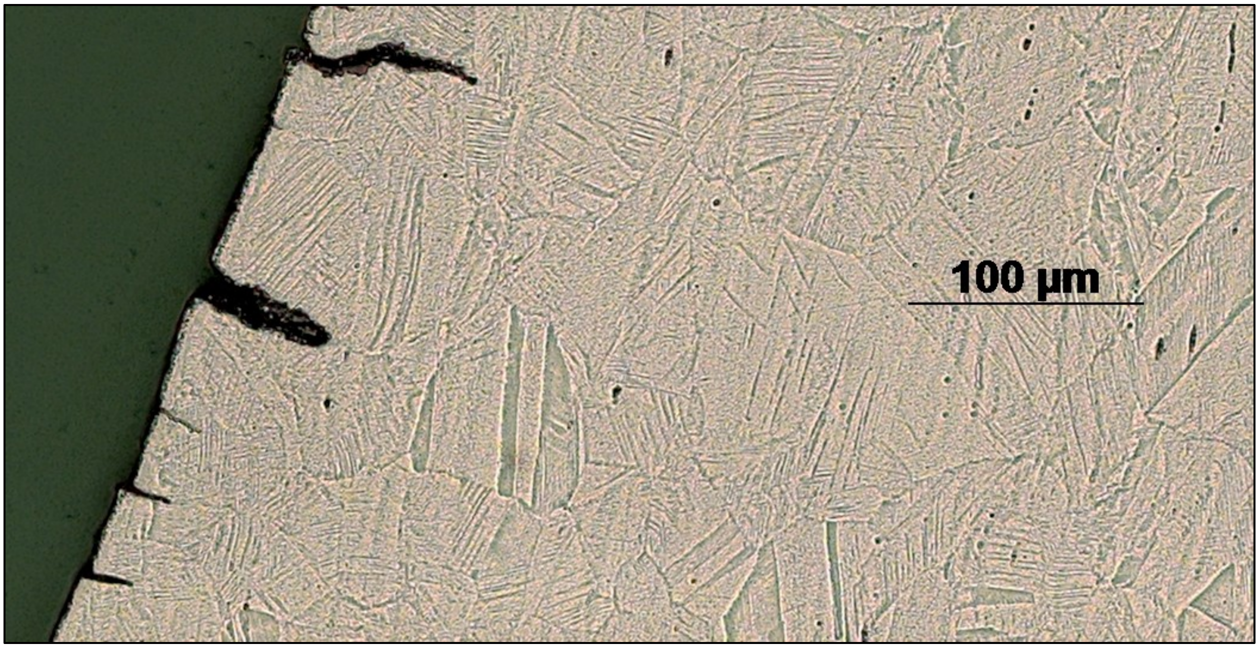

Figure 5.20: An open Type II crack is present amongst several Type I cracks in the blunt notch of a 200°C/600°C (473°K/873°K) OPTMF specimen cycled at $\Delta\varepsilon_{mech}$ = 1.0% with K_t = 1.73.

Table 5-1: Observed oxide intrusion depths with test temperature and dwell duration

Specimen #	Cycle Type	Tensile Dwell (sec)	Average Cycle Temperature (°K)	Type	Maximum Observed Oxide Intrusion (μm)
1	LCF	60	473	Type I	37
2	LCF	0	873	Type I	136
3	IPTMF	0	673	Type I	115
4	LCF	0	473	Surface	17
5	LCF	0	873	Type I	63
6	LCF	60	873	Type I	118
7	IPTMF	0	673	Type I	113
8	OPTMF	0	673	Type II	118
9	IPTMF	60	713	Type I	133
10	LCF	60	473	Type I	35
11	LCF	0	473	Surface	17
12	LCF	0	873	Type I	60
13	LCF	0	473	Surface	18
14	LCF	0	873	Type I	63
15	IPTMF	60	713	Type I	141
16	IPTMF	0	673	Type I	104
17	OPTMF	0	673	Type II	121
18	OPTMF	0	673	Type II	120
19	LCF	60	873	Type I	129
20	IPTMF	60	713	Type I	122
21	LCF	0	473	Surface	14
22	LCF	0	873	Type I	52
23	LCF	0	473	Surface	14
24	LCF	0	873	Type I	48
25	IPTMF	0	673	Type I	108

5.4 Scanning Electron Microscopy

Application of a scanning electron microscope (SEM) is a method which couples a significant depth field with better contrast than visible light microscopes, enabling resolution of the finest details on specimen surfaces. Inspection of specimen exteriors and fracture patterns was performed in order to determine which mechanisms were prevalent in the course of failure of the material. An additional benefit of the system utilized in this study is that it included EDS (Electron Dispersive Spectroscopy) hardware, consisting of a small X-ray tube and detector which quantifies emitted electron potentials when materials are bombarded with the X-ray beam. Electron spectra are unique for every atomic structure, and thus enable identification of the elements that target features are comprised of.

The most important implication of the SEM images involves what can be inferred from the qualitative appearance of fatigue damage. When high magnification comparisons of the slow fracture regions of the specimens are made, it is apparent from the shape and width of the beachmarks that dissimilar loadings advance the crack at the same rate. Ostensibly the damage is primarily and strongly dependent on mechanical strain range alone. Except at the initiation point of a primary crack, geometric effects are inconsequential. Similarly, neither tensile hold nor temperature or cycle type appears to impact the general shape of the crack fronts. Figure 5.21 below compares a 600°C (873°K) LCF case at $\Delta\varepsilon = 1.0\%$ with and without the presence of a tensile dwell period. Figure 5.22 similarly compares an LCF specimen tested at 200°C (473°K) with an OPTMF specimen, at a mechanical strain range of 0.7%. Features other than beachmarks are present in all specimens, with areas of local shear, ductile overload, intergranular voids, and cleavage identifiable, with specimens at 200°C (473°K) LCF being most likely to exhibit these secondary mechanisms. Specimens that encounter elevated temperatures do not favor specific mechanisms based on cycle type, but both IPTMF and 600°C (873°K) LCF cases were less likely to exhibit shearing and cleavage when a tensile dwell was included in the cycle. These incidental mechanisms, however prevalent in the fracture images, did not impact the general fatigue damage and subsequent propagation of the crack. As crack front form and width vary most strongly with differing strain ranges, it is logical to assume that an existing strain-life relation serves as a good foundation for the fatigue damage term, reserving the secondary consequences to be built in via slightly conservative fitting of the relation.

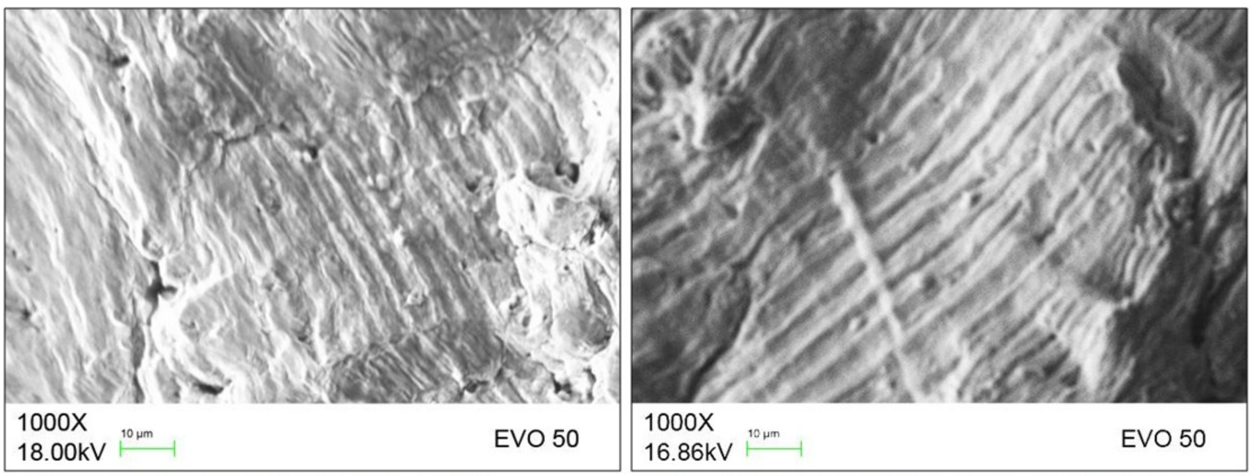

LCF specimen tested at 600°C with $\Delta\varepsilon_{mech}$=1.0%

LCF specimen tested at 600°C with $\Delta\varepsilon_{mech}$=1.0% incorporating 60s tensile hold

Figure 5.21: Comparison of 600°C (873°K) LCF specimens at $\Delta\varepsilon_{mech}$ = 1.0% without holds (left) and with 60s tensile holds (right).

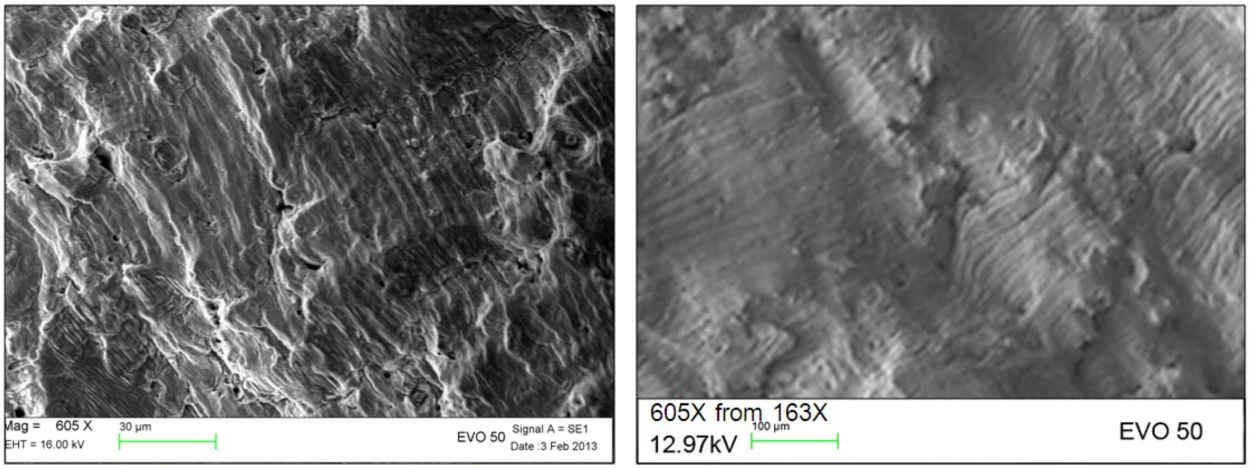

OPTMF specimen tested with $\Delta\varepsilon_{mech}$=1.0%   LCF specimen tested at 200°C with $\Delta\varepsilon_{mech}$=1.0%

Figure 5.22: An OPTMF specimen (left) tested with a strain range of $\Delta\varepsilon_{mech}$ = 1.0% is compared with a 200°C (473°K) LCF specimen (right) cycled at an identical strain range.

In addition to observations collected to support a simplistic train-life fatigue damage formulation, information regarding the extent of oxide intrusion can be confirmed from EDS examination of the region where slow fracture meets tensile fracture. In LCF cases, little to no oxygen was found during spectroscopy of the fracture type interface when 200°C specimens were analyzed. When maximum temperatures are increased to 600°C (873°K), LCF and TMF cases alike show evidence of oxide intrusion as far forward as the crack front itself. This result chemically confirms some of the implied results from metallographic analysis, and offers correlation between the oxide penetration in secondary cracks versus primary cracks. Figures 5.23 through 5.25 show images of the crack front interface target areas and the corresponding EDS spectra. Tensile fracture surfaces show a fast fracture, identifiable by heavy cavitation and sudden intergranular failure.

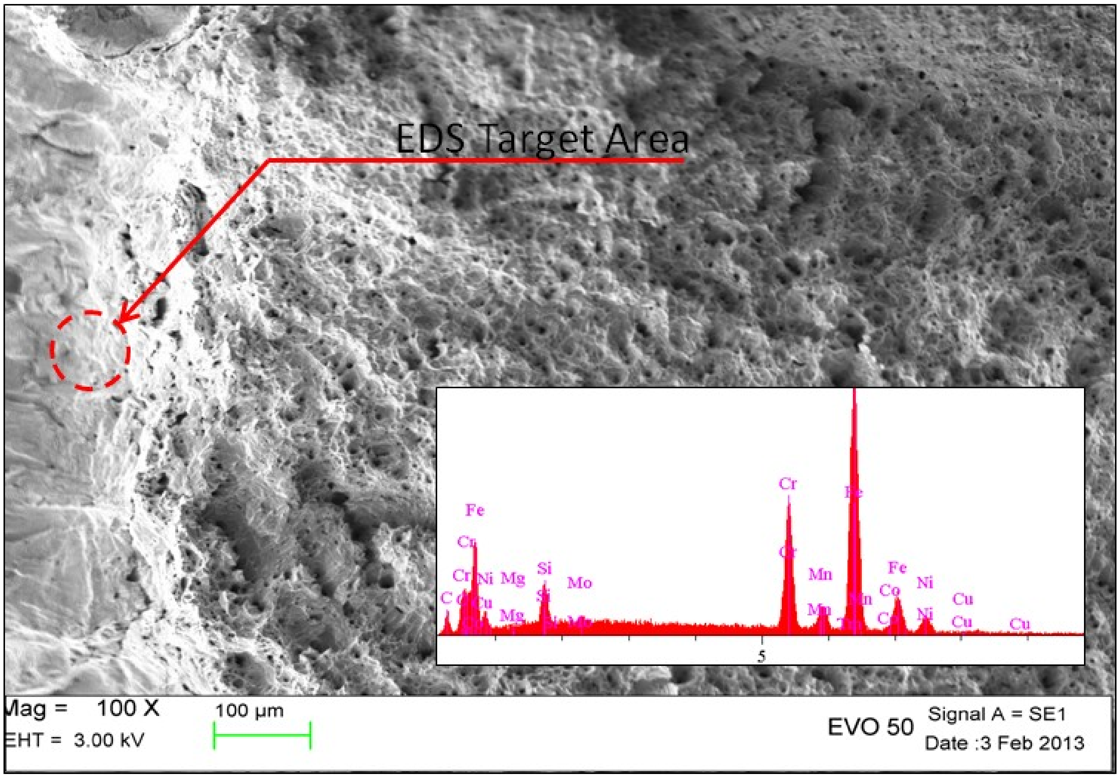

Figure 5.23: EDS spectra (inset) from crack interface of an LCF specimen cycled at 200°C (473°K) with $\Delta\varepsilon_{mech}$ = 0.7%.

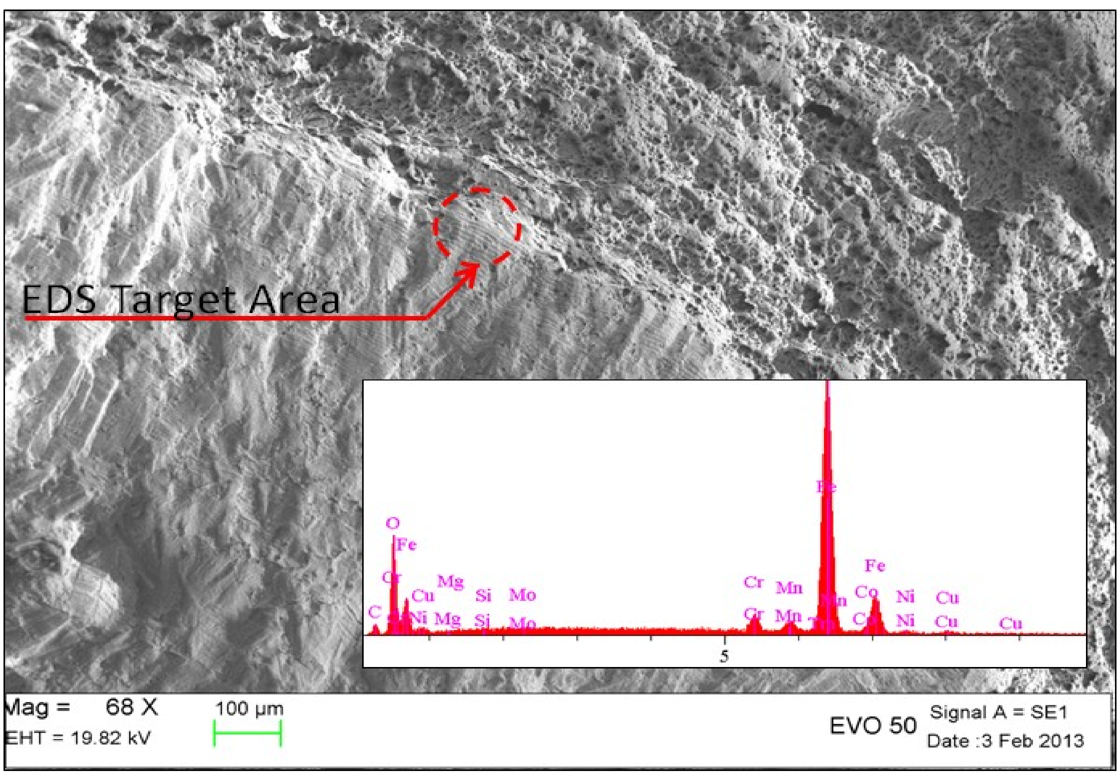

Figure 5.24: EDS spectra (inset) from crack interface of an LCF specimen cycled at 600°C (873°K) with $\Delta\varepsilon_{mech}$ = 1.0%.

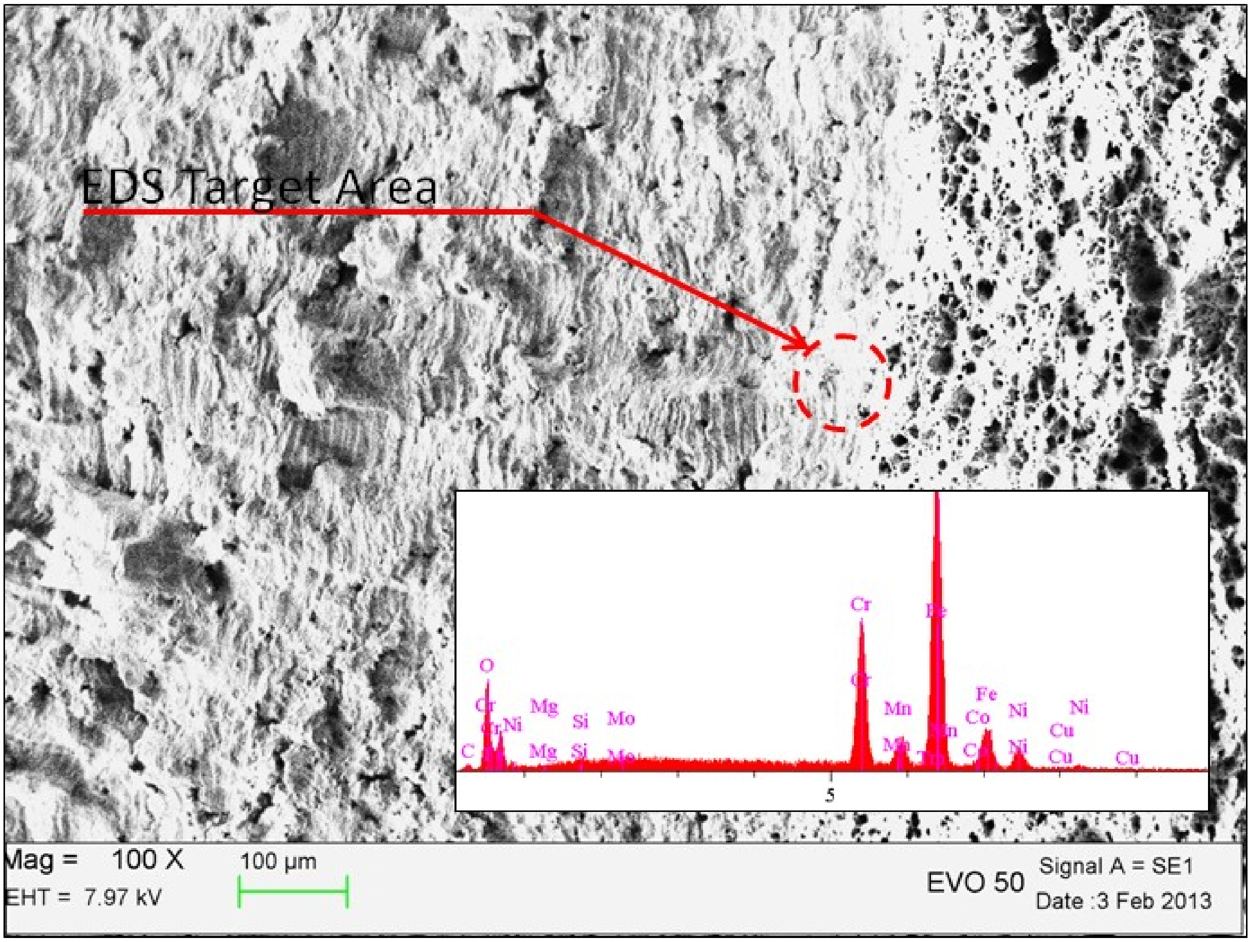

Figure 5.25: EDS spectra (inset) from crack interface of an OPTMF specimen cycled with $\Delta\varepsilon_{mech} = 1.0\%$.

In addition to oxide intrusion, EDS spectra can be obtained to identify certain features in the microstructure which appear significantly different than the surrounding material. Inclusions of silicon particles and chromium carbides were suspected based on metallographic analysis, so anomalous structures were targeted with EDS to verify these assumptions. Large (>150μm) bright spherules visible on the fracture surface of 200°C (473°K) LCF specimens were confirmed via their spectra to be silicon inclusions from the alloying process. The spherules were ruled out as contamination, as they were embedded in the structure itself. These features did not impact the fracture properties of the specimen, despite being microscopic discontinuities themselves. Figure 5.26 details the target particle and analysis results.

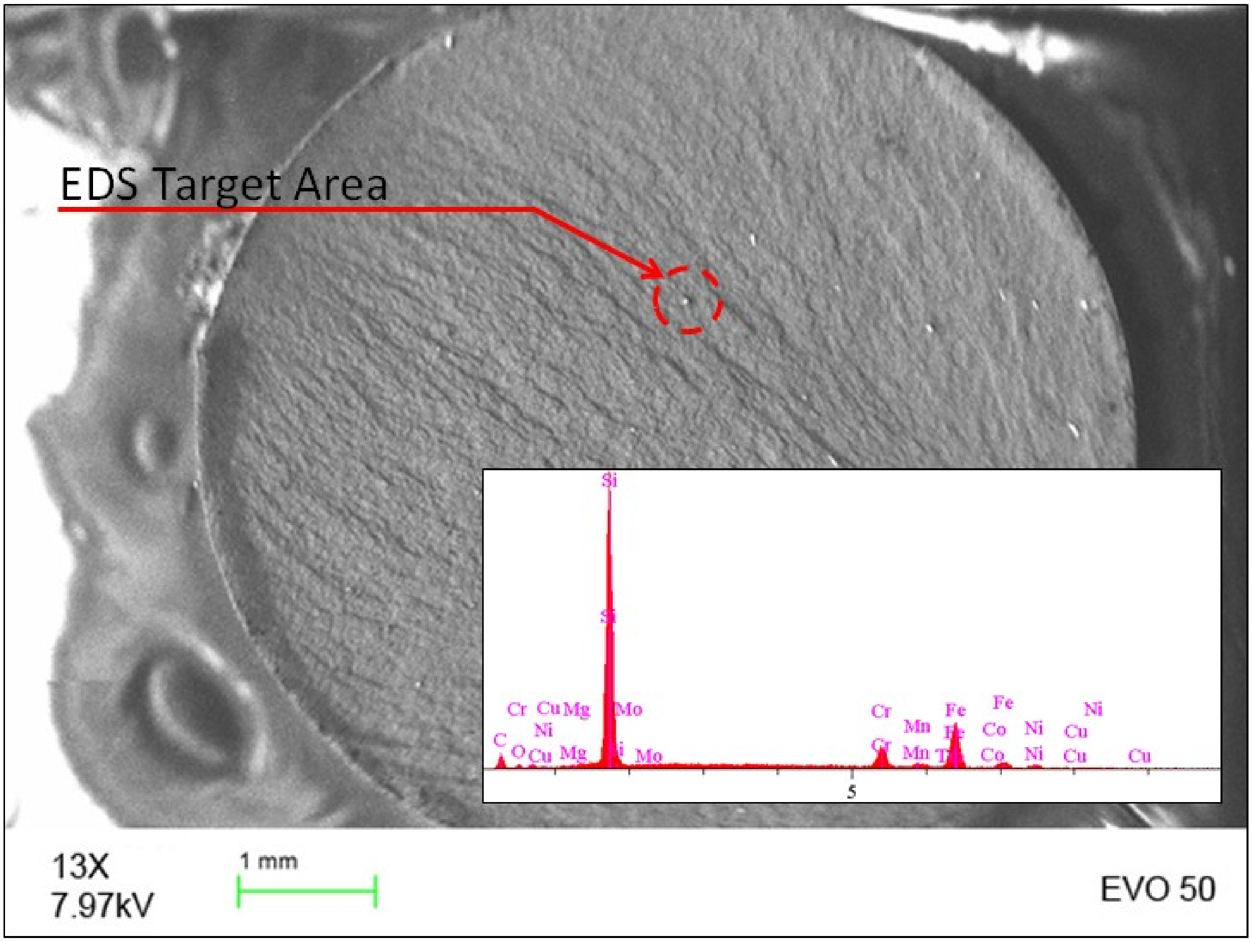

Figure 5.26: EDS spectrum of a silicon inclusion in a smooth 200°C (473°K) LCF specimen cycled at $\Delta\varepsilon_{mech}$ = 1.4%.

In 600°C (873°K) LCF and TMF cases, chromium carbides appear as smaller (<10μm), more angular crystalline features that protrude from between the austenite grains on the fracture surface. Also brightly reflective in SEM images, they are easily identified and EDS spectra verify carbon and chromium present in quantities greater than any other elements. Figure 5.27 details the targeting and identification of chromium carbide features.

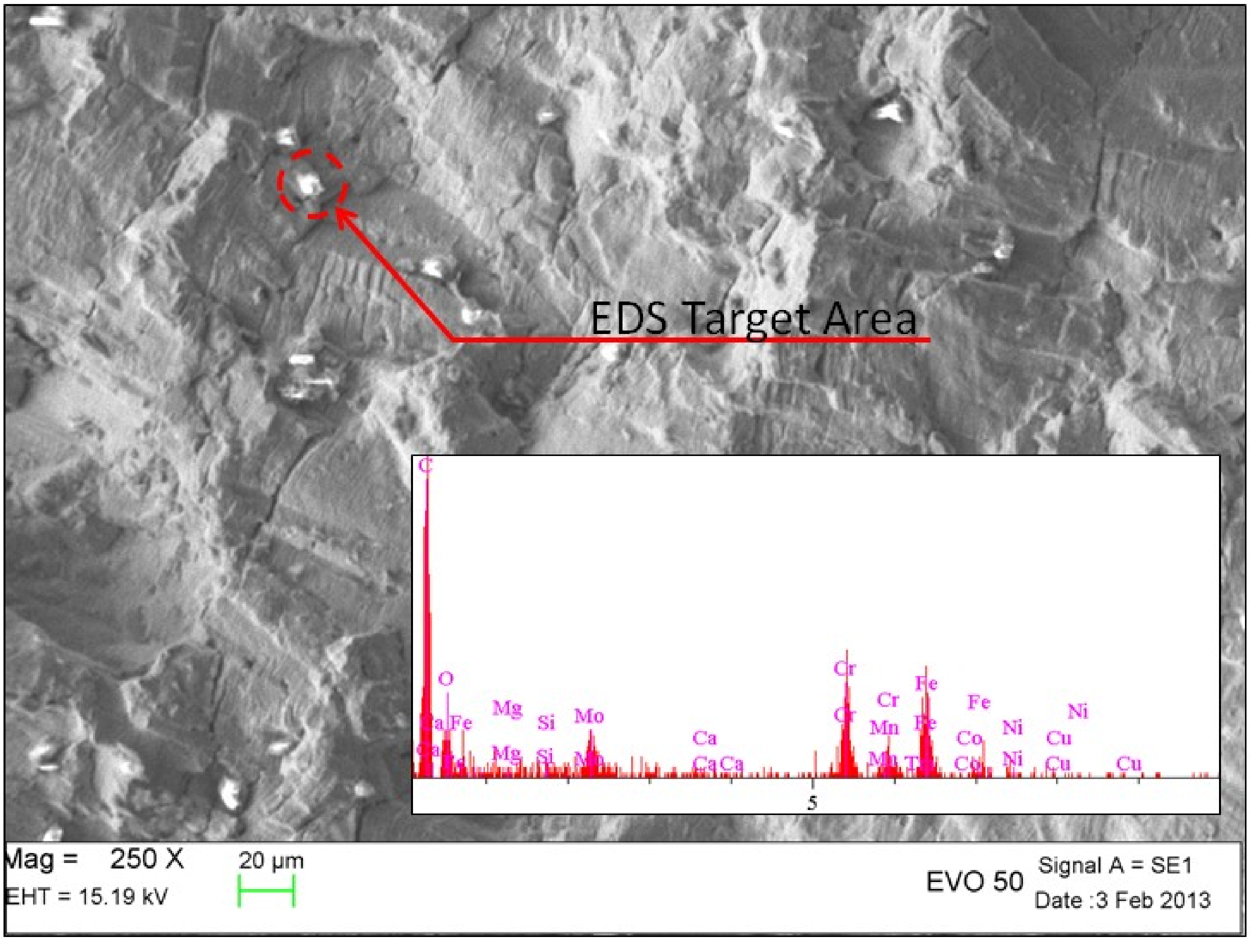

Figure 5.27: Chromium carbide verified by EDS spectra in a 600°C (873°K) LCF specimen with $\Delta\varepsilon_{mech}$ = 1.0%.

CHAPTER 6

PHYSICAL MODEL

A life prediction approach was constructed in order to relate measurable behaviors and observable effects with the number of cycles until crack initiation. This approach, which takes the form of a constitutive model, is tasked with offering a life prediction within a factor of two in both LCF and TMF cases, with and without geometric discontinuities.

6.1 Model Development

The fundamental construct of the life prediction model is that of damage summation, wherein damage quantities are derived from sub-approaches that best describe the type of damage present. The effects of individual types of damage mechanics are quantified and then assembled together to provide a measure of the overall reduction effect on the specimen caused by specific load conditions. In the case of LCF and TMF conditions, the primary types of damage are pure fatigue, oxidation, and creep. The constituent components for this model's summation relation are thusly based on life reduction effects modeled by a strain-life fatigue approach, an oxide growth and penetration formulation, and an energy-based creep law.

6.1.1 Fatigue Damage Formulation

Specimen damage which is incurred due to the effects of fatigue is ubiquitously present in low cycle fatigue, creep-fatigue, corrosion fatigue, and thermomechanical fatigue (Linde and Henderson, 1998). As such, pure fatigue damage can serve as a baseline to which the effects of oxidation- and creep- driven mechanisms can be added (Halford, et al., 1993). Supported by the idealized nature of the experimental conditions used in the study, the selected method of quantifying life reduction due to fatigue is developed with Basquin's extension to the Manson-Coffin relation as the central component. Justification of this selection is rooted in the nature of the experiments, which are strain-controlled, and with a strain ratio value of R_{ε} = -1, are absent of any mean stress effects. The Basquin-augmented Manson-Coffin approach is a strain-life formulation which equates total strain range $\Delta\varepsilon$ to life N_f as

$$\frac{\Delta\varepsilon}{2} = \frac{\sigma_f'}{E}\left(2N_f\right)^b + \varepsilon_f'\left(2N_f\right)^c \tag{6.1}$$

where b and c denote the fatigue strength and fatigue ductility exponents, respectively. The terms σ'_f and ε'_f represent the fatigue strength and fatigue ductility exponents. For the purpose of this investigation, TMF cycles have been assumed comparable to LCF when considering the mechanical strain range $\Delta\varepsilon_{mech}$ substituted for the total strain range $\Delta\varepsilon$, and that the desired cycles to initiation N_i correspond with the cycles to failure N_f of the original relation (Kleinpass, et Al., 2000). Thus, the form utilized for this study

$$\Delta\varepsilon_{mech} = 2\left[\frac{\sigma'_f}{E}\left(2N_i^{fat}\right)^b + \left(2N_i^{fat}\right)^c\right] \tag{6.2}$$

consists only of substitution of like terms and rearrangement. When Equations 6.1 and 6.2 are evaluated, they require the fatigue strength and fatigue ductility parameters for the specific application. The parameters for this case were developed based on a set of room temperature data (Roessle and Fatemi, 2000) given for 304 stainless steel which has been regressed to be consistent with the parameters that more closely modeled the behavior at the minimum study temperature of T_{min} = 473°K. Fatigue behavior modeling at the lowest applied temperatures reflects the intent to model a conservative pure fatigue baseline without reducing theoretical damage below the scope of the study. Resultant parameters are available in Table 6-1.

Table 6-1: Parameters for Manson-Coffin-Basquin strain-life relation for 200°C (473°K) 304SS

Parameter	Description	Value	Units
E	Elastic modulus at T = 473°K	168	GPa
σ'_f	Fatigue strength coefficient	1400	MPa
ε'_f	Fatigue ductility coefficient	0.105	mm/mm
b	Fatigue strength exponent	-0.13	---
c	Fatigue ductility exponent	-0.41	---

When plotting the response of the Manson-Coffin-Basquin relation, it presents as a power-law curve which can itself be re-fit to capture the life prediction values in terms of the applied mechanical strain range only. This effectively removes the necessity of any iterative mathematics that would be required if the model were left in the original form of Equation 6.2, and decreases the computational workload for subsequent fatigue damage predictions based on strain. Thus, the finalized fatigue damage term is simply an inverse of the number of expected cycles to initiation as re-fit in the power law form

$$D_{fat} = \frac{1}{N_i^{fat}} = \frac{1}{C_1(\Delta\varepsilon_{mech})^{b_1}} \tag{6.3}$$

in which dimensionless constants C_1 and b_1 have values of 4236.5 and -3.068, respectively, for the particular blend of 304SS utilized in the model development.

Though not intended as a stand-alone predictive model, the relation of Equation 6.3 can be applied to its initial purpose in order to verify the general form and the correctness of fatigue predictive capabilities. Utilizing the relation to estimate the lives of smooth isothermal fatigue cases provides a benchmark for accuracy of the model term. When used exclusively for this purpose against the lifetimes in the experimental plan, the plotted result shows a few specimens

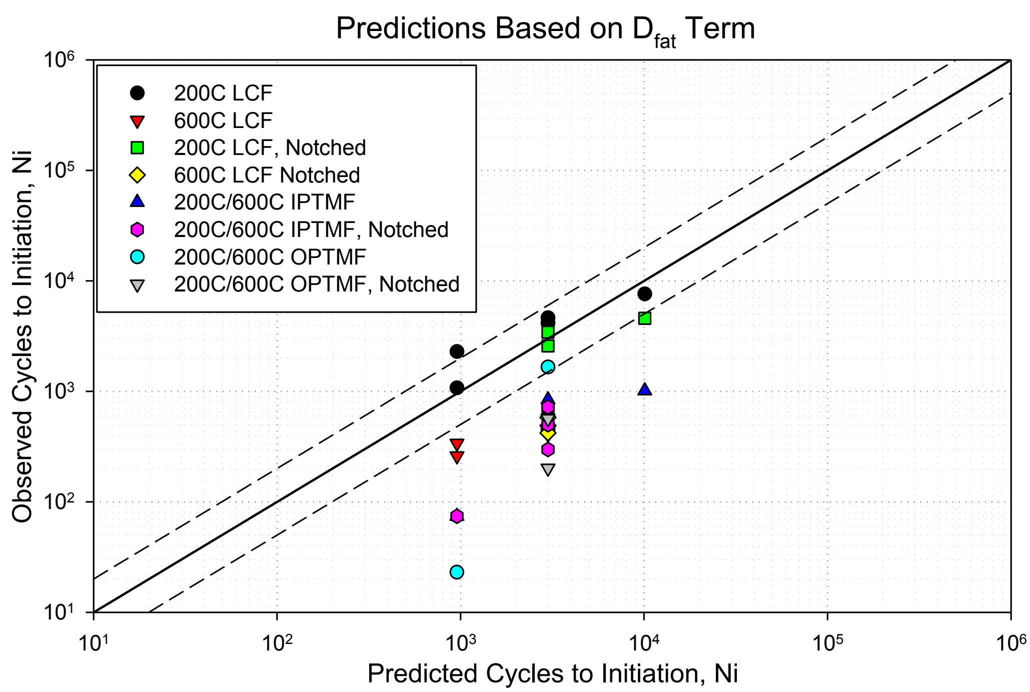

Figure 6.1: Predictions of lifetimes for study samples in the study utilizing the fatigue damage term only.

which fall inside the bounds of the +/-50% accuracy goal. These particular tests are low in temperature, with all but one being isothermal. Tests which fall outside the goal have the observable trend of becoming less accurate as temperature and severity of geometry increase. Though the 600°C smooth LCF tests fall within an order of magnitude, the best-case error is 65%, with the worst-case being 86%. This is an expected result, as the estimate would be based only on the 200°C universal strain-life equation for smooth specimens. If comparing the predicted lifetimes of historical data encountered in literature, the same general trends exist, though the model accuracy appears better except in the highest temperature and non-isothermal cases. Smooth LCF specimens tested at temperatures between 300°C and 538°C correlate well, though at very low strain ranges of 6.0%, error is a maximum 87%. Considering the previous

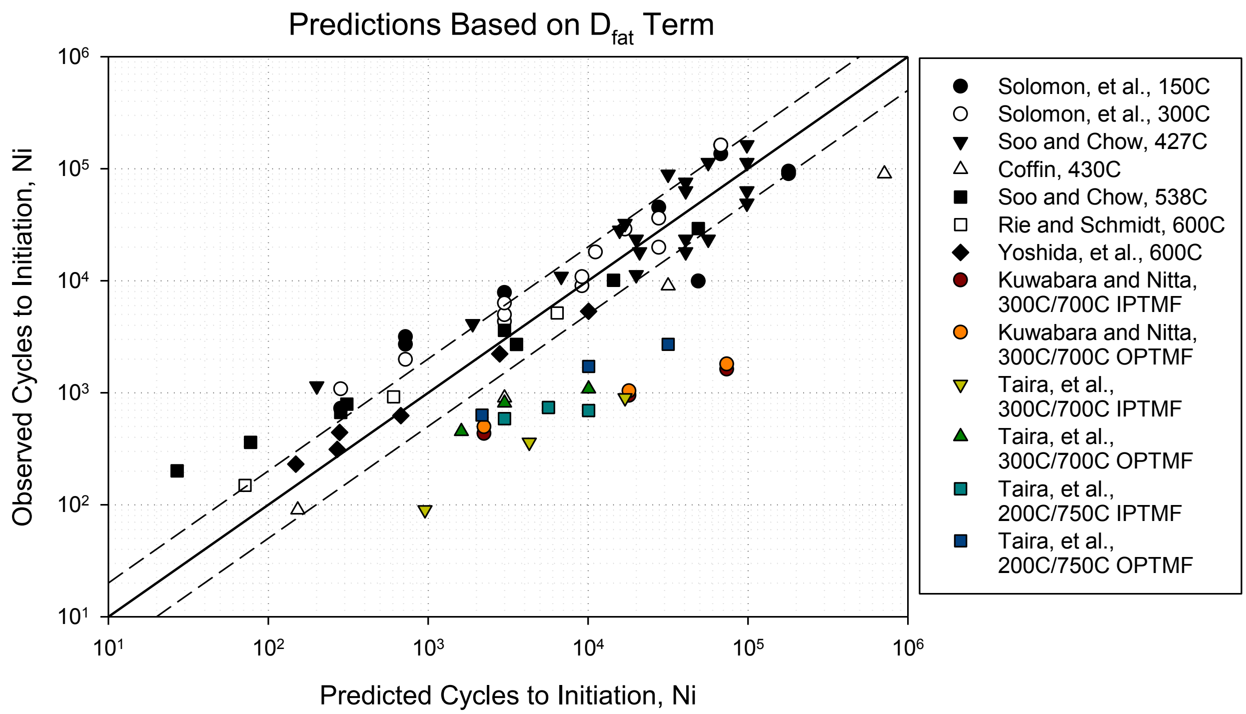

Figure 6.2: Life predictions based on the fatigue damage term for smooth specimen LCF and TMF data available in literature.

assumption that the primary life correlation for pure fatigue is based on strain range alone, the model is suitable for the purposes of predicting simple cases within temperatures between 150 C and 600°C (873°K), especially if acknowledging that the study's blend of 304SS is weaker in fatigue than that of the average.

6.1.2 Oxidation Damage Formulation

The basis for the modeling of oxidation-related mechanical damage is driven by the strong correlation evident when analyzing material durability with respect to oxide growth and penetration. In cases of TMF, environmental effects have been cited as the most damaging contributor at elevated temperatures (Antolovich, et Al., 2011) and thusly used as a primary component in some lifing models. This study characterizes environmental damage as a function of the maximum observed oxide depth, including surface and Type II crack front oxides. Corrections for cycle phasing and specimen geometry are introduced to reflect the propensity of intergranular oxide-assisted cracks to propogate, which do so more readily under favorable stress conditions (Wise, Grauss, and Matlock, 2000).

The elementary form of the oxide model is presented as a parabolic growth formulation, which calculates expected oxide depth h_0 based on exposure duration t and parabolic constant K_p. The parabolic constant is fit based on the material and exposure conditions. The parabolic oxide growth law is generally given as

$$h_0 = \sqrt{K_p t} \tag{6.4}$$

but is more readily integrated with the study's imposed conditions when made relative to cycle time t_{cyc}. This particular modification is done so with the assumption that the cycle time and total time of exposure are in direct correlation. In cases of the slow cycling rates of LCF and TMF testing, the correlation is satisfactory. The updated form of the law is therefore presented as

$$h = \sqrt{K_p^{eff} t_{cyc}} \tag{6.5}$$

with h denoting oxide depth from outer surface to the deepest oxide-penetrated fissure, and effective parabolic constant K_p^{eff} in place of the original constant. Replacement of the constant provides flexibility in allowing stress and non-isothermal temperature conditions to be incorporated into the new formulation. The effective parabolic constant is thus calculated via the modified Arrhenius equation

$$K_p^{eff} = e^{\left[\left(\frac{\beta_1}{\sigma_{max}}\right)+\left(\beta_2 \frac{1}{t_{cyc}} \int_0^{t_{cyc}} T(t)dt\right)\right]} e^{\left(\frac{-Q}{R \frac{1}{t_{cyc}} \int_0^{t_{cyc}} T(t)dt}\right)} \tag{6.6}$$

wherein average temperature per cycle is considered, and σ_{max} denotes the maximum stress value of the cyclic response after stabilization. Terms β_1 and β_2 serve as regression constants whose fit promotes goodness of inverse correlation between oxide depth h and observed life N_i in the resultant growth law. The constants and fit parameters necessary for calculation of the effective parabolic constant are given below in Table 6-2.

Table 6-2: Constants required for determination of the effective parabolic constant

Parameter	Description	Value	Units
Q	Oxygen diffusion activation energy	226.0	kJ/mol
R	Boltzmann's constant for energy and diffusion	8.31446	J/mol-K
β_1	Stress regression constant	-105.58	---
β_2	Temperature regression constant	0.00654	---

While the modification of the parabolic constant allows for good correlation between life reduction and oxide depth, the use of this correlation as a predictive relation is further enhanced by the addition of two weighting parameters which reflect the susceptibility of a specimen to degradation via oxide intrusion based on cycle type and geometry. The first weighting parameter is Φ_{ox}, which accounts for differing effects in TMF and LCF at high and low temperatures, as well as the presence of a dwell period. This parameter is determined via mapping of a Gaussian curve, as influenced by the approach of Neu and Sehitoglu in 1989, but is repeated for separate T_{max} values and hold conditions. Three Gaussian fits are produced, reflecting high temperature conditions with and without holds, as well as the lower temperature condition which responded .without and hold time dependence. The equation of the phasing constant is thus

$$\Phi_{ox} = [S]\frac{1}{s\sqrt{2\pi}}e^{-\frac{(\varphi-\mu)^2}{2s^2}} \quad (6.7)$$

where μ, *[S]*, and s parameters are optimized for each condition, whose values are available in Table 6-3. The resulting curves are depicted in Figure 6.3.

Table 6-3: Gaussian fit parameters for cycle type and temperature condition

Maximum Temperature	Dwell Period	Magnitude, [S]	Deviation, s	Phase shift, μ
873K	Yes	3.0	1.35	0
873K	No	3.75	1.5	-1
473K	---	0.1	1.5	-1

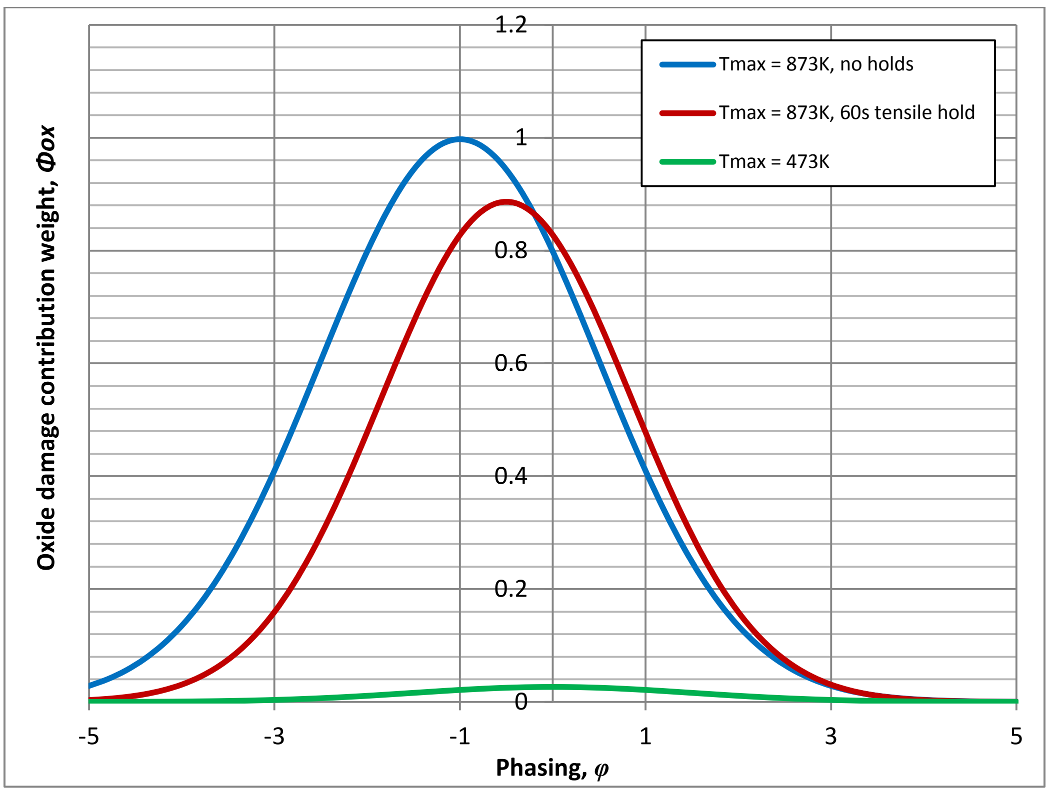

Figure 6.3: Oxide damage phasing susceptibility curves.

When conditions from the empirical study are considered via this method, damage weight values from Φ_{ox} = 1.0 to Φ_{ox} = 0.01 arise. The calculated susceptibility weights for test parameters imposed during this study are available in Table 6-4.

Table 6-4: Resultant oxide damage susceptibility per cycle type and temperature condition

Cycle Type	Maximum Temperature	Hold Time	Φ_{ox}
IPTMF	873K	---	0.41
IPTMF	873K	60s	0.53
OPTMF	873K	---	1.0
LCF	873K	---	0.80
LCF	873K	60s	0.83
LCF	473K	---	0.01

The geometric parameter Z_{ox} is constructed primarily on the basis of observations collected during microscopy, wherein oxide intrusion in the case of notched specimens did not adequately correlate with life reduction without the presence of a scaling factor. Comparison of observed intrusion depth h weighted by applied plastic strain range $\Delta\varepsilon_{pl}$ and average elastic modulus E slightly improved model fitting. Bluntly notched (K_t = 1.73) specimens appeared to be five times more likely to initiate a primary crack than smooth specimens of comparable observed oxide intrusion depths, while sharply notched specimens (K_t = 3.0) appeared 9 to 10 times more likely to initiate a primary crack than comparably-damaged smooth specimens. Noting this relation, a cubic dependency on stress concentration factor K_t was deemed appropriate to describe the behavior. The resulting formulation

$$Z_{ox} = K_t{}^3\left(\Delta\varepsilon'_{pl}\right)\frac{1}{t_{cyc}}\int_0^{t_{cyc}} E(T(t))dt \qquad (6.8)$$

thus is a multiplicative combination of geometric (K_t), initial plastic strain $\Delta\varepsilon'_{pl}$, and average stiffness $E(T)$ values which more readily correlate the observed oxide depths versus the propensity to resist initiating a primary crack.

When the oxide penetration model is fitted with the appropriate parabolic constant and the weighting coefficients determined, a final comparative formula between the oxidation effects and expected life is assembled. The projected life expectancy if oxide damage was a single dominant mechanism is noted in Equation 6.9 as:

$$N_i^{ox} = Z_{ox}\Phi_{ox}h \tag{6.9}$$

When Equation 6.9 is visualized, the $Z_{ox}\Phi_{ox}h$ versus life relation strongly follows a power law curve, which is apparent as a trendline in Figure 6.4.

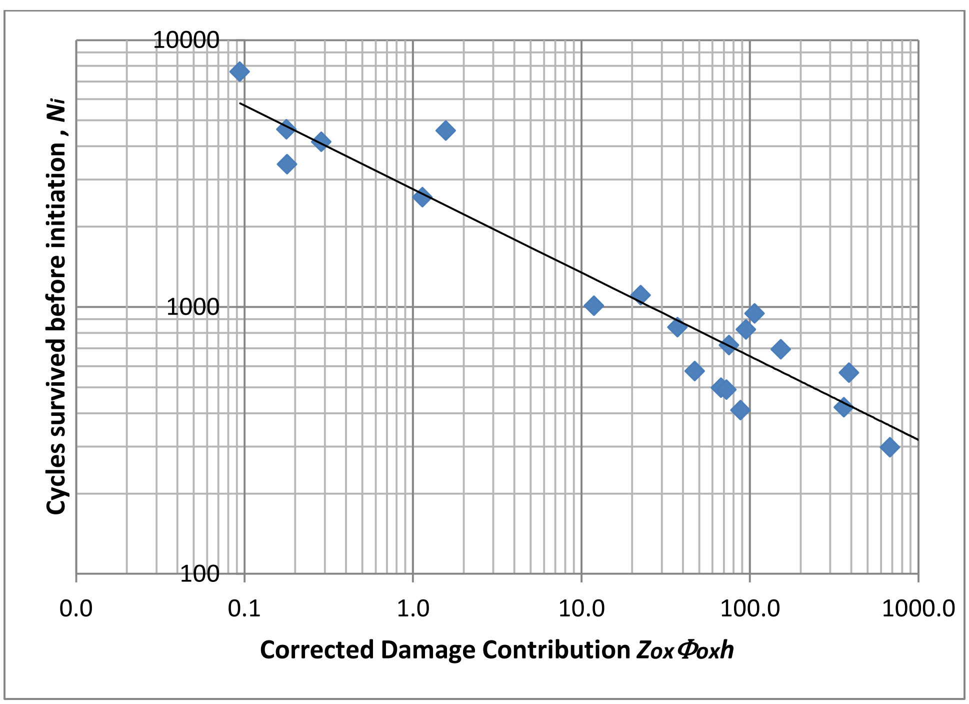

Figure 6.4: Oxide damage survivability versus oxide damage contribution term

The trendline is subsequently utilized to quickly regress the power law parameters. Although no immediate accuracy is gained or lost in this simplification, the overall scatter in the empirical data is decreased in the global constitutive relation. In this case, fitting constants C_2 and b_2 are tuned to values of 36.532 and -0.313, respectively. Therefore, the final oxidation damage term can be expressed as the inverse of the life expectancy N_i^{ox}:

$$D_{ox} = \frac{1}{N_i^{ox}} = \frac{1}{C_2(Z_{ox}\Phi_{ox}h)^{b_2}} \tag{6.10}$$

Similar to the approach in the previous section with fatigue alone, enough data is readily available to adequately assess the performance of the oxidation damage term. Plots of the results are pictured in Figure 6.5 below, with blunt and sharp notches grouped together, and dwell and non-dwell cycles grouped together with their phasing type. Predictions of life based on the D_{ox} term reinforce the assertion of good general correlation, as 21 of 31 sampled specimens result

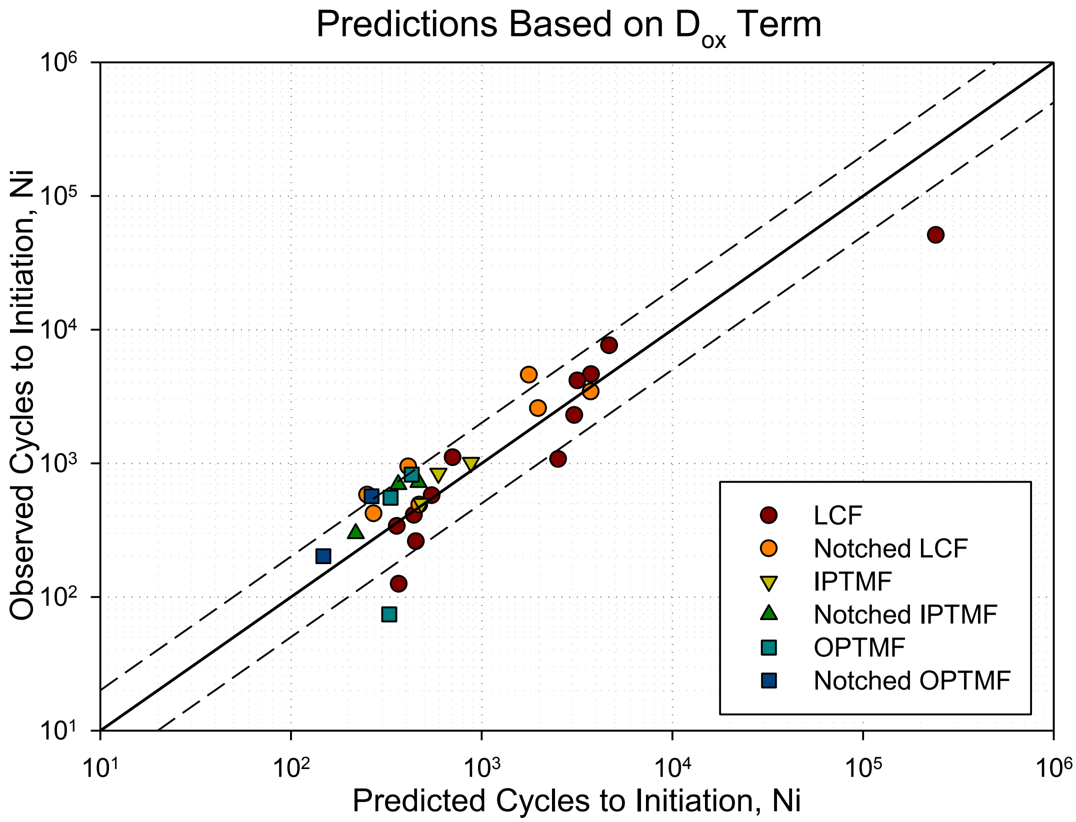

Figure 6.5: Predictions of specimen lifetimes in the experimental study based on the oxide damage term.

in erros within the 50% performance goal, and an additional 4 specimens within a 65% error band. If applying the formulation to historical data, isothermal cases for temperatures within the

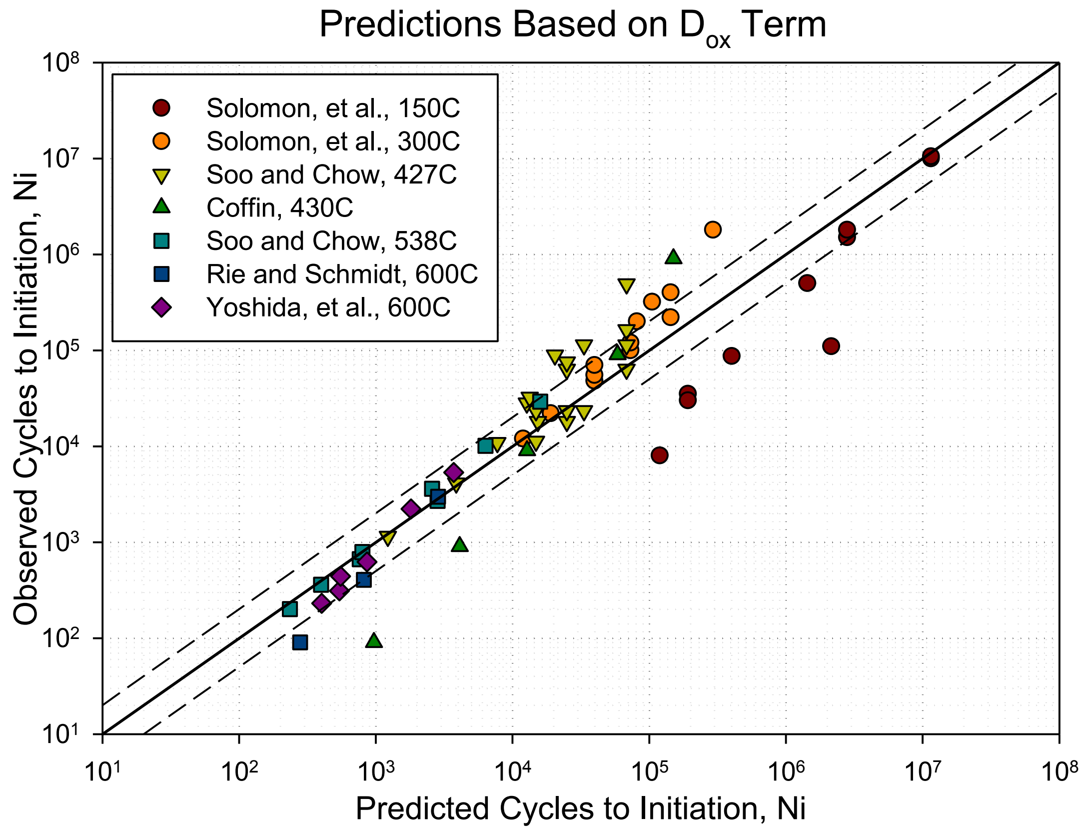

Figure 6.6: Llifetime predictions of historical isothermal fatigue data based on the oxide damage term.

bounds of the study fit within an order of magnitude of the observed. Although this is not as accurate as the predictions based on study data, a clearly identifiable trend is shown on Figure 6.6, with a band following a straight line from non-conservative to conservative as cycle counts increase. This feature identifies that the model's foundation is well-suited for the current study, as well as possibly extendable into high cycle fatigue cases. Correlation for non-isothermal data was not assessed, however, as measurements of cycle shape and associated initial plastic strain parameters were not available in historical data.

6.1.3 Creep Damage Formulation

The last damage term required in the life prediction model is that which accounts for reduction of life due to creep. While the tests conducted in the study did not impart high stress, high temperature conditions for extended periods of time, the onset of creep in the material was expected and observed in some of the loadings. Because microscopic evidence in the form of cavitation and dislocation pileups was minimal, a direct measurement-based method was omitted in favor of a parametric argument. Stress and temperature terms can be used in relatively simplistic approaches that quantify time and intensity of creep-favorable conditions during a TMF or LCF cycle. The Robinson technique in particular has been proven effective in TMF situations, and allows extension of the model to include conditions where significantly more creep damage occurs (Šeruga, Fajdiga, and Nagode, 2011). Thus, a modification of this method serves as the basis for the creep damage term.

The premise behind the Robinson formulation is that of quantifying the ratio of time spent at a certain temperature and stress condition versus the expected creep rupture time at the same condition. Although temperatures in stresses may be constantly changing, the summed effect of all states can be compared. This is evident in the original formulation (Robinson, 1938)

$$D = \sum_{i=0}^{n_i} \sum_{j=0}^{m_{ij}} \frac{\Delta t_{ij}\left(\sigma_{ij}, T_{ij}\right)}{t_{ij}^{r}\left(\sigma_{ij}, T_{ij}\right)} \tag{6.11}$$

where damage *D* depends on summed effects during time *t* versus summed effects necessary for rupture at time t^r. In order to avoid the necessity of complex integration or summing many discrete cases, some simplified terms comparable to the original quantities are substituted. The numerator Δt term is supplanted by the time per cycle spent in tension, denoted by t^{+}_{cyc}. The denominator terms are similarly exchanged to reflect the time-to-rupture for the average temperature and tensile stress experienced during the time spent in tension. This simplified ratio provides per-cycle creep damage D_{cr} as

$$D_{cr} = \frac{t^{+}_{cyc}}{t^{r}(\sigma^{+}_{avg}, T^{+}_{avg})} \tag{6.12}$$

where σ^{+}_{avg} and T^{+}_{avg} denotes the average stress and temperature, respectively, during the tensile portion of the cycle. Some geometry-based averaging techniques are given in Appendix E for fully-reversed cycling with triangular ramp segments. Note that using the average applied tensile stress does not account for stress concentrations, on the basis that for appropriately sized parts and specimens the local stresses will be total constrained, and that creep effects will be measured by the average effect in the cross-section (Hayhurst and Webster, 1987).

In order to apply the modified Robinson's method, the rupture time t^{r} for the cycle's average conditions must be determined antecedently. Because historical creep rupture data may not be available for conditions specific to the cycle, it is necessary to use an alternate method to provide the rupture time. One such method that has gained wide acceptance is the use of the Larson-Miller Parameter, LMP, which is a stress-based parameter that directly relates itself to a function of rupture time and temperature. Formulated as

$$LMP = T(C_{LMP} + \log(t^{r})) * 10^{-3} \tag{6.13}$$

the parameter utilizes a material-fit constant C_{LMP} in a logarithmic function of applied temperature T and time to rupture t^r, which are expressed in degrees Kelvin and hours, respectively. In the case of standard 304 SS, the value of C_{LMP} has been found to be 18.265 (Simmons and Van Echo, 1965) and this value is to be utilized in this formulation, as slight differences in 304SS blends so not significantly improve creep resistance. The Larson-Miller Parameter itself can be expressed as a power-law relation with respect to applied stress, with historical data over many temperatures and rupture times (Swindeman, 1975) used to formulate such a relation as

$$LMP = C_{SF}\sigma^{b_{SF}} \tag{6.14}$$

where C_{SF} = 43.31703 and b_{SF} = -0.17174 for standard Type 304 stainless steel. Consequently, Equation 6.13 and 6.14 can be unified to provide the stress-temperature-time relation

$$43.31703\left(\sigma_{avg}^{+}\right)^{-0.17174} = T_{avg}^{+}(18.265 + \log(t^r)) * 10^{-3} \tag{6.15}$$

in which applied stress and temperature terms are exchanged for average tensile stress σ^{+}_{avg} and average tensile temperature T^{+}_{avg}. The assessment of the creep damage term alone was not performed, as stress and temperature conditions against rupture stress and temperature conditions would always yield a result based on unity. The damage term effectiveness is thus reserved for measurement included in the combined damage model performance.

6.1.4 Combination of Damage Terms

The final form of the prediction model is an arrangement of the individual constituent fatigue, oxidation, and creep damage terms. Ultimately, the number of cycles until initiation will be estimated by a fixed relation with damage as the independent variable. Due to the non-unified nature of the methods utilized to determine each term, a final weighting function is developed for each damage type to correctly proportion the contributions before fitting. Weighting functions are chosen based on overall goodness of fit, as well as to provide a target level combined damage amount of 1.0 for the case of a failure during the first cycle. The best-case solution for the damage weight proportioning was expected to produce a finalized model which predicted well throughout the entire damage range, and meet the accuracy requirements of within a factor of 2 of the observed data. The fitting form which met the requirements set forth for the model is an uncomplicated Palmgren-Miner like linear accumulation scheme with damage type coefficients. This relation is given as

$$D_{tot} = W_{fat}D_{fat} + W_{ox}D_{ox} + W_{cr}D_{cr} \tag{6.16}$$

where weight coefficients W_{fat}, W_{ox}, and W_{cr} are assigned values 17.2, 12.6, and 6.2 respectively for this particular study. A plot of damage parameter D_{tot} versus observed N_i offers a preliminary measure of the correlation level in the model, with clustered trending as shown in Figure 6.7.

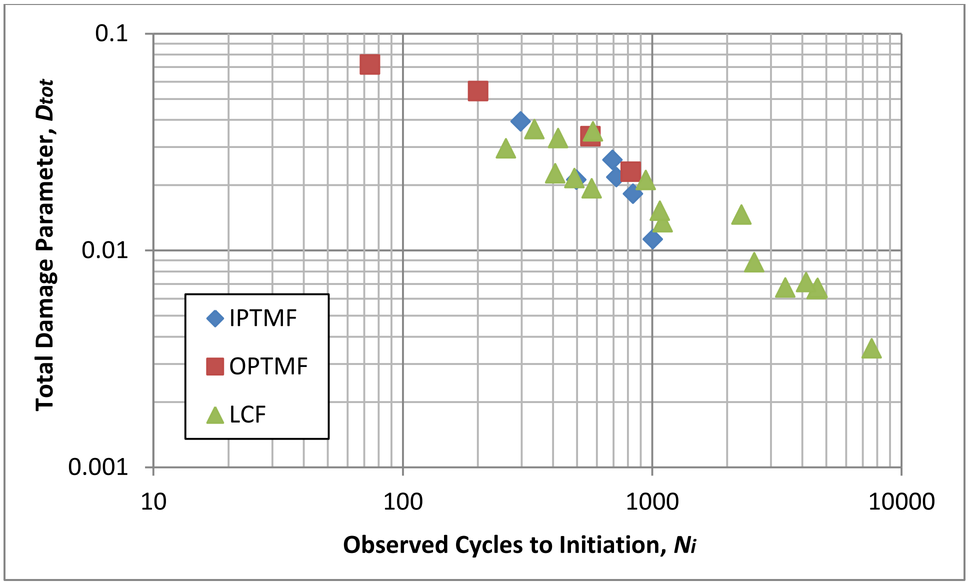

Figure 6.7: Plot of total damage versus observed cycles to initiation.

With clearly observable structure in the results, it was desirable to provide an additional fit to create a final relation between damage and predicted initiation cycle. Mathematical regression offered a power-law relation of the form

$$N_i^{pred} = k_1(D_{tot})^{k_2} \tag{6.17}$$

where values of k_1 = 1.6403 and k_2 = -1.566 provide a function which fits the data with a coefficient of determination of R^2 = 0.9557. Plots of the resulting N_i^{pred} values of this function

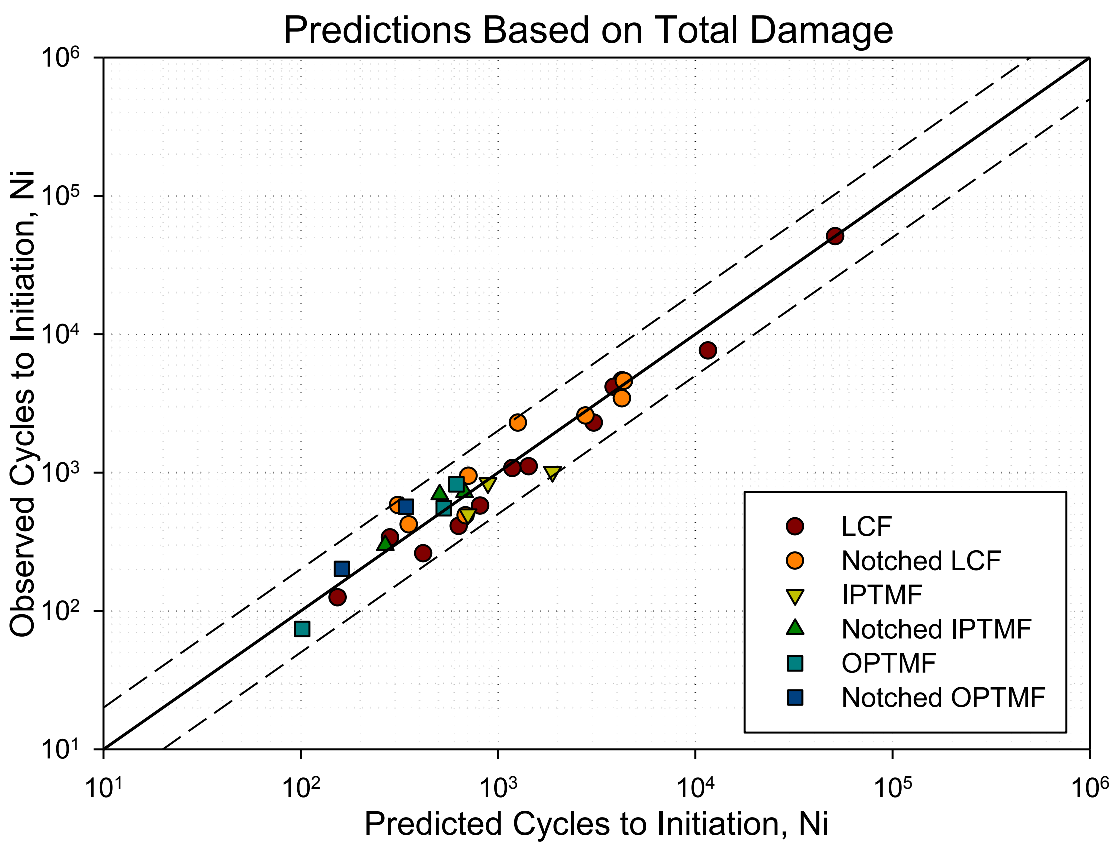

Figure 6.8: Plot of observed cycles to initiation versus model-predicted cycles to initiation.

versus observed N_i values demonstrate the strength of the model, which accurately predicts crack initiation within a factor of 2 for TMF and LCF cases regardless of geometry, temperature, dwell periods, and strain ranges. When considering the precision of the model against historical data,

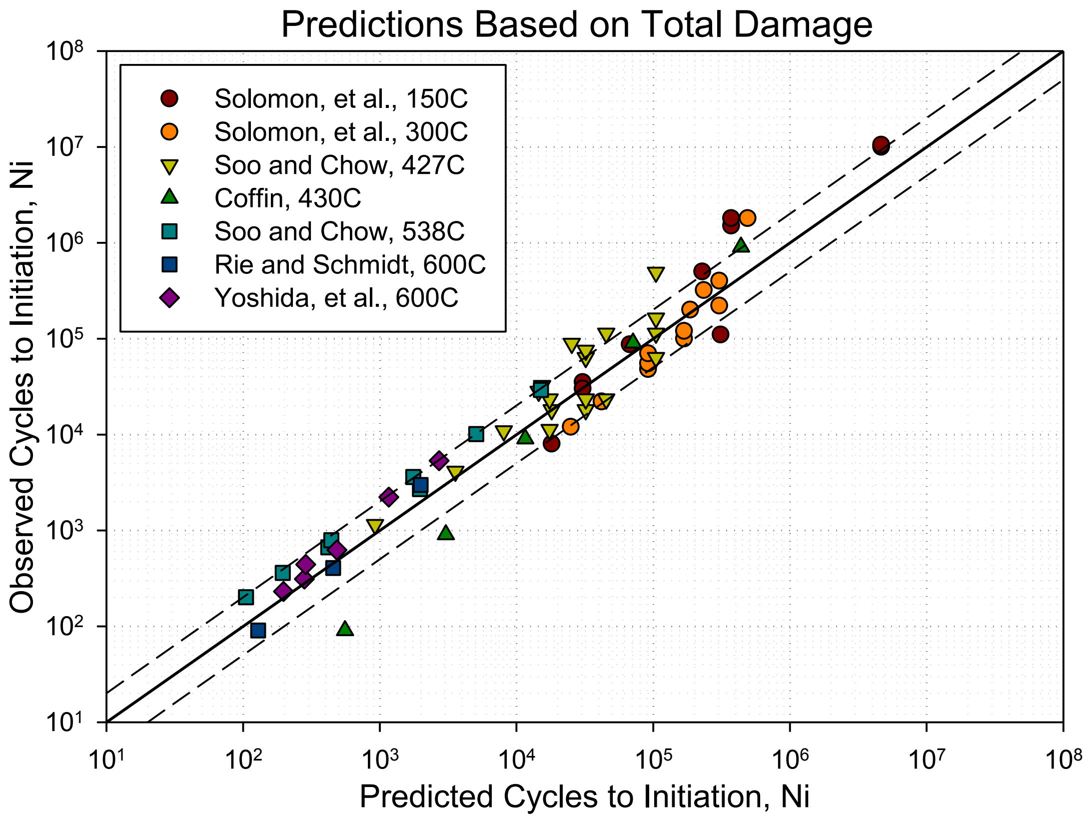

Figure 6.9: Lifetime predictions of isothermal fatigue specimens from literature, based on total damage formulation.

the same set of isothermal fatigue specimens from a range of temperatures pictured in Figures 6.2 and 6.6 are plotted in Figure 6.9. Improvement in scatter reduction versus use of the fatigue or oxide damage formulations alone is clearly evident.

6.2 Discussion of Model

Though target performance values for prediction are met, it is important to clearly define the strengths and weaknesses of the model. Identification of trends in the resultant predictions versus certain load conditions provide insight into the boundaries of the model's performance envelope.

6.2.1 Trends in Model Response

The model was exercised under a number of hypothetical conditions, while cataloguing the resulting constituent damage levels and life prediction values. Maximum temperature, cycle time, hold time, mechanical strain range, and stress concentration levels had varying effect on the outcomes of LCF, IPTMF, and OPTMF cycles. Dependent terms such as elastic moduli or plastic strain response are extrapolated from study data. The general trends are in agreement with published low cycle fatigue and thermomechanical test data (ASM, 2007). A table of the conditions for each type of model exercise is given in Table 6.3.

Table 6-5: Conditions for prediction model range exercises

Exercise Variable	Range of Values	Supplementary Conditions
T_{max}	273K – 1073K	$\Delta\varepsilon_{mech}$=1.0%, K_t=1.0%, t_{hold}=0, t_{cyc}=20s/240s (LCF/TMF), T_{min}=273K (TMF)
t_{cyc}	1s-340s	$\Delta\varepsilon_{mech}$=1.0%, K_t=1.0%, t_{hold}=0, T_{max}=873K (LCF/TMF), T_{min}=273K (TMF)
t_{hold}	0s-4610s	$\Delta\varepsilon_{mech}$=1.0%, K_t=1.0%, T_{max}=873K, t_{cyc}=20s/240s (LCF/TMF), T_{min}=273K (TMF)
$\Delta\varepsilon_{mech}$	0.1%-2.5%	K_t=1.0%, t_{hold}=0, T_{max}=873K, t_{cyc}=20s/240s (LCF/TMF), T_{min}=273K (TMF)
K_t	1.0-5.0	$\Delta\varepsilon_{mech}$=1.0%, t_{hold}=0, T_{max}=873K, t_{cyc}=20s/240s (LCF/TMF), T_{min}=273K (TMF)

Variance in maximum temperature was exercised from 273°K (0°C) to 1073°K (800°C) with the intention of mapping effects within the normal usability range of the material. In LCF cases, fatigue damage levels are dominant at low temperatures, with oxidation damage being the major life reducing factor for temperatures in excess of 473°K. Oxidation damage dominance gives way to creep damage dominance near 1000°K, with creep damage being at very low levels at temperatures below 973°K. Damage contributions from IPTMF tests are similar in quality,

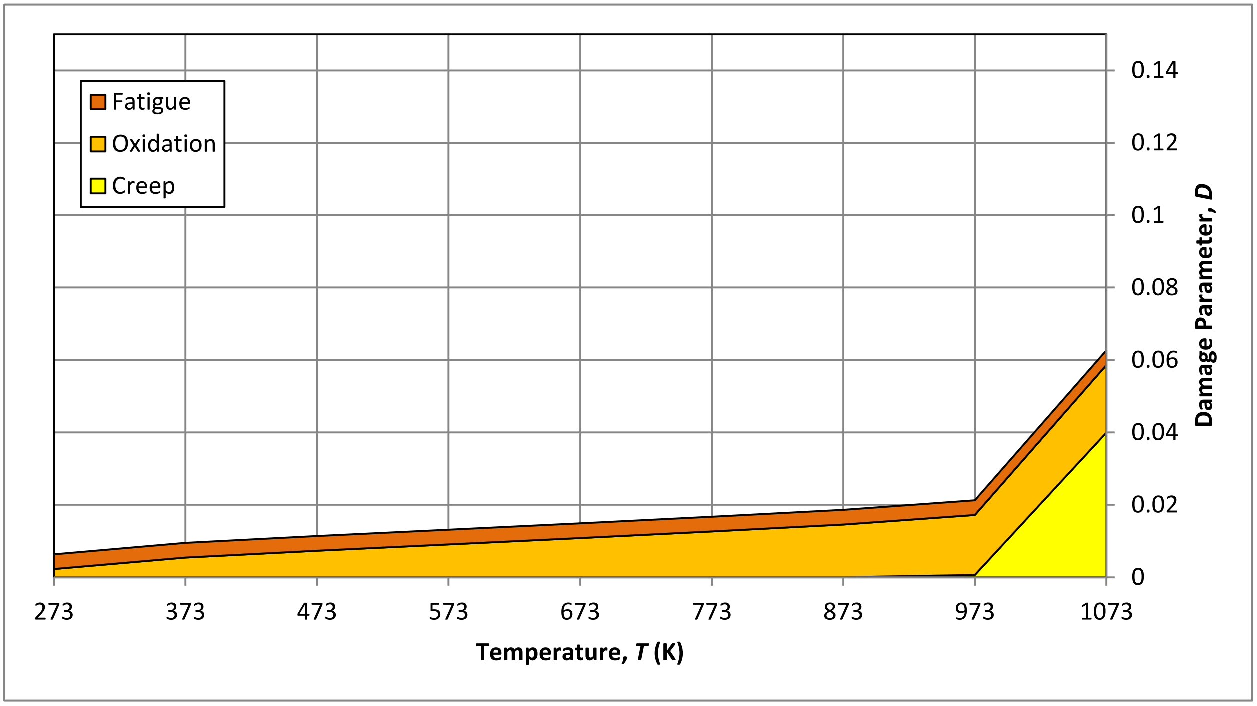

Figure 6.10: Effect on damage contribution in smooth, 1.0% mechanical strain range, 600°C (873°K) LCF tests as maximum temperature varies.

with slightly higher overall damage levels. Damage from OPTMF tests remains oxidation-dominated above 473°K, as creep in OPTMF cycles is less profound. Figures 6.11 and 6.12 illustrate the damage in IPTMF and OPTMF cycles with varying temperature.

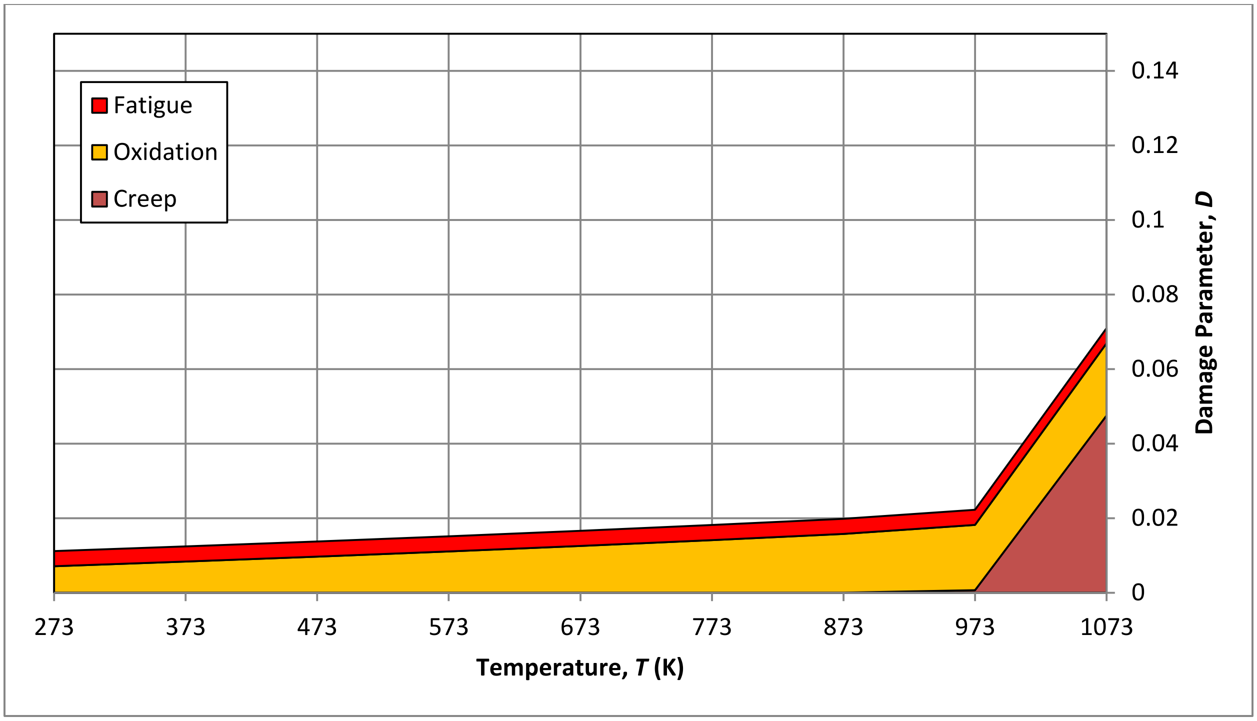

Figure 6.11: Effect on damage contribution in smooth, 1.0% mechanical strain range IPTMF tests as maximum temperature varies.

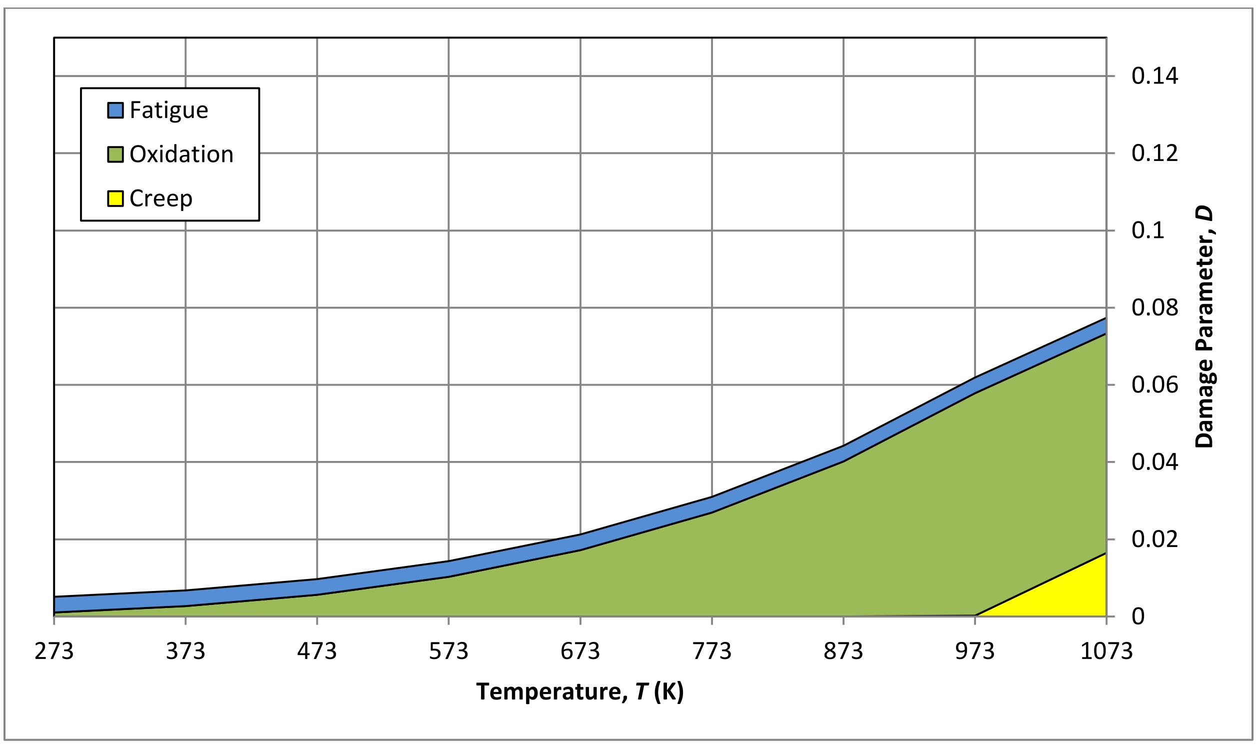

Figure 6.12: Effect on damage contribution in smooth 1.0% mechanical strain range OPTMF tests as maximum temperature varies.

Effects on lifespan in LCF and IPTMF cases follow the same general trend, with very short lifetimes for the highest temperatures, and a slow trend toward longer lifetimes as temperatures decrease. LCF liftimes exceed the IP TMF cases at all temperature ranges. In the case of OPTMF, life is severely reduced at high temperatures but at less intense thermal loads, the out-of-phase case reveals longer life resulting from apparent lower oxidation damage predictions.

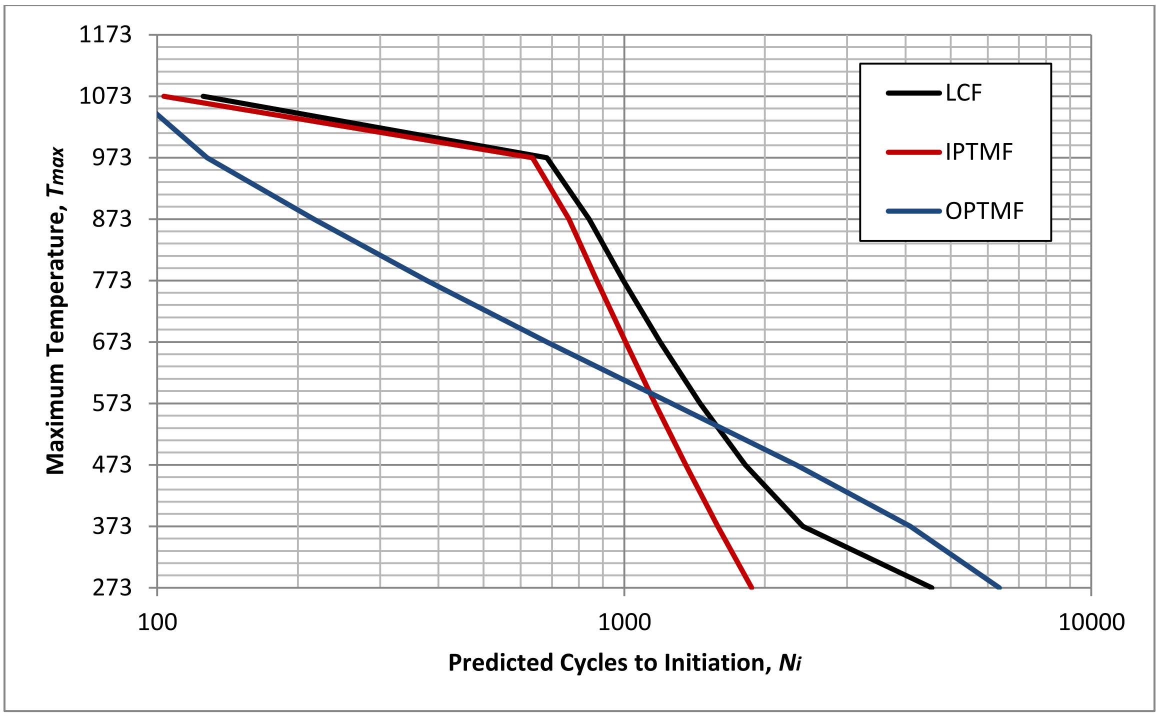

Figure 6.13: Effect on predicted life in smooth, 1.0% mechanical strain range tests maximum temperature is varied.

As cycle-duration is increased, it is initially appears to be a disjuncture in the model that LCF cases at TMF-like cycle times show greater damage, which is attributed to slightly higher oxidation levels throughout all ranges. This effect is likely a sub-consequence of the temperature dependence, where at TMF-like cycle times, LCF specimens are exposed to higher average temperatures. Lifetimes for OPTMF and LCF vary slightly, with IPTMF having a minimal life advantage over the other loading types. Oxidation intrusion remains the dominant mechanism in all studied cases.

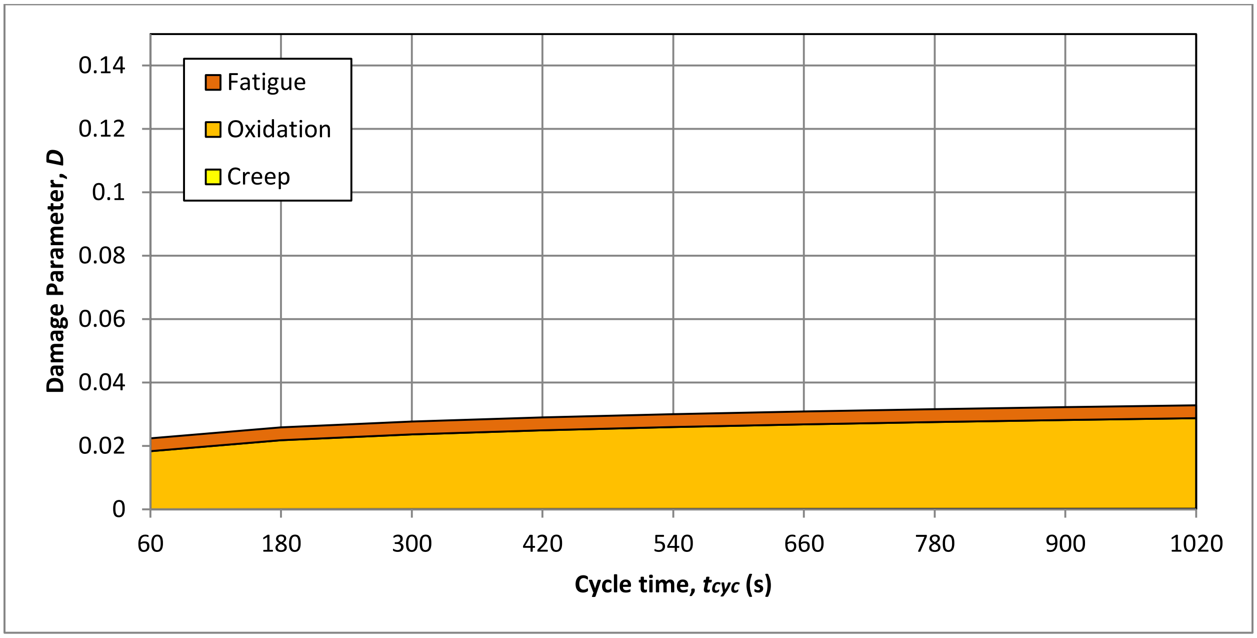

Figure 6.14: Effect on damage contribution in smooth, 1.0% mechanical strain range, 600°C (873°K) LCF tests as cycle duration varies.

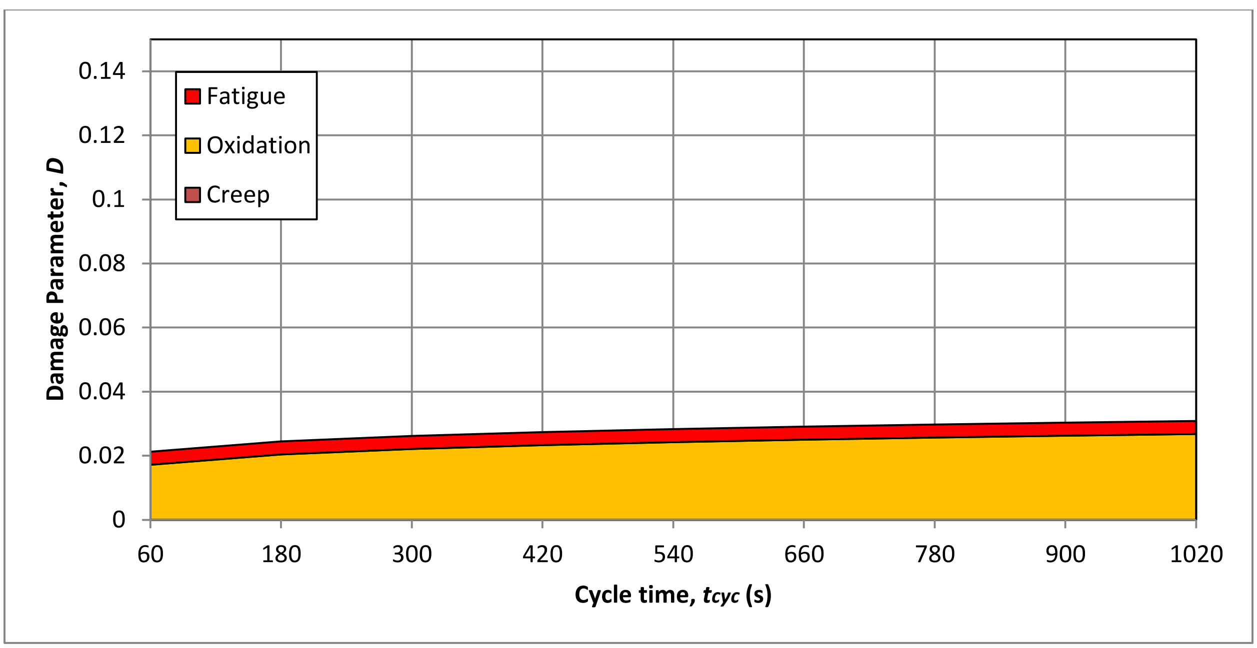

Figure 6.15: Effect on damage contribution in smooth, 1.0% mechanical strain range, 200°C/600°C (473°K/873°K) IPTMF tests as cycle duration varies.

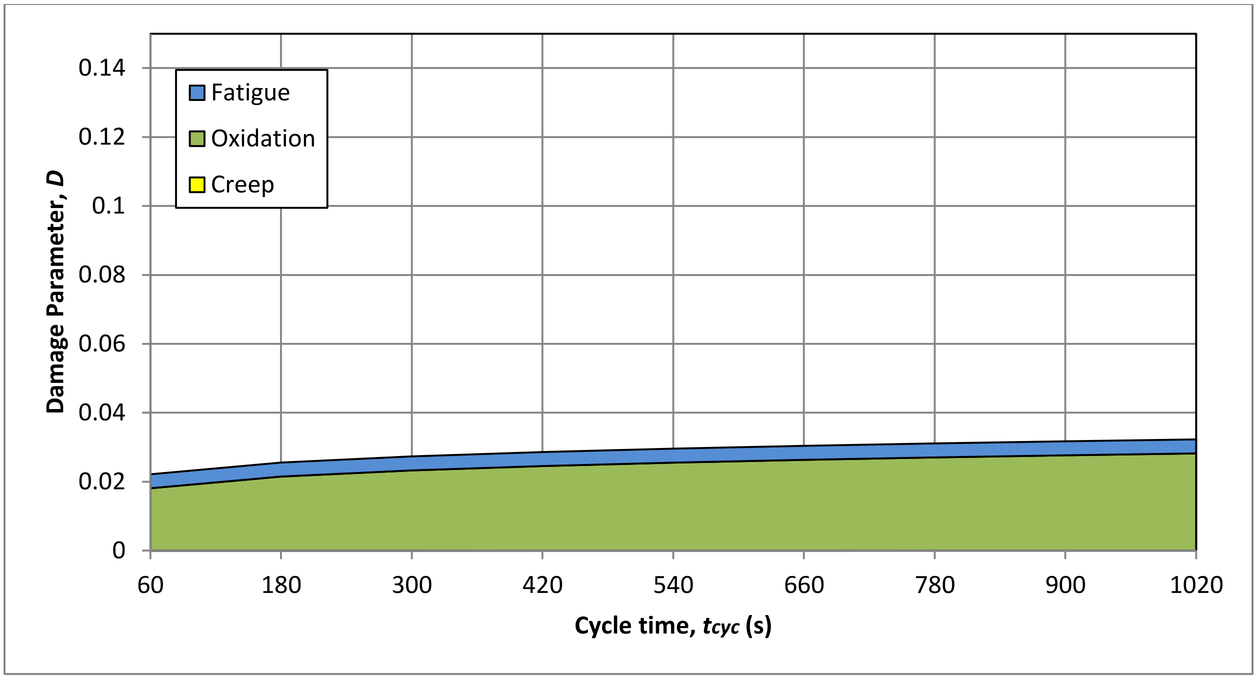

Figure 6.16: Effect on damage contribution in smooth, 1.0% mechanical strain range, 200°C/600°C (473°K/873°K) OPTMF tests as cycle duration varies.

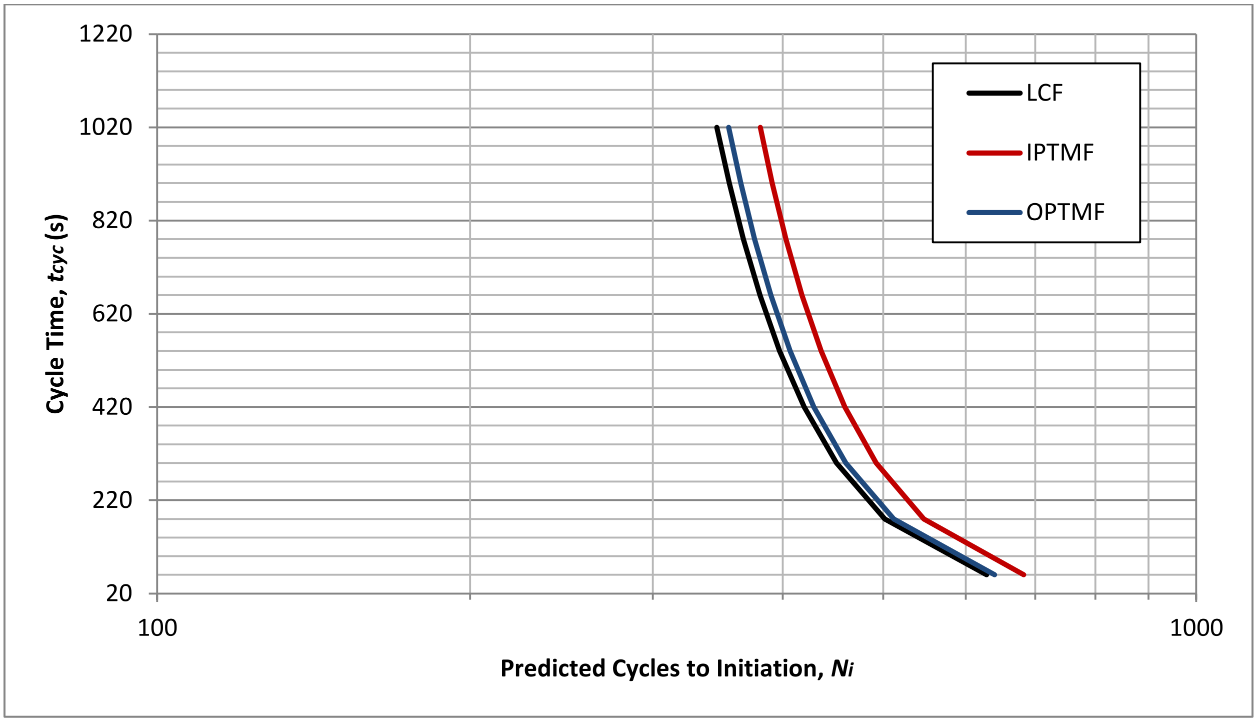

Figure 6.17: Effect on predicted life in smooth, 1.0% mechanical strain range tests with a maximum temperature of 600°C (873°K) as cycle duration varies.

As longer hold times in the 1.0% mechanical strain range case are considered, creep damage becomes a very significant contributor to life reduction than encountered in the empirical studies. At hold times longer than 300 seconds, creep becomes the dominant mechanism in LCF cases. In TMF, creep becomes dominant after 1600 seconds. However, in OPTMF at holds approaching one hour, the overall damage decreases as creep slowly becomes less dominant. Analysis of the life plots confirms the change in OPTMF behavior with respect to the others. Historical TMF data suggests a benefit to TMF-loaded specimens at long hold times, due to a relaxation and reinforcement effect in the steel. This particular behavior was not a model design target, the extra stress relaxation at long hold times decreases creep contribution significantly, and thus extends model usage regimes measurably.

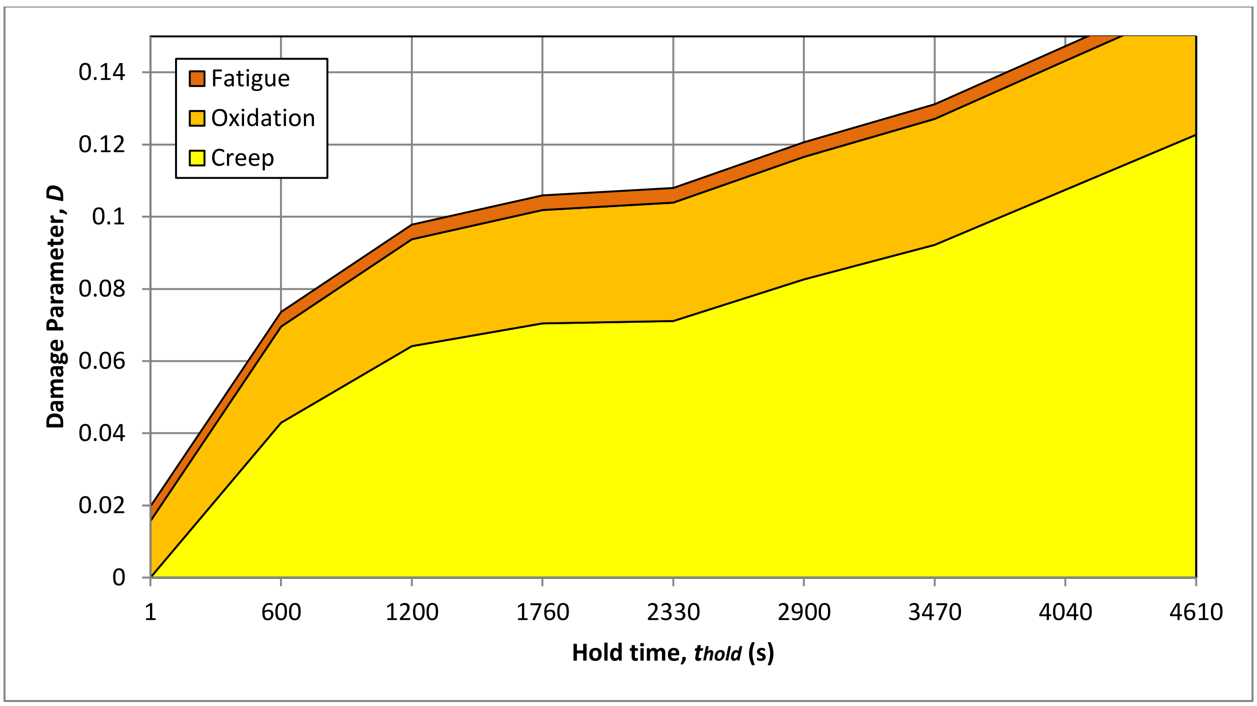

Figure 6.18: Effect on damage contribution in smooth, 873°K, 1.0% mechanical strain range LCF tests as tensile dwell duration varies.

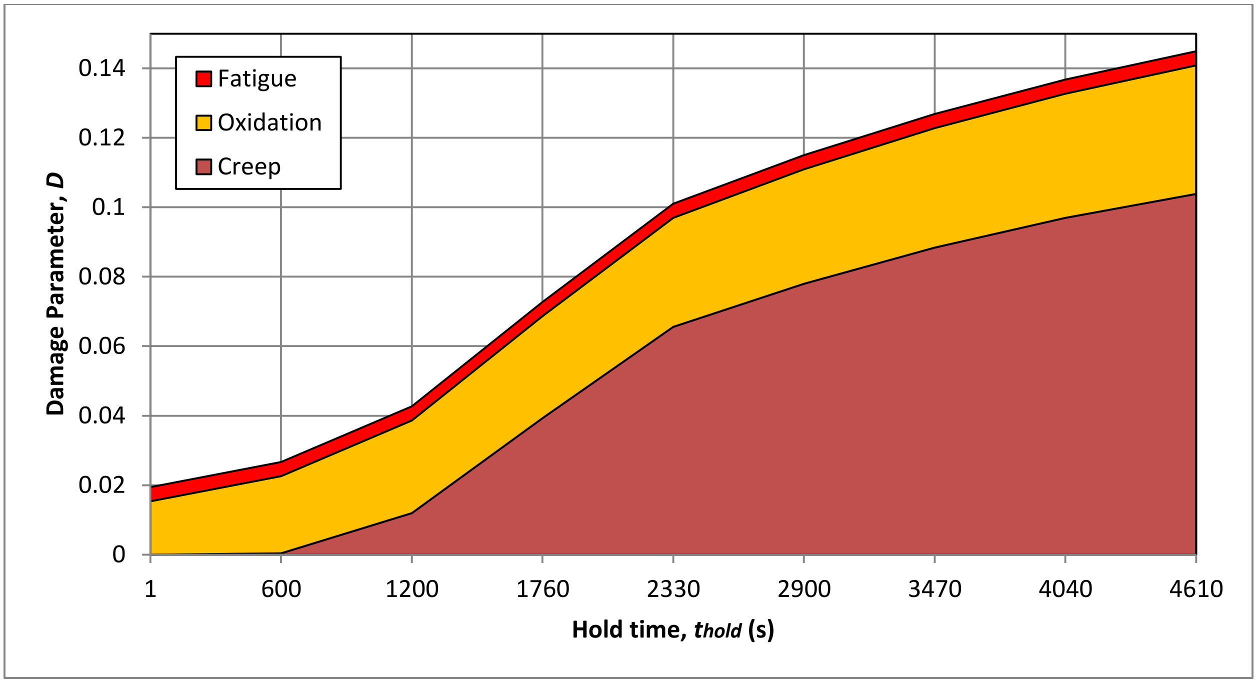

Figure 6.19: Effect on damage contribution in smooth, 1.0% mechanical strain range, 200°C/600°C (473°K/873°K) IPTMF tests as tensile dwell duration varies.

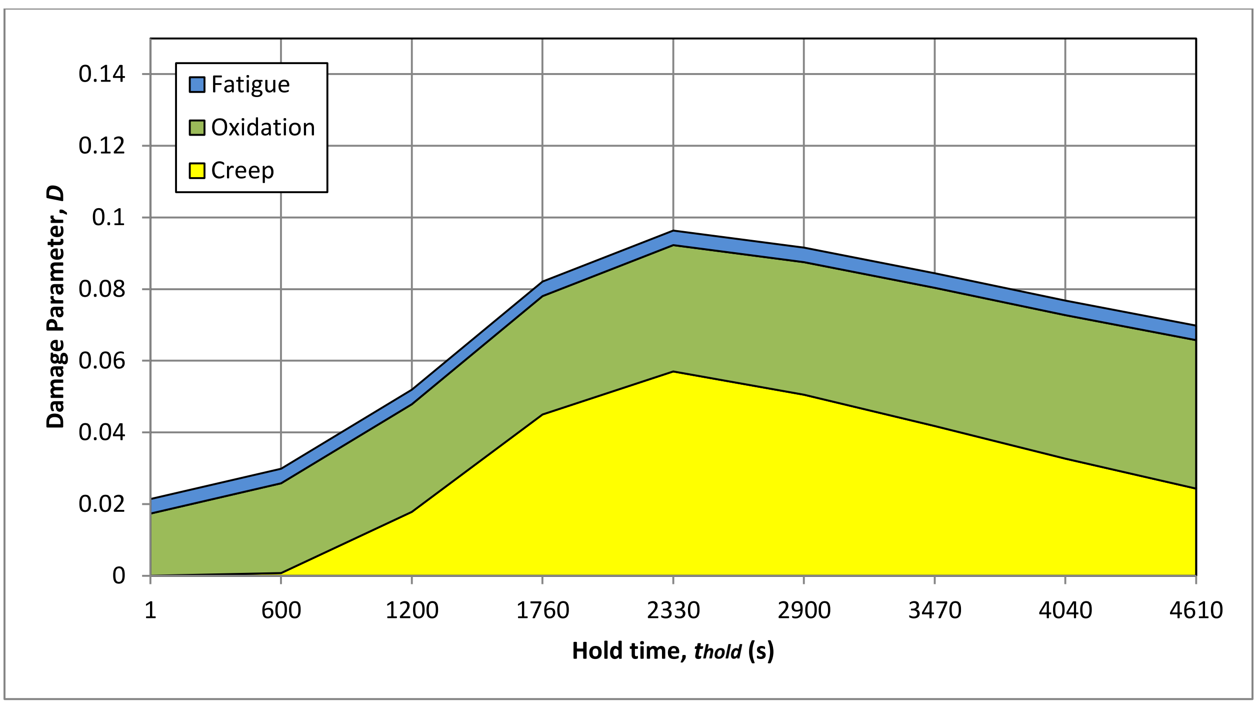

Figure 6.20: Effect on damage contribution in smooth, 1.0% mechanical strain range, 200°C/600°C (473°K/873°K) OPTMF tests as tensile dwell duration varies.

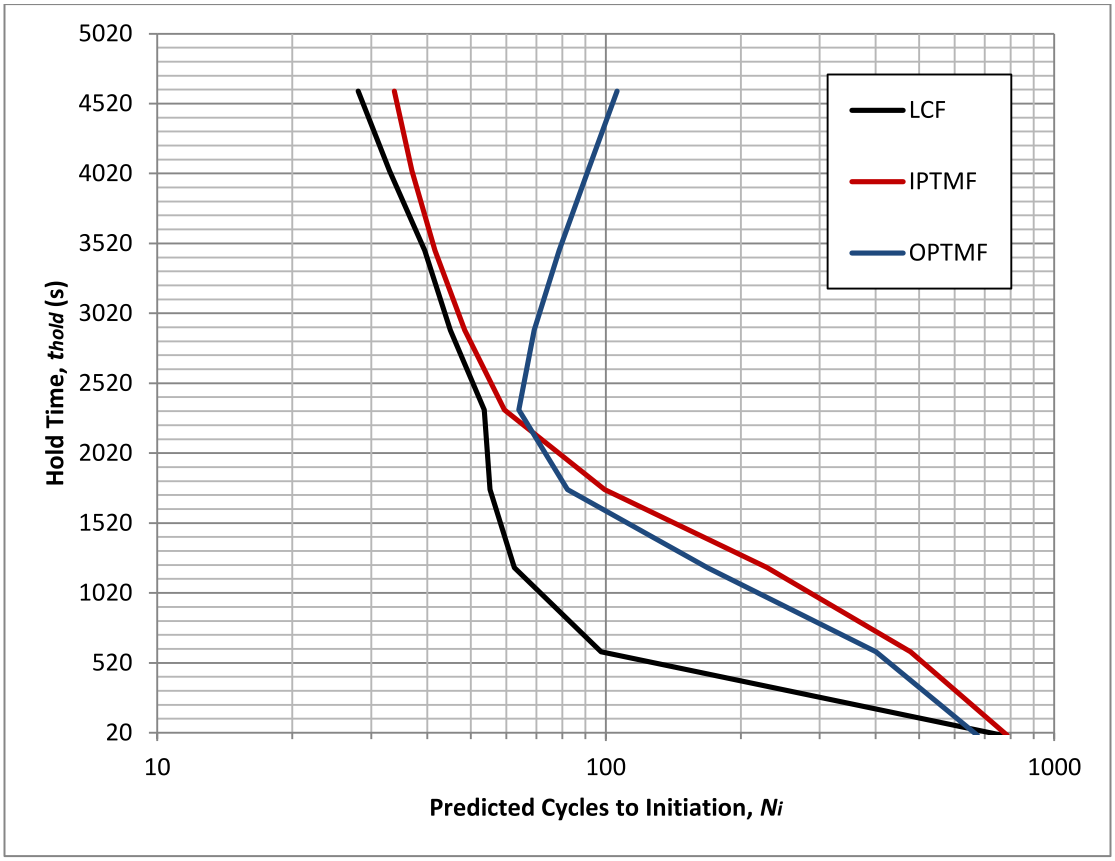

Figure 6.21: Effect on predicted life in smooth, 1.0% mechanical strain range tests at a maximum temperature of 600°C (873°K) as dwell duration varies.

When model test load conditions are conducted with differing mechanical strain ranges, oxidation damage in LCF and TMF cycle types continually increase as strain range grows beyond the empirically-tested range. In high strain range cases, oxidation damage contributions are reduced. As fatigue damage increases dramatically at high strain ranges, oxidation damage does not occur due to the life reduction and inherent lower exposure time. At high strain ranges, TMF cycle types display slightly longer lifespans that the LCF counterpart cycles. Creep in all cycle types remains nearly equal in LCF and IPTMF cycles, with a significant increase at the highest strain ranges. In the case of OPTMF, creep is not a significant contributing factor at any range that the model was exercised.

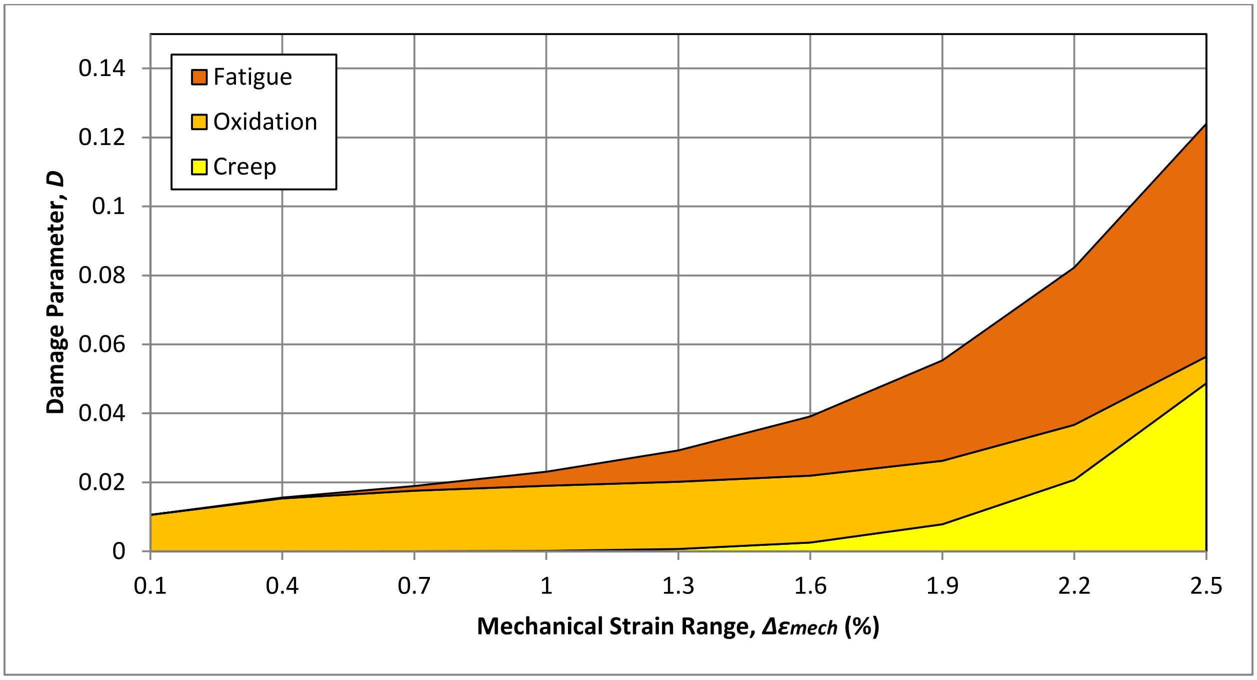

Figure 6.22: Effect on damage contribution in smooth, 600°C (873°K) LCF tests as mechanical strain range is varied.

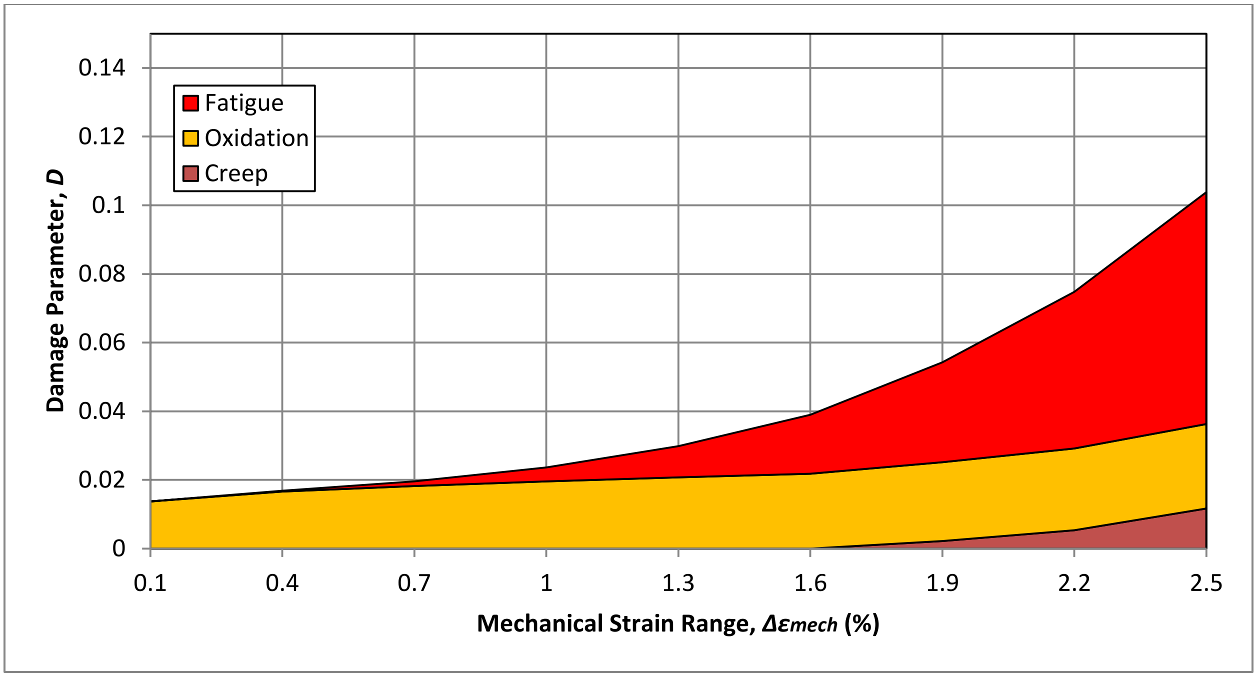

Figure 6.23: Effect on damage contribution in smooth, 200°C/600°C (473°K/873°K) IPTMF tests as mechanical strain range is varied.

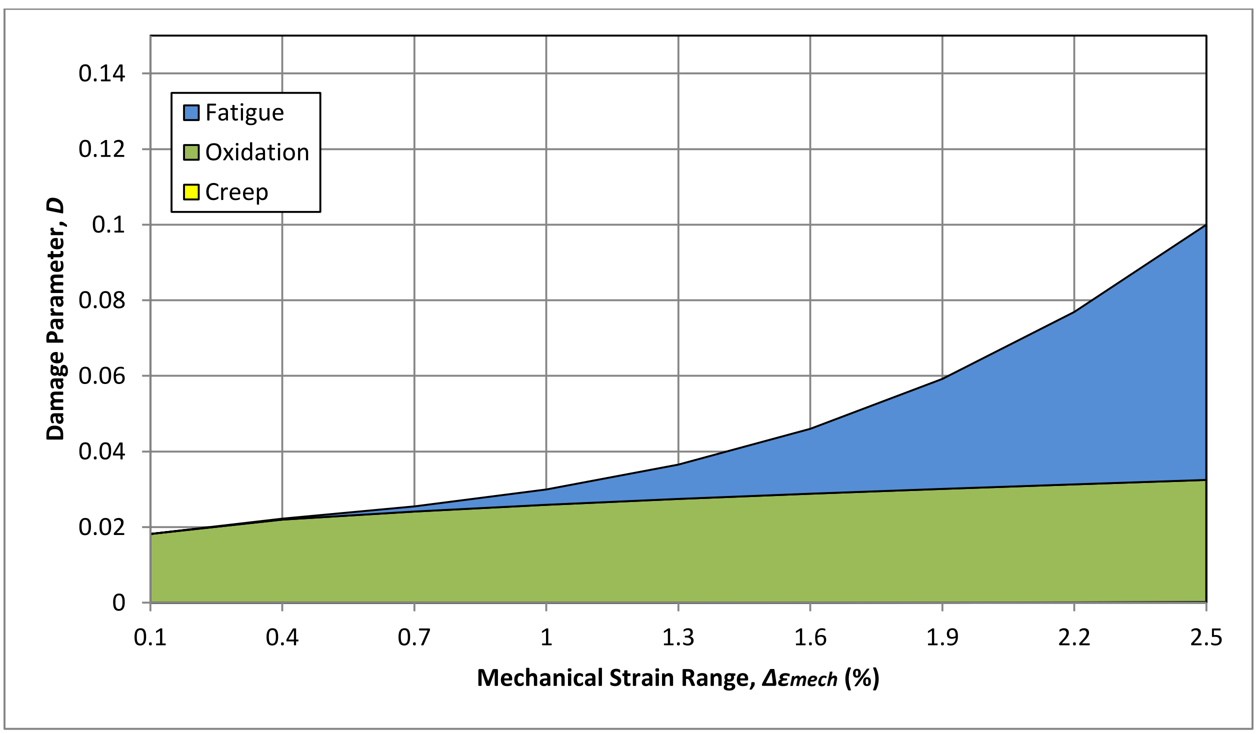

Figure 6.24: Effect on damage contribution in smooth, 200°C/600°C (473°K/873°K) OPTMF tests as mechanical strain range is varied.

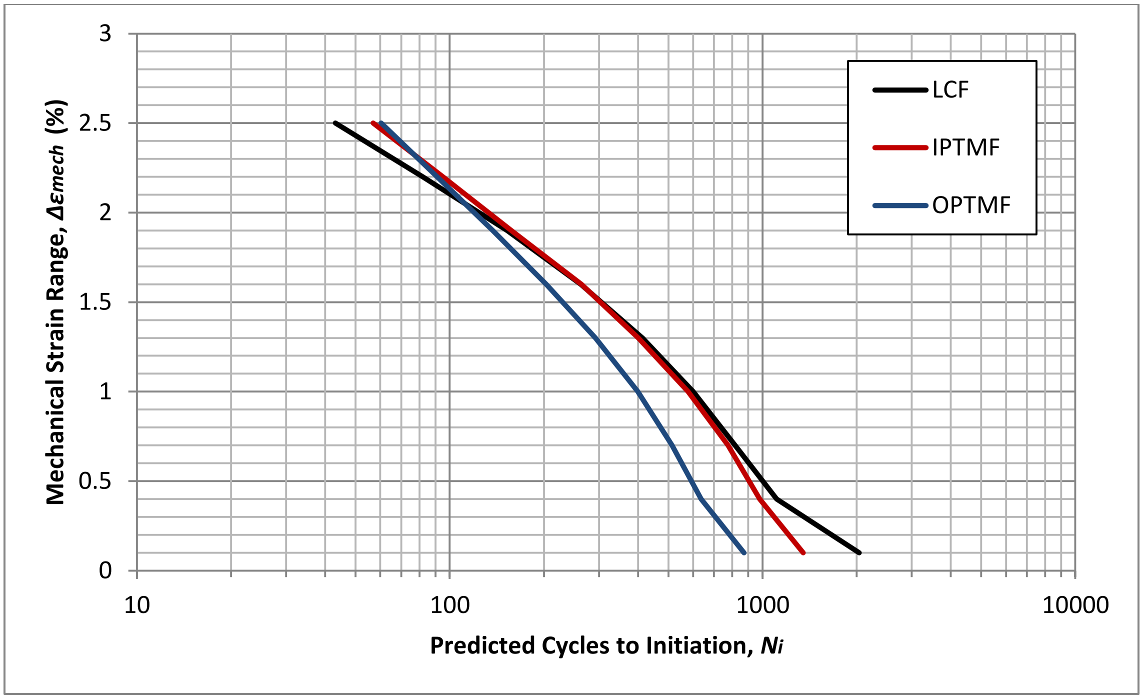

Figure 6.25: Effect on predicted life in smooth tests at a maximum temperature of 600°C (873°K) as mechanical strain range varies.

Lastly, the geometric dependence of the model is assessed from stress concentration factors of K_t = 1.0 to K_t = 5.0. As non-smooth geometries with more severe notches are encountered, damage in every case is dominated initially by fatigue, and then by increasing oxidation damage. Life expectancy in TMF cases decreases more significantly with increased SCF, as a consequence of a major dependence of oxidation damage on SCF in non-isothermal cases. Creep damage is present in LCF as a non-dominant mechanism at high K_t values, but not significant in TMF cases. An inflection point visible in each lifing curve between K_t = *1.0* and K_t = 2.0 is likely an artifact from the fitting of the model based on data from K_t = 1.73 tests.

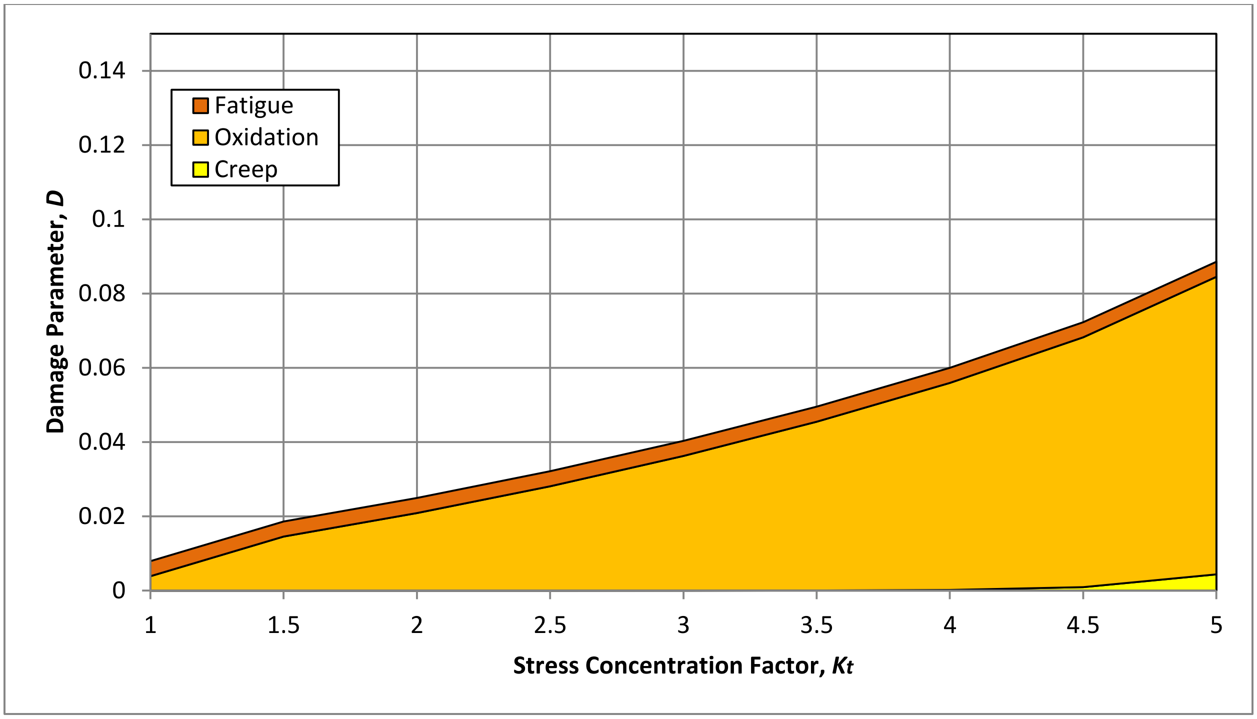

Figure 6.26: Effect on damage contribution in smooth, 600°C (873°K) LCF tests with a mechanical strain range of 1.0% as stress concentration factor is varied.

Figure 6.27: Effect on damage contribution in smooth, 200°C/600°C (473°K/873°K) IPTMF tests with a mechanical strain range of 1.0% as stress concentration factor is varied.

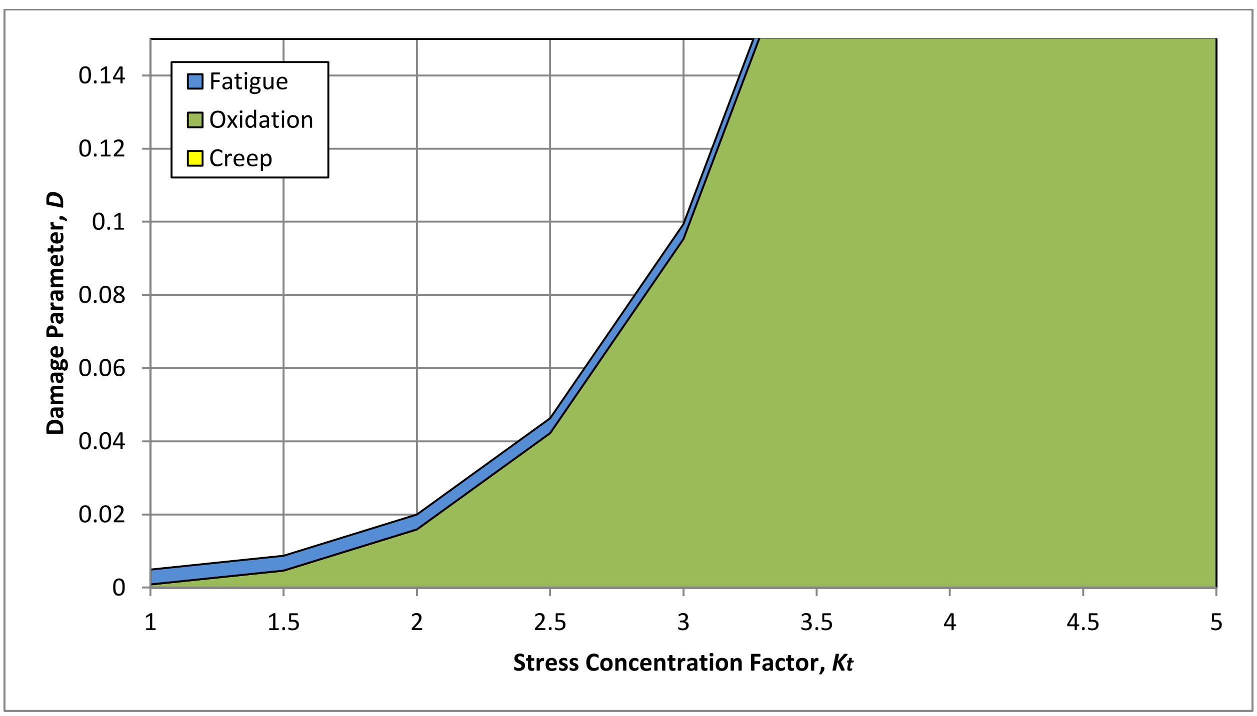

Figure 6.28: Effect on damage contribution in smooth, 200°C/600°C (473°K/873°K) OPTMF tests with a mechanical strain range of 1.0% as stress concentration factor is varied.

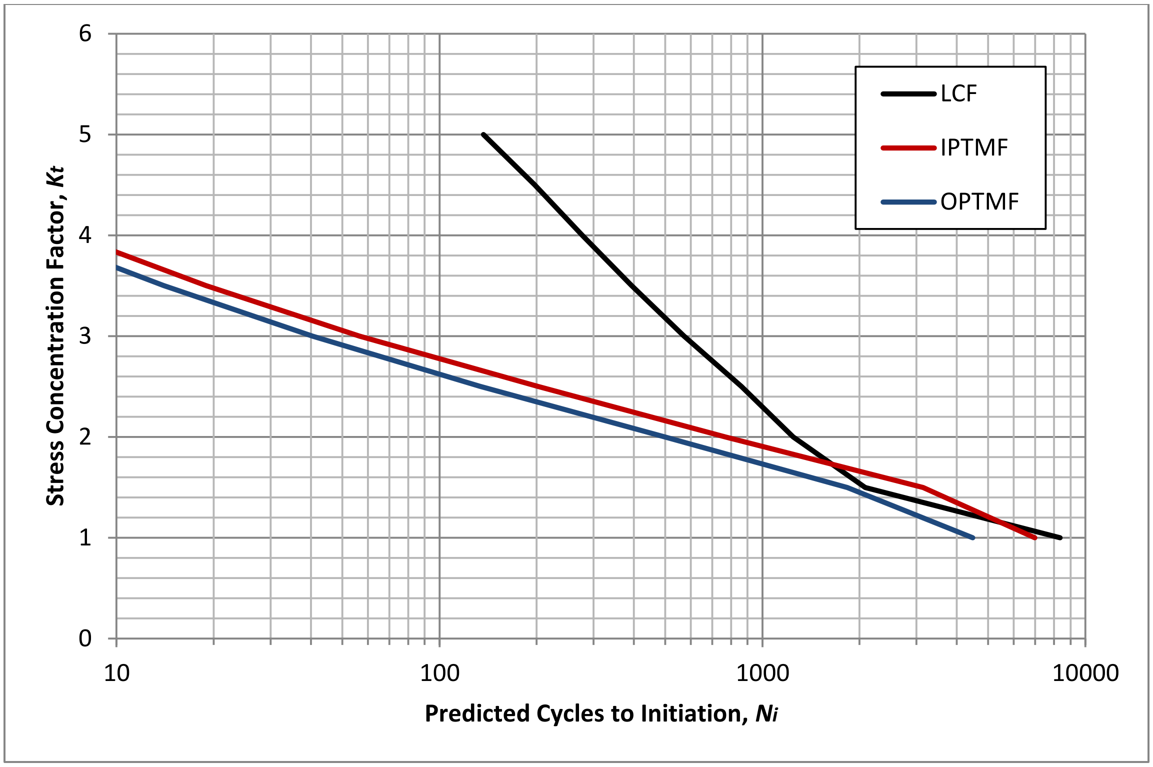

Figure 6.29: Effect on predicted life in smooth tests at a maximum temperature of 600°C (873°K) with a mechanical strain range of 1.0% as stress concentration factor varies.

When performance is considered across the variety of trials wherein the model was exercised, some clear trends are identifiable in the predictions. The damage type contributions are useful in providing estimates of regions of dominance that may not be apparent otherwise. Fatigue-dominated damage at the lowest temperatures and highest strain rates are apparent, but the model also reveals thresholds where environmental effects compound the damage, and where creep becomes a factor. The model effectively eliminates some damage types from certain cycles, and in others shows strong enough dependence to warrant secondary investigation. Predictions which are backed by historical data yet not interpolated from the study's experimental data are a strong indicator that additional usefulness exists outside the bounds of the model's empirically-supported envelope.

6.2.2 Known Limitations

A number of limitations are recognizable during model exercising and comparison to known data. The method of development and structure of the model itself leads to a number of shortcomings, which are described and discussed to facilitate understanding of future areas of improvement.

It is foremost clear that some aspects of the model are simplistic. While favorable for computational purposes, it does not necessarily follow that these parts of the overall formulation are elegant in nature. The fatigue term in particular does not carry any direct dependence on the stress concentration factor, and thusly can only be used as a baseline for damage levels originating from a best-case scenario. Similarly, the creep model is also very basic, which can lead to inaccuracies in situations beyond its originally intended use. Although previous studies have proven its merit in thermomechanical fatigue cases, it has not been extensively tested in that of a per-cycle form or with complex geometries. Despite the fact that use of a stress-based term does incorporate some effects of the notch stress field, tests which could provide a clearer picture of its utility require longer dwell or cycle periods than were encountered in the study's conditions. Creep damage as estimated by the model should thusly be understood to carry more extrapolation than other parts of the model.

The close correlation of the oxidation damage and observed life offer an argument for the favorable performance of the model when considering the more minimal contributions of the fatigue and creep formulations. While this is a positive end result, it is prudent to re-think the dominance of the oxidation term. It is likely that the overall damage levels are correct, but the geometric and phasing scaling factors may contain terms that would be better suited in altering the other damage type contributions under certain conditions. It is important to note that although the oxidation damage term offers a strong indicator of life expectancy on its own, it is possible that the scaling factors overstate the oxidation alone. A likelier case is that the oxidation damage factors may actually be indicative of oxide-fatigue or oxide-creep interactions, or could be re-formulated for use in a more global sense.

Another important detail to consider involves the material utilized in the study. Type 304 stainless steel was originally selected as a candidate material due to its wide application and availability. However, the "Type 304" moniker is given to a number of blends of similarly-formulated steels. As each blend has its own characteristic behavior, it is possible that the steel utilized in the study may serve to create a model that better describes the behavior of some alloys than others. It is likely that the model would not yield inaccurate results for steels in the same family, but caution should be exercised when application to other alloys with other base metals or other material systems altogether.

A final consideration involves the availability of directly-measurable load conditions and responses. The model utilizes average stress terms which are influenced by virtue of the notch effects and minimum diameter being inherently linked together, but for crack initiation purposes, it is likely more effective if a local stress measurement were available. Similarly, the strain control correction algorithm introduces an additional computation level where error could be introduced. The strain terms used by the model are assumed correct or in direct correlation with the actual condition, but a local strain measurement would be preferable.

6.2.3 Regarding Mathematical Fits

During the course of model development, a number of mathematical fits derived from regression methods were utilized in an effort to better constrain the model terms to stricter correlation with a set of data specific to this study. It is important to note that fitting and re-fitting of data can add to lack of robustness in the model and should be done so only if either specific conditions are undergoing study, or a known relation is being presented in a simplified manner.

In the instance of the fatigue damage term, the constants and exponents that provide measures of strength and ductility are widely regarded as material properties themselves and therefore not addressed. The mathematical re-fit is of the resultant formulation to a single power law which is dependent on strain only is completely unnecessary and thus is performed only for the purposes of simplification. When considering the oxidation damage term, the re-fit of the final $Z_{ox}\Phi_{ox}h$ combination of terms to observed life is not entirely necessary, yet offers a marked improvement. For other materials or wider study conditions, determination of new constants or lack of fitting altogether will likely result in better predictions. Lastly, the damage weighting and power law fitting of the total damage is ultimately also optional. Proper ratios of the damage are not necessary if accounted for in the damage terms themselves, and the final fit can be thus be improved as a linear summation in the same way. However, limited use of fitting techniques has proven useful in the past for the purposes of defining tightly-fitting models for specific purposes.

6.3 Guide for Model Application

Successful application of the model is contingent upon management of the execution process, which by nature for a constitutive model is somewhat convoluted. This section provides an overview of the required input variables for complete model execution, and includes a process map which can be followed by subsequent users and developers. Firstly, the minimum required input parameters are given in Table 6-6. Required fitting coefficients and exponents are given in Table 6-7.

Table 6-6: Minimum required parameters for model execution

Parameter	Description	Unit	Source
$\Delta\varepsilon_{mech}$	Applied local mechanical strain range	%	Test parameter
t_{cyc}	Cycle duration	sec	Test parameter
T(t)	Cycle temperature function	°K	Test parameter
σ_{max}	Maximum tensile stress	MPa	First cycle data
φ	Cycle thermal/mechanical phasing	---	Test parameter
K_t	Theoretical stress concentration factor	---	Specimen descriptor
$\Delta\varepsilon'_{pl}$	Assumed plastic strain range	%	First cycle data
E(T(t))	Elastic Modulus at temperature	GPa	Test Parameter
t^{+}_{cyc}	Time in tensile strain per cycle	sec	Test parameter
σ^{+}_{avg}	Average tensile stress	MPa	Stable cycle data
T^{+}_{avg}	Average temperature under tensile strain	°K	Test Parameter

Table 6-7: Required fitting constants for model execution (unitless)

Parameter	Description	Default Value
C_1	Fatigue term fitting coefficient	4236.50
b_1	Fatigue term fitting exponent	-3.068
β_1	Oxidation term stress regression constant	-105.58
β_2	Oxidation term temperature regression constant	0.00654
C_2	Oxidation term fitting coefficient	36.532
b_2	Oxidation term fitting exponent	-0.313
C_{SF}	Larson-Miller Parameter fitting coefficient	43.31703
b_{SF}	Larson-Miller Parameter fitting exponent	-0.17174
W_{fat}	Fatigue damage contribution weight	17.20
W_{ox}	Oxidation damage contribution weight	12.60
W_{cr}	Creep damage contribution weight	6.20
k_1	Regressed total damage law coefficient	1.6403
k_2	Regressed total damage law exponent	-1.566

When the necessary parameters and fitting constants have been assembled, the execution process begins. Individual damage terms are calculated, geometry and phasing susceptibility terms are determined and applied in the case of oxidation, and then regression is performed on the fatigue and oxidation resultant functions to provide a single continuous curve for each. Final fatigue, oxidation, and creep damage values are summed and a final fit is performed. The process is outlined in the flowchart of Figure 6.25.

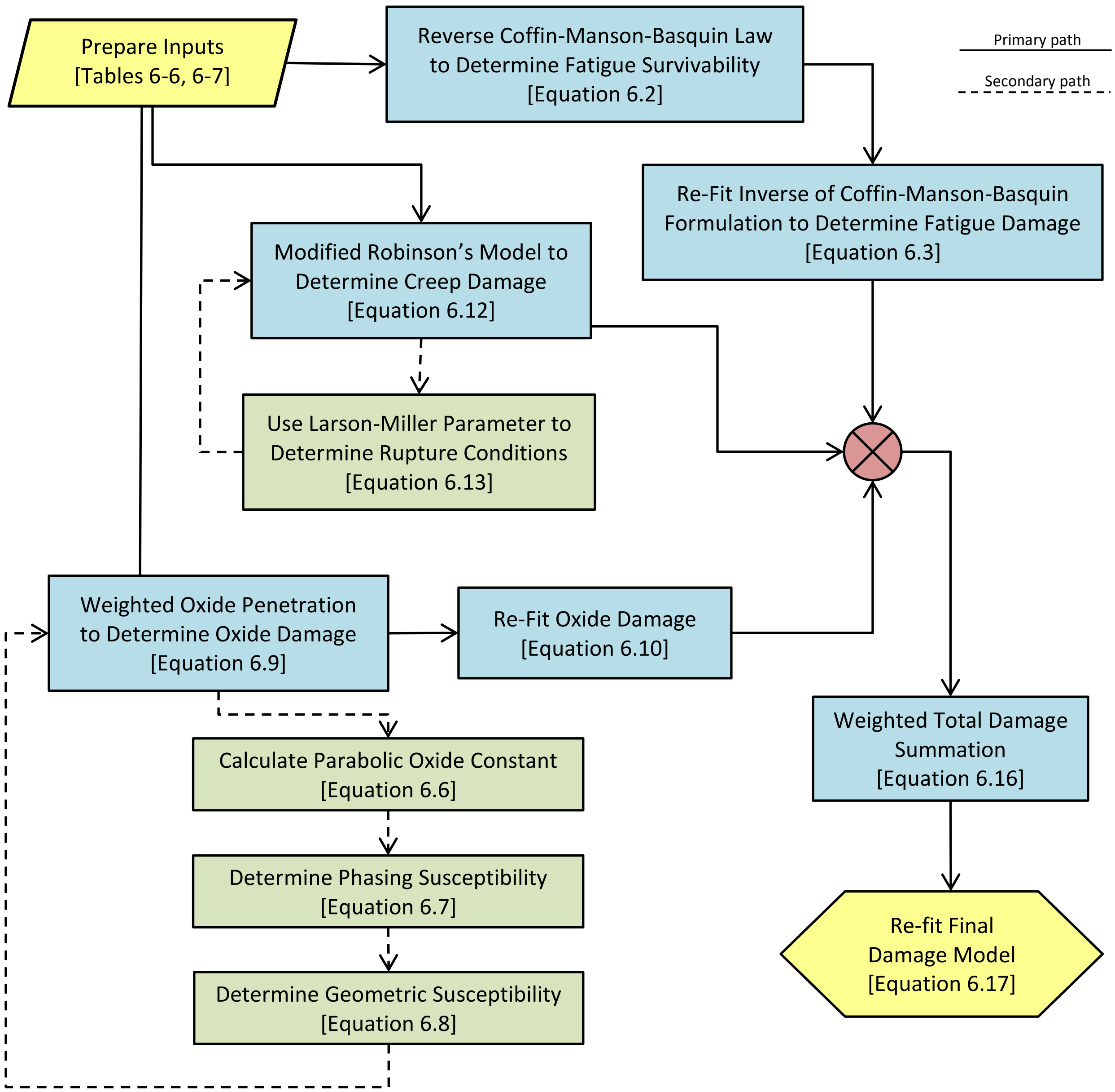

Figure 6.30: Model execution process flow.

CHAPTER 7

PHENOMENOLOGICAL MODEL

A model based on phenomenological effects was constructed to approximate the expected behavior of the test material under conditions like those in the study. This formulation is less computationally intensive than the constitutive physical model, requiring five input variables to describe the test condition coupled with a number of material and fitting constants to complete the relation. The precision of the model meets the prediction goal set forth for the physical model, providing life estimates within a factor of two of empirical data. However, the model scope is confined to that of the experimental conditions, and is thus better suited for interpolation purposes than extrapolation into new domains.

7.1 Model Development

During establishment of the model framework, phenomenology of the experimental results were analyzed in order to determine the most apparent dependencies on candidate variables. This initial analysis was based on heuristics supported by mathematical empiricism, which indicated strong dependencies of expected initiation cycle *Ni* on the variables listed in Table 7-1.

Table 7-1: Input requirements for phenomenological model

Variable	Description	Unit
$\Delta\varepsilon_{mech}$	Applied mechanical strain range	%
K_t	Theoretical Stress Concentration	---
$T(t)$	Test Temperature	°K
t_{cyc}	Cycle time	Sec
φ	Cycle phasing	---

The variables with the strongest correlations were then assumed to be the required inputs for a structure-less proto-model. This proto-model served as a starting point for an evolutionary computation process, which was managed by the commercial software package Formulize™.

Modern evolutionary computation is an approach in which software-based problem solving incorporates biology-inspired genetic algorithms and neural networks to quickly produce and test possible solutions (Schwefel, 1981). The genetic component directly drives the evolution of the computer model, which is done so through minor perturbations in the previous generation's model (Fogel, Owens, and Walsh, 1966). With modern computing capabilities, billions of child models from a single parent can be constructed per generation, leading to many possible better-optimized solutions (Yao and Xu, 2006). The addition of scoring by an artificial neural network allows for rapid testing of the child models, and determination of the favorable directions of perturbation. Neural network training leads to more optimal generation of subsequent models, until convergence criterion are met and the process is considered complete (Karl, 2006).

In the Formulize™ computing package, candidate models are ranked by correlation and complexity. Model evolution was halted when a correlation coefficient of 0.9 or better was encountered in a candidate model of relatively low complexity. The equation meeting the aforementioned requirements gives the preliminary formulation is given as Equation 7.1.

$$N_i = \frac{E\sqrt{K_t}}{K_t \Delta\varepsilon_{mech}{}^2 (T_{max})^3} \tag{7.1}$$

This particular model was sufficiently simple, but a second iteration with manually-introduced material constants and cycle phasing information provided improved performance. This updated form of the equation normalizes the maximum temperature T_{max}, temperature-dependent elastic modulus E, and applied mechanical strain range $\Delta\varepsilon_{mech}$ with the melting temperature T_m, room temperature modulus E_0 and ductility ε'_0 at room temperature, respectively. The phasing value denoted by φ imparts the ability of the model to predict for non-isothermal cases. Given as

$$N_i = \frac{1}{t_{cyc}} \int_0^{t_{cyc}} \frac{E(T(t))}{E_0} dt \left\{ \frac{C_1 K_t^{p_1}}{\left(\frac{\Delta\varepsilon}{\varepsilon'_0}\right)^{p_2} \left(\frac{T_{max}}{T_m}\right)^3} \right\} - C_2 \left[t_{cyc} \left(\frac{\Delta\varepsilon}{\varepsilon'_0}\right)^{p_3} \varphi^2 \right] \qquad (7.2)$$

the final phenomenological relation provides an appropriately tight-fitting model. Major terms for isothermal and non-isothermal cycle types are optimally weighted by fitting coefficients C_1 and C_2, respectively. The incorporation of tuned exponents p_1, p_2, and p_3, provide support for additional accuracy in life prediction solutions. Optimization of weight coefficients and fitting exponents are handled by the Formulize™ computing package, which performs a goal-seeking function on the current model, given that it is adequately constrained in the software setup.

7.2 Model Application

The phenomenological model of Equation 7.2 can calculate life predictions after material property values are applied and fitting of optimal constants and exponents has been performed. Due to the normalization of model terms, variances in the properties will provide particularized results for different materials. Specific to the 304SS blend utilized in the study, material constants, weight coefficients, and fitting exponents are provided in Table 7-2.

Table 7-2: Additional parameters in phenomenological model

Variable	Description	Value(s)	Unit
E	Elastic Modulus (per temperature)	183-143	GPa
E_0	Room-Temperature Elastic Modulus	193	GPa
ε'_f	Room temperature ductility	54	%
Tm	Melting temperature	1743	°K
C1	Isothermal fitting coefficient	0.0336	---
$C2$	Non-isothermal fitting coefficient	-28.2	---
$p1$	Geometric effect fitting exponent	0.85	---
$p2$	Isothermal strain fitting exponent	1.3	---
$p3$	Non-isothermal strain fitting exponent	1.8	---

With fitting parameters optimized, the model offers a fit with a maximum error of 44.91%, which falls within the goal of less than a factor of 2 deviation from the empirical findings. The performance of the model as a whole is evident in Figure 7.1, comparing predictions against observations from the study. Additional robustness as well as some limitations can be inferred from the similar plot pictured in Figure 7.2. The comparison utilizing historical data shows that the model retains usefulness beyond the bounds of the study when subjected to isothermal cases at elevated temperatures. In temperatures below 200°C in LCF cases or TMF cases with minimum temperatures of 300°C or higher, the model does not provide accurate predictions. Thus, the model is useful for TMF in less of a capacity than it is for LCF.

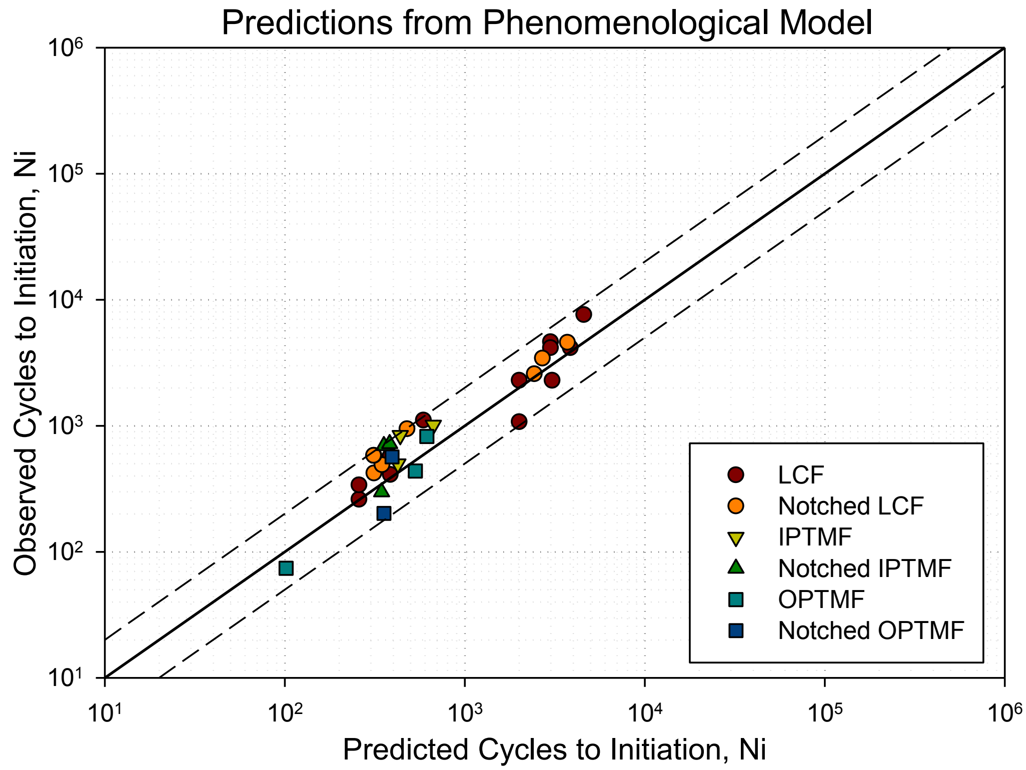

Figure 7.1: Comparison of phenomenological model predictions with observed data from the experimental study.

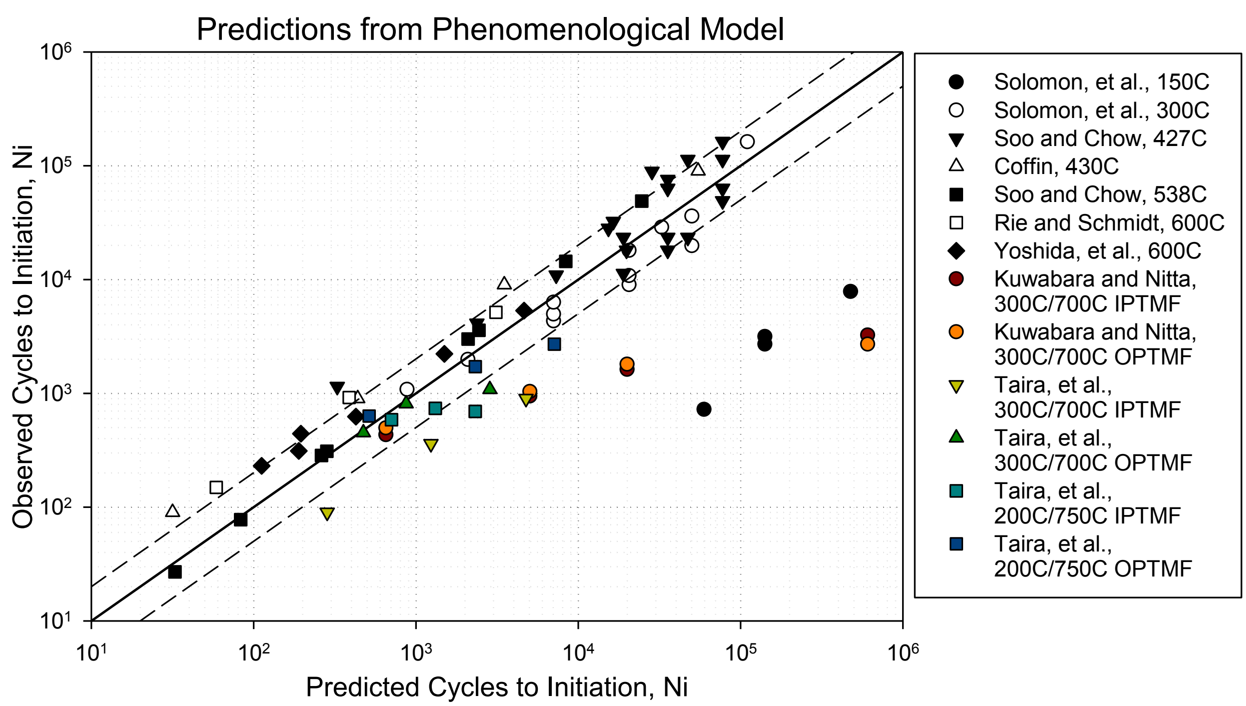

Figure 7.2: Comparison of phenomenological model predictions with historical LCF and TMF data.

7.3 Strengths and Limitations

While the primary function of the phenomenological model is to provide interpolative estimates of untested conditions within the scope of the experimental plan, some exercising of the model reveals the full capability envelope of the formulation. In general, the model predicts TMF lifetimes shorter in all cases than LCF, and with geometric and load-based trends that agree with common fatigue behavioral characteristics. A number of cases are examined to determine the predictive strength as the model is subjected to decreasingly common loadings at the edge of the model's useful calculation space.

The first case involves smooth specimen geometries at standard cycle times (t_{cyc} = 20s for isothermal, t_{cyc} = 400s for non-isothermal) and compares life with mechanical strain application and maximum cycle temperature. Resulting constant life plots show a theoretical convergence of lifetimes at high temperature and low strain ranges, yet no handling of material degradation at significant percentages of the melting temperature. Observable in Figure 7.3, these trends therefore indicate an inability for the model to handle temperatures significantly higher than those in the study. Additionally, it can be inferred from the trends that non-isothermal cycling at low temperatures could result in lifetimes that exceed those of LCF, which has not been explored. Sample data from historical sources shows that LCF within the bounds of the study is handled accurately.

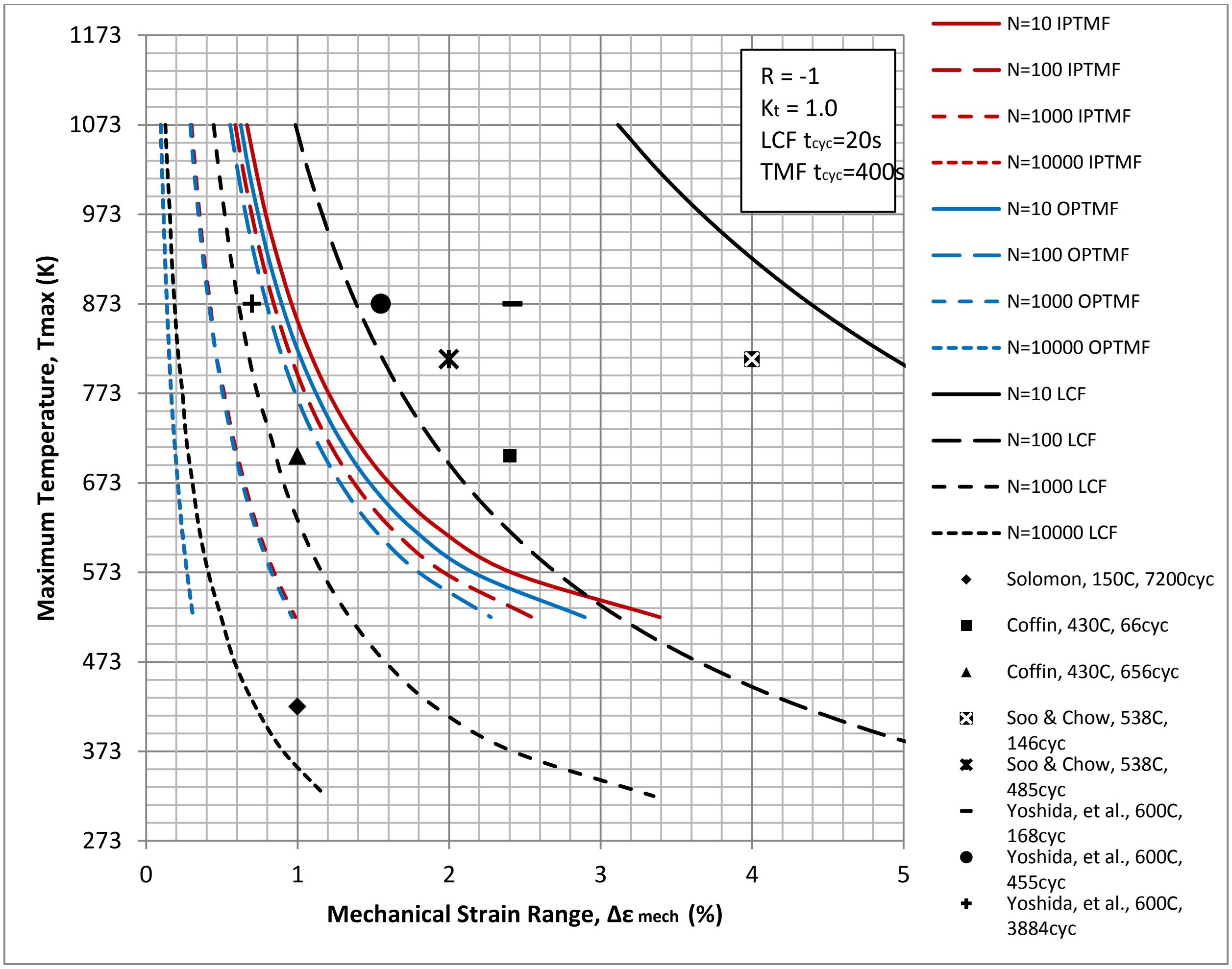

Figure 7.3: Phenomenological model response for varying mechanical strain range and maximum temperature with smooth specimens and standard cycle times, overlaid with samples from historical data.

The next case examines dependency on geometry at different temperatures, assuming an applied mechanical strain range of 1.0%. This particular exercise shows that the model is least robust at low temperatures, and has some mathematical features that do not relate to physically possible conditions. Shown in Figure 7.4, high K_t values do not promote life reduction at low temperatures as severely as previous research suggests (Peterson, 1993). Additionally, the model results in some longer life solutions requiring K_t values of less than 1.0, and temperatures less than 0°K. As this temperature condition is not possible but longer lifetimes at a $\Delta\varepsilon_{mech}$ value of

1.0% exist, so it is clear that the model lacks the ability to handle a combination of low stress concentration values and low temperatures simultaneously.

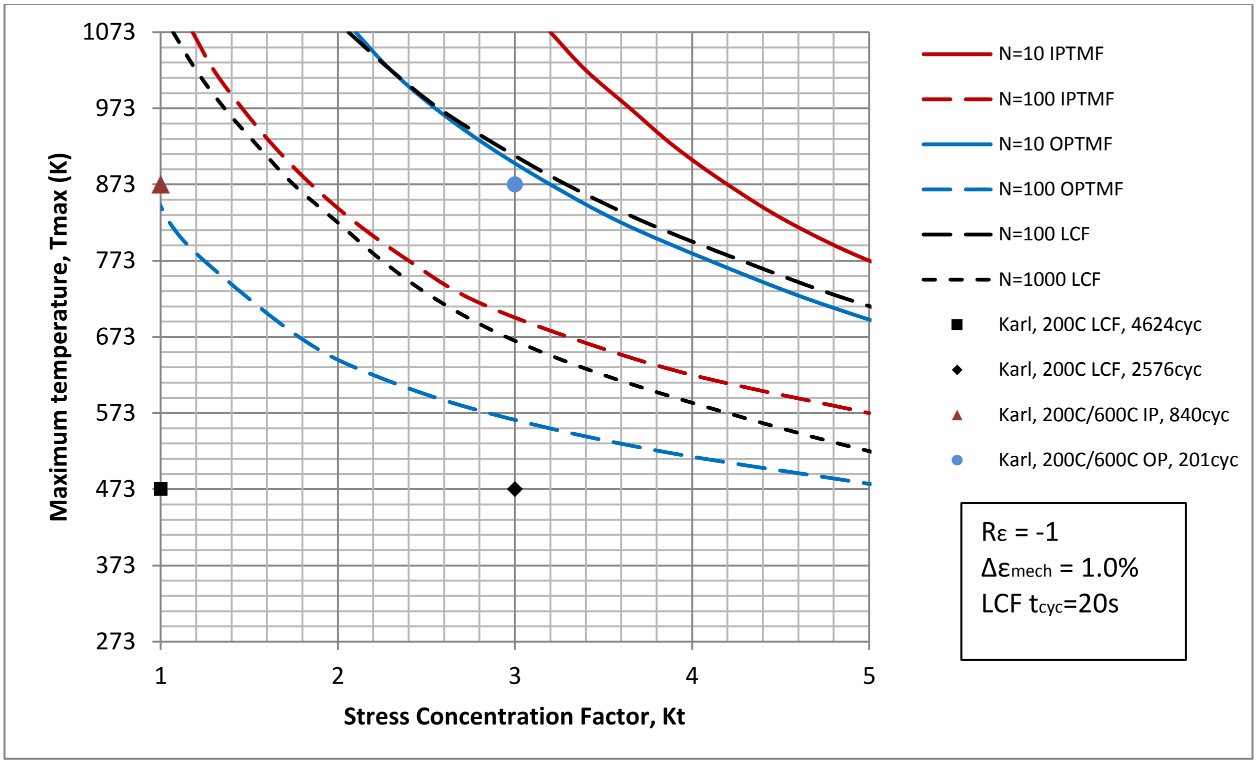

Figure 7.4: Constant life plots for phenomenological model with varied temperature and strain.

A final evaluation of the phenomenological model was conducted with cycle time variance at different temperatures. With a mechanical strain range of 1.0%, LCF lifetimes with at lower temperatures appear to eventually allow for infinite cycle times, which are known to be impossible conditions. Additionally, TMF cycling with low cycle times is generally not feasible under field or laboratory conditions and thus cannot be refuted, but the divergence in TMF cycle types at low durations and high temperatures suggests it to be a mathematical artifact.

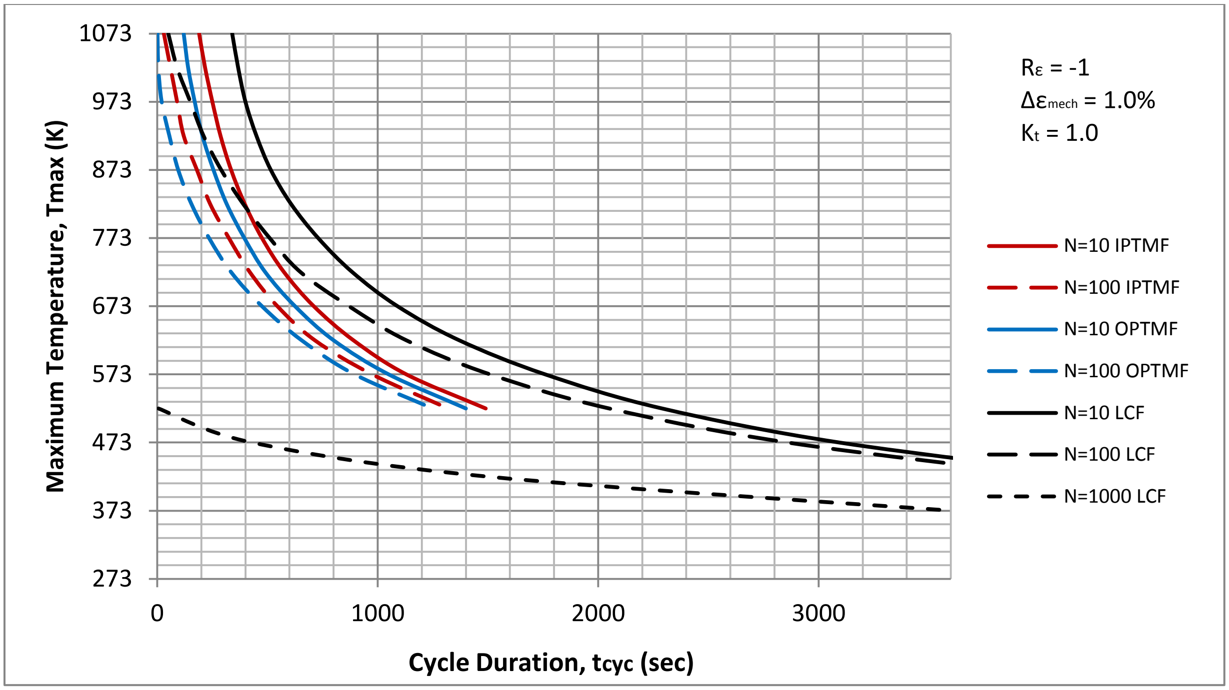

Figure 7.5: Phenomenological model response with variable temperature and cycle duration.

Further analysis of the model and its response in Figure 7.5 indicate that there is no evidence of any long-duration reinforcement effects in LCF or TMF, which has been previously observed (Westwood, 1979). Another important point regarding the model's consideration time-based effects is the fact that it makes no distinction between cycles with and without a dwell period, and that it is not strain rate dependent.

Thus, a final performance review of the phenomenological model would conclude that it is highly suitable for interpolation within the confines of the study, and moderately useful in extrapolated cases that lie just beyond the study's conditions. The model does not provide precise predictions in the case of temperature, strain, or geometric extremes, and thus is not suitable for exploratory purposes outside the envelope of available empirical data.

CHAPTER 8

CONCLUSIONS

In modern energy and aerospace industries, the need for accurate life assessment techniques for components is paramount for safe and efficient operation of complex turbomachinery. The prevalence of thermomechanical loadings in complexly shaped parts has necessitated the extension of existing approaches to include geometries which induce stress concentrations. This study has resulted in the development of two approaches that predict the number of fatigue cycles to crack initiation in 304SS specimens subjected to fully-reversed, idealized low cycle fatigue and thermomechanical fatigue conditions, incorporating stress concentration values ranging from K_t = 1.0 to K_t = 3.0. In the physically-backed damage summation method, strain-life, oxidation penetration, and Robinson creep models are modified and augmented to determine the contributions of fatigue, environmentally assisted, and creep damage contributions during widely varying cyclic conditions. A phenomenological model is also developed via evolutionary computational processes that reveal a prediction formulation based on common strain-based testing parameters. An overview of the achievements produced by this investigation is presented:

1. **A method for pseudo-local strain measurement and control was developed for implementation in the mechanical testing process.** Utilizing the results of finite element analysis representative of conditions experienced by notched specimens, a priori corrective algorithms were incorporated into the test frame control and acquisition signals. A standard high-temperature extensometer mounted at remote locations on the gage section of test specimens was therefore able to provide an estimate of local strain

conditions within the notch that are otherwise physically unobtainable. This augmentation to the testing system's total strain control method allowed for the study to include test parameters based on local target strain values.

2. **Development of a simplified temperature control method for servohydraulic testing hardware.** In order to perform complex thermal cycling with low cycle times, a control method whose implementation was feasible on simpler test controllers. In favor of direct digital communication between a modern temperature controller and test system, an alternate method was developed which incorporated analog industrial control signals whose feedback was monitored through a repurposed auxiliary port on obsolete MTS Systems™ hardware. This method allows for TMF testing on a greater range of machinery that is commonly more available to university-level research groups

3. **Development of a damage-based, non-uniform constitutive model to predict lifetimes of smooth and notched specimens subjected to LCF and TMF conditions.** Data relating the stress response of specimens to applied fully-reversed strain cycling was used in conjunction with physical microscopic observations to create a model that accurately predicted life reduction of 304SS specimens. Fatigue, oxidation penetration, and creep damage sub-models utilized a mixture of data and observations on a per-constituent basis to provide the best correlation between cycle counts to initiation with applied and measurable conditions. Predictions fall within a factor of 2 of observed initiation values, which is commonly considered to indicate significant accuracy in TMF life prediction.

4. **Development of simplified model based on phenomenological effects from pre-test load parameters.** A formulation which predicts life in LCF and TMF specimens of

variable geometry was discovered through use of evolutionary computational methods applied to strongly-correlating test parameters. A single mathematical relation predicts the number of cycles to initiation of a primary crack based solely on mechanical strain range $\Delta\varepsilon_{mech}$, stress concentration factor K_t, temperature condition $T(t)$, cycle time t_{cyc}, and thermal-mechanical phasing φ values.

5. **Confirmed general applicability of TMF life prediction models to variable geometries.** The predictive performance of damage-based and phenomenological formulations developed within the study confirm the feasibility of TMF life prediction techniques to be extended into cases which involve stress concentrations. Modifications to individual approaches utilized in non-uniform constitutive models can effectively increase the capability of each model segment, thus leading to a final arrangement capable of accurate assessments in notched cases. A study-specific phenomenological approach which utilizes common load parameters without the need for data from tested specimens further indicates the viability of TMF-capable predictions in discontinuous geometries.

CHAPTER 9

RECOMMENDATIONS

During the course of this investigation it was made clear that results from the damage-based and phenomenological models discussed in Chapters 6 and 7 warrant future development. Implementation of the models beyond their originally constructed regimes is highly desirable, as well as refined experimental and developmental techniques that would increase accuracy and breadth for these and yet-to-be-developed models. Specific issues addressed in sections 6.2.2 and 7.3 are presented along with the author's recommended proposals for future resolutions of such limitations:

1. **Revise complexity level of individual damage term formulations.** In the current form of the damage-based model, the fatigue and creep terms offer a baseline and addition to the oxidation damage term. Though providing good correlation with life expectancy, the oxidation damage formulation is far more complex than the fatigue and creep offerings. Additionally, the oxidation damage contribution during exercising of the model is very high in some cases where fatigue damage in particular intuitively should be higher. It is likely that the oxidation damage formulation incorporates some of the fatigue contribution, possibly through handling of the geometric susceptibility terms. It is therefore recommended that the oxidation and fatigue sub-models be revisited to determine if it would be more suitable to add additional dependencies to the fatigue damage term and/or reduce the complexity in the fatigue damage term. When considering the creep term, another developmental basis which requires less extrapolation may be useful. Diffusion creep in particular is known to occur in 304SS but requires additional experimental data to be obtained in order to provide a proper fit.

2. **Expand models to incorporate additional load waveforms that are more prevalent in practical use.** In many cases of utilization in industrial practices, parts are subjected to loadings which are not fully-reversed, with non-isothermal conditions other than in-phase and out-of-phase being widespread. Modification to the model to allow for accurate prediction under different wave shapes is therefore an important future goal. Incorporation of a mean stress term may serve as a basis for augmentation. Additionally, exploration of model usefulness beyond the temperatures encountered in the study will be necessary. Normalization of parameters by temperature-dependent material properties and temperature dependence in the fatigue damage term are the likely starting points for these modifications.
3. **Assess model usefulness in varying material types.** Although 304SS is widely used, behavior in other materials must be verified in the current or future models to allow for widespread applicability. Nickel-based alloys and ceramics that are utilized in similar thermomechanical conditions have widely varying material properties whose dependence must be incorporated into all aspects of the models.
4. **Apply model formulations to computational methods.** The feasibility of applying the formulations in part or as a whole to finite element modeling and analysis has not been attempted. With constant performance increases in modern computing packages, use of FEA has gained widespread industrial popularity while making implementations of complex formulations less taxing on overall resources. It is essential to test the performance of future models in FEA simulations, and compare the result against experimental data, as this will allow expansion into the real-world complex geometries encountered in components.

5. **Explore incorporation of more complex behaviors.** This study retains simplicity in its scrutiny of stress and strain effects in the specimen cross-section, and does not account for several behaviors that are more complex to model. Expansion to multiaxial cases, use of stress gradient information, and estimates of the plastic zone growth across the specimen cross-section are some recommended avenues of development in this sense.
6. **Increase precision of local strain measurement and control methods.** Considering the fact that quality of future studies and expansion of the current formulations are dependent on reliable data, the local strain correction algorithms are worthy of study and development themselves. Incorporation of proper balances between elastic and plastic behavior with a variable plastic zone size in the specimen gage section will relieve issues regarding skewing of measured values.

APPENDIX A: LOW CYCLE FATIGUE DATA

Specimen K11O

LCF

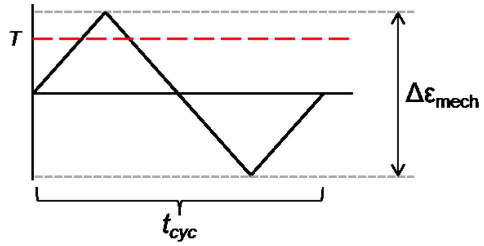

T_{max} (°C):	600	$\Delta\varepsilon_{mech}$:(%)	1.4
T_{min} (°C):	600	K_t:	1.0
t_{cyc} (s):	28	t_{hold} (s):	0

Initial	Stable
σ_{max} (MPa): 290	σ_{max} (MPa): 225
σ_{min} (MPa): -284	σ_{min} (MPa): -220
$\Delta\varepsilon'_{pl}$ (%): 0.97	$\Delta\varepsilon'_{pl}$ (%): 1.03

Hysteretic Response:

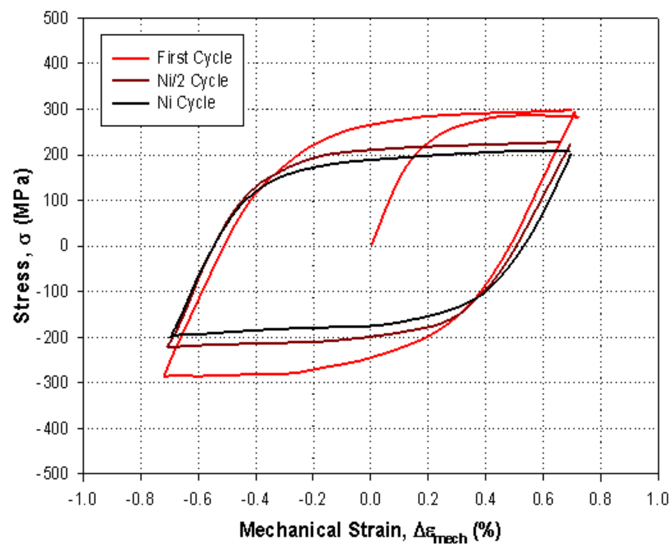

Cycles to Initiation: 260

Stress History:

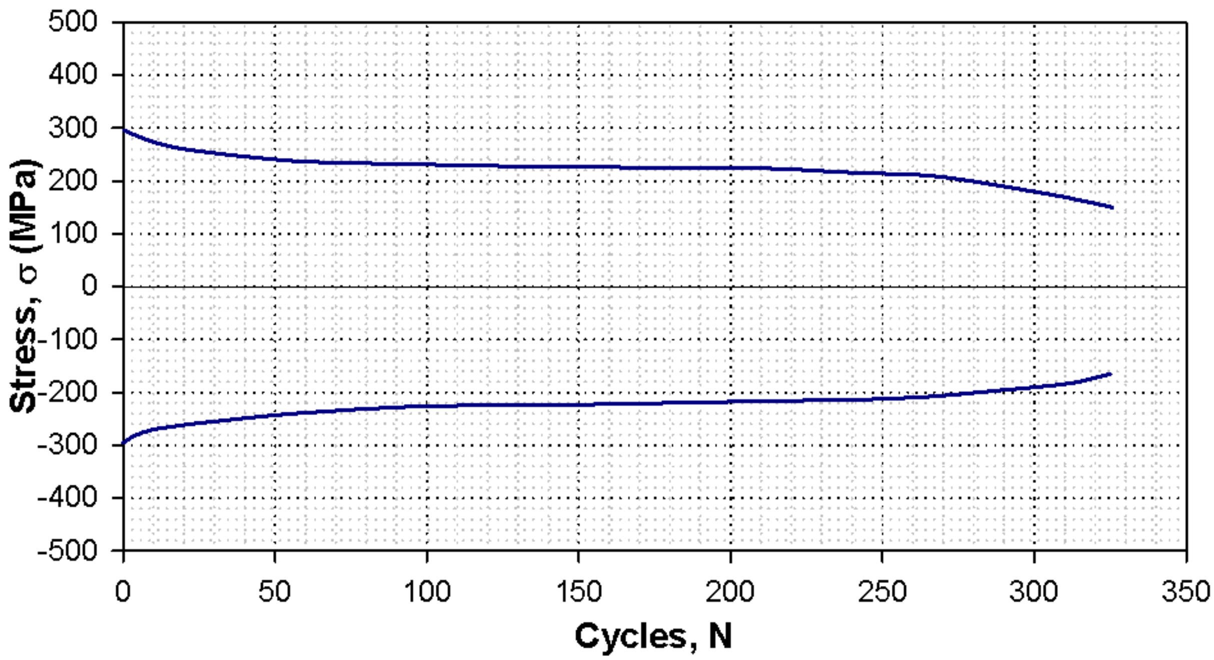

Specimen K005

LCF

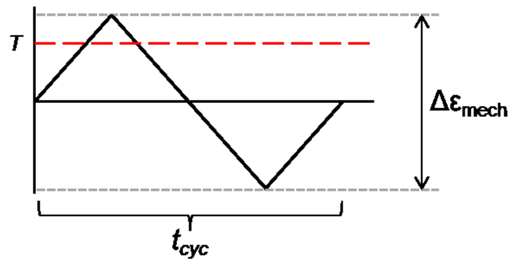

T_{max} (°C):	600	$\Delta\varepsilon_{mech}$:(%)	1.0
T_{min} (°C):	600	K_t:	1.0
t_{cyc} (s):	20	t_{hold} (s):	0

Initial		Stable	
σ_{max} (MPa):	261	σ_{max} (MPa):	258
σ_{min} (MPa):	-248	σ_{min} (MPa):	-250
$\Delta\varepsilon'_{pl}$ (%):	0.64	$\Delta\varepsilon'_{pl}$ (%):	0.60

Hysteretic Response:

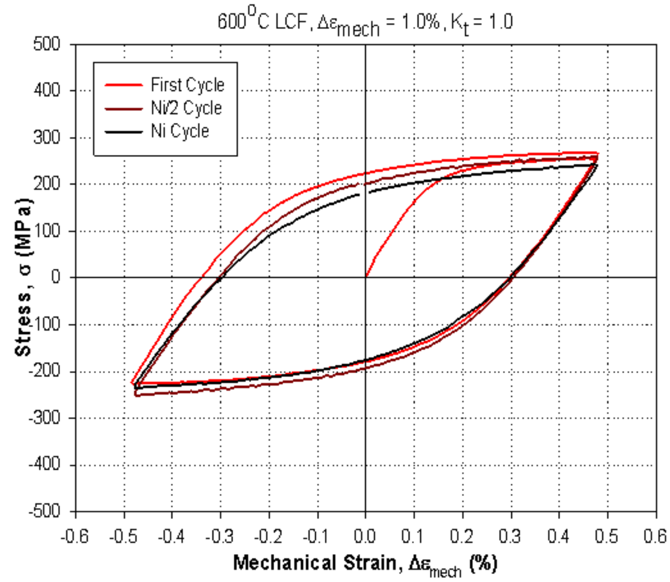

Cycles to Initiation: 421

Stress History:

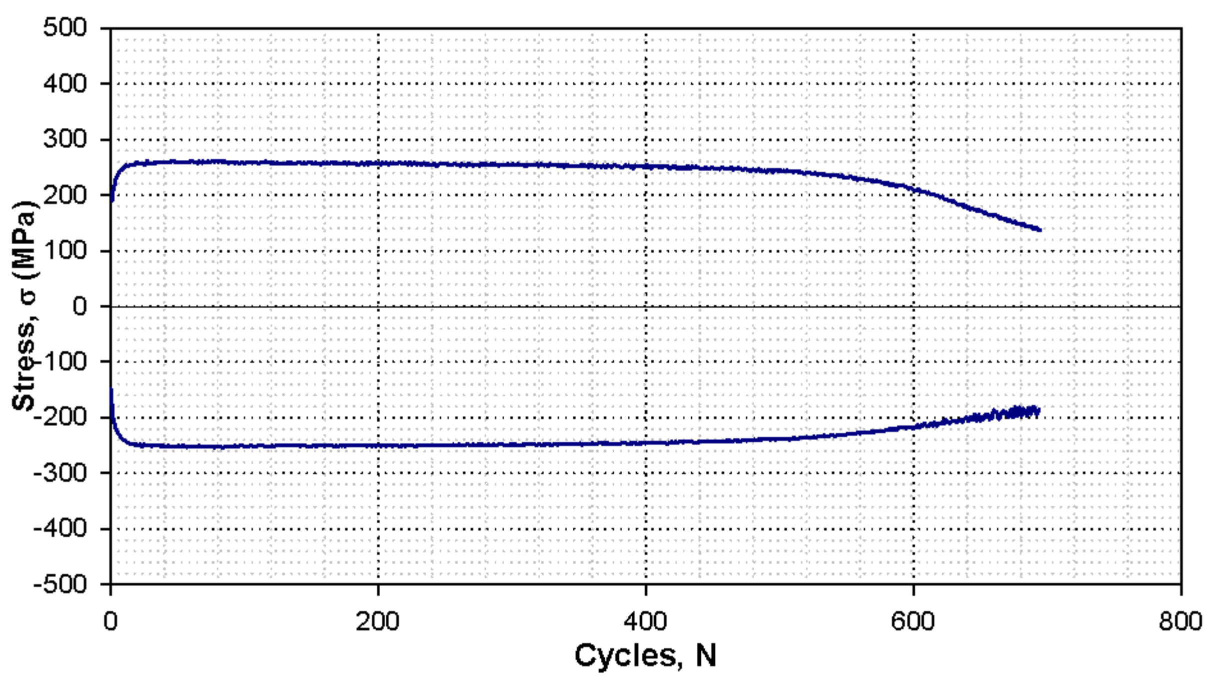

Specimen K022

LCF

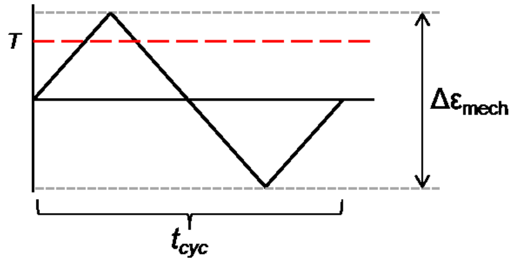

T_{max} (°C):	600	$\Delta\varepsilon_{mech}$:(%)	0.7
T_{min} (°C):	600	K_t:	1.0
t_{cyc} (s):	14	t_{hold} (s):	0

Initial		Stable	
σ_{max} (MPa):	291	σ_{max} (MPa):	243
σ_{min} (MPa):	-291	σ_{min} (MPa):	-245
$\Delta\varepsilon'_{pl}$ (%):	0.37	$\Delta\varepsilon'_{pl}$ (%):	0.36

Hysteretic Response:

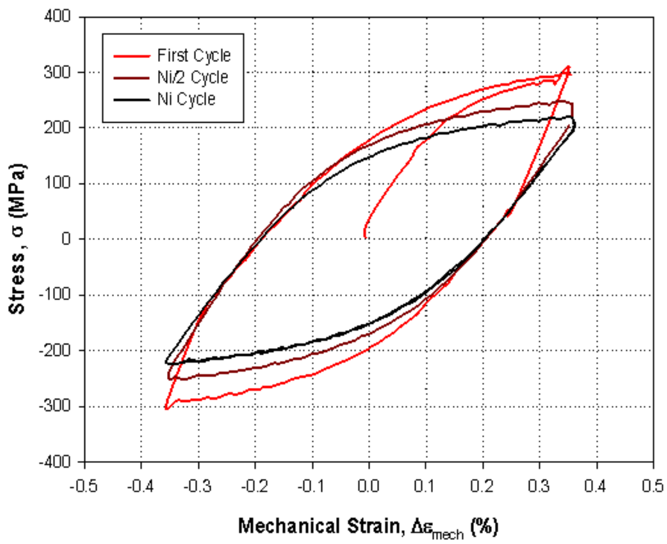

Cycles to Initiation: 1105

Stress History:

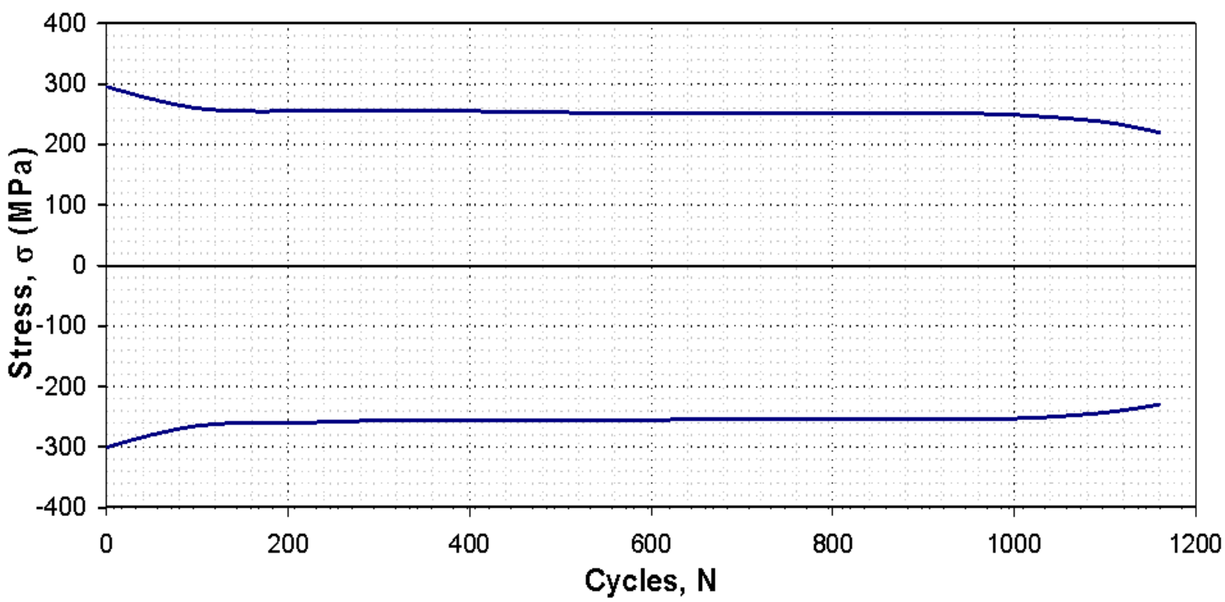

Specimen K11N

LCF

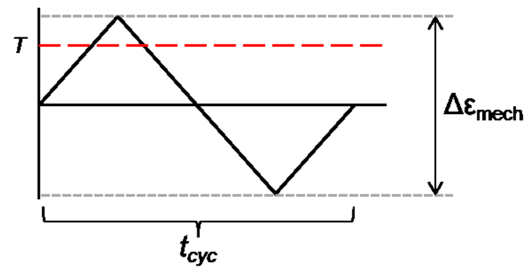

T_{max} (°C):	200	$\Delta\varepsilon_{mech}$:(%)	1.4
T_{min} (°C):	200	K_t:	1.0
t_{cyc} (s):	28	t_{hold} (s):	0

Initial	Stable
σ_{max} (MPa): 458	σ_{max} (MPa): 350
σ_{min} (MPa): -420	σ_{min} (MPa): -347
$\Delta\varepsilon'_{pl}$ (%): 0.84	$\Delta\varepsilon'_{pl}$ (%): 0.95

Hysteretic Response:

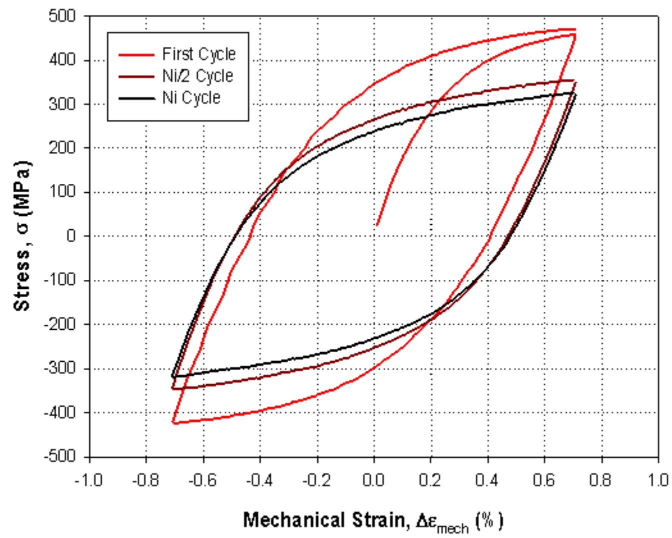

Cycles to Initiation: 2290

Stress History:

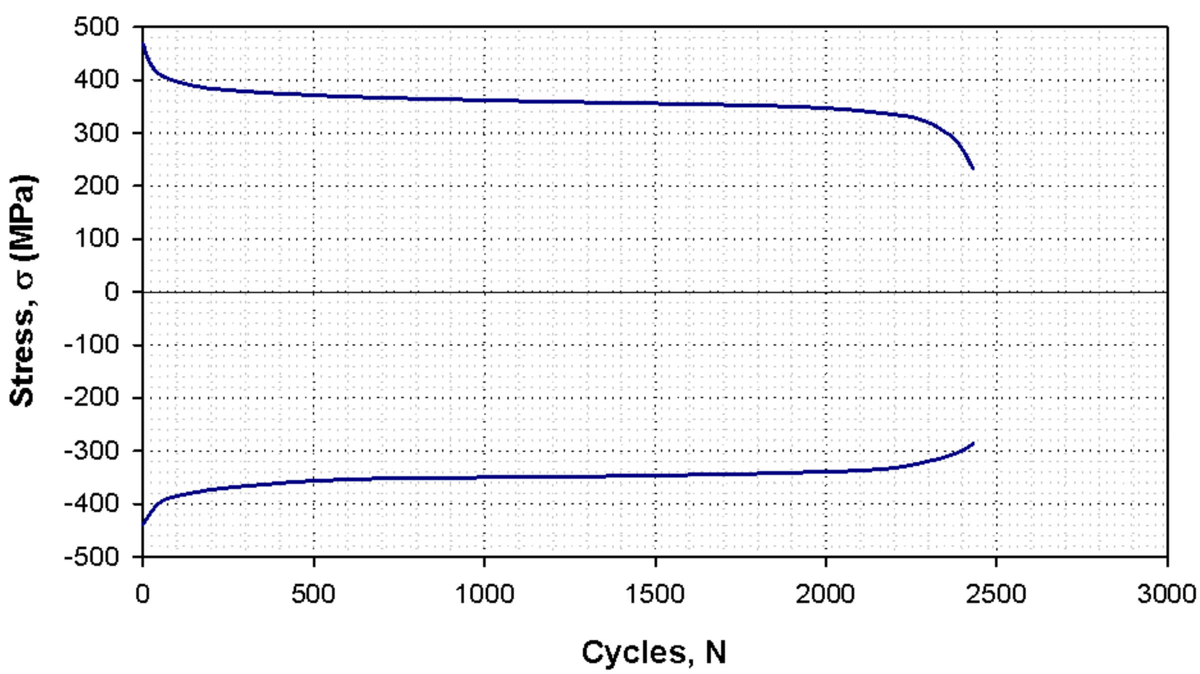

Specimen K004

LCF

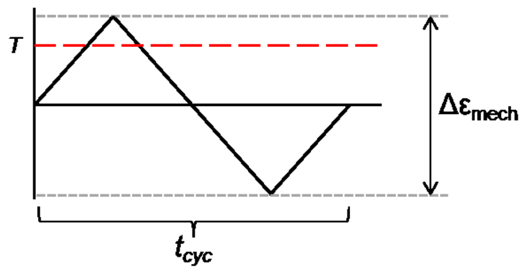

T_{max} (°C):	200	$\Delta\varepsilon_{mech}$:(%)	1.4
T_{min} (°C):	200	K_t:	1.0
t_{cyc} (s):	20	t_{hold} (s):	0

Initial	Stable
σ_{max} (MPa): 328	σ_{max} (MPa): 265
σ_{min} (MPa): -317	σ_{min} (MPa): -260
$\Delta\varepsilon'_{pl}$ (%): 0.58	$\Delta\varepsilon'_{pl}$ (%): 0.66

Hysteretic Response:

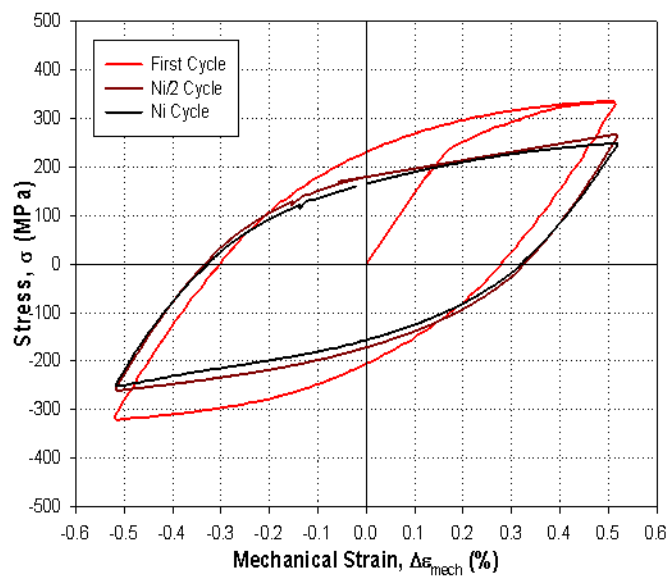

Cycles to Initiation: 4624

Stress History:

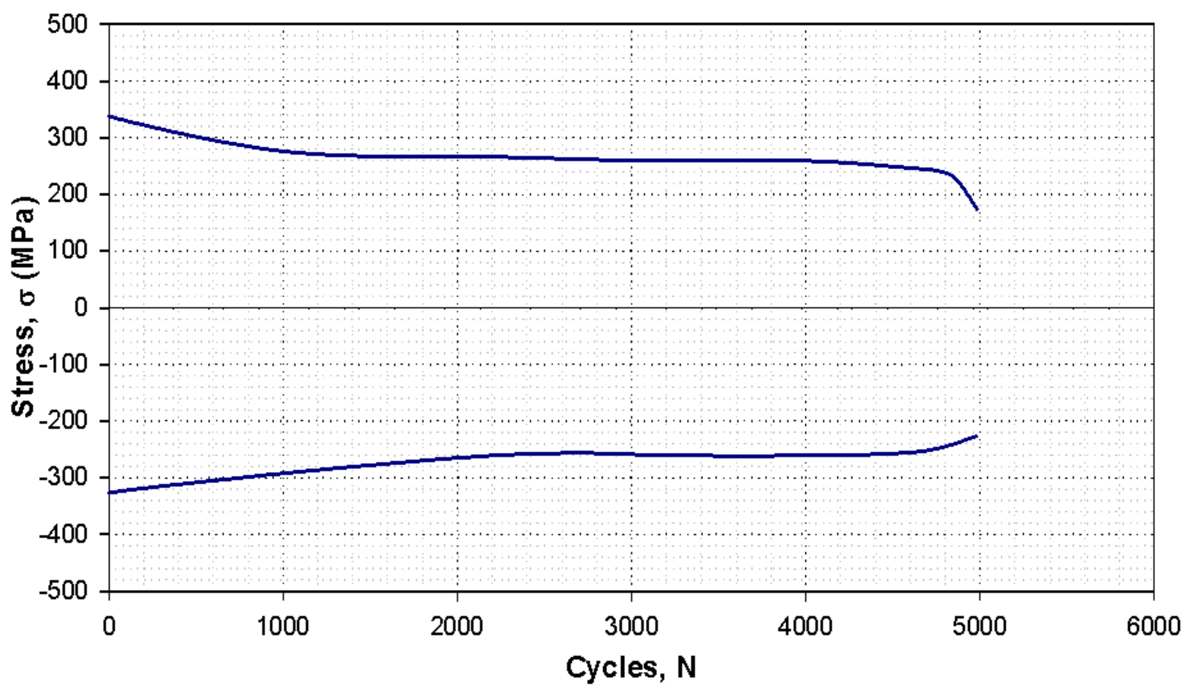

Specimen K021

LCF

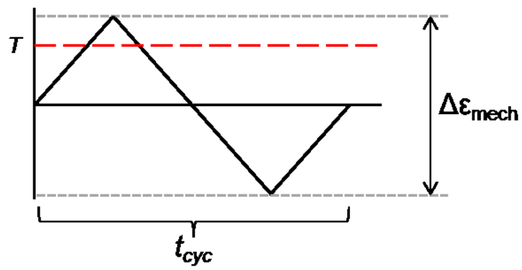

T_{max} (°C):	200	$\Delta\varepsilon_{mech}$:(%)	0.7
T_{min} (°C):	200	K_t:	1.0
t_{cyc} (s):	14	t_{hold} (s):	0

Initial		Stable	
σ_{max} (MPa):	324	σ_{max} (MPa):	254
σ_{min} (MPa):	-287	σ_{min} (MPa):	-250
$\Delta\varepsilon'_{pl}$ (%):	0.37	$\Delta\varepsilon'_{pl}$ (%):	0.37

Hysteretic Response:

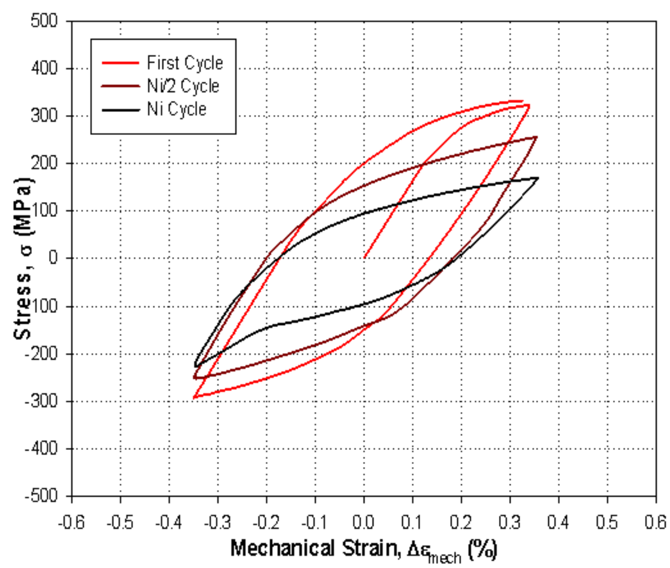

Cycles to Initiation: 7607

Stress History:

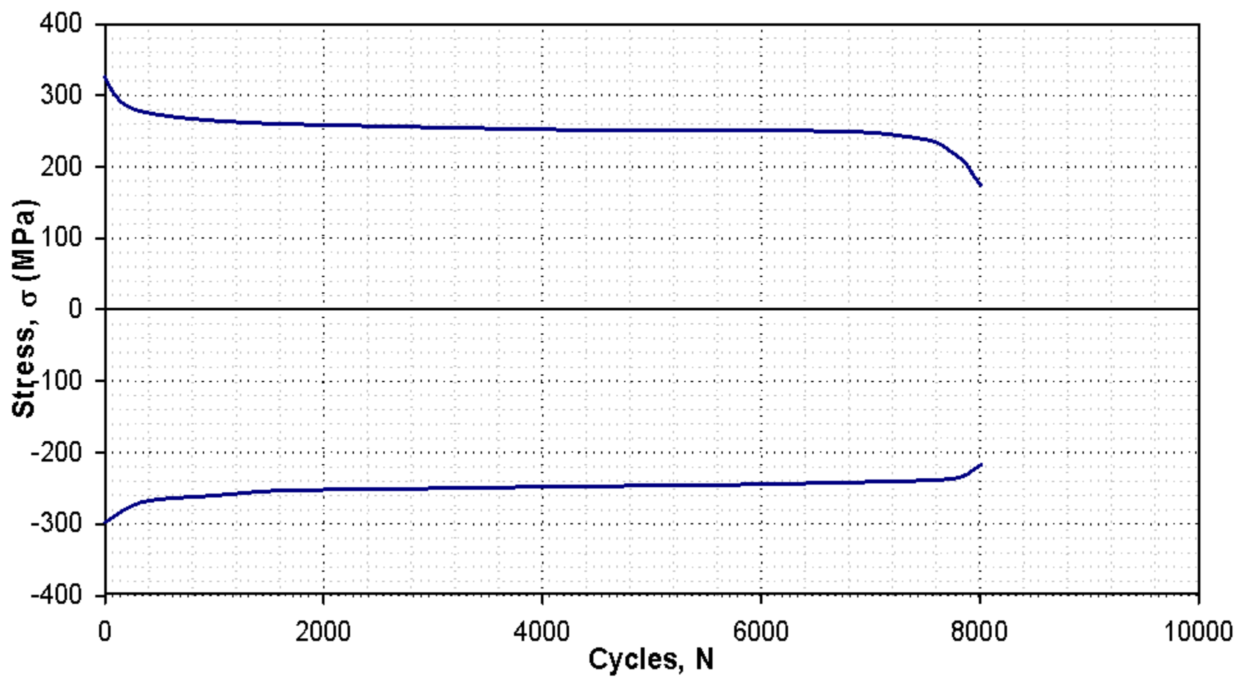

Specimen K014

LCF

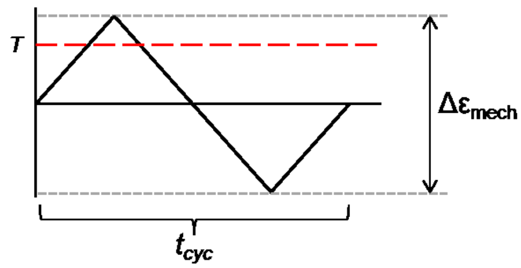

T_{max} (°C):	600	$\Delta\varepsilon_{mech}$:(%)	1.0
T_{min} (°C):	600	K_t:	1.73
t_{cyc} (s):	20	t_{hold} (s):	0

Initial	Stable
σ_{max} (MPa): 227	σ_{max} (MPa): 262
σ_{min} (MPa): -292	σ_{min} (MPa): -266
$\Delta\varepsilon'_{pl}$ (%): 0.19	$\Delta\varepsilon'_{pl}$ (%): 0.29

Hysteretic Response:

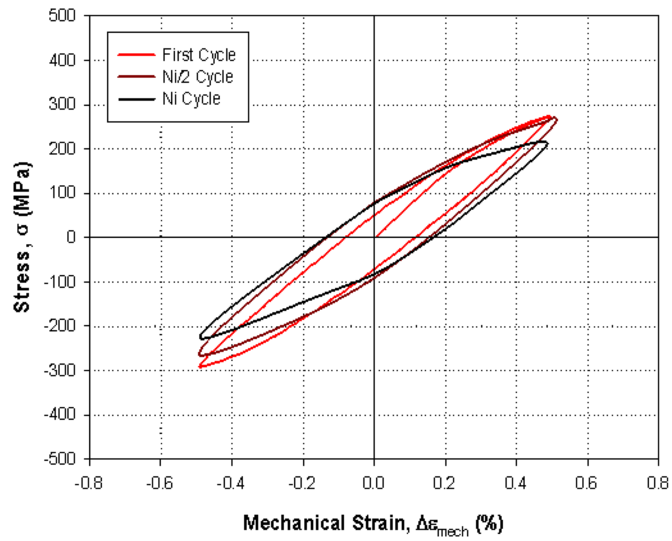

Cycles to Initiation: 489

Stress History:

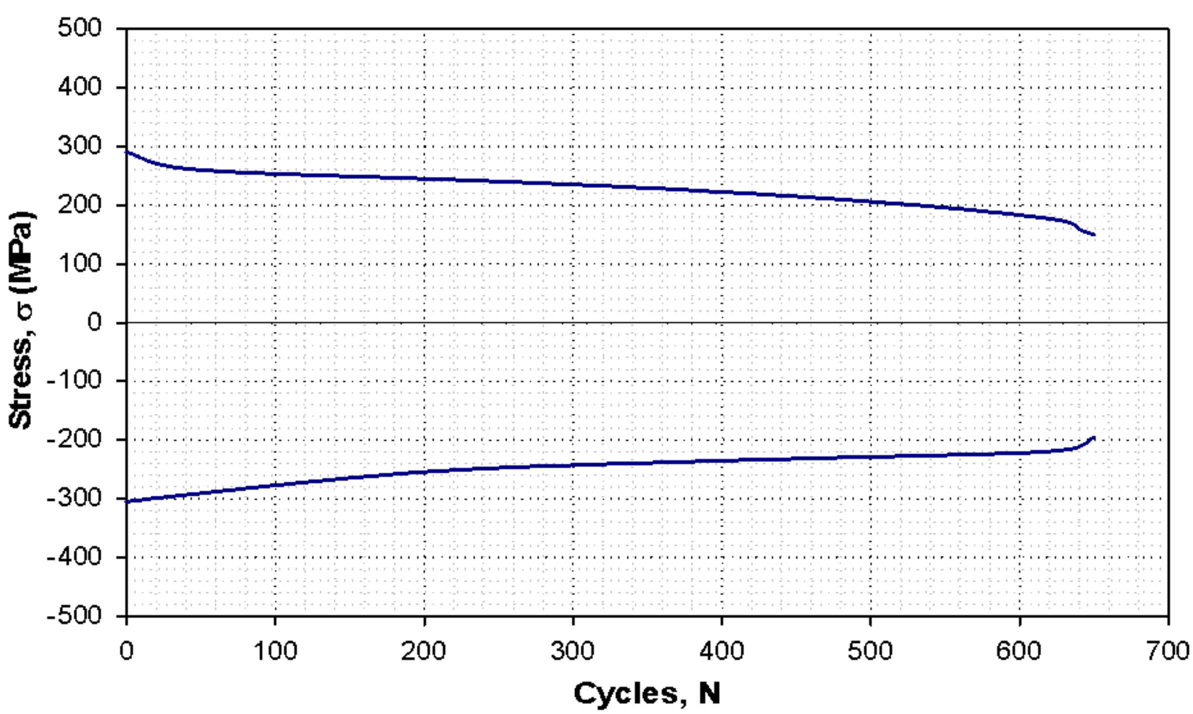

Specimen K012

LCF

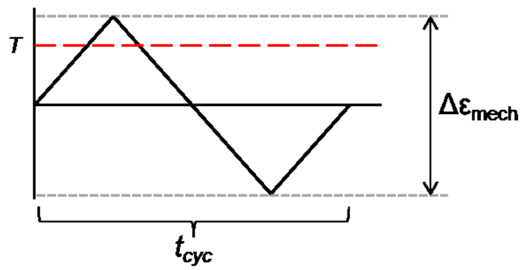

T_{max} (°C):	600	$\Delta\varepsilon_{mech}$:(%)	1.0
T_{min} (°C):	600	K_t:	3.0
t_{cyc} (s):	20	t_{hold} (s):	0

Initial		Stable	
σ_{max} (MPa):	243	σ_{max} (MPa):	212
σ_{min} (MPa):	-203	σ_{min} (MPa):	-183
$\Delta\varepsilon'_{pl}$ (%):	0.19	$\Delta\varepsilon'_{pl}$ (%):	0.22

Hysteretic Response:

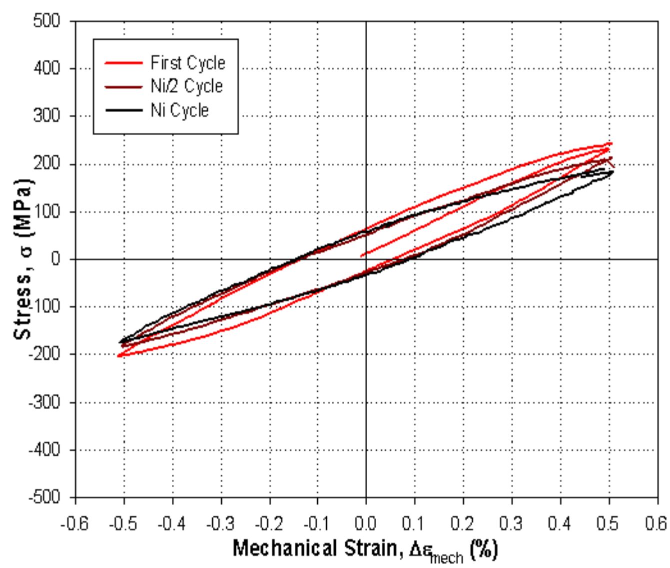

Cycles to Initiation: 421

Stress History:

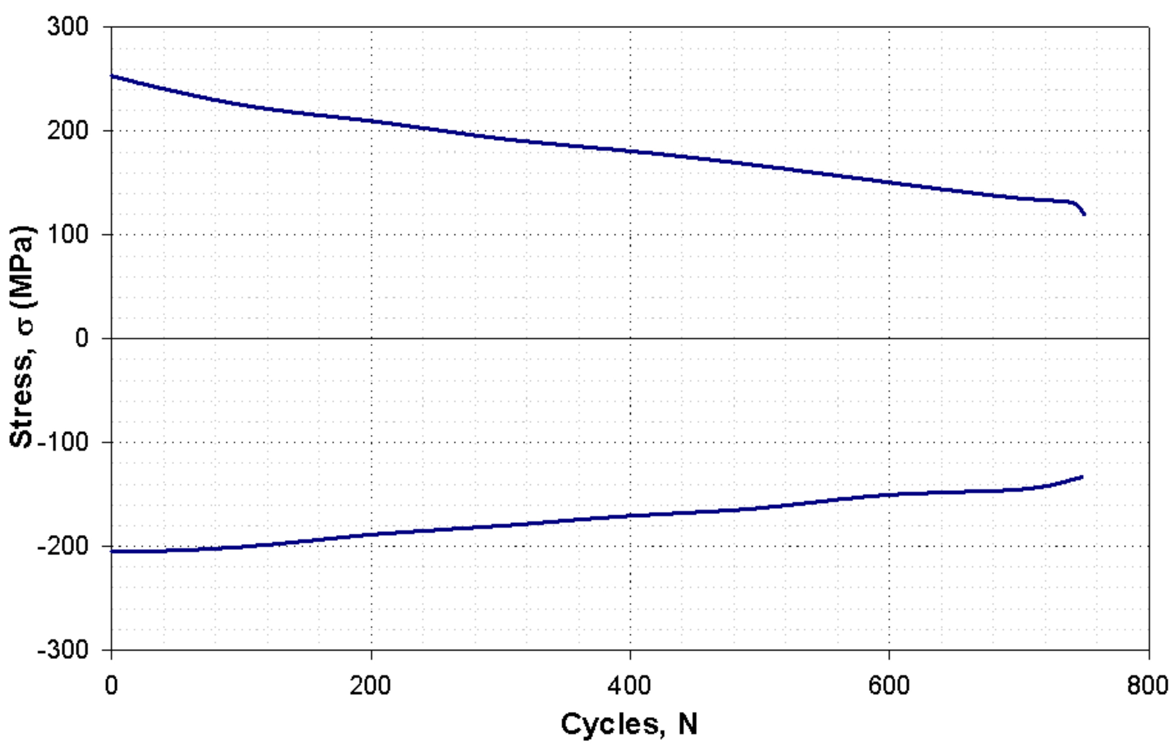

Specimen K024

LCF

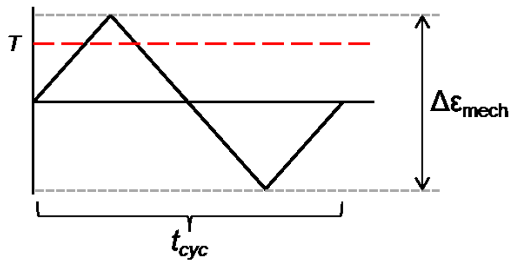

T_{max} (°C):	600	$\Delta\varepsilon_{mech}$:(%)	0.7
T_{min} (°C):	600	K_t:	3.0
t_{cyc} (s):	14	t_{hold} (s):	0

Initial	Stable
σ_{max} (MPa): 192	σ_{max} (MPa): 181
σ_{min} (MPa): -191	σ_{min} (MPa): -172
$\Delta\varepsilon'_{pl}$ (%): 0.07	$\Delta\varepsilon'_{pl}$ (%): 0.10

Hysteretic Response:

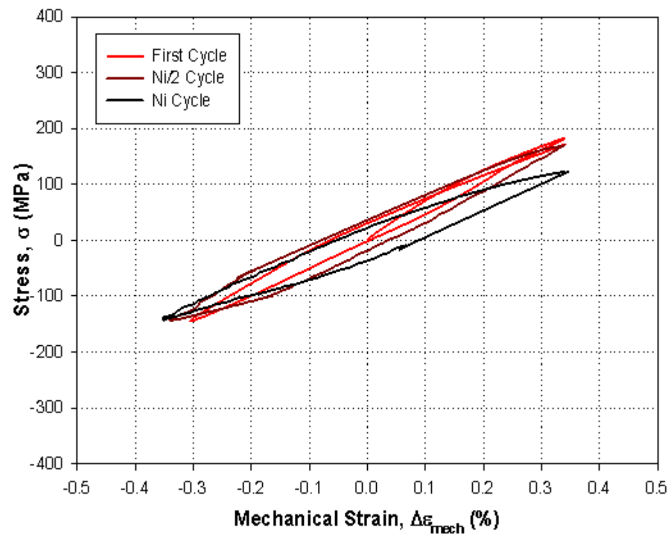

Cycles to Initiation: 945

Stress History:

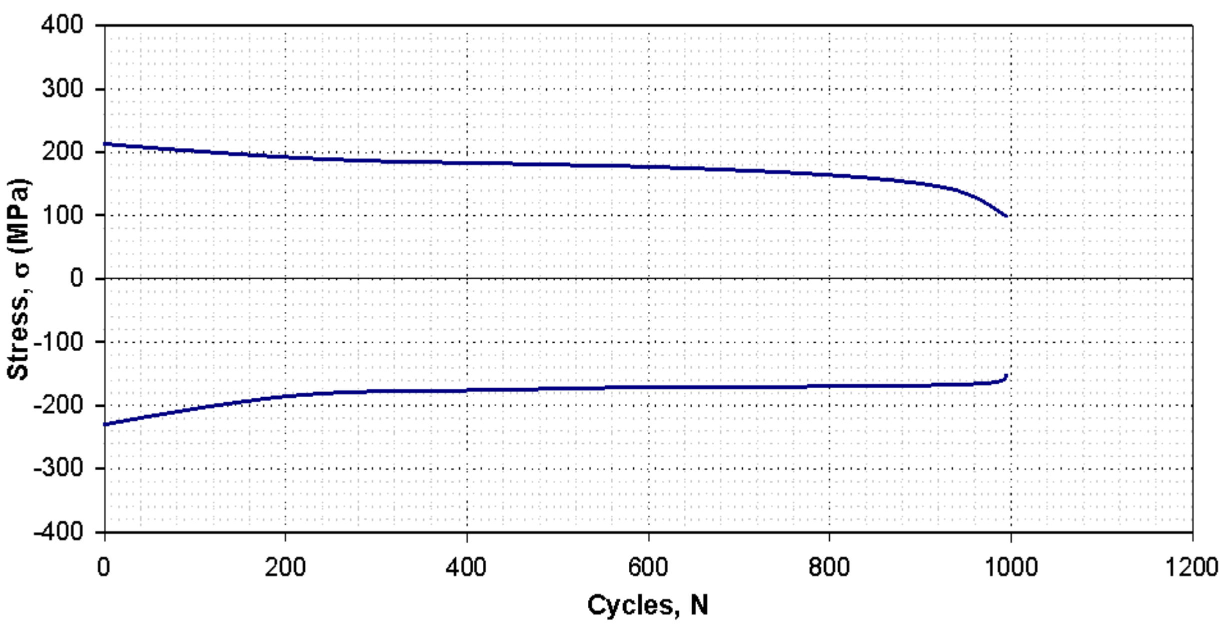

Specimen K013

LCF

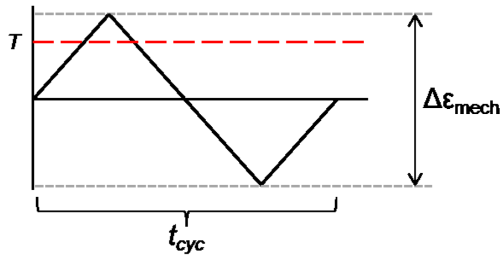

T_{max} (°C):	200	$\Delta\varepsilon_{mech}$:(%)	1.0
T_{min} (°C):	200	K_t:	1.73
t_{cyc} (s):	20	t_{hold} (s):	0

Initial		Stable	
σ_{max} (MPa):	353	σ_{max} (MPa):	311
σ_{min} (MPa):	-418	σ_{min} (MPa):	-365
$\Delta\varepsilon'_{pl}$ (%):	0.11	$\Delta\varepsilon'_{pl}$ (%):	0.12

Hysteretic Response:

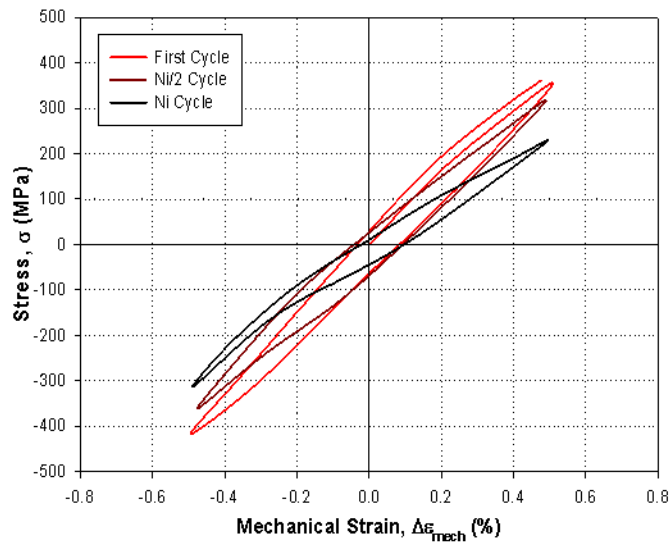

Cycles to Initiation: 3428

Stress History:

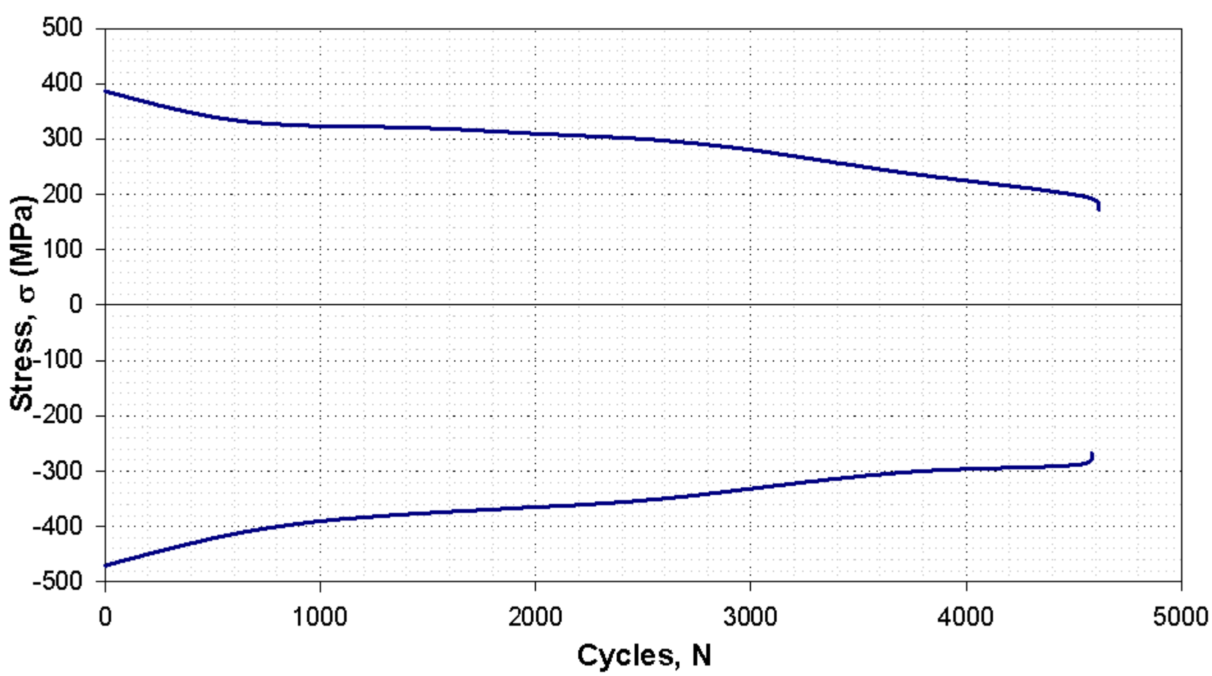

Specimen K011

LCF

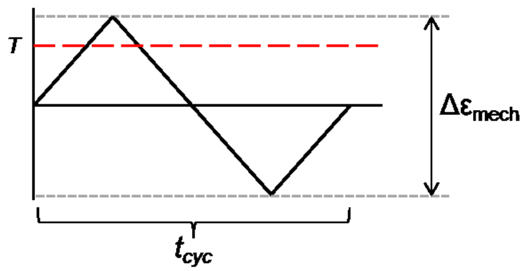

T_{max} (°C):	200	$\Delta\varepsilon_{mech}$:(%)	1.0
T_{min} (°C):	200	K_t:	3.0
t_{cyc} (s):	20	t_{hold} (s):	0

Initial	Stable
σ_{max} (MPa): 334	σ_{max} (MPa): 246
σ_{min} (MPa): -250	σ_{min} (MPa): -240
$\Delta\varepsilon'_{pl}$ (%): 0.14	$\Delta\varepsilon'_{pl}$ (%): 0.13

Hysteretic Response:

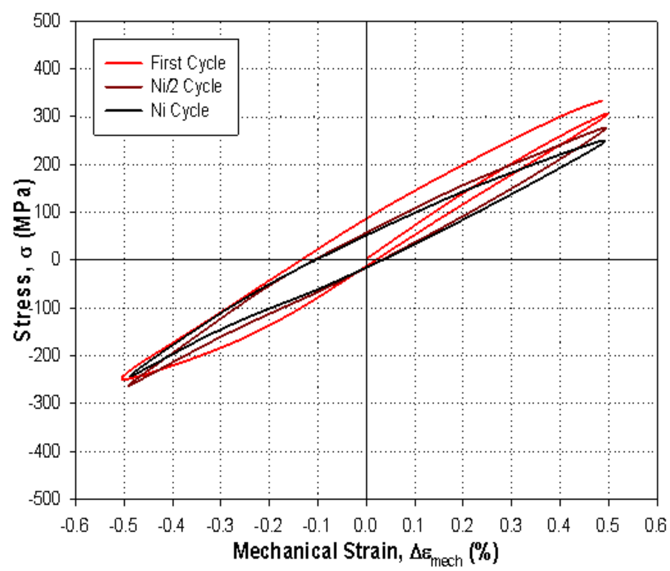

Cycles to Initiation: 2576

Stress History:

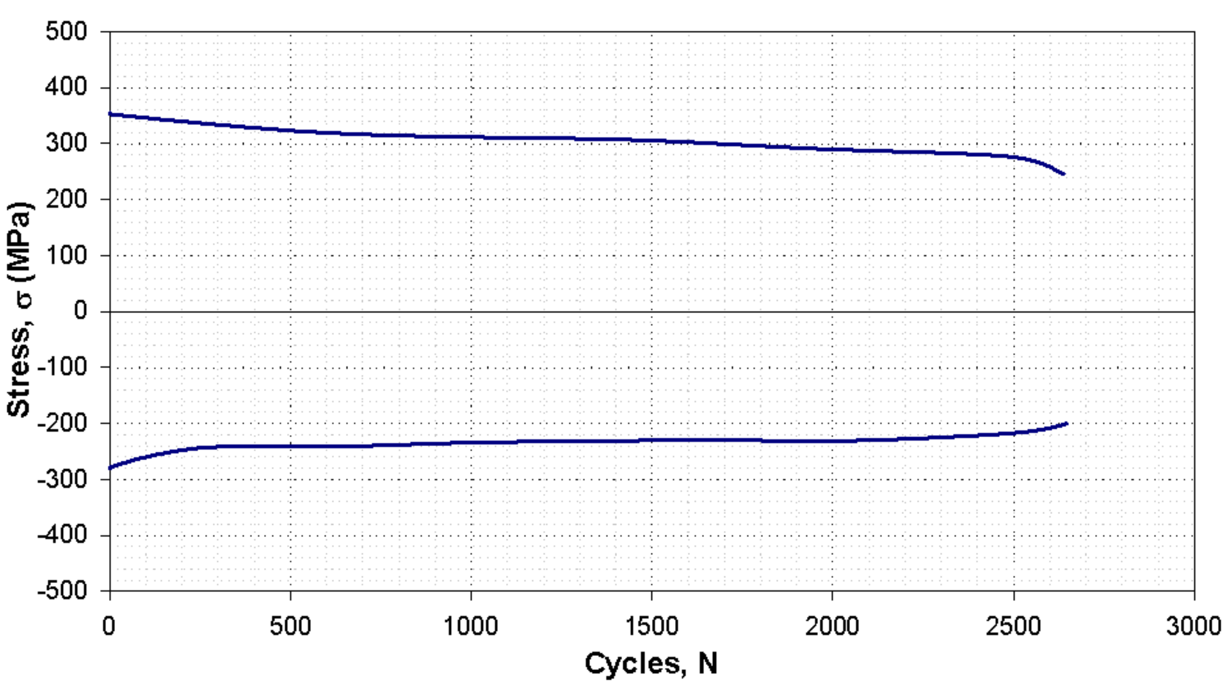

Specimen K023

LCF

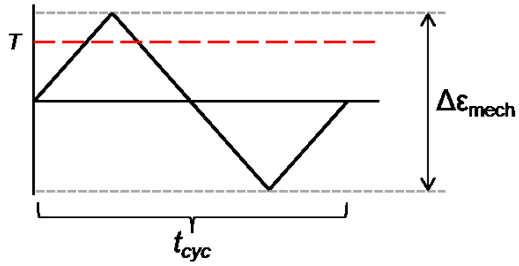

T_{max} (°C):	200	$\Delta\varepsilon_{mech}$:(%)	0.7
T_{min} (°C):	200	K_t:	3.0
t_{cyc} (s):	14	t_{hold} (s):	0

Initial	Stable
σ_{max} (MPa): 269	σ_{max} (MPa): 225
σ_{min} (MPa): -257	σ_{min} (MPa): -220
$\Delta\varepsilon'_{pl}$ (%): 0.23	$\Delta\varepsilon'_{pl}$ (%): 0.27

Hysteretic Response:

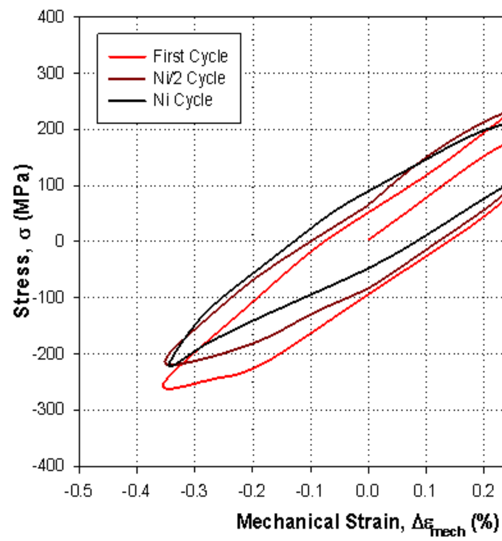

Cycles to Initiation: 4580

Stress History:

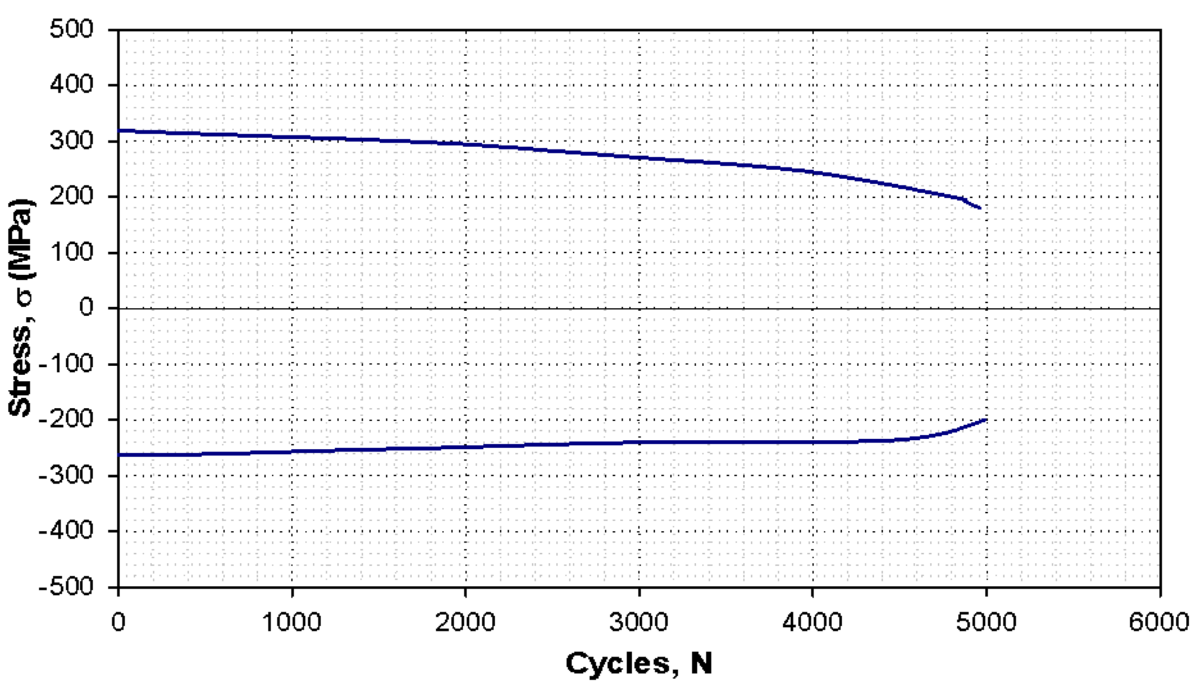

APPENDIX B: CREEP-FATIGUE DATA

Specimen K002

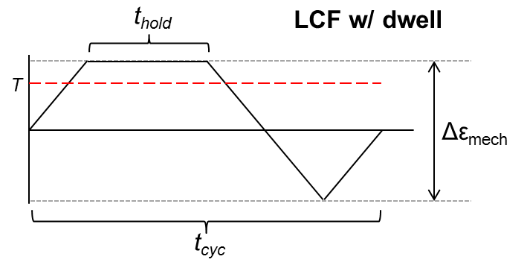

T_{max} (°C):	600	$\Delta\varepsilon_{mech}$:(%)	1.4
T_{min} (°C):	600	K_t:	1.0
t_{cyc} (s):	88	t_{hold} (s):	60

Initial		Stable	
σ_{max} (MPa):	341	σ_{max} (MPa):	312
σ_{min} (MPa):	-337	σ_{min} (MPa):	-301
σ_{relax} (MPa):	46	σ_{relax} (MPa):	42
$\Delta\varepsilon'_{pl}$ (%):	0.96	$\Delta\varepsilon'_{pl}$ (%):	1.03

Hysteretic Response:

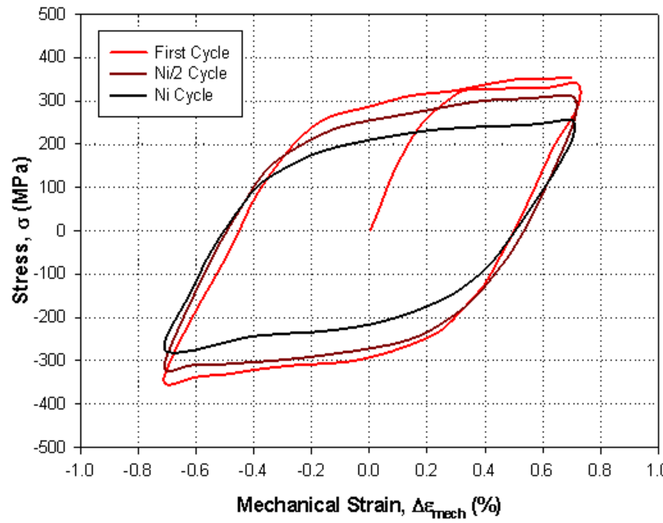

Cycles to Initiation: 338

Stress History:

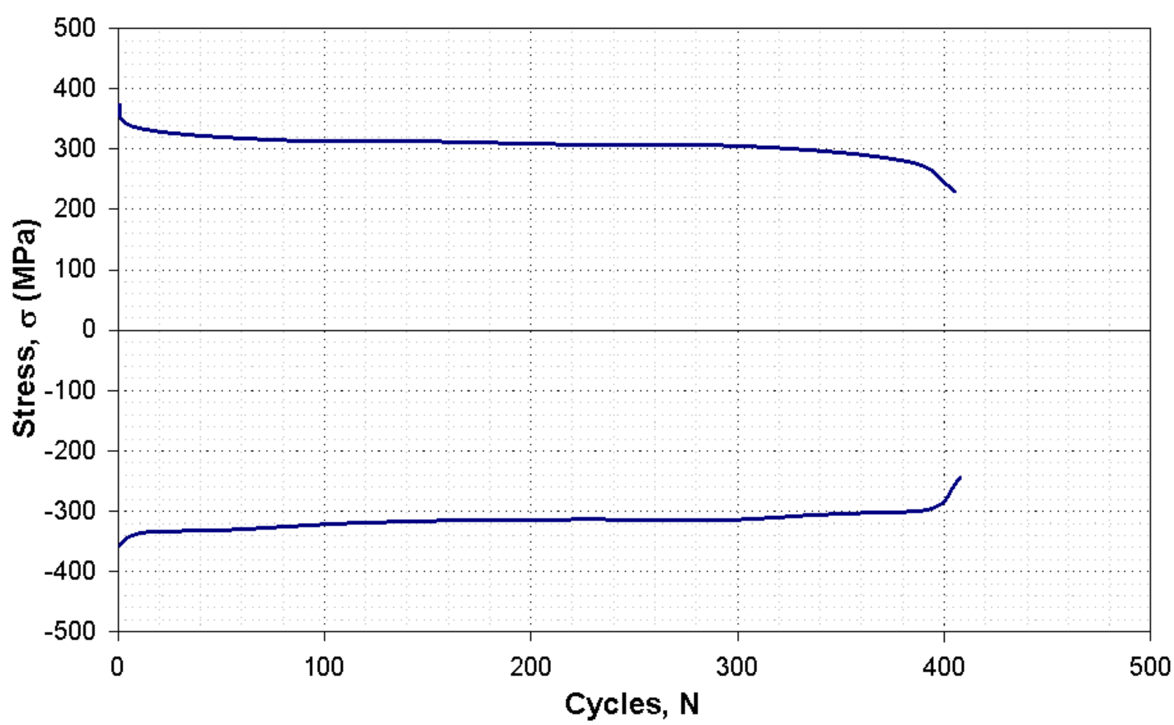

Specimen K006

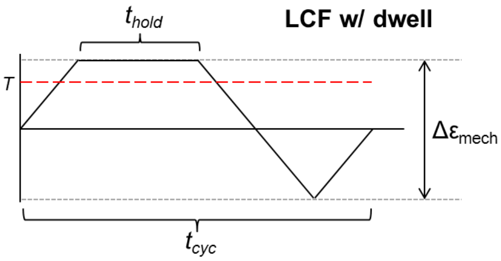

T_{max} (°C):	600	$\Delta\varepsilon_{mech}$:(%)	1.0
T_{min} (°C):	600	K_t:	1.0
t_{cyc} (s):	80	t_{hold} (s):	60

Initial		Stable	
σ_{max} (MPa):	213	σ_{max} (MPa):	203
σ_{min} (MPa):	-210	σ_{min} (MPa):	-205
σ_{relax} (MPa):	107	σ_{relax} (MPa):	56
$\Delta\varepsilon'_{pl}$ (%):	0.61	$\Delta\varepsilon'_{pl}$ (%):	0.51

Hysteretic Response:

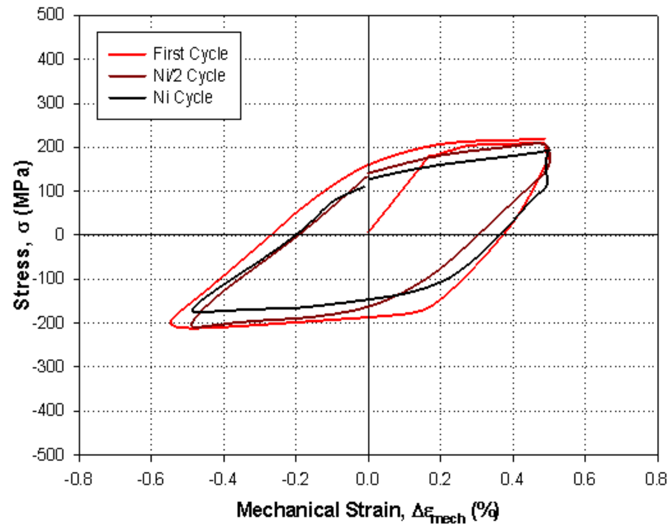

Cycles to Initiation: 410

Stress History:

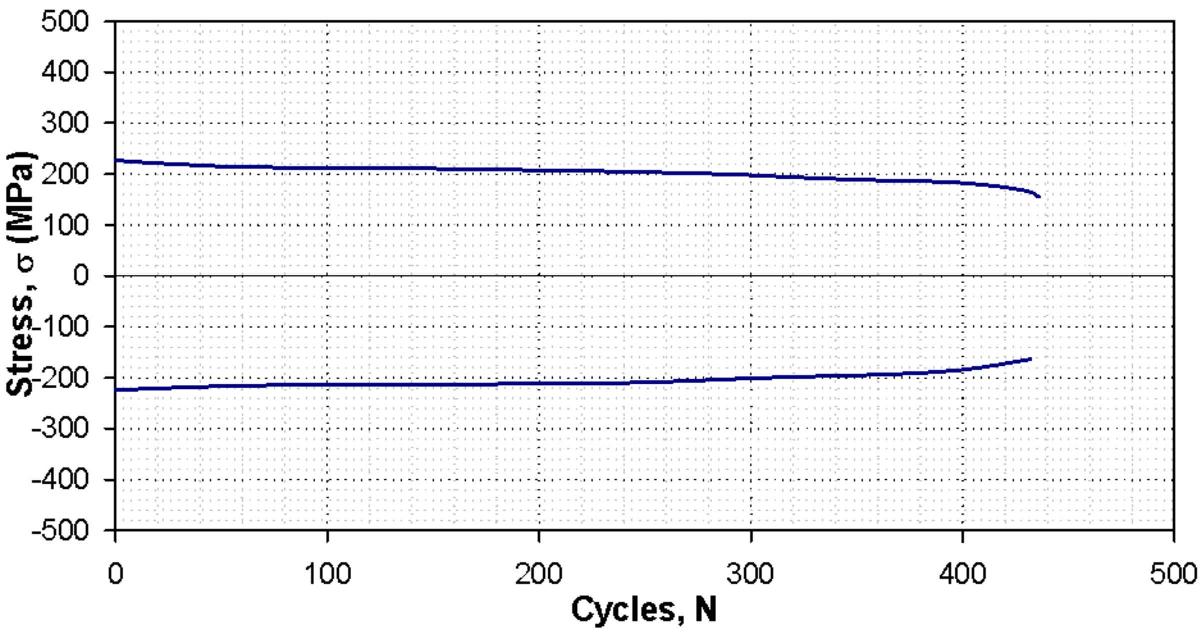

Specimen K019

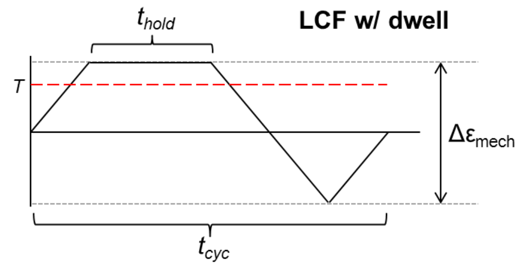

T_{max} (°C):	600	$\Delta\varepsilon_{mech}$:(%)	1.0
T_{min} (°C):	600	K_t:	3.0
t_{cyc} (s):	80	t_{hold} (s):	60

Initial	Stable
σ_{max} (MPa): 368	σ_{max} (MPa): 306
σ_{min} (MPa): -254	σ_{min} (MPa): -245
σ_{relax} (MPa): 135	σ_{relax} (MPa): 104
$\Delta\varepsilon'_{pl}$ (%): 0.32	$\Delta\varepsilon'_{pl}$ (%): 0.31

Hysteretic Response:

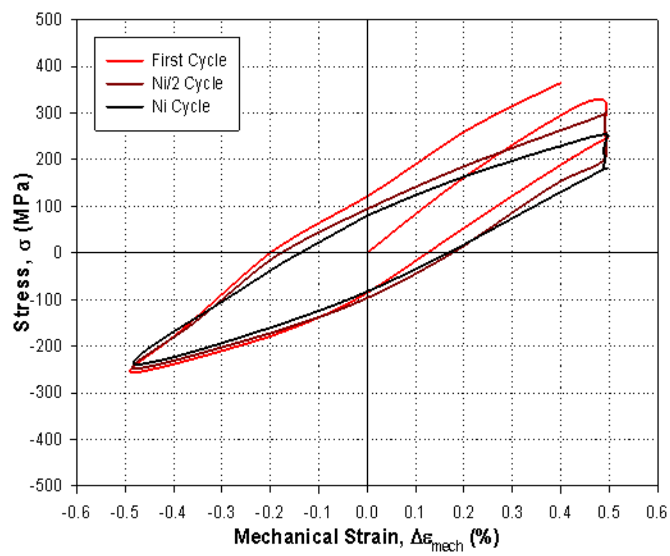

Cycles to Initiation: 580

Stress History:

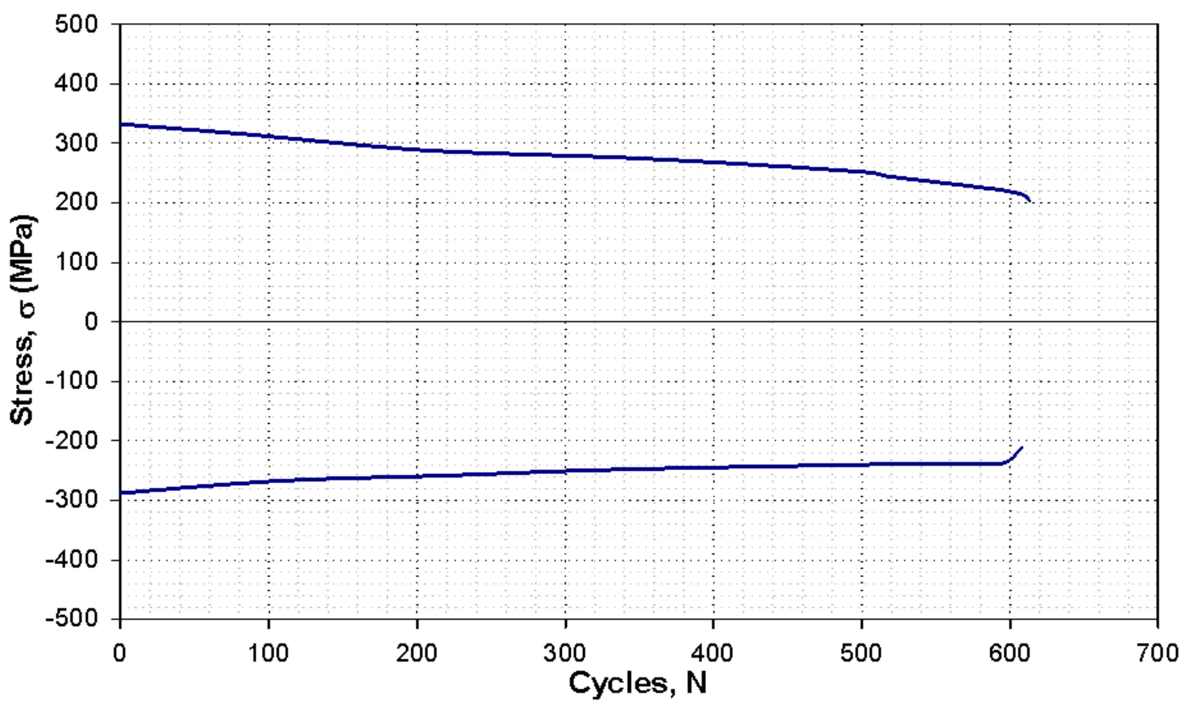

Specimen K010

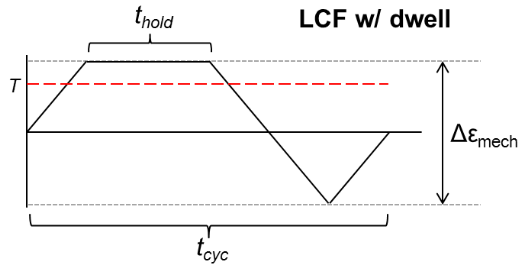

T_{max} (°C):	200	$\Delta\varepsilon_{mech}$:(%)	1.0
T_{min} (°C):	200	K_t:	1.0
t_{cyc} (s):	80	t_{hold} (s):	60

Initial		Stable	
σ_{max} (MPa):	435	σ_{max} (MPa):	327
σ_{min} (MPa):	-420	σ_{min} (MPa):	-338
σ_{relax} (MPa):	18	σ_{relax} (MPa):	9
$\Delta\varepsilon'_{pl}$ (%):	0.45	$\Delta\varepsilon'_{pl}$ (%):	0.57

Hysteretic Response:

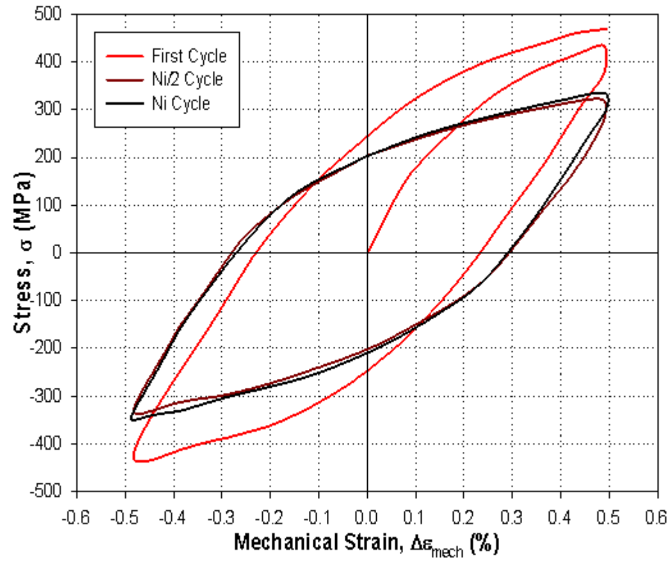

Cycles to Initiation: 4151

Stress History:

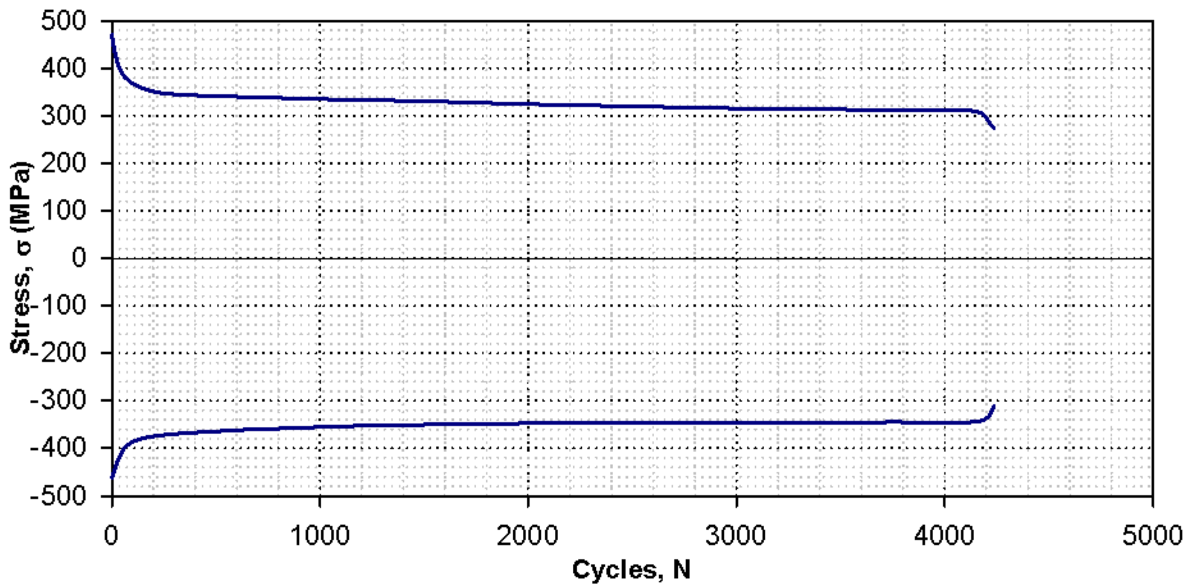

Specimen K001

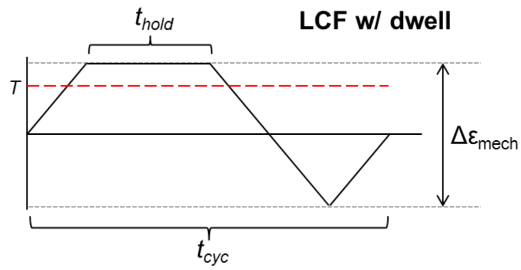

T_{max} (°C):	200	$\Delta\varepsilon_{mech}$:(%)	1.4
T_{min} (°C):	200	K_t:	1.0
t_{cyc} (s):	88	t_{hold} (s):	60

Initial		Stable	
σ_{max} (MPa):	456	σ_{max} (MPa):	353
σ_{min} (MPa):	-435	σ_{min} (MPa):	-362
σ_{relax} (MPa):	80	σ_{relax} (MPa):	57
$\Delta\varepsilon'_{pl}$ (%):	0.83	$\Delta\varepsilon'_{pl}$ (%):	0.93

Hysteretic Response:

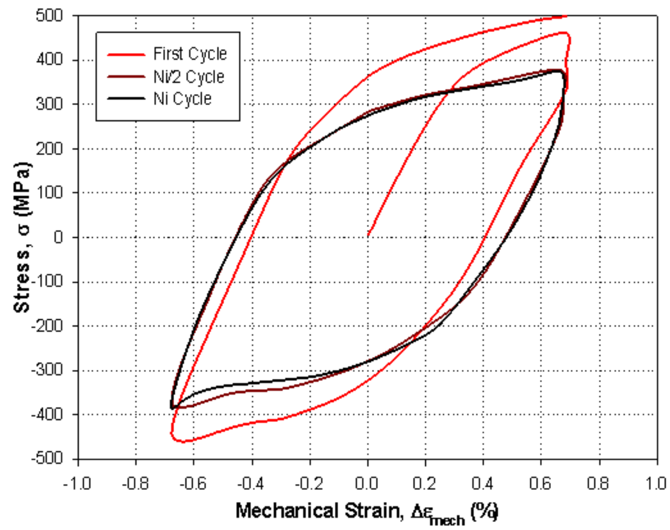

Cycles to Initiation: 1075

Stress History:

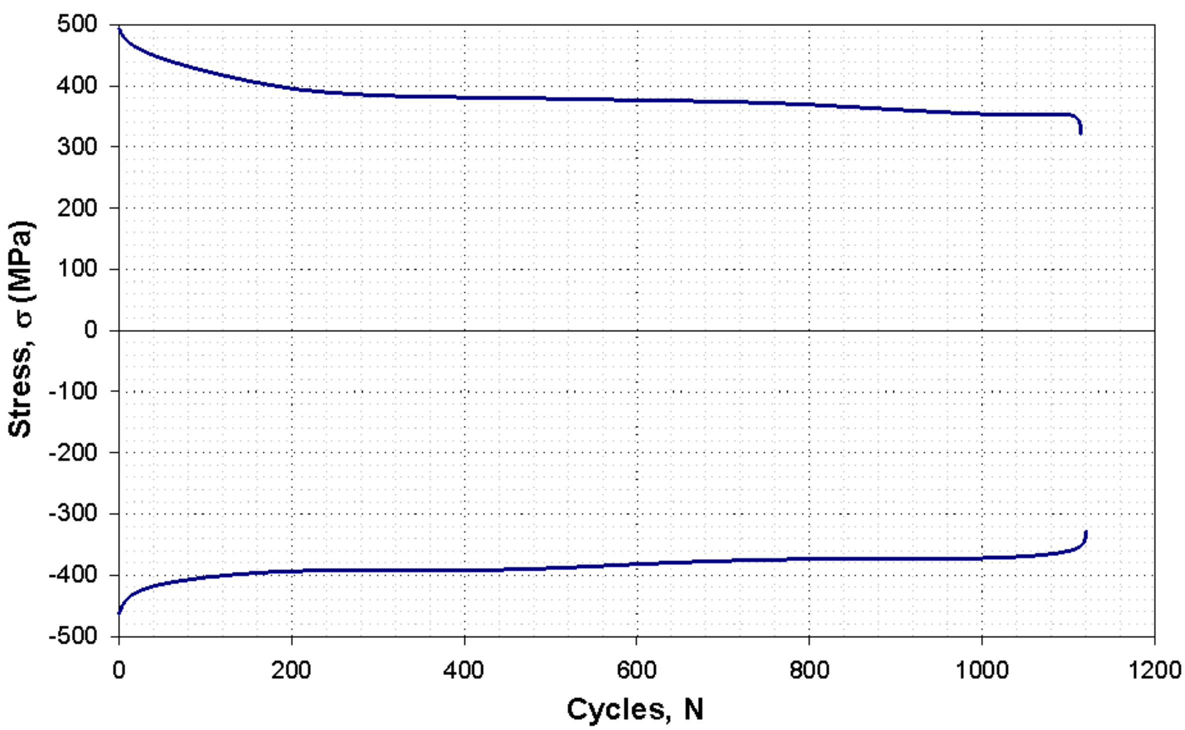

APPENDIX C: THERMOMECHANICAL FATIGUE TEST DATA

Results from all geometry types under 200°C/600°C (473°K/873°K) IPTMF:

Results from all geometry types under 200°C/600°C (473°K/873°K) OPTMF:

Results from all geometry types under 200°C/600°C (473°K/873°K) IPTMF with 60s tensile dwell:

Specimen K003

IPTMF

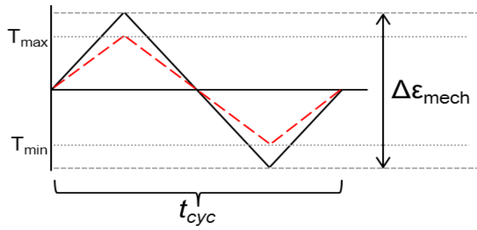

T_{max} (°C):	600	$\Delta\varepsilon_{mech}$:(%)	1.4
T_{min} (°C):	200	K_t:	1.0
t_{cyc} (s):	240	t_{hold} (s):	0

Initial		Stable	
$\boldsymbol{\sigma}_{\mathbf{max}}$ (MPa):	311	$\boldsymbol{\sigma}_{\mathbf{max}}$ (MPa):	292
$\boldsymbol{\sigma}_{\mathbf{min}}$ (MPa):	-422	$\boldsymbol{\sigma}_{\mathbf{min}}$ (MPa):	-385
$\boldsymbol{\Delta\varepsilon'}_{\mathbf{pl}}$ (%):	0.95	$\boldsymbol{\Delta\varepsilon'}_{\mathbf{pl}}$ (%):	0.90

Hysteretic Response:

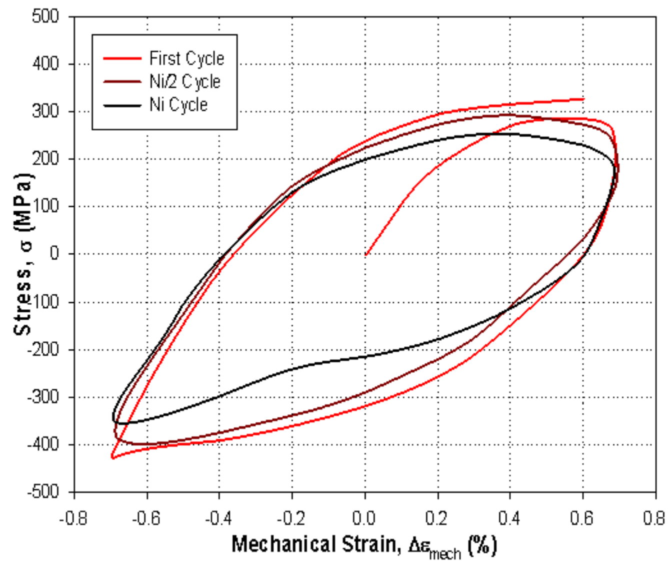

Cycles to Initiation: 74

Stress History:

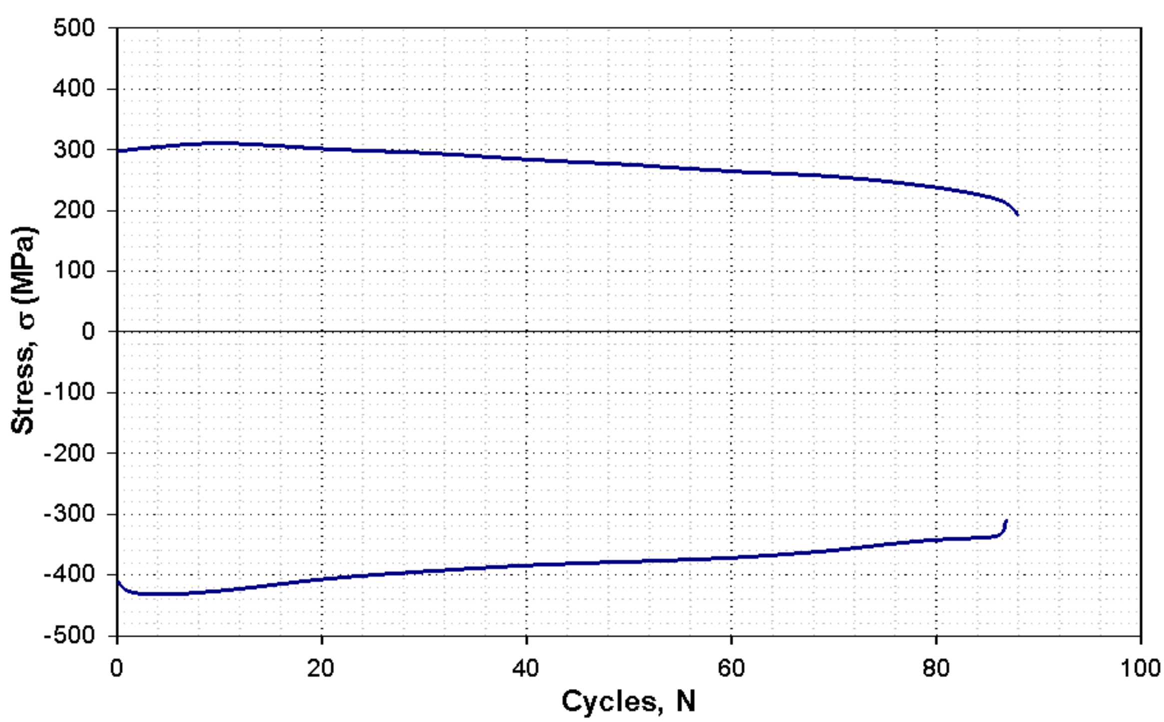

Specimen K016

IPTMF

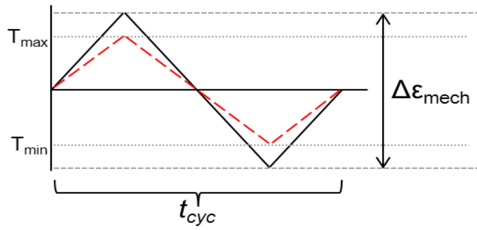

T_{max} (°C):	600	$\Delta\varepsilon_{mech}$:(%)	1.0
T_{min} (°C):	200	K_t:	3.0
t_{cyc} (s):	240	t_{hold} (s):	0

Initial	Stable
$\boldsymbol{\sigma}_{\mathbf{max}}$ (MPa): 222	$\boldsymbol{\sigma}_{\mathbf{max}}$ (MPa): 185
$\boldsymbol{\sigma}_{\mathbf{min}}$ (MPa): -310	$\boldsymbol{\sigma}_{\mathbf{min}}$ (MPa): -303
$\boldsymbol{\Delta\varepsilon'}_{\mathbf{pl}}$ (%): 0.08	$\boldsymbol{\Delta\varepsilon'}_{\mathbf{pl}}$ (%): 0.05

Hysteretic Response:

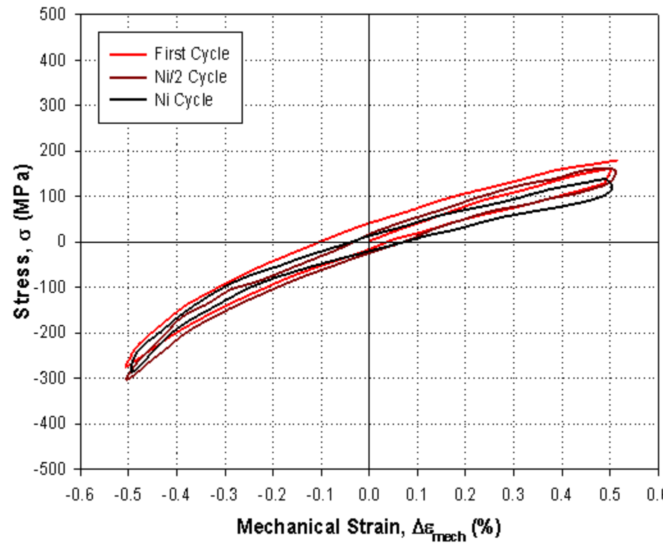

Cycles to Initiation: 694

Stress History:

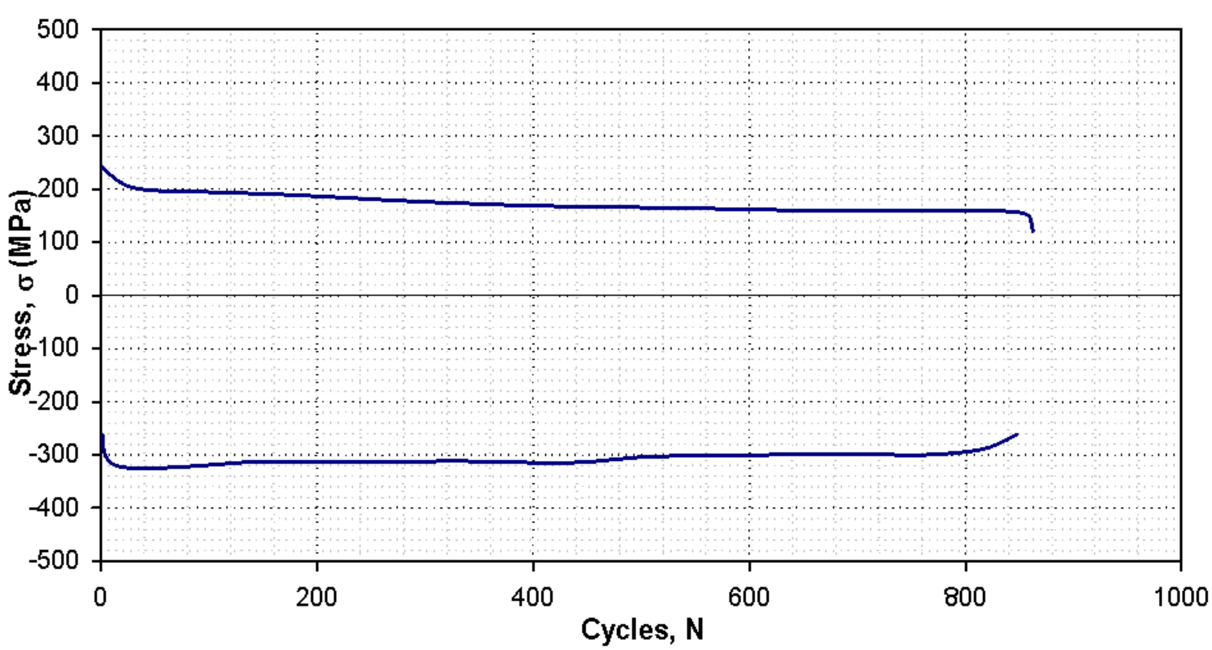

Specimen K007

IPTMF

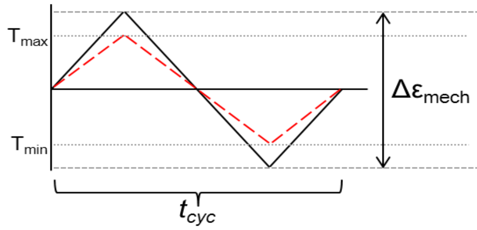

T_{max} (°C):	600	$\Delta\varepsilon_{mech}$:(%)	1.0
T_{min} (°C):	200	K_t:	1.0
t_{cyc} (s):	240	t_{hold} (s):	0

Initial	Stable
$\boldsymbol{\sigma_{max}}$ (MPa): 301	$\boldsymbol{\sigma_{max}}$ (MPa): 268
$\boldsymbol{\sigma_{min}}$ (MPa): -431	$\boldsymbol{\sigma_{min}}$ (MPa): -349
$\boldsymbol{\Delta\varepsilon'_{pl}}$ (%): 0.48	$\boldsymbol{\Delta\varepsilon'_{pl}}$ (%): 0.52

Hysteretic Response:

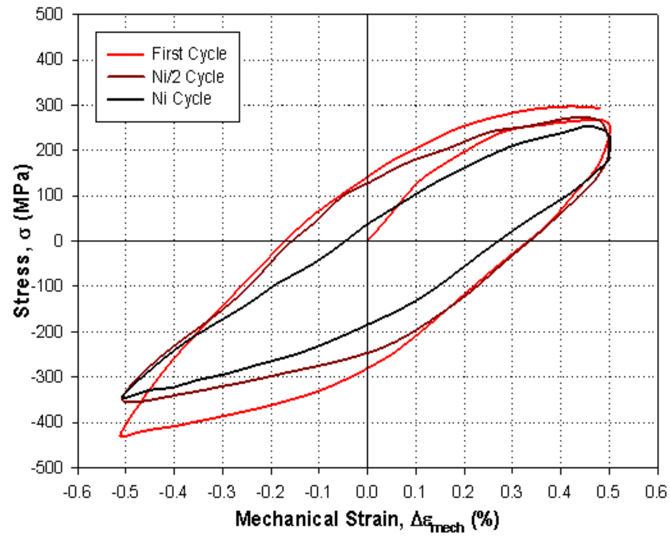

Cycles to Initiation: 840

Stress History:

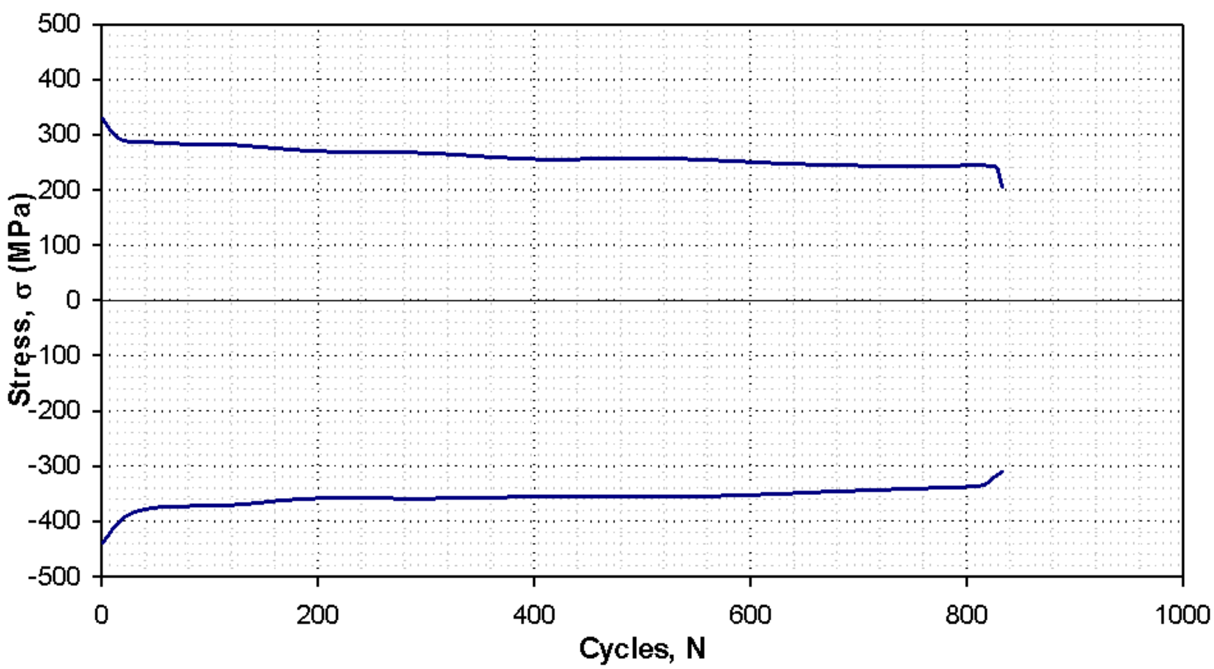

Specimen K025

IPTMF

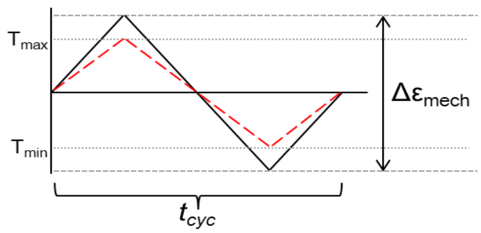

T_{max} (°C):	600	$\Delta\varepsilon_{mech}$:(%)	0.7
T_{min} (°C):	200	K_t:	1.0
t_{cyc} (s):	240	t_{hold} (s):	0

Initial	Stable
$\boldsymbol{\sigma_{max}}$ (MPa): 231	$\boldsymbol{\sigma_{max}}$ (MPa): 219
$\boldsymbol{\sigma_{min}}$ (MPa): -316	$\boldsymbol{\sigma_{min}}$ (MPa): -318
$\boldsymbol{\Delta\varepsilon'_{pl}}$ (%): 0.16	$\boldsymbol{\Delta\varepsilon'_{pl}}$ (%): 0.27

Hysteretic Response:

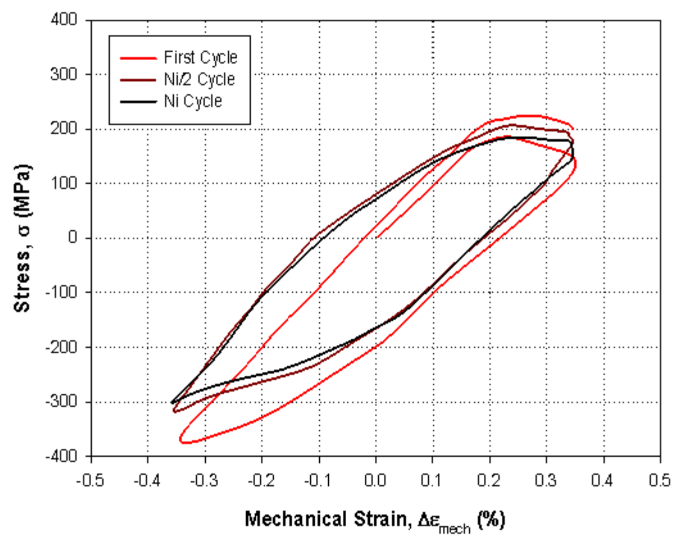

Cycles to Initiation: 1010

Stress History:

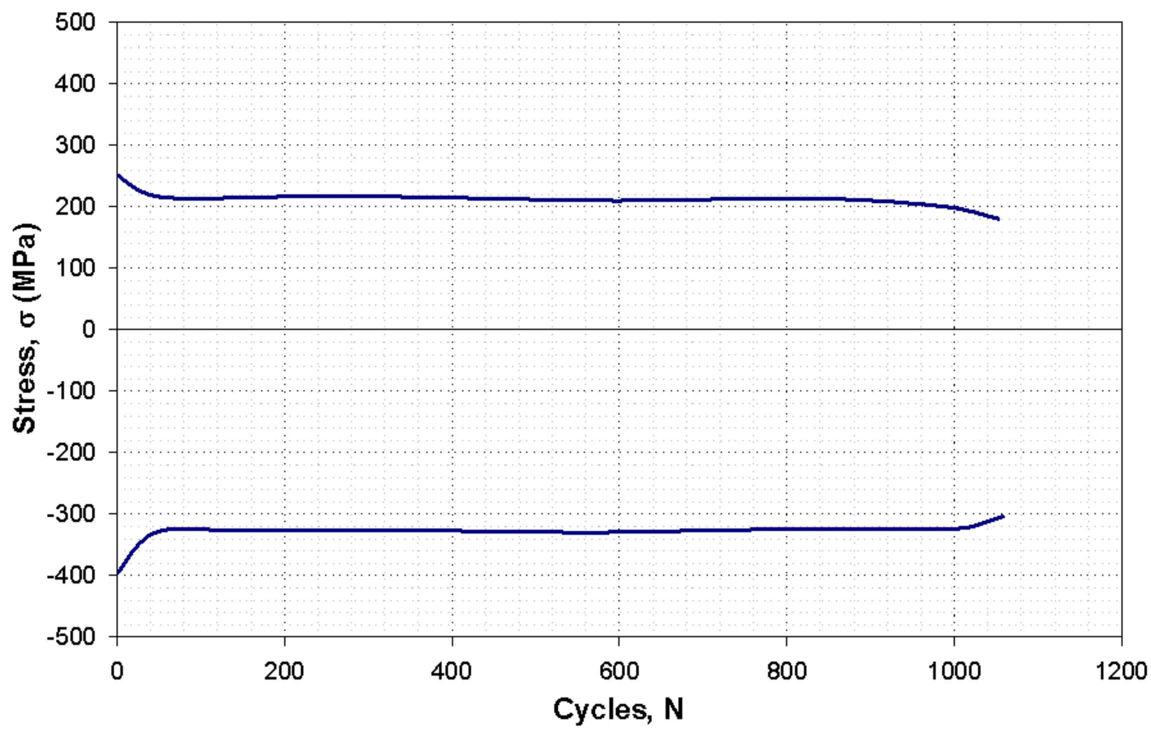

Specimen K11P

OPTMF

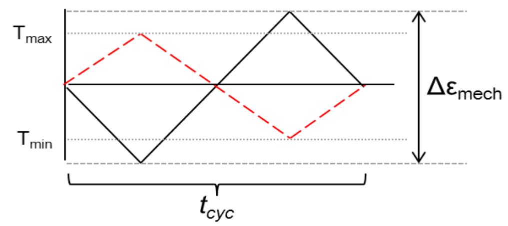

T_{max} (°C):	600	$\Delta\varepsilon_{mech}$:(%)	1.4
T_{min} (°C):	200	K_t:	1.0
t_{cyc} (s):	240	t_{hold} (s):	0

Initial		Stable	
σ_{max} (MPa):	478	σ_{max} (MPa):	449
σ_{min} (MPa):	-305	σ_{min} (MPa):	-318
$\Delta\varepsilon'_{pl}$ (%):	1.02	$\Delta\varepsilon'_{pl}$ (%):	0.97

Hysteretic Response:

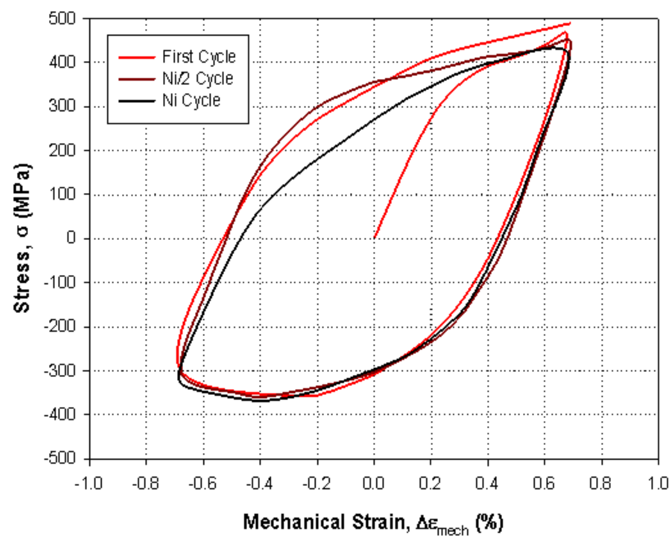

Cycles to Initiation: 23

Stress History:

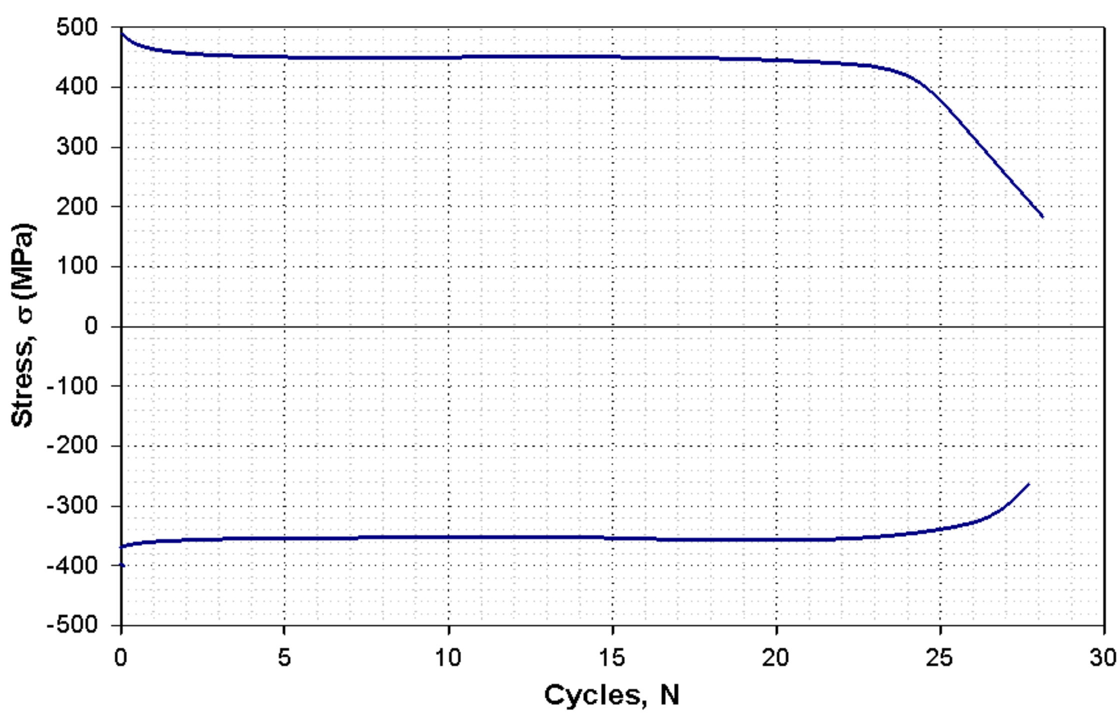

Specimen K008

OPTMF

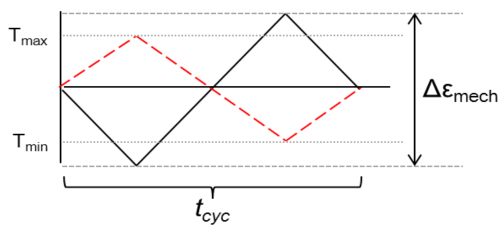

T_{max} (°C):	600	$\Delta\varepsilon_{mech}$:(%)	1.0
T_{min} (°C):	200	K_t:	1.0
t_{cyc} (s):	240	t_{hold} (s):	0

Initial	Stable
σ_{max} (MPa): 480	σ_{max} (MPa): 350
σ_{min} (MPa): -282	σ_{min} (MPa): -285
$\Delta\varepsilon'_{pl}$ (%): 0.48	$\Delta\varepsilon'_{pl}$ (%): 0.54

Hysteretic Response:

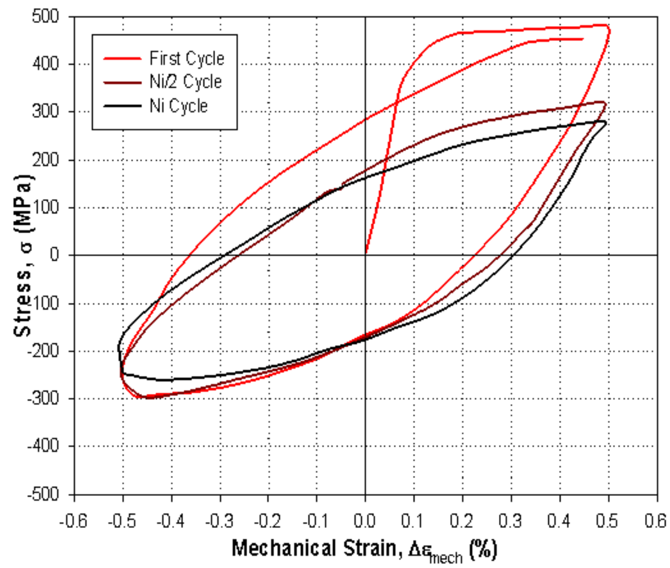

Cycles to Initiation: 822

Stress History:

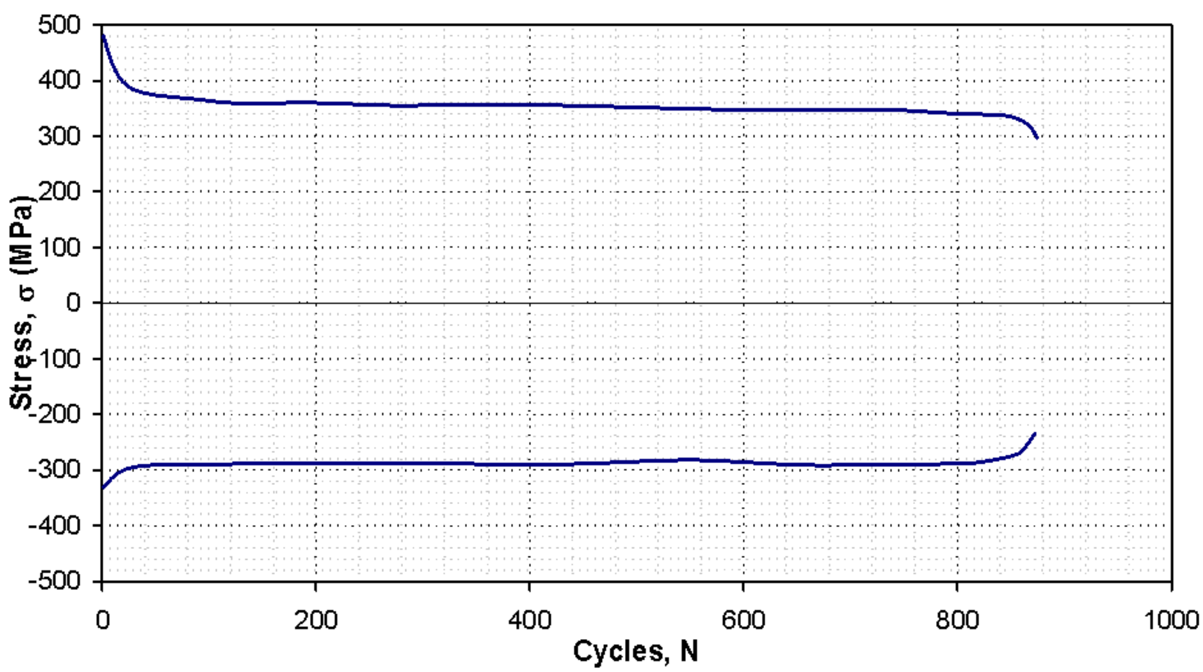

Specimen K017

OPTMF

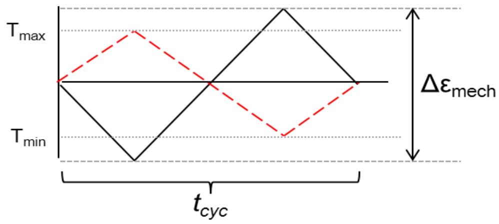

T_{max} (°C):	600	$\Delta\varepsilon_{mech}$:(%)	1.0
T_{min} (°C):	200	K_t:	1.73
t_{cyc} (s):	240	t_{hold} (s):	0

Initial	Stable
σ_{max} (MPa): 490	σ_{max} (MPa): 418
σ_{min} (MPa): -320	σ_{min} (MPa): -300
$\Delta\varepsilon'_{pl}$ (%): 0.37	$\Delta\varepsilon'_{pl}$ (%): 0.33

Hysteretic Response:

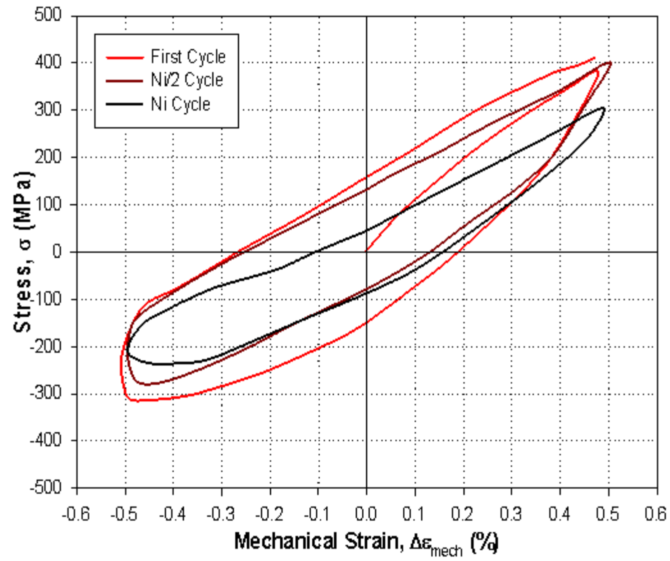

Cycles to Initiation: 566

Stress History:

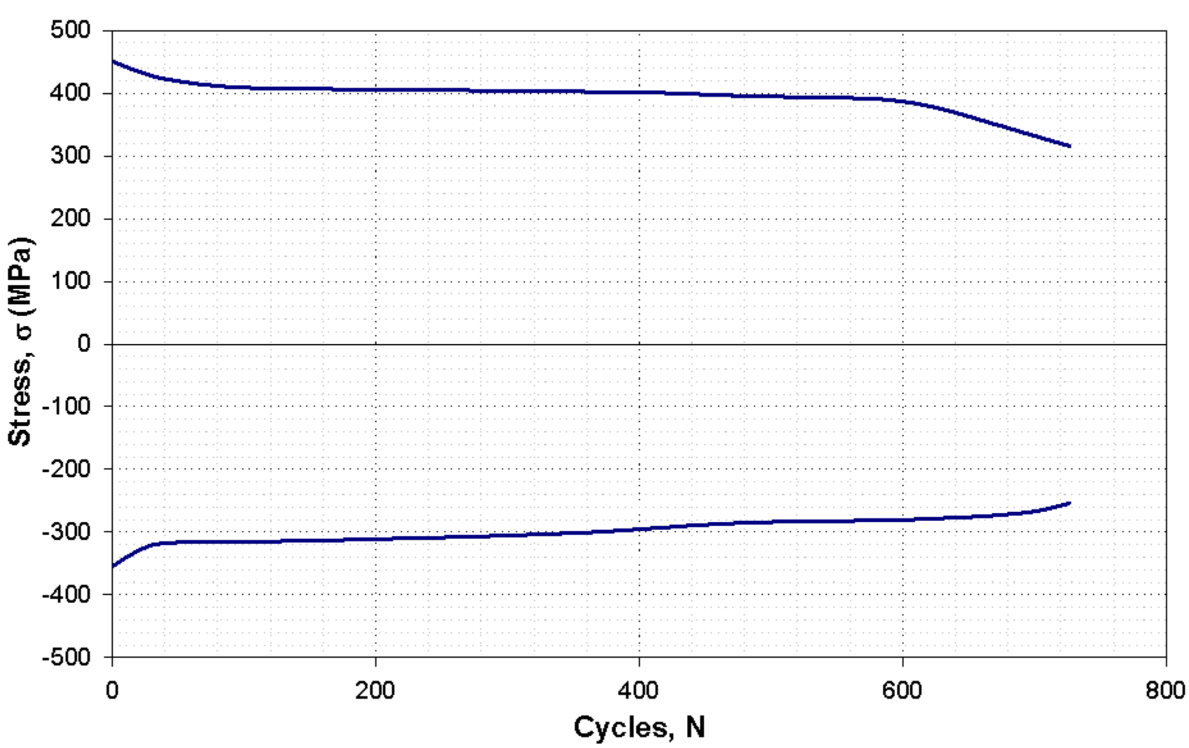

Specimen K018

OPTMF

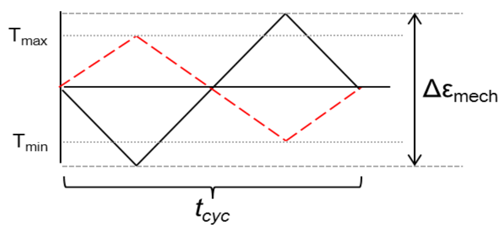

T_{max} (°C):	600	$\Delta\varepsilon_{mech}$:(%)	1.0
T_{min} (°C):	200	K_t:	3.0
t_{cyc} (s):	240	t_{hold} (s):	0

Initial		Stable	
σ_{max} (MPa):	386	σ_{max} (MPa):	384
σ_{min} (MPa):	-246	σ_{min} (MPa):	-229
$\Delta\varepsilon'_{pl}$ (%):	0.39	$\Delta\varepsilon'_{pl}$ (%):	0.31

Hysteretic Response:

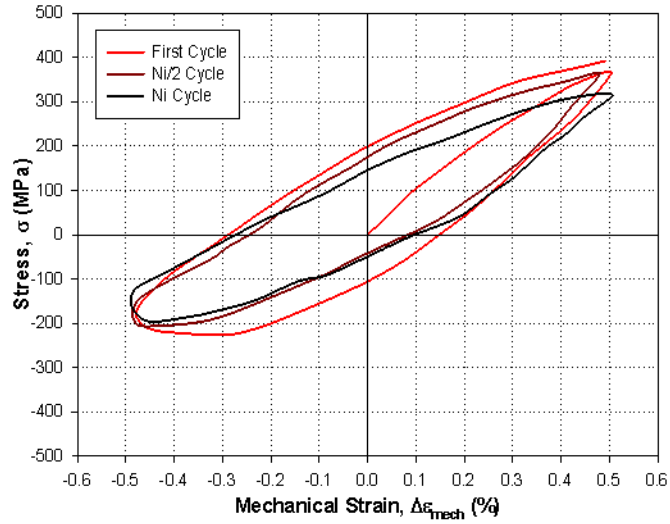

Cycles to Initiation: 201

Stress History:

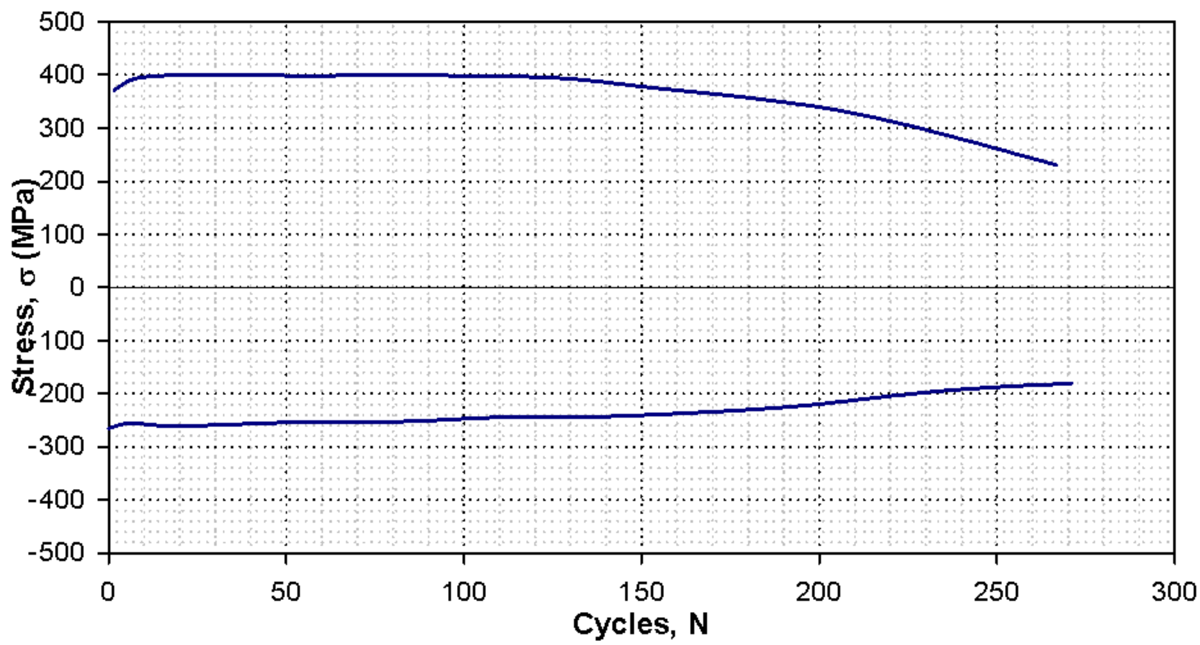

Specimen K009

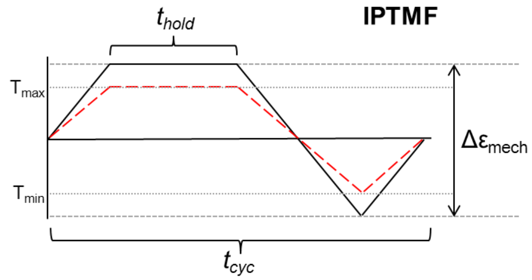

T_{max} (°C):	600	$\Delta\varepsilon_{mech}$:(%)	1.0
T_{min} (°C):	200	K_t:	1.0
t_{cyc} (s):	300	t_{hold} (s):	60

Initial		Stable	
σ_{max} (MPa):	318	σ_{max} (MPa):	191
σ_{min} (MPa):	-366	σ_{min} (MPa):	-299
σ_{relax} (MPa):	180	σ_{relax} (MPa):	58
$\Delta\varepsilon'_{pl}$ (%):	0.59	$\Delta\varepsilon'_{pl}$ (%):	0.57

Hysteretic Response:

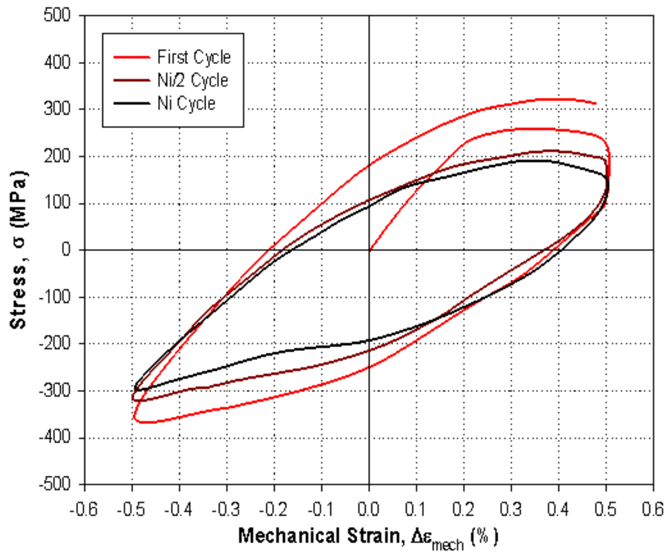

Cycles to Initiation: 498

Stress History:

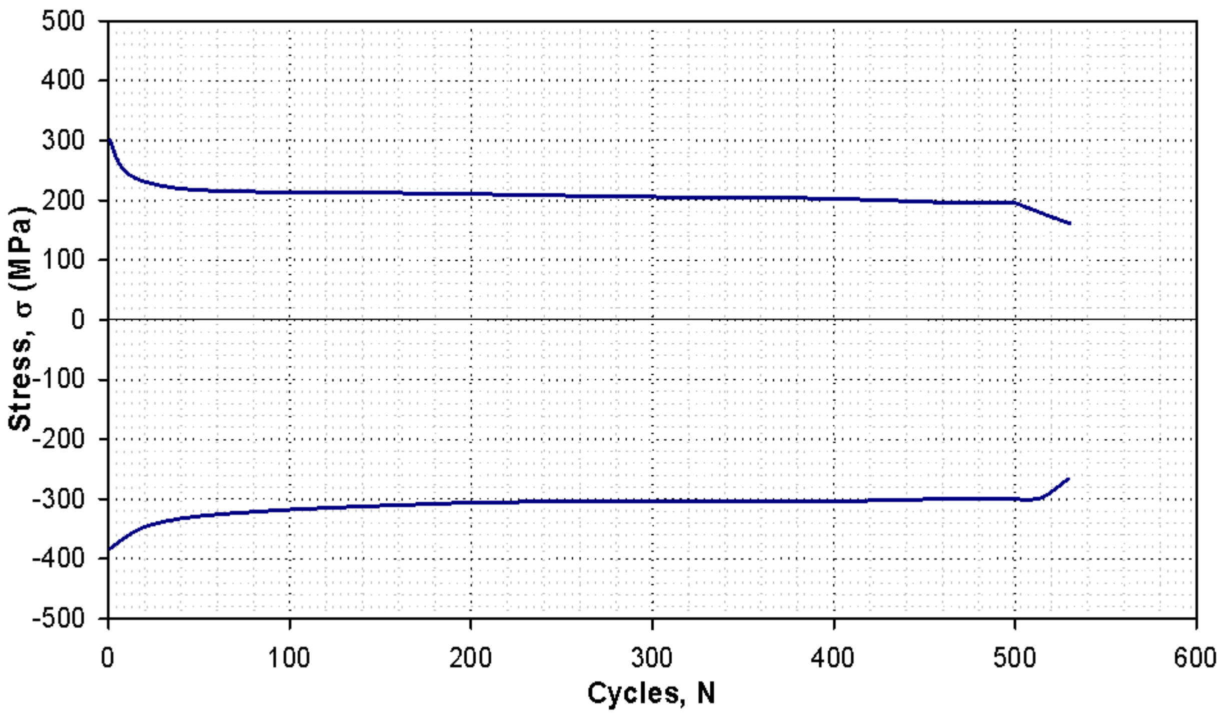

Specimen K015

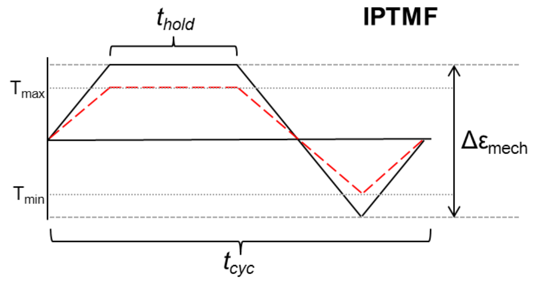

T_{max} (°C):	600	$\Delta\varepsilon_{mech}$:(%)	1.0
T_{min} (°C):	200	K_t:	1.73
t_{cyc} (s):	300	t_{hold} (s):	60

Initial		Stable	
σ_{max} (MPa):	316	σ_{max} (MPa):	240
σ_{min} (MPa):	-327	σ_{min} (MPa):	-337
σ_{relax} (MPa):	25	σ_{relax} (MPa):	17
$\Delta\varepsilon'_{pl}$ (%):	0.12	$\Delta\varepsilon'_{pl}$ (%):	0.06

Hysteretic Response:

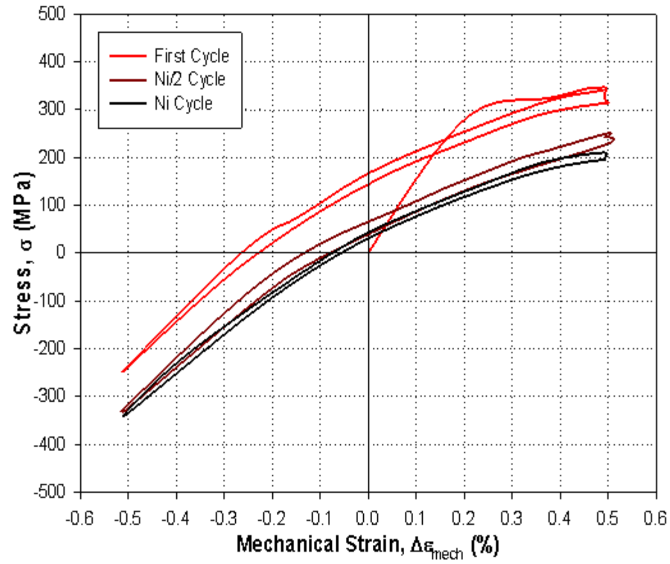

Cycles to Initiation: 719

Stress History:

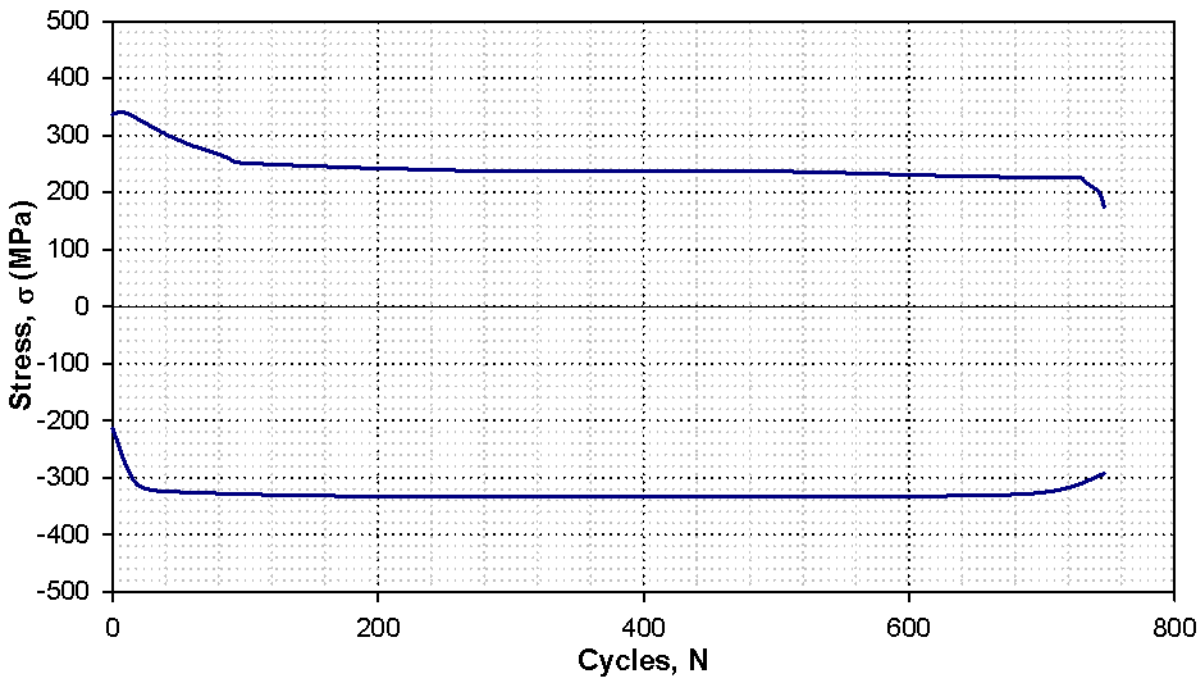

Specimen K020

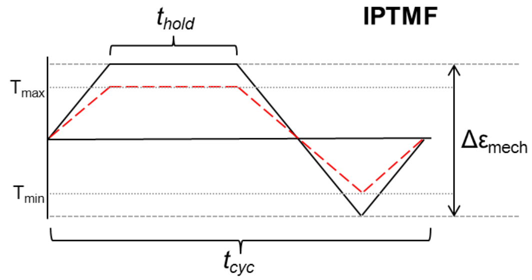

T_{max} (°C):	600	$\Delta\varepsilon_{mech}$:(%)	1.0
T_{min} (°C):	20	K_t:	30
t_{cyc} (s):	300	t_{hold} (s):	60

Initial		Stable	
σ_{max} (MPa):	429	σ_{max} (MPa):	145
σ_{min} (MPa):	-317	σ_{min} (MPa):	-309
σ_{relax} (MPa):	191	σ_{relax} (MPa):	40
$\Delta\varepsilon'_{pl}$ (%):	0.24	$\Delta\varepsilon'_{pl}$ (%):	0.06

Hysteretic Response:

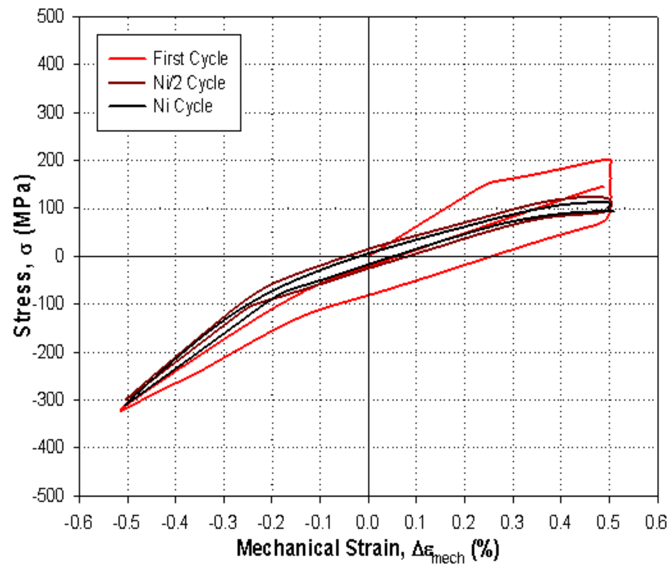

Cycles to Initiation: 298

Stress History:

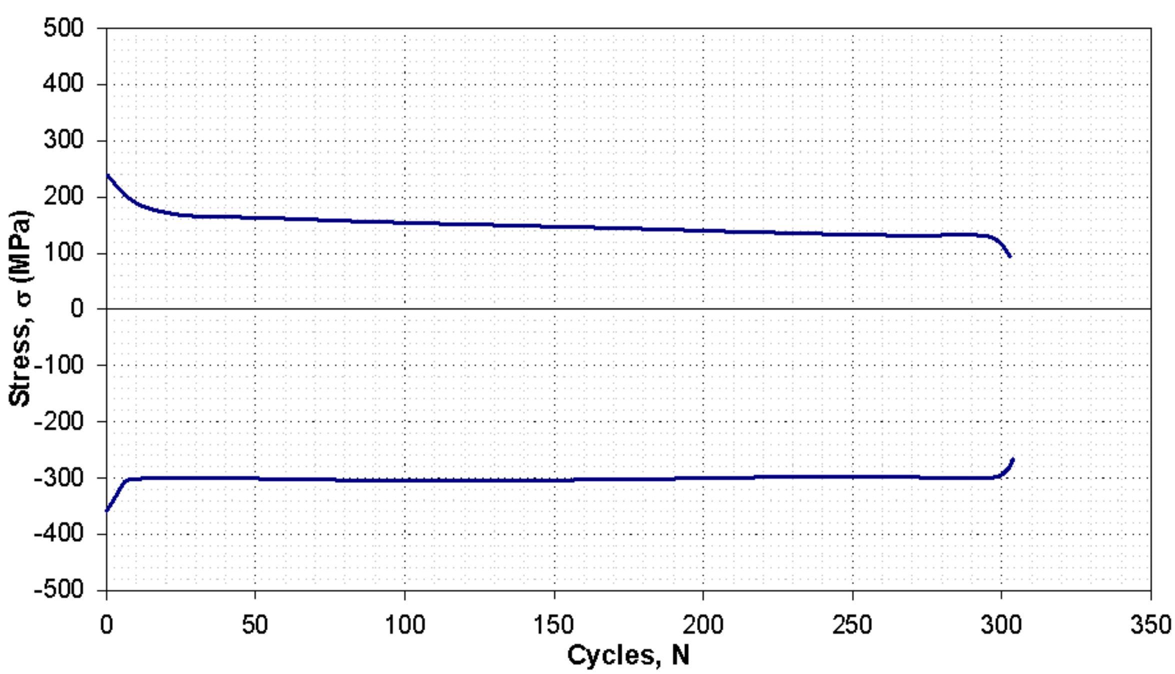

APPENDIX D: NUMERICAL SIMULATION CODE

Numerical code used for fatigue simulations via ANSYS 13.0:

```
!Combined Parametric with Thermocycling of a V notch cylindrical specimen
!Thomas Bouchenot
!Rev 33
!12-18-12
!
!Modified 3-15-2013 by Justin Karl for 10 cycles, 304SS, output file only
!
Finish
/Clear
/PREP7
/OUTPUT,junk,txt

!*******************************************************************************

! Parametric Setup:

shape=1                                                   ! Shape of the specimen (1=V-notched)
material=3                                                ! Material to be tested (3=304 stainless steel)
isotherm=0.0                                              ! 0=Yes, 1=No
sconst=1.0                                                ! 0=strain range at notch const between tests (strain range
applied to notch), 1=strain range at test location const between tests (strain range applied to grip)
makecontourplots=0                                        ! 0=dont plot contours, 1= plot contours

!Specimen Dimensions
DIA_ini=6.35                                              ! Initial notch diameter [mm]
DIA_inc=1                                                 ! Increment for notch diameter [mm]
DIA_fin=6.35                                              ! Final notch diameter [mm]
ANGN_ini=60                                               ! Initial notch angle [deg]
ANGN_inc=5                                                ! Increment for notch angle [deg]
ANGN_fin=60                                               ! Final notch angle [deg]
RAD_ini=.013      !.06 for U-notch     !.013     for v-notch                        !    Initial    notch
radius [mm]
RAD_inc=1.7                                               ! Increment for notch radius [mm]
RAD_fin=.013      !.06 for U-notch     !.013     for v-notch                        !    Final    notch
radius [mm]

!Thermal Cycling
tmt_ini=200.00         !1050.00              ! Initial Min temperature [degrees C]
tmt_inc=50.00          !-50.00                    ! Increment Min temperature [degrees C]
tmt_fin=200.00         !20.00                     ! Final Min temperature [degrees C]
tmc_ini=200.00         !950.0                     ! Initial Max temperature [degrees C]
tmc_inc=50.00          !-54.21                    ! Increment Max temperature [degrees C]
tmc_fin=200.00         !1050.0                    ! Final Max temperature [degrees C]

!Mechanical Cycling
mrat_ini=-1.0                                     ! Initial strain ratio (1=z-t, 0=cr, -1=z-c)
mrat_inc=1.0                                      ! Increment strain ratio
mrat_fin=-1.0          !1                         ! Final strain ratio
sr_ini=0.005           !.0005 !0.0001 !0.0005     !0.0015                 !    Initial    Strain
range
sr_inc=0.0001                                     ! Increment Strain range
sr_fin=0.005           !.0005 ! 0.01 !0.005  ! Final Strain range

!Material Orientation
ang_ini=0         !0.0                  ! Orientation angle where 0 is L-oriented 90 is T-oriented
ang_inc=45.0
ang_fin=0         !90.0

definedKTS=3.0                                    !Used to hard define a KTS (dont forget to remove '!' under
the kts calculation to activate it) !1.73 for u notch, 3 for v notch
!*******************************************************************************

!Configuring the Cleaned Results File
```

```
LABEL1='....sr.......'
LABEL2='......tmca......'
LABEL3='.......tmt......'
LABEL4='.......re.......'
LABEL5='.......ang......'
LABEL6='.....MAXTEMP....'
LABEL7='.....MINTEMP....'
LABEL8='...NMAXESTRAIN...'
LABEL9='...NMINESTRAIN...'
LABEL10='...NMAXPSTRAIN...'
LABEL11='...NMINPSTRAIN...'
LABEL12='...NMAXCSTRAIN...'
LABEL13='...NMINCSTRAIN...'
LABEL14='...NMAXSTRESS...'
LABEL15='...NMINSTRESS...'
LABEL16='...TMAXESTRAIN...'
LABEL17='...TMINESTRAIN...'
LABEL18='...TMAXPSTRAIN...'
LABEL19='...TMINPSTRAIN...'
LABEL20='...TMAXCSTRAIN...'
LABEL21='...TMINCSTRAIN...'
LABEL22='...TMAXSTRESS...'
LABEL23='...TMINSTRESS...'
LABEL24='..NMAXTOTSTRAIN..'
LABEL25='..NMINTOTSTRAIN..'
LABEL26='..TMAXTOTSTRAIN..'
LABEL27='..TMINTOTSTRAIN..'
LABEL28='...Strain_Rate...'
LABEL29='..Total_Cycles...'
LABEL30='.....Ten_Hold....'
LABEL31='....Comp_Hold....'
LABEL32='..N_Ext_Initial..'
LABEL33='.N_Relax_Stress1.'
LABEL34='.N_Relax_Stress2.'
LABEL35='..N_Min_Stress1..'
LABEL36='..N_Max_Stress1..'
LABEL37='..N_Min_Stress2..'
LABEL38='..N_Max_Stress2..'
LABEL39='..N_P_Str_Range1.'
LABEL40='..N_P_Str_Range2.'
LABEL41='..T_Ext_Initial..'
LABEL42='.T_Relax_Stress1.'
LABEL43='.T_Relax_Stress2.'
LABEL44='..T_Min_Stress1..'
LABEL45='..T_Max_Stress1..'
LABEL46='..T_Min_Stress2..'
LABEL47='..T_Max_Stress2..'
LABEL48='..T_P_Str_Range1.'
LABEL49='..T_P_Str_Range2.'


!*CFOPEN,
FEA_NOTCH_CLEANED_%tens_hold%_%comp_hold%_%first_hold%_%strain_rate%_%total_cycles%_%DIA_NTCH%_%ANG_
NTCH%_%RAD_NTCH%,data,
*CFOPEN, FEA_NOTCH_CLEANED,data,
*VWRITE, LABEL1, LABEL2, LABEL3,
LABEL4,LABEL5,LABEL6,LABEL7,LABEL8,LABEL9,LABEL10,LABEL11,LABEL12,LABEL13,LABEL14,LABEL15,
LABEL24,LABEL25
%C%C%C%C%C%C%C%C%C%C%C%C%C%C%C%C%C

!*CFOPEN,
FEA_TEST_CLEANED_%tens_hold%_%comp_hold%_%first_hold%_%strain_rate%_%total_cycles%_%DIA_NTCH%_%ANG_N
TCH%_%RAD_NTCH%,data,
*CFOPEN, FEA_TEST_CLEANED,data,
*VWRITE, LABEL1, LABEL2, LABEL3,
LABEL4,LABEL5,LABEL6,LABEL7,LABEL16,LABEL17,LABEL18,LABEL19,LABEL20,LABEL21,LABEL22,LABEL23,
LABEL26,LABEL27
%C%C%C%C%C%C%C%C%C%C%C%C%C%C%C%C%C
```

```
!*CFOPEN,
FEA_CLEANED_TOTALS_%tens_hold%_%comp_hold%_%first_hold%_%strain_rate%_%total_cycles%_%DIA_NTCH%_%ANG
_NTCH%_%RAD_NTCH%,data,
*CFOPEN, FEA_CLEANED_TOTALS,data,
*VWRITE,                    LABEL1,                    LABEL2,                    LABEL3,
LABEL4,LABEL5,LABEL6,LABEL7,LABEL24,LABEL25,LABEL14,LABEL15,LABEL26,LABEL27,LABEL22,LABEL23
%C%C%C%C%C%C%C%C%C%C%C%C%C%C%C

*CFOPEN, FEA_NOTCH_CLEANED2,data,,
*VWRITE, LABEL1, LABEL2, LABEL3, LABEL4, LABEL28, LABEL29, LABEL5, LABEL30, LABEL31, LABEL32, LABEL33,
LABEL34, LABEL35, LABEL36, LABEL37, LABEL38, LABEL39, LABEL40
%C%C%C%C%C%C%C%C%C%C%C%C%C%C%C%C%C%C

*CFOPEN, FEA_TEST_CLEANED2,data,,
*VWRITE, LABEL1, LABEL2, LABEL3, LABEL4, LABEL28, LABEL29, LABEL5, LABEL30, LABEL31, LABEL41, LABEL42,
LABEL43, LABEL44, LABEL45, LABEL46, LABEL47, LABEL48, LABEL49
%C%C%C%C%C%C%C%C%C%C%C%C%C%C%C%C%C%C

/OUTPUT,FEA_Junk10,txt

!*******************************************************************************

!Parametric Start and Naming

i=1

*DO,DIA_NTCH,DIA_ini,DIA_fin,DIA_inc                  ! Diameter of specimen at notch        [mm]
*DO,ANG_NTCH,ANGN_ini,ANGN_fin,ANGN_inc               ! Angle of notch              [deg]
*DO,RAD_NTCH,RAD_ini,RAD_fin,RAD_inc                  ! Root radius of notch                 [mm]
*DO,tmc,tmc_ini,tmc_fin,tmc_inc                       ! Compressive temperature [degrees C]
*DO,tmt,tmt_ini,tmt_fin,tmt_inc                       ! Tensile temperature [degrees C]
*DO,mrat,mrat_ini,mrat_fin,mrat_inc             ! strain ratio                [1=z-t, 2=cr, 3=z-c]
*DO,sr,sr_ini,sr_fin,sr_inc                     ! Strain range
*DO,ang,ang_ini,ang_fin,ang_inc                       ! Angle of the specimen       [deg]

PARSAV,,parameters,txt
*IF,i,GT,1,THEN
finish
/clear
/PREP7
PARRES,,parameters,txt
*ENDIF

finish
/FILNAME, Parametric V Notched Tensile TMF
/title, Parametric V Notched Tensile TMF

/prep7
/OUTPUT,junk1,txt

!*******************************************************************************

! Input parameters:

! Geometric:

DIA_RED=7.62                       ! Reduced diameter of specimen           [mm]
RAD_SHLD=33                        ! Radius of reduction shoulder [mm]
DIA_GRIP=12.7                      ! Diameter of specimen grip     [mm]
LEN_GRIP=19                        ! Length of specimen grip       [mm]
LEN_BAR=101.6                      ! Total length of specimen      [mm]
DIA_BAR=7.62                       ! Diameter (width) of rectangular specimen [mm]

! Test Location:                         ! Test location is set at the top of the grip to simulate remote
conditions, but this can be changed if other locations are desired

TEST_DIST=0                             ! Distance from grip end to horizontal test line [mm]
TEST_THICK=0                            ! Thickness of horizontal test line [mm]

!*******************************************************************************
```

```
! Parameters Derived From Geometric Relationships:

*AFUN, DEG
l1=LEN_BAR/2.0
l2=LEN_GRIP
d1=DIA_GRIP/2.0
d2=DIA_RED/2.0
r1=RAD_SHLD
r2=RAD_NTCH
t=DIA_NTCH/2.0
a=ANG_NTCH/2.0
x1=d2+r1-d1
y1=sqrt((r1*r1)-(x1*x1))
x2=sin(a)*r2
y2=cos(a)*r2
x3=(y2/tan(a))-(r2-x2)-t
y3=tan(a)*(d2+x3)
ltesttop=l1-TEST_DIST+TEST_THICK
ltestbottom=l1-TEST_DIST-TEST_THICK
D_ratio=DIA_GRIP/DIA_NTCH                    ! Ratio of the major to minor diameter of specimen
r_ratio=RAD_NTCH/DIA_NTCH                    ! Ratio of radius to minor diameter
*IF,RAD_NTCH, EQ, 0.0, THEN
DIA_RED = DIA_NTCH
D_ratio = DIA_RED/DIA_NTCH
*ENDIF

!*******************************************************************************

! Theoretical (Elastic) Stress Concentration Factor:
*IF, ANG_NTCH, GE, 60, THEN
*IF, D_ratio, GE, 1.5, THEN
A_kt = 1.0582
b_kt = -0.386
*ELSEIF, D_ratio, GE, 1.1, THEN
A_kt = 1.0684
b_kt = -0.297
*ELSEIF, D_ratio, GE, 1.05, THEN
A_kt = 1.0538
b_kt = -0.252
*ELSEIF, D_ratio, GE, 1.0, THEN
A_kt = 1.0
b_kt = 0.0
*ENDIF

Kts = A_kt*(r_ratio)**b_kt               ! Stress concentration factor Kts

Kts=definedKTS                           ! Temp hard assign value until above for v notch is finalized

!*******************************************************************************

! Elastic Properties (Hooke's Law)


*IF,material,eq,3,THEN
!mpread,Stl_AISI-304,SI_MPL,,lib          ! Values for 304SS material
MPTEMP,1,20,200,400,600
MPDATA,EX,1,1,193000,183000,168000,148000
MPDATA,PRXY,1,1,0.3,0.3,0.3,0.3
*ENDIF

!*******************************************************************************

! Plastic and Hardening:


!Bilinear Kinematic Hardening for 304 Stainless Steel

*IF,material,eq,3,THEN
TB,BKIN, 1, 3,, 1                        ! TB, Lab, MAT, NTEMP, NPTS, TBOPT, EOSOPT
```

```
TBTEMP, 20                                              ! TBTEMP, TEMP, KMOD
TBDATA, 1,268895.6043842394, 2153.218789         ! TBDATA, STLOC, C1, C2
TBTEMP, 315                                             ! C1=yield, c2= tangent modulus
TBDATA, 1,164095.2662652538, 1601.512234
TBTEMP, 426
TBDATA, 1,156166.29331546213, 2005.862781

!*ENDIF

!*******************************************************************************

! Creep

*IF,material,eq,3,THEN
TB,CREEP,1,4,,10            ! Material No., No of Temps, Points in Table
TBTEMP, 20 !293.15            ! Temperature = 20.0
TBDATA,1,1.27E-60,11.2,0
TBTEMP, 400 !673.15            ! Temperature = 400
TBDATA,1,1.27E-60,11.2,0
TBTEMP, 500 !773.15            ! Temperature = 500
TBDATA,1,1.27E-60,11.2,0
TBTEMP, 600 !873.15            ! Temperature = 600
TBDATA,1,1.96215e-35,11.2,0
*ENDIF
!*******************************************************************************

! Specimen Geometry:

*IF,shape,eq,1,THEN

! Keypoints:

k,  1,   0.0,    0.0
k,  2,   0.0,    l1
k,  3,   d1,     l1
k,  4,   d1,     l1-l2
k,  5,   d2,     l1-l2-y1
k,  6,   d2+r1,  l1-l2-y1
k,  7,   d2,     y3
k,  8,  t+r2-x2, y2
k,  9,    t,     0.0
k, 10,  t+r2,    0.0

! Lines:

L,  1,  2                                        ! Line 1
L,  2,  3                                        ! Line 2
L,  3,  4                                        ! Line 3
Larc,  4, 5, 6, r1                               ! Line 4
L,  5,  7                                        ! Line 5
L,  7,  8                                        ! Line 6
Larc, 8, 9, 10, r2                               ! Line 7
L,  9,  1                                        ! Line 8

*ENDIF



! Areas:

AL, ALL
ksel, ALL

!*******************************************************************************

! Meshing Element Type and Orientation:

! Define a local system to transform material properties into desired orientation

!local,11,0,0,0,0,0,0,ang,,        ! the material is rotated into the theta orientation
```

```
!!!!!!local,11,0,0,0,0,0,ang,0,,        ! the material is rotated into the theta orientation
local,11,0,0,0,0,0,ang,0,0,,
ESYS,11                         ! the local system is selected for all defined elements

ET,1,PLANE183                                                   ! using Plane183 element


*IF,shape,eq,1,THEN
KEYOPT,1,3,1                                                    ! Axisymmetric key option (last number)  !0=plane     stress,
1=axisymmetric, 2=plane strain (z strain=0), 3=plane stress with thinkness real constant input, 5=generalized plane strain
*ENDIF

!********************************************************************************

! Meshing:

MSHAPE, 0, 2D                                                   ! Mesh with quadrilateral-shaped elements
MSHKEY, 0                                                       ! Free mesh
SMRTSIZE, 2                                                     ! Smart sizing refinement level 4 (1=dense, 5= rough)
AMESH, 1

*IF,shape,eq,1,THEN
!LREFINE, 7,7,1,3,6!7,7,1,1,1            !7,7,1,3,6              !7,7,1,3,2 !7,7,1,2,3 !7,7,1,4,3              !    Refine    mesh
along notch tip
!!LREFINE, 8,8,1,2,4           !8,8,1,2,3 !8,8,1,2,3            ! Refine mesh along axial boundary !l1, l2, lincrement, level
(1=minimal refinement, 5=max refinement), depth (elements outward)
*ENDIF


! Getting the Notch and Test Area Element

*IF,shape,eq,1,THEN
NSEL,S,NODE,,8,8,1
*ENDIF

ESLN,R,0,all
*get,e13,ELEM,,NUM,MIN

LSEL,all
NSEL,all
ASEL,all
ESEL,all

NSEL,S,LOC ,y,  ltestbottom, ltesttop, .001
ESLN,R,0,all
*get,e12,ELEM,,NUM,MIN                                          ! Get the number of first element  of selected elements

LSEL,all
NSEL,all
ASEL,all
ESEL,all

!********************************************************************************

! Input Cyclic Parameters:

strain_range = sr                                     ! Difference in Max and Min strains [mm/mm]
strain_rate = 0.01/(5*60)           !0.025/60          !0.001              !3.33E-5  !0.01/(5*60)
            ! Strain rate [mm/mm/s]   ! Tested with values: 0.005(CR) !0.001 (ZtT)   !was 0.004
tol=0.0001
re=(mrat-1+tol)/(mrat+1+tol)                          ! Strain ratio (0 = Z-to-T, -1 = CR, -900 = Z-to-C)
strain_ratio=re                                                 ! Frequency of data capture
*IF, mrat, EQ, 2, THEN
strain_ratio=0.05
*ENDIF
tens_hold = 1.00e-2/3600            !120.0/3600        !1.01/3600 !1.01e-5/3600                    ! Tension hold [hr]
comp_hold = 1.01e-2/3600            !120.0/3600        !1.00/3600 !1.00e-5/3600                    !      Compression
hold [hr]
first_hold = 1.02e-2/3600           !120.0/3600                 !5000                              !   First   hold   [hr]
ex:5000 hr hold
```

```
! Cyclic Parameters Derived From Relationships:

gross_strain_range = (strain_range/(Kts-(Kts+1)*sconst))/((D_ratio*D_ratio)-((D_ratio*D_ratio)+1)*sconst)    ! modified to support what strain gage gets fixed ! If not using Axisymmetic option, dont forget to modify the d ratio's
*IF,shape,eq,1,THEN
displ_range = gross_strain_range*l1    !!!!!changed this for the test, if the strain is constant between tests at notch, needs to be gross strain range, if strain is constant between test at the grip needs to be strain range
*ENDIF
*IF,shape,eq,2,THEN
displ_range = gross_strain_range*l1
*ENDIF
*IF,shape,eq,3,THEN
displ_range = strain_range*l1
*ENDIF
*IF,shape,eq,4,THEN
displ_range = gross_strain_range*l1    !!!!!changed this for the test, if the strain is constant between tests at notch, needs to be gross strain range, if strain is constant between test at the grip needs to be strain range
*ENDIF
displ_max = displ_range/(1.0-strain_ratio)          ! Displacement [mm]
displ_min = displ_max-displ_range                   ! Displacement [mm]
SRANGE_MAX = sr/(1.0-strain_ratio)          ! Displacement [mm]
SRANGE_MIN = SRANGE_MAX-sr                          ! Displacement [mm]
displ_mean = 0.5*(displ_max+displ_min)                      ! Displacement [mm]
strain_rate_hr = strain_rate*3600.0                 ! Strain rate [mm/mm/hr]
half_cycle = strain_range/strain_rate_hr/2.0        ! Half cycle [hr]
full_cycle = 2.0*half_cycle                         ! Full cycle [hr]

! Cycle Stepping and Ramping Time
num_cycles = 2
tot_load_steps=num_cycles*4+2
load_init_time = 1.0E-2/3600.0                              ! Initial Load Time [hr]
load_mini_time = 1.0E-3/3600.0                              ! Minimum Deltim step time [hr]
load_maxi_time = 10.0/3600.0                        ! Maximum Deltim step time [hr]
load_maxi_dwell_time = 10000.0/3600.0               ! Maximum Deltim step time [hr]
load_ramp_time = 1.0E-10/3600.0                             ! Ramp time used in Deltim [hr]
data_freq = 1.0                                             ! Frequency of data capture

! Temperature Cycling
tmca=tmc*isotherm+(1-isotherm)*tmt
max_temp=0.5*(tmt+tmca+abs(tmt-tmca))
min_temp=0.5*(tmt+tmca-abs(tmt-tmca))
temp_range=abs(tmt-tmca)
temp_rate=temp_range/full_cycle

!*IF, tmt, NE, tmca, THEN                            !temp controlled strain rate for TMF
!temp_rate = 3          !3 degress per second for TMF
!temp_rate_hr = temp_rate*3600.0
!half_cycle = temp_range/temp_rate_hr/2.0           ! Half cycle [hr] ! needs to be modified for z-t and z-c
!full_cycle = 2.0*half_cycle                        ! Full cycle [hr]
!*ENDIF

!*******************************************************************************

! Assign the Peak-Valley-Period Values: (modified with Dr. Gordon's rules for clarity)

! Cycling rules:
!       Rule #2: If CR and compression hold exceeds tensile hold, then go to compression first
!    Rule #3: If zero-to-compression, proceed to minimum displacement first
!    Rule #4: If zero-to-tension, proceed to maximum displacement first
!    Rule #5: Initial portion of the cycle goes from zero-displacement and mean temp

peak_displ=displ_max
valley_displ=displ_min
peak_hold=tens_hold
valley_hold=comp_hold
mean_temp=0.5*(tmt+tmca)
temp_init=mean_temp
peak_temp=tmt
valley_temp=tmca
```

```
*IF,mrat,eq,0,and,comp_hold,gt,tens_hold,THEN ! See Rule #2
peak_displ=displ_min
valley_displ=displ_max
*ENDIF

*IF,mrat,eq,-1,THEN             ! See Rule #3 (only in Z-to-C case)
peak_displ=displ_min
valley_displ=displ_max
peak_hold=comp_hold
valley_hold=tens_hold
half_cycle=half_cycle*2
peak_temp=tmca
valley_temp=tmt
temp_init=tmt
*ENDIF

*IF,mrat,eq,1,THEN ! See Rule #4 (only in Z-to-T case)
peak_displ=displ_max
valley_displ=displ_min
peak_hold=tens_hold
valley_hold=comp_hold
half_cycle=half_cycle*2
peak_temp=tmt
valley_temp=tmca
temp_init=tmca
*ENDIF

*IF,mrat,eq,-1,THEN ! See Rule #5
init_period_hr=half_cycle*peak_displ/displ_range   ! Period of Step 1 cycle [hr]
displ_init=.000001                                 ! Initial displacement for Step 0 [mm]
*ENDIF

!*******************************************************************************

! Boundary Conditions:

LSEL,S,LINE,,1,1,1                    ! Constrain movement in x direction for nodes on line 1 (line of symmetry)
NSLL,S,1
D,ALL,UX,0
LSEL,ALL
NSEL,ALL

*IF,shape,eq,1,THEN
LSEL,S,LINE,,8,8,1                    ! Constrain movement in y direction for nodes along line 8 (line of symmetry)
*ENDIF

NSLL,S,1
D,ALL,UY,0
LSEL,ALL
NSEL,ALL

FINISH

!*******************************************************************************

! Solution:

/CONFIG,NRES,500000
/NERR,5000000,5000000,,0
*DIM,LOADSUBS,ARRAY,1,tot_load_steps               !array for amount of substeps

/SOLU

! Step 1:

total_time = abs(load_ramp_time)                   ! Total time [s]
Antype, trans                                      ! ANTYPE, Antype, Status, LDSTEP, SUBSTEP, Action
```

```
nropt,auto                                              ! Uses Newton-Raphson
lnsrch,auto                                             ! Auto line searching for NR
NLGEOM,auto                                     ! Non-linear geometry
Solcontrol, 1                                           ! Optimizes nonlinear solutions
Cnvtol,F,3
Time, total_time                                ! Time at end of step
!NSUBST,20,400,20                                       ! Specifies substeps
Deltim, load_init_time, load_mini_time, load_maxi_time  ! DELTIM, DTIME, DTMIN, DTMAX, Carry
Autots, 1                                       ! Auto Time Stepping

FLST,2,1,4,ORDE,1
FITEM,2,2
/GO
DL,P51X, ,UY,displ_init                                 ! Displacement of selected line

NSEL,ALL
BF,ALL,TEMP,temp_init                                   ! Nodal body force load
Outres, All, data_freq                                  ! Outputs data to be read by ESOL
Crplim, 20, 1                                           ! CRPLIM, CRCR, Option, !Creep Ratio Limit
Rate, 1                                                 ! Activates Creep for step
Kbc, 0                                                  ! Specifies stepped or ramped load, 1=stepped
Solve
*GET, LOADSUBS(1,1),ACTIVE,0,SOLU, NCMSS        !getting the number of substeps in the load case and putting it into
the array

! Step 2:

total_time = abs(half_cycle)+total_time
Antype, trans
nropt,auto
lnsrch,auto
NLGEOM,auto
Solcontrol, 1
Cnvtol,F,3
Time, total_time
!NSUBST,20,400,20

Deltim, load_init_time, load_mini_time, load_maxi_time

Autots, 1

FLST,2,1,4,ORDE,1
FITEM,2,2
/GO
DL,P51X, ,UY,peak_displ

NSEL,ALL
BF,ALL,TEMP,peak_temp
Outres, All, data_freq
Crplim, 20, 1
Rate, 1
Kbc, 0
Solve
*GET, LOADSUBS(1,2),ACTIVE,0,SOLU, NCMSS

!*******************************************************************************

!Extra Cycling

total_cycles=num_cycles                                         ! Number of cycles
*do,cycle,1,total_cycles,1                      ! Do cycles from 1 to total_cycles with increment 1

! Step 3:

*GET, LOADNUM,ACTIVE,0,SOLU, NCMLS
*IF, LOADNUM, EQ, 2, THEN                       ! Equal to 2 because the 3rd load step hasn't started yet
total_time = abs(first_hold) + total_time
*ELSE
total_time = abs(peak_hold) + total_time
*ENDIF
```

```
Antype, trans
nropt,auto
lnsrch,auto
NLGEOM,auto                    ! Non-linear geometry
Solcontrol, 1
Cnvtol,F,3
Time, total_time
!NSUBST,20,1000,20
Deltim, load_init_time, load_mini_time, load_maxi_dwell_time
Autots, 1

FLST,2,1,4,ORDE,1
FITEM,2,2
/go
DL,P51X, ,UY,peak_displ

NSEL,ALL
BF,ALL,TEMP,peak_temp
Outres, All, data_freq
Crplim, 20, 1
Rate, 1
Kbc, 0
Solve
*GET, LOADSUBS(1,2+num_cycles*4-3),ACTIVE,0,SOLU, NCMSS

! Step 4:

total_time = abs(full_cycle) + total_time
Antype, trans
nropt,auto
lnsrch,auto
NLGEOM,auto                    ! Non-linear geometry
Solcontrol, 1
Cnvtol,F,3
Time, total_time
!NSUBST,20,1000,20
Deltim, load_init_time, load_mini_time, load_maxi_time
Autots, 1

FLST,2,1,4,ORDE,1
FITEM,2,2
/go
DL,P51X, ,UY,valley_displ

NSEL,ALL
BF,ALL,TEMP,valley_temp
Outres, All, data_freq
Crplim, 20, 1
Rate, 1
Kbc, 0
Solve
*GET, LOADSUBS(1,2+num_cycles*4-2),ACTIVE,0,SOLU, NCMSS

! Step 5:

total_time = abs(valley_hold) + total_time
Antype, trans
nropt,auto
lnsrch,auto
NLGEOM,auto                    ! Non-linear geometry
Solcontrol, 1
Cnvtol,F,3
Time, total_time
!NSUBST,20,1000,20
Deltim, load_init_time, load_mini_time, load_maxi_dwell_time
Autots, 1

FLST,2,1,4,ORDE,1
FITEM,2,2
/go
```

```
DL,P51X, ,UY,valley_displ

NSEL,ALL
BF,ALL,TEMP,valley_temp
Outres, all, data_freq
Crplim, 20, 1
Rate, 1
Kbc, 0
Solve
*GET, LOADSUBS(1,2+num_cycles*4-1),ACTIVE,0,SOLU, NCMSS

! Step 6:

total_time = abs(full_cycle) + total_time
Antype, trans
nropt,auto
lnsrch,auto
NLGEOM,auto                    ! Non-linear geometry
Solcontrol, 1
Cnvtol,F,3
Time, total_time
!NSUBST,25,1000,20
Deltim, load_init_time, load_mini_time, load_maxi_time
Autots, 1

FLST,2,1,4,ORDE,1
FITEM,2,2
/go
DL,P51X, ,UY,peak_displ

NSEL,ALL
BF,ALL,TEMP,peak_temp
Outres, all, data_freq
Crplim, 20, 1
Rate, 1
Kbc, 0
Solve
rescontrol,file_summary
*GET, LOADSUBS(1,2+num_cycles*4),ACTIVE,0,SOLU, NCMSS
*enddo
FINISH

!*********************************************************************************

! Post Processing:

! Values

NMAXSTRESS=-999999999
NMINSTRESS=999999999
NMAXPSTRAIN=-999999999
NMINPSTRAIN=999999999
NMAXCSTRAIN=-999999999
NMINCSTRAIN=999999999
NMAXESTRAIN=-999999999
NMINESTRAIN=999999999
MAXTEMP=-999999999
MINTEMP=999999999
TMAXSTRESS=-999999999
TMINSTRESS=999999999
TMAXPSTRAIN=-999999999
TMINPSTRAIN=999999999
TMAXCSTRAIN=-999999999
TMINCSTRAIN=999999999
TMAXESTRAIN=-999999999
TMINESTRAIN=999999999

NSTRESSPT1=999999999
*IF, mrat, EQ, 1, THEN
NSTRESSPT1=-999999999
```

```
*ENDIF
TSTRESSPT1=999999999
*IF, mrat, EQ, 1, THEN
TSTRESSPT1=-999999999
*ENDIF

NMAXPSTRAINCYC1=-999999999
NMINPSTRAINCYC1=999999999
NMAXPSTRAINCYC2=-999999999
NMINPSTRAINCYC2=999999999
TMAXPSTRAINCYC1=-999999999
TMINPSTRAINCYC1=999999999
TMAXPSTRAINCYC2=-999999999
TMINPSTRAINCYC2=999999999

NMINSTRESSCYC1=999999999
NMAXSTRESSCYC1=-999999999
TMINSTRESSCYC1=999999999
TMAXSTRESSCYC1=-999999999
NMINSTRESSCYC2=999999999
NMAXSTRESSCYC2=-999999999
TMINSTRESSCYC2=999999999
TMAXSTRESSCYC2=-999999999


*DO,curloadstep,1,tot_load_steps

!/Post1
!/OUTPUT, FEA_Junk7,txt
!*CFOPEN, temp1,data,,append
!*VWRITE, LOADSUBS(1,curloadstep)
!(F10.5)
!FINISH

/Post1
/OUTPUT, FEA_Junk3,txt
RSYS,0                  ! global

*DO,t,1,LOADSUBS(1,curloadstep),1                          !2nd value is number of substeps in the load step
SET,curloadstep,t                          !SET, Lstep, Sbstep, Fact, KIMG, TIME, ANGLE, NSET, ORDER
ETABLE, TEMPVAL, BFE, TEMP                     !getting the solution values and putting them in a table
ETABLE, NESTRAVL, EPEL, Y                  !changing z to y
ETABLE, NPSTRAVL, EPPL, Y
ETABLE, NCSTRAVL, EPCR, Y
ETABLE, NSTRESVL, S, Y
ETABLE, TESTRAVL, EPEL, Y
ETABLE, TPSTRAVL, EPPL, Y
ETABLE, TCSTRAVL, EPCR, Y
ETABLE, TSTRESVL, S, Y
*GET,RES1, ELEM, e13, ETAB,TEMPVAL             ! getting the values from the element table and putting it into an array
*GET,RES2, ELEM, e13, ETAB,NESTRAVL                  ! elastic strain at notch
*GET,RES3, ELEM, e13, ETAB,NPSTRAVL                  ! plastic strain at notch
*GET,RES4, ELEM, e13, ETAB,NCSTRAVL                  ! creep strain at notch
*GET,RES5, ELEM, e13, ETAB,NSTRESVL                  ! stress at notch
*GET,RES6, ELEM, e12, ETAB,TESTRAVL                  ! elastic strain at test loc
*GET,RES7, ELEM, e12, ETAB,TPSTRAVL                  ! plastic strain at test loc
*GET,RES8, ELEM, e12, ETAB,TCSTRAVL                  ! creep strain at test loc
*GET,RES9, ELEM, e12, ETAB,TSTRESVL                  ! stress at test loc
*GET,RESTIME, ACTIVE,0, SET, TIME
*CFOPEN, FEA_%tmt%_%tmca%_%sr%_%mrat%_%ang%_%DIA_NTCH%_%ANG_NTCH%_%RAD_NTCH%_,data,,append
*VWRITE, RESTIME, RES1, RES2, RES3, RES4, RES5, RES6, RES7, RES8, RES9
(E11.5,6X F10.2,6X E11.5,6X E11.5,6X E11.5,6X F10.4,6X E11.5,6X E11.5,6X E11.5,6X F10.4)
!(E11.5,6X F10.2,6X E11.5,6X E11.5,6X E11.5,6X F10.5,6X E11.5,6X E11.5,6X E11.5,6X F10.5)

*IF,RES5,GT,NMAXSTRESS,THEN
NMAXSTRESS=RES5
*ENDIF
*IF,RES5,LT,NMINSTRESS,THEN
NMINSTRESS=RES5
*ENDIF
```

```
*IF,RES2,GT,NMAXESTRAIN,THEN
NMAXESTRAIN=RES2
*ENDIF
*IF,RES2,LT,NMINESTRAIN,THEN
NMINESTRAIN=RES2
*ENDIF

*IF,RES3,GT,NMAXPSTRAIN,THEN
NMAXPSTRAIN=RES3
*ENDIF
*IF,RES3,LT,NMINPSTRAIN,THEN
NMINPSTRAIN=RES3
*ENDIF

*IF,RES4,GT,NMAXCSTRAIN,THEN
NMAXCSTRAIN=RES4
*ENDIF
*IF,RES4,LT,NMINCSTRAIN,THEN
NMINCSTRAIN=RES4
*ENDIF

*IF,RES1,GT,MAXTEMP,THEN
MAXTEMP=RES1
*ENDIF
*IF,RES1,LT,MINTEMP,THEN
MINTEMP=RES1
*ENDIF

*IF,RES9,GT,TMAXSTRESS,THEN
TMAXSTRESS=RES9
*ENDIF
*IF,RES9,LT,TMINSTRESS,THEN
TMINSTRESS=RES9
*ENDIF

*IF,RES6,GT,TMAXESTRAIN,THEN
TMAXESTRAIN=RES6
*ENDIF
*IF,RES6,LT,TMINESTRAIN,THEN
TMINESTRAIN=RES6
*ENDIF

*IF,RES7,GT,TMAXPSTRAIN,THEN
TMAXPSTRAIN=RES7
*ENDIF
*IF,RES7,LT,TMINPSTRAIN,THEN
TMINPSTRAIN=RES7
*ENDIF

*IF,RES8,GT,TMAXCSTRAIN,THEN
TMAXCSTRAIN=RES8
*ENDIF
*IF,RES8,LT,TMINCSTRAIN,THEN
TMINCSTRAIN=RES8
*ENDIF

!stress locations

*IF, mrat, NE, 1, THEN

*IF,RES5,LT,NSTRESSPT1,AND,curloadstep,EQ,2,THEN
NSTRESSPT1=RES5
TSTRESSPT1=RES9
*ENDIF

*ENDIF

*IF, mrat, EQ, 1, THEN
```

```
*IF,RES5,GT,NSTRESSPT1,AND,curloadstep,EQ,2,THEN
NSTRESSPT1=RES5
TSTRESSPT1=RES9
*ENDIF

*ENDIF




*IF, curloadstep,GE,3,AND,curloadstep,LE,6,THEN
*IF,RES5,LT,NMINSTRESSCYC1,THEN
NMINSTRESSCYC1=RES5
TMINSTRESSCYC1=RES9
*ENDIF
*ENDIF

*IF, curloadstep,GE,3,AND,curloadstep,LE,6,THEN
*IF,RES5,GT,NMAXSTRESSCYC1,THEN
NMAXSTRESSCYC1=RES5
TMAXSTRESSCYC1=RES9
*ENDIF
*ENDIF

*IF, curloadstep,GE,7,AND,curloadstep,LE,10,THEN
*IF,RES5,LT,NMINSTRESSCYC2,THEN
NMINSTRESSCYC2=RES5
TMAXSTRESSCYC1=RES9
*ENDIF
*ENDIF


*IF, curloadstep,GE,7,AND,curloadstep,LE,10,THEN
*IF,RES5,GT,NMAXSTRESSCYC2,THEN
NMAXSTRESSCYC2=RES5
TMAXSTRESSCYC2=RES9
*ENDIF
*ENDIF






*IF,t,EQ,LOADSUBS(1,2),AND,curloadstep,EQ,2,THEN
NSTRESSPT2=RES5
TSTRESSPT2=RES9
*ENDIF

*IF,t,EQ,LOADSUBS(1,6),AND,curloadstep,EQ,6,THEN
NSTRESSPT3=RES5
TSTRESSPT3=RES9
*ENDIF

*IF,t,EQ,LOADSUBS(1,3),AND,curloadstep,EQ,3,THEN
NSTRESSPT4=RES5
TSTRESSPT4=RES9
*ENDIF

*IF,t,EQ,LOADSUBS(1,7),AND,curloadstep,EQ,7,THEN
NSTRESSPT5=RES5
TSTRESSPT5=RES9
*ENDIF

*IF,t,EQ,LOADSUBS(1,4),AND,curloadstep,EQ,4,THEN
NSTRESSPT6=RES5
TSTRESSPT6=RES9
*ENDIF
```

```
*IF,t,EQ,LOADSUBS(1,8),AND,curloadstep,EQ,8,THEN
NSTRESSPT7=RES5
TSTRESSPT7=RES9
*ENDIF

*IF,t,EQ,LOADSUBS(1,10),AND,curloadstep,EQ,10,THEN
NSTRESSPT8=RES5
TSTRESSPT8=RES9
*ENDIF

!*IF,RES3,GT,NMAXPSTRAINCYC1,AND,curloadstep,EQ,6,THEN
!NMAXPSTRAINCYC2=RES3
!*ENDIF
!*IF,RES3,LT,NMINPSTRAINCYC1,AND,curloadstep,EQ,4,THEN
!NMINPSTRAINCYC2=RES3
!*ENDIF

!*IF,RES3,GT,NMAXPSTRAINCYC2,AND,curloadstep,EQ,10,THEN
!NMAXPSTRAINCYC2=RES3
!*ENDIF
!*IF,RES3,LT,NMINPSTRAINCYC2,AND,curloadstep,EQ,8,THEN
!NMINPSTRAINCYC2=RES3
!*ENDIF

!*IF,RES7,GT,TMAXPSTRAINCYC1,AND,curloadstep,EQ,6,THEN
!TMAXPSTRAINCYC2=RES7
!*ENDIF
!*IF,RES7,LT,TMINPSTRAINCYC1,AND,curloadstep,EQ,4,THEN
!TMINPSTRAINCYC2=RES7
!*ENDIF

!*IF,RES7,GT,TMAXPSTRAINCYC2,AND,curloadstep,EQ,10,THEN
!TMAXPSTRAINCYC2=RES7
!*ENDIF
!*IF,RES7,LT,TMINPSTRAINCYC2,AND,curloadstep,EQ,8,THEN
!TMINPSTRAINCYC2=RES7
!*ENDIF



*IF, curloadstep,GE,3,AND,curloadstep,LE,6,THEN
*IF,RES3,LT,NMINPSTRAINCYC1,THEN
NMINPSTRAINCYC1=RES3
TMINPSTRAINCYC1=RES7
*ENDIF
*ENDIF

*IF, curloadstep,GE,3,AND,curloadstep,LE,6,THEN
*IF,RES3,GT,NMAXPSTRAINCYC1,THEN
NMAXPSTRAINCYC1=RES3
TMAXPSTRAINCYC1=RES7
*ENDIF
*ENDIF

*IF, curloadstep,GE,7,AND,curloadstep,LE,10,THEN
*IF,RES3,LT,NMINPSTRAINCYC2,THEN
NMINPSTRAINCYC2=RES3
TMINPSTRAINCYC2=RES7
*ENDIF
*ENDIF


*IF, curloadstep,GE,7,AND,curloadstep,LE,10,THEN
*IF,RES3,GT,NMAXPSTRAINCYC2,THEN
NMAXPSTRAINCYC2=RES3
TMAXPSTRAINCYC2=RES7
*ENDIF
*ENDIF
```

```
*ENDDO

!*CFOPEN,    FEA_%tmt%_%tmca%_%sr%_%mrat%_%ang%_%DIA_NTCH%_%ANG_NTCH%_%RAD_NTCH%_,data,,append
                        ! lists the num of substeps and the load step after each load step
!TESTSUBNUM='TESTSUBNUM'
!*VWRITE, TESTSUBNUM
!%C
!*VWRITE, curloadstep, LOADSUBS(1,curloadstep)
!(f10.3, 6x f10.3)


*ENDDO

NMAXTOTSTRAIN=NMAXESTRAIN+NMAXPSTRAIN+NMAXCSTRAIN
TMAXTOTSTRAIN=TMAXESTRAIN+TMAXPSTRAIN+TMAXCSTRAIN
NMINTOTSTRAIN=NMINESTRAIN+NMINPSTRAIN+NMINCSTRAIN
TMINTOTSTRAIN=TMINESTRAIN+TMINPSTRAIN+TMINCSTRAIN




NPSTRAINRNGCYC1=abs(NMAXPSTRAINCYC1-NMINPSTRAINCYC1)
NPSTRAINRNGCYC2=abs(NMAXPSTRAINCYC2-NMINPSTRAINCYC2)
NSRELAXCYC1=abs(abs(NSTRESSPT4)-abs(NSTRESSPT2))
NSRELAXCYC2=abs(abs(NSTRESSPT5)-abs(NSTRESSPT3))
!NSTRESSRANGECYC1=abs(NSTRESSPT6-NSTRESSPT2)
!NSTRESSRANGECYC2=abs(NSTRESSPT7-NSTRESSPT3)
!NSTRESSAMPCYC1=(NSTRESSPT6-NSTRESSPT2)/2
!NSTRESSAMPCYC2=(NSTRESSPT7-NSTRESSPT3)/2
!NSTRESSMEANCYC1=(NSTRESSPT6+NSTRESSPT2)/2
!NSTRESSMEANCYC2=(NSTRESSPT7+NSTRESSPT3)/2
TPSTRAINRNGCYC1=abs(TMAXPSTRAINCYC1-TMINPSTRAINCYC1)
TPSTRAINRNGCYC2=abs(TMAXPSTRAINCYC2-TMINPSTRAINCYC2)
TSRELAXCYC1=abs(abs(TSTRESSPT4)-abs(TSTRESSPT2))
TSRELAXCYC2=abs(abs(TSTRESSPT5)-abs(TSTRESSPT3))
!TSTRESSRANGECYC1=abs(TSTRESSPT6-TSTRESSPT2)
!TSTRESSRANGECYC2=abs(TSTRESSPT7-TSTRESSPT3)
!TSTRESSAMPCYC1=(TSTRESSPT6-TSTRESSPT2)/2
!TSTRESSAMPCYC2=(TSTRESSPT7-TSTRESSPT3)/2
!TSTRESSMEANCYC1=(TSTRESSPT6+TSTRESSPT2)/2
!TSTRESSMEANCYC2=(TSTRESSPT7+TSTRESSPT3)/2

!*IF, NSTRESSPT2, LT, NSTRESSPT3, AND, mrat, NE, 1, THEN
!NMINSTRESSCYC1=NSTRESSPT2
!NMAXSTRESSCYC1=NSTRESSPT6
!TMINSTRESSCYC1=TSTRESSPT2
!TMAXSTRESSCYC1=TSTRESSPT6
!*ENDIF

!*IF, NSTRESSPT3, LT, NSTRESSPT8, AND, mrat, NE, 1, THEN
!NMINSTRESSCYC2=NSTRESSPT3
!NMAXSTRESSCYC2=NSTRESSPT7
!TMINSTRESSCYC2=TSTRESSPT3
!TMAXSTRESSCYC2=TSTRESSPT7
!*ENDIF

!*IF, NSTRESSPT2, GE, NSTRESSPT3, AND, mrat, NE, 1, THEN
!NMINSTRESSCYC1=NSTRESSPT3
!NMAXSTRESSCYC1=NSTRESSPT6
!TMINSTRESSCYC1=TSTRESSPT3
!TMAXSTRESSCYC1=TSTRESSPT6
!*ENDIF

!*IF, NSTRESSPT3, GE, NSTRESSPT8, AND, mrat, NE, 1, THEN
!NMINSTRESSCYC2=NSTRESSPT8
!NMAXSTRESSCYC2=NSTRESSPT7
!TMINSTRESSCYC2=TSTRESSPT8
!TMAXSTRESSCYC2=TSTRESSPT7
!*ENDIF
```

```
!*IF, NSTRESSPT2, GE, NSTRESSPT3, AND, mrat, EQ, 1, THEN
!NMAXSTRESSCYC1=NSTRESSPT2
!NMINSTRESSCYC1=NSTRESSPT6
!TMAXSTRESSCYC1=TSTRESSPT2
!TMINSTRESSCYC1=TSTRESSPT6
!*ENDIF

!*IF, NSTRESSPT3, GE, NSTRESSPT8, AND, mrat, EQ, 1, THEN
!NMAXSTRESSCYC2=NSTRESSPT3
!NMINSTRESSCYC2=NSTRESSPT7
!TMAXSTRESSCYC2=TSTRESSPT3
!TMINSTRESSCYC2=TSTRESSPT7
!*ENDIF

!*IF, NSTRESSPT2, LT, NSTRESSPT3, AND, mrat, EQ, 1, THEN
!NMAXSTRESSCYC1=NSTRESSPT3
!NMINSTRESSCYC1=NSTRESSPT6
!TMAXSTRESSCYC1=TSTRESSPT3
!TMINSTRESSCYC1=TSTRESSPT6
!*ENDIF

!*IF, NSTRESSPT3, LT, NSTRESSPT8, AND, mrat, EQ, 1, THEN
!NMAXSTRESSCYC2=NSTRESSPT8
!NMINSTRESSCYC2=NSTRESSPT7
!TMAXSTRESSCYC2=TSTRESSPT8
!TMINSTRESSCYC2=TSTRESSPT7
!*ENDIF


*CFOPEN, FEA_%tmt%_%tmca%_%sr%_%mrat%_%ang%_%DIA_NTCH%_%ANG_NTCH%_%RAD_NTCH%_,data,,append
PARAMETERS='PARAMETERS'
*VWRITE, PARAMETERS
%C
*VWRITE, sr, tmca, tmt, re, strain_rate, total_cycles, ang, tens_hold, comp_hold, Kts
(e10.3, 6x f10.3, 6x f10.3, 6x f10.3, 6x e10.3, 6x f10.3, 6x f10.3, 6x e10.3, 6x e10.3, 6x f10.3)
EXTREME_VALUES='EXTREME_VALUES'
*VWRITE, EXTREME_VALUES
%C
*VWRITE, MAXTEMP,MINTEMP, NMAXESTRAIN, NMINESTRAIN, NMAXPSTRAIN, NMINPSTRAIN, NMAXCSTRAIN,
NMINCSTRAIN, NMAXSTRESS, NMINSTRESS, TMAXESTRAIN, TMINESTRAIN, TMAXPSTRAIN, TMINPSTRAIN,
TMAXCSTRAIN, TMINCSTRAIN, TMAXSTRESS, TMINSTRESS
(F10.2,6X F10.2, 6X E11.5, 6X E11.5,6X E11.5, 6X E11.5,6X E11.5, 6X E11.5,6X F10.4,6X F10.4, 6X E11.5, 6X E11.5,6X E11.5,
6X E11.5,6X E11.5, 6X E11.5,6X F10.4,6X F10.4)

!*CFOPEN,
FEA_NOTCH_CLEANED_%tens_hold%_%comp_hold%_%first_hold%_%strain_rate%_%total_cycles%_%DIA_NTCH%_%ANG_
NTCH%_%RAD_NTCH%_,data,,append
*CFOPEN, FEA_NOTCH_CLEANED,data,,append
*VWRITE, sr, tmca, tmt, re, ang, MAXTEMP,MINTEMP, NMAXESTRAIN, NMINESTRAIN, NMAXPSTRAIN, NMINPSTRAIN,
NMAXCSTRAIN, NMINCSTRAIN, NMAXSTRESS, NMINSTRESS, NMAXTOTSTRAIN, NMINTOTSTRAIN
(e10.3, 6x f10.3, 6x f10.3, 6x f10.3, 6x F10.3, 6x F10.2,6X F10.2, 6X E11.5, 6X E11.5,6X E11.5, 6X E11.5,6X E11.5, 6X E11.5,6X
F10.4,6X F10.4,6X E11.5, 6X E11.5)

!*CFOPEN,
FEA_TEST_CLEANED_%tens_hold%_%comp_hold%_%first_hold%_%strain_rate%_%total_cycles%_%DIA_NTCH%_%ANG_N
TCH%_%RAD_NTCH%_,data,,append
*CFOPEN, FEA_TEST_CLEANED,data,,append
*VWRITE, sr, tmca, tmt, re, ang, MAXTEMP,MINTEMP, TMAXESTRAIN, TMINESTRAIN, TMAXPSTRAIN, TMINPSTRAIN,
TMAXCSTRAIN, TMINCSTRAIN, TMAXSTRESS, TMINSTRESS, TMAXTOTSTRAIN, TMINTOTSTRAIN
(e10.3, 6x f10.3, 6x f10.3, 6x f10.3, 6x F10.3, 6x F10.2,6X F10.2, 6X E11.5, 6X E11.5,6X E11.5, 6X E11.5,6X E11.5, 6X E11.5,6X
F10.4,6X F10.4,6X E11.5, 6X E11.5)

!*CFOPEN,
FEA_CLEANED_TOTALS_%tens_hold%_%comp_hold%_%first_hold%_%strain_rate%_%total_cycles%_%DIA_NTCH%_%ANG
_NTCH%_%RAD_NTCH%_,data,,append
*CFOPEN, FEA_CLEANED_TOTALS,data,,append
```

```
*VWRITE, sr, tmca, tmt, re, ang, MAXTEMP,MINTEMP, NMAXTOTSTRAIN, NMINTOTSTRAIN, NMAXSTRESS, NMINSTRESS,
TMAXTOTSTRAIN, TMINTOTSTRAIN, TMAXSTRESS, TMINSTRESS
(e10.3, 6x f10.3, 6x f10.3, 6x f10.3, 6x F10.3, 6x F10.2,6X F10.2, 6X E11.5, 6X E11.5,6X F10.4,6X F10.4, 6X E11.5, 6X E11.5,6X
F10.4,6X F10.4)

*CFOPEN, FEA_NOTCH_CLEANED2,data,,append
*VWRITE, sr, tmca, tmt, re, strain_rate, total_cycles, ang, ten_hold, comp_hold, NSTRESSPT1, NSRELAXCYC1,
NSRELAXCYC2, NMINSTRESSCYC1, NMAXSTRESSCYC1, NMINSTRESSCYC2, NMAXSTRESSCYC2,
NPSTRAINRNGCYC1, NPSTRAINRNGCYC2
(e10.3, 6x f10.3, 6x f10.3, 6x f10.3, 6x e10.3, 6x f10.3, 6x f10.3, 6x e10.3, 6x e10.3, 6X F10.4, 6X F10.4, 6X F10.4, 6X F10.4, 6X
F10.4, 6X F10.4, 6X F10.4, 6X E11.5, 6X E11.5)

*CFOPEN, FEA_TEST_CLEANED2,data,,append
*VWRITE, sr, tmca, tmt, re, strain_rate, total_cycles, ang, ten_hold, comp_hold, TSTRESSPT1, TSRELAXCYC1, TSRELAXCYC2,
TMINSTRESSCYC1, TMAXSTRESSCYC1, TMINSTRESSCYC2, TMAXSTRESSCYC2, TPSTRAINRNGCYC1,
TPSTRAINRNGCYC2
(e10.3, 6x f10.3, 6x f10.3, 6x f10.3, 6x e10.3, 6x f10.3, 6x f10.3, 6x e10.3, 6x e10.3, 6X F10.4, 6X F10.4, 6X F10.4, 6X F10.4, 6X
F10.4, 6X F10.4, 6X F10.4, 6X E11.5, 6X E11.5)

/OUTPUT,FEA_Junk5,txt

!********************************************************************************
```

APPENDIX E: AVERAGE TENSILE STRESS ESTIMATION

Area-based methods for estimation of average tensile stress σ^{+}_{avg}:

LCF / OPTMF:

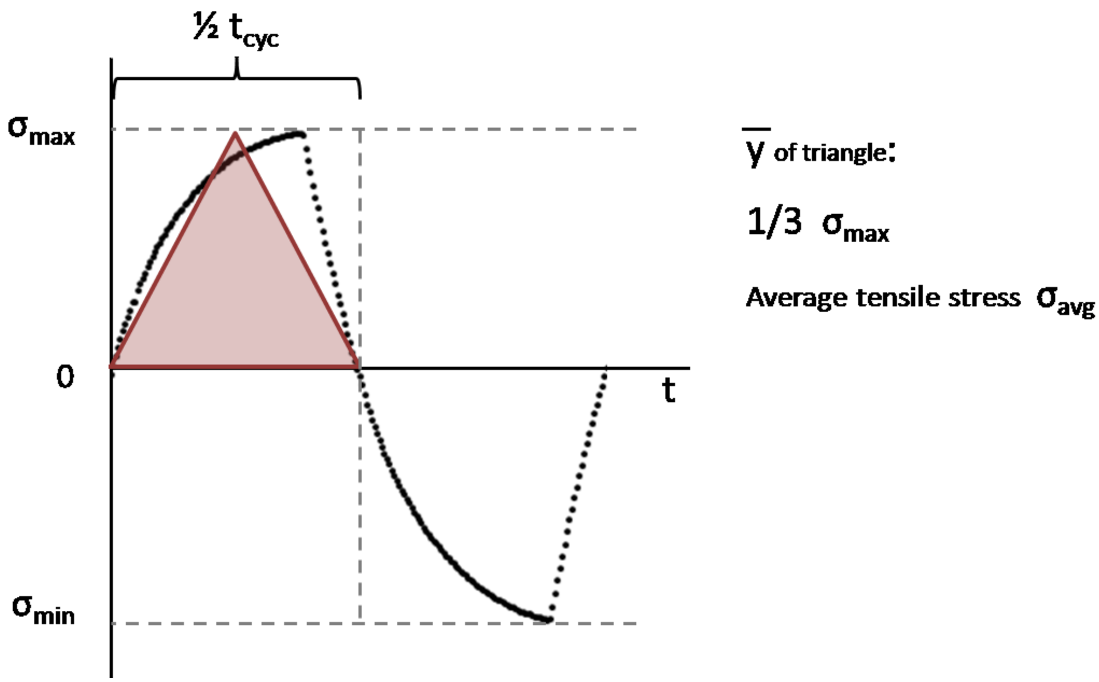

Notes: Slightly over-conservative. Executed similarly regardless of mean stress presence. Isosceles triangle base can be adjusted to reflect time in tension instead of ½ cycle time for OPTMF cases.

IPTMF:

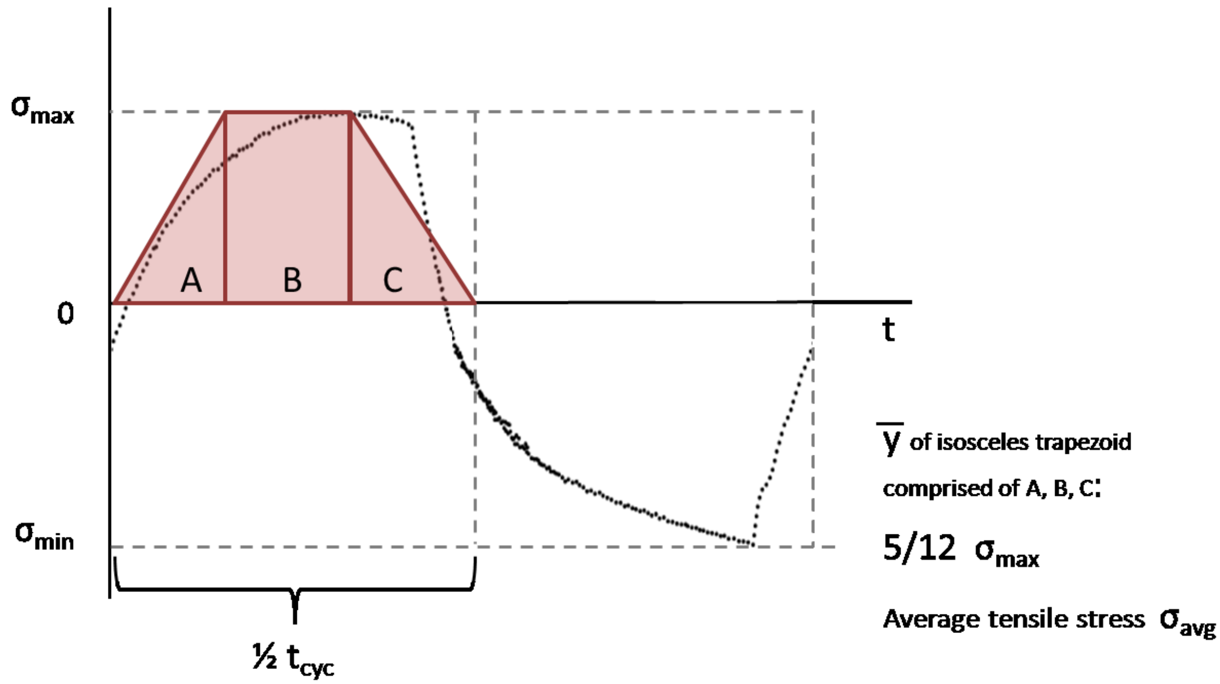

Notes: Assumes compressive mean stress. Base lengths of A, B, C are identical. Over-estimates stress in region A and under-estimates stress in region C.

LCF / IPTMF with dwell period:

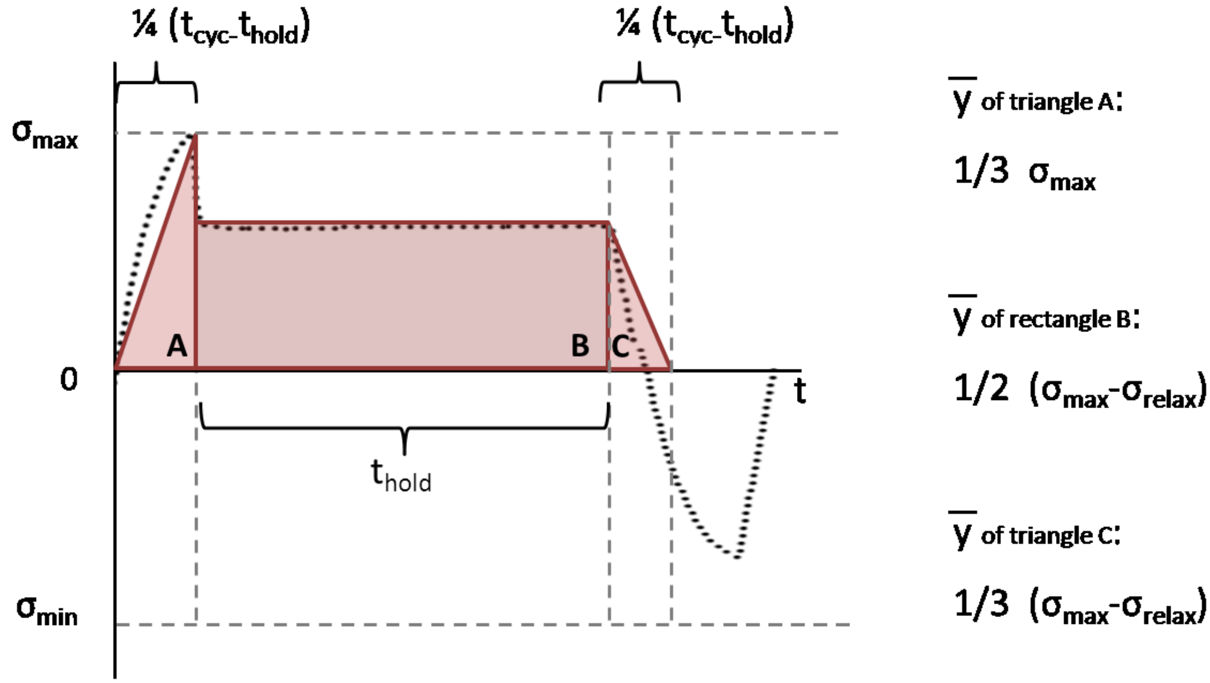

$$\sigma_{avg} = \frac{\frac{1}{4}(t_{cyc}-t_{hold})(y_A + y_C) + t_{hold}(y_B)}{\frac{1}{2}(t_{cyc}-t_{hold}) + t_{hold}}$$

Notes: Assumes small compressive mean stress. Under-estimates stress in region A, over-estimates stress in region C.

LIST OF REFERENCES

Aghajani, A., Somsen, C., Pesicka, J., Bendick, W., Hahn, B., and Eggler, G., “Microstructural evolution in T24, a modified 2(1/4)Cr–1Mo steel during creep after different heat treatments,” Materials Science & Engineering: A. Vols. 510-511, pp. 130-135, 2009.

Ahmad, H. Y., de los Rios, E. R., and Yates, J. R., “The Influence of Notch Plasticity on Short Fatigue Crack Behavior,” Fatigue Fracture of Engineering Materials and Structures. Vol. 17(2), pp. 235-242, 1994.

Ahmad, H., and Yates, J., “An Elastic-plastic Model for Fatigue Crack Growth at Notches,” Fatigue and Fracture in Engineering Materials Structures. Vol. 17(6), pp.651-660, 1994.

Algarni, M. S., Jia, Y., Karl, J., Gordon, A. P. and Bai, Y., "Linkage Between Ductile Fracture and Extremely Low Cycle Fatigue of Inconel 718 under Multiaxial Loading Conditions," Proceedings of ASME Turbo Expo, 2013.

Argon, A., Chen, I., and Lau, C., “Intergranular Cavitation in Creep: Theory and Experiments,” AGARD Conference Proceedings, pp. 46-85, 1980.

Ashby, M. F., 2005. Materials Selection in Mechanical Design, Third Edition, Elsevier Butterworth-Heinemann, Oxford, UK.

Bayoumi, M.R., and Abd El Latif, A.K., “Low-cycle fatigue behaviour of notched AISI 304 stainless steel specimens,” Journal of Materials Science. Vol. 30(15), pp. 3944-3953, 1995.

Beckitt, F.R., and Gladman, T., Report No. PROD/PM/6041/l/71A, British Steel, Special Steels Department, 1971.

Bhaduri, A.K., Gill, T.P.S., Albert, S.K., Shanmugam, K., and Iyer, D.R., "Repair Welding of Cracked Steam Turbine Blades using Austenitic and Martensitic Stainless Steel Consumables," Nuclear Engineering and Design. Vol. 206(2-3), pp. 249-259, 2001.

Boss, M., Gadoury, T., Feeny, S., and Montgomery, M., "Recent Advances in Ultra Super Critical Steam Turbine Technology," GE Energy, 2010.

Boyer, H. and Gall, T., Editors, 1985. Metals Handbook, American Society for Metals, Materials Park, OH.

Cai, C., Liaw, P.K., Ye, M., and Yu, J., "Recent Developments in the Thermomechanical Fatigue Life Prediction of Superalloys," Journal of Materials. Vol. 51(4), 1999.

Chataigner, E., and Remy, L., "Thermomechanical Fatigue Behavior of Coated and Bare Nickel-Based Superalloy Single Crystals," Thermomechanical Fatigue Behavior of Materials, ASTM STP 1263, pp. 3–25, 1996.

Chen, I-W., and Argon, A. S., "Creep Cavitation in 304 Stainless Steel," Acta Metallurgica. Vol. 29(7), pp. 1321-1333, 1981.

Chopra, O.K., and Natesan, K., "Interpretation of High-Temperature Creep of Type 304 Stainless Steel," Metallurgical Transactions A (Physical Metallurgy and Materials Science). Vol. 8A(4), pp. 633-638, 1977.

Coble, R.L., "Model for Boundary Diffusion Controlled Creep in Polycrystalline Materials," Journal of Applied Physics. Vol. 34(6), pp. 1679-1682, 1963.

Coffin, Jr., L., "Study of Effects of Cyclic Thermal Stresses on Ductile Metal," Transactions of the American Society of Mechanical Engineers. Vol. 76(6), pp. 931-949, 1954.

Coffin, L. F., 1979. "Fatigue in Machines and Structures – Power Generation," Fatigue and Microstructure, Meshii, M., Editor, ASM International, Metals Park, OH.

Coffin, L.F., “Design Aspects of High Temperature Fatigue with Particular Reference to Thermal Stresses,” American Society for Mechanical Engineers - Papers, 1954.

Colin, J., Fatemi, A., Taheri, S., “Fatigue Behavior of Stainless Steel 304L Including Strain Hardening, Prestraining, and Mean Stress Effects,” Journal of Engineering Materials and Technology. Vol. 132, pp. 08-13, 2010.

Coppola, T., Riscifuli, S., Tassa, O., and Pasquero, G., “Thermomechanical Fatigue Behavior of Bare and Coated CMSX-4,” Journal of Engineering for Gas Turbines and Power. Vol. 132(1), pp. 12101/01-12101/05, 2010.

Davis, J., Editor, 1994. ASM Specialty Handbook- Stainless Steels, ASM International, Materials Park, OH.

Deleury, M. J., Donati, J. R., and Strudel, J. L., “Fluage et Evolution Structurale d'Aciers Austinetiques,” Annales de Chimie – Science des Materiaux. Vol. 6, p. 59, 1981.

DeMarco, J. P., Hogan, E. A., Stewart, C. M., and Gordon, A. P., “An Efficient Method for the Optimization of Viscoplastic Constitutive Model Constants,” Proceedings of ASME Turbo Expo, 2010.

Di Schino, A., Kenny, J. M., Mecozzi, M. G., and Barteri, M., “Development of High Nitrogen, Low Nickel, 18% Cr Austenitic Stainless Steels,” Journal of Materials Science. Vol. 35(19), pp. 4803-4808, 2000.

E-2368, 2004. Standard Practice for Strain-Controlled Thermomechanical Fatigue Testing, ASTM International, West Conshocken, PA.

Embley, G. T., and Russell, E. S., “Thermal-Mechanical Failure of Gas Turbine Bucket Alloys,” Proceedings of the First Parsons International Turbine Conference, 1984.

Endo, T., Kondo, Y., & Kadoya, Y., “Establishment of Fatigue Test Method for Turbine Blade Fastener,” Structural Integrity of Fasteners, ASTM STP 1236, pp. 20-31, 1995.

Engler-Pinto, C., Sehitoglu, H., and Maier, H., “Cyclic Behavior of AL319-T7B Under Isothermal and Nonisothermal Conditions,” ASTM Special Technical Publication, ASTM STP 1428, pp. 45–64, 2003.

Engler-Pinto, C.C., Jr., and Rezai-Aria F., “Thermo-mechancial Fatigue Investgation of Single Crystal Nickel Base Superalloy SRR99,” Thermo-mechanical Fatigue Behaviors of Materials Volume Three, ASTM STP 1371, pp. 150-164, 2000.

Esmaeili, S., Engler-Pinto, C.C., Jr., Ilschner, B., and Rezai-Aria, F., “Interaction Between Oxidation and Thermomechanical Fatigue in IN738LC Superalloy – I,” Scripta Metallurgica et Materialia. Vol. 32(11), pp. 1777-1781, 1995.

Evans, W., Jones, J., and Williams, S., “The Interaction Between Fatigue, Creep, and Environmental damage in Ti6246 and Udimet 720Li,” International Journal of Fatigue. Vol. 27, pp. 1473-1484, 2005.

Farmer, R., “Elk River Peaking Plant Does 0-to-150 MW in 10 Minutes,” Gas Turbine World. Vol. 40(1), pp. 10-13, 2010.

FengXu, Jian. “Discussion on the Sustainability of Stainless Steel applied in Architecture,” Advanced Materials Research. Vol. 476-478, pp. 1553-1556, 2012.

Fogel, L.J., Owens, A.J., and Walsh, M.J., Editors. 1966. Artificial Intelligence Through Simulated Evolution, John Wiley & Sons, New York, NY.

Frost, H.J., and Ashby, M.F., Editors, 1982. Deformation-Mechanism Maps: The Plasticity and Creep of Metals and Ceramics, Pergamon Press, Oxford, UK.

Frost, H.J., Ashby, M.F., 1977. Fundamental Aspects of Structural Alloy Design, Jaffee, R.I., and Wilcox, B.A., Editors. Plenum Press, New York, NY.

Frost, N., "A Relation Between the Critical Alternating Propagation Stress and Crack Length for Mild Steel," Proceedings of the Institution of Mechanical Engineers. Vol. 173, pp. 811-834, 1959.

Frost, N., "Crack Formation and Stress Concentration Effects in Direct Stress Fatigue," Engineer. Vol. 200, pp. 464-467, 501-503, 1955.

Frost, N., "Non-Propagating Cracks in Vee-Notched Specimens Subject to Fatigue Loading," Aeronautical Quarterly. Vol. 8, pp.1-20, 1955.

Frost, N., and Dugdale, D., "Fatigue Tests on Notched Mild Steel Plates with Measurements of Fatigue Cracks," Journal of Mechanics and Physics of Solids. Vol. 5, pp. 182-192, 1957.

Fujino, M., and Taira, S., "Effect of Thermal Cycling of Low Cycle Fatigue Life of Steels and Grain Boundary Sliding Characteristics," Proceedings of the International Conference on Mechanics 3, 1979.

Glinka, G., "Calculation of Inelastic Notch-Tip Strain-Stress Histories Under Cyclic Loading," Engineering Fracture Mechanics. Vol. 22(5), pp. 839-854, 1985.

Glinka, G., "Energy Density Approach to Calculation of Inelastic Strain-Stress Near Notches and Cracks," Engineering Fracture Mechanics. Vol. 22(3), pp. 485-508, 1985.

Gordon, A. P., Williams, E. P., and Schulist, M., "Applicability of Neuber's Rule to Thermomechanical Fatigue," Proceedings of ASME Turbo Expo, 2008.

Goswami, T., and Hanninen, H., "Dwell Effects on High Temperature Fatigue Damage Mechanisms," Materials and Design. Vol. 22(3), pp. 217-236, 2001.

Halford, G. R., and Manson, S. S., “Life Prediction of Thermal-Mechanical Fatigue using Strain Range Partitioning,” Thermal Fatigue of Materials and Components, ASTM STP 612, pp. 239-254, 1976.

Halford, G. R., Saltsman, J. F., Verrilli, M. J., Arya, V., “Application of a Thermal Fatigue Life Prediction Model to High-Temperature Aerospace Alloys B1900+HF and Haynes 188”, Advances in Fatigue Lifetime Predictive Techniques, ASTM STP 1122, pp. 107–119, 1992.

Halford, G.R., Lerch, B.A., Saltsman, J.F., and Arya, V.K., “Proposed Framework for Thermomechanical Fatigue Life Prediction of Metal Matrix Composites,” Thermomechanical Fatigue Behavior of Materials, ASTM STP 1186, pp.176-194, 1993.

Hammouda, M., 1978. “Fatigue Crack Initiation at Notches,” Ph.D. Thesis, University of Cambridge.

Hammouda, M., and Miller, K. J., “Prediction of Fatigue Lifetime of Notched Members,” Fatigue of Engineering Materials and Structures. Vol. 2, pp. 377-386, 1980.

Hansen, D. and Puyear, R., Editors, 1996. Materials Selection for Hydrocarbon and Chemical Plants, CRC Press, Boca Raton, FL.

Harvey, P., Editor, 1982. Engineering Properties of Steels, ASM International, Materials Park, OH.

Hayhurst, D. R., “Estimates of the Creep Rupture Lives of Structures Subjected to Cyclic Loading,” International Journal of Mechanical Sciences. Vol. 18, pp. 75-83, 1976.

Hayhurst, D.R., and Webster, G.A., 1987. “An Overview on Studies of Stress State Effects During Creep of Circumferentially Notched Bars,” Techniques for Multiaxial Creep

Testing, pp. 137-175, Gooch, D.J., and How, I.M., Editors. Elsevier Applied Science, Amsterdam, The Netherlands.

Holdsworth, S.R., Mazza, E., Jung, A., "Creep-Fatigue Damage Development During Service-Cycle Thermo-Mechanical Fatigue Tests of 1CrMoV Rotor Steel," 9th International Conference on The Mechanical Behavior of Materials, 2003.

Howe, A., Parker, S., Beaverstock, R., & Van Haaften, W., "Progress and Issues in Thermomechanical Simulation: Experience in Tata Steel (Europe)," Materials Science Forum. Vol. 706-709, pp. 43-48, 2012.

Huntz, A., Reckmann, A., Haut, C., Severac, C., Herbst, M., Resende, F., and Sabioni, A., "Oxidation of AISI 304 and AISI 439 stainless steels," Materials Science & Engineering: A. Vol. 447(1-2), pp. 266-76, 2007.

Hyde, T. H., Sabesan, R., and Leen, S. B., "Approximate Prediction Methods for Notch Stresses and Strain under Elastic-Plastic and Creep Conditions," Journal of Strain Analysis. 1989. Vol. 39(5), pp. 515-527, 2004.

Ishida, T., Harayama, Y., and Yaguchi, S., "Oxidation of 304 stainless steel in high-temperature steam," Journal of Nuclear Materials, Vol. 140, pp. 74-84, 1986.

James, G.H., "An Experimental Comparison of Several Current Viscoplastic Constitutive Models at Elevated Temperature," Journal of Engineering Materials and Technology, Transactions of the ASME. Vol. 109(2), pp. 130-139, 1987.

Kadioglu, Y., and Sehitoglu, H., "Modeling of Thermomechanical Fatigue Damage in Coated Alloys," Thermomechanical Fatigue Behavior of Materials, ASTM STP 1186, pp. 17–34, 1993.

Kagawa, H., and Asada, Y., “Extension of Miller's Constitutive Model for Multiaxial Deformation,” ASME International Conference on Advances in Life Prediction Methods. Pp. 33-39, 1983.

Karl, J., 2006. “Automated Filtering of Acoustic Emission Data Using Frequency Principal Component Extraction,” M.S. Thesis, Embry-Riddle Aeronautical University.

Karl, J., and Gordon, A. P., "Life Prediction Feasibility in TMF via Stress/Strain Data from a Viscoplasticity Numerical Model," Proceedings of ASME Turbo Expo, 2012.

Karl, J., and Gordon, A. P., “Computational Viscoplasticity-Based Modeling of Stress/Strain Response in Thermomechanical Fatigue Loads,” Proceedings of the 50th AIAA Aerospace Sciences Meeting, 2012.

Kassner, M.E., and Perez-Prado, M.-T., Editors, 2004. Fundamentals of Creep in Metals and Alloys, Elsevier B.V., Amsterdam, The Netherlands.

Kawamoto, M., Tanaka, T., and Nakajima, H., “Effect of Several Factors on Thermal Fatigue,” Journal of Materials. Vol. 1(4), pp. 719-758, 1966.

Keisler, J. M., Chopra, O. K., Shack, W. J., “Statistical Models for Estimating Fatigue Strain-Life Behavior of Pressure Boundary Materials in Light Water Reactor Environments,” Nuclear Engineering and Design. Vol. 167, pp 129-154, 1996.

Kitagawa, H., and Takahashi, S., “Applicability of Fracture Mechanics to Very Small Cracks or Cracks in the Early Stage,” Proceedings of the Second International Conference on the Mechanical Behavior of Materials. Pp. 627-631, 1976.

Kleinpass, B., Löhe, D., Lang, K.-H., and Macherauch, E., “Influence of the Mechanical Strain Amplitude on the In-Phase and Out-of-Phase Thermo-Mechanical Fatigue Behaviour of

NiCr22Co12Mo9," Thermo-mechanical Fatigue Behavior of Materials Volume Three, ASTM STP 1371, pp. 36-52, 2000

Kraft, S., and Gordon, A. P., "Yield Behavior of a Twill Dutch Woven Wire Mesh Via Experiments and Numerical Modeling," ASME Journal of Applied Mechanics, (Accepted for publication, 2012).

Kunio, T., Shimizu, M., Yamada, K., Fukomoto, M., and Ito, M., "Role of Oxidation in Micro-Fracture Process of AISI 316 Stainless Steel in High Temperature Low Cycle Fatigue," Advances in Fracture Research (Fracture 84). Proceedings of the 6th International Conference on Fracture. Vol. 3, pp. 2257-2264, 1984.

Kuwabara, K., and Nitta, A., "Effect of Strain Hold Time of High Temperature on Thermal Fatigue of Type 304 Stainless Steel," Proceedings of the ASME-MPC Symposium on Creep-Fatigue Interaction, 1976.

Kuwabara, K., and Nitta, A., "Isothermal and Thermal Fatigue Strength of Cr-Mo-V Steel for Turbine Rotors," Central Research Institute of Electric Power Industry Reports. E277005, 1977.

Kuwabara, K., and Nitta, A., "Thermal-Mechanical Low Cycle Fatigue under Creep-Fatigue Interaction on Type 304 Stainless Steels," Fatigue and Fracture of Engineering Materials and Structures. Vol. 2, pp. 293-304, 1979.

Lacombe, P., Baroux, B., Béranger, Editors, 1993. Les Aciers Inoxydables, Davidson, J.H., and Lindquist, J.B., Translators. Les Editions de Physique, Les Ulis, France.

Laidler, K.J., Editor, 1993. The World of Physical Chemistry, Oxford University Press, New York, NY.

Lampman, S. and Zorc, T., Editors, 1981. ASM Handbook- Properties and Selection: Irons, Steels, and High-Performance Alloys, ASM International, Metals Park, OH.

Lampman, S. and Zorc, T., Editors, 2007. ASM Handbook- Properties and Selection: Irons, Steels, and High-Performance Alloys, ASM International, Metals Park, OH.

Landgraf, R.W., Morrow, J.D., and Endo, T., "Determination of Cyclic Stress-Strain Curve," Journal of Materials. Vol. 4(1), pp. 176-188, 1969.

Langevoort, J., Hanekamp, L., and Gellings, P., "On the kinetics of oxidization of austenitic stainless steels AISI 304 and Incoloy 800H," Applied Surface Science. Vol. 28(3), pp. 189-203, 1987.

Langevoort, J., Sutherland, I., Hanekamp, L., and Gellings, P., "On the oxide formation on stainless steels AISI 304 and Incoloy 800H investigated with XPS," Applied Surface Science. Vol. 28(2), pp. 167-79, 1987.

Leckie, F. R., and Hayhurst, D. R., "Constitutive Equations for Creep Rupture," Acta Metallurgica. Vol. 24(11), pp. 1059-1070, 1977.

Lemaitre, J., and Chaboche, J. L., "A Non-Linear Model of Creep-Fatigue Damage Accumulation and Interaction," Proceedings of the International Union of Theoretical and Applied Mechanics Symposium on Mechanics of Visco-elastic Media and Bodies, 1974.

Lemaitre, J., and Chaboche, J. L., "A Non-Linear Model of Creep-Fatigue Damage Accumulation and Interaction," Proceedings of the International Union of Theoretical and Applied Mechanics Symposium on Mechanics of Visco-elastic Media and Bodies, 1974.

Lemaitre, J., and Plumtree, A., "Application of Damage Concepts to Predict Creep-Fatigue Failures," Proceedings of the Joint ASME/CSME Pressure Vessels and Piping Conference, 1978.

Linde, L., and Henderson, P.J., 1998. "High Temperature Fatigue Behavior of Coated IN738LC," Low Cycle Fatigue and Elasto-Plastic Behavior of Materials, pp. 143-148, Rie, K.-T., and Portella, P.D. Elsevier Science, Amsterdam, The Netherlands.

Lozano-Perez, S., Kruska, K., Iyengar, I., Terachi, T., and Yamada, T., "The role of cold work and applied stress on surface oxidation of 304 stainless steel," Journal of Corrosion Science. Vol. 56, pp 78-85, 2012.

Majumdar, S., 1987. "Thermo-Mechanical Fatigue of Type 304 Stainless Steel," Thermal Stress, Material Deformation, and Thermo-Mechanical Fatigue, Sehitoglu, H. and Zamrik, S. Y., Editors, ASME Press, New York, NY.

Manson, S. S., Halford, G. R., and Hirschberg, M. H., 1971. "Creep-Fatigue Analysis by Strain Range Partitioning," Design for Elevated Temperature Environment, pp. 12-24, Zamrik, S. Y., Editor. ASME, New York, NY.

Manson, S.S., "Behavior of materials under conditions of thermal stress," National Advisory Committee for Aeronautics -- Technical Notes, 1953.

Marshall, P., 1994. Austenitic Stainless Steels: Microstructure and Mechanical Properties, Elsevier, New York, NY.

Maziasz, P.J., Swindeman, R.W., Montague, J.P., Fitzpatrick, M., Browning, P.F., Grubb, J.F., and Klug, R.C., "Improved Creep-resistance of Austenitic Stainless Steel for Compact Gas Turbine Recuperators," Materials at High Temperatures. Vol. 16(4), pp. 207-212, 1999.

Mazur, Z., Luna-Ramirez, A., Juarez-Islas, J. A., Campos-Amezcua, A., "Failure Analysis of a Gas Turbine Blade Made of Inconel 738LC Alloy," Engineering Failure Analysis. Vol. 12, pp. 474-486, 2005.

Mazza, E., Hollenstein, M., Holdsworth, S., and Skelton, R. P., "Notched Specimens Thermo-Mechanical Fatigue of a 1CrMoV Turbine Steel," Nuclear Engineering and Design. Vol. 234, pp. 11-24, 2004.

McGuire, M.F., Editor, 2008. Stainless Steel for Design Engineers, ASM International, Materials Park, OH.

Meyers, M.A., and Chawla, K.K., Editors, 2009. Mechanical Behavior of Materials, Cambridge University Press, Cambridge, UK.

Miller, A., "Inelastic Constitutive Model for Monotonic, Cyclic, and Creep Deformation: Part II-Application to Type 304 Stainless Steel," Journal of Engineering Materials and Technology. Vol. 98H(2), pp. 106-113, 1976.

Miller, D., and Priest, R., 1983. "Material Response to Thermal-Mechanical Strain Cycling," High Temperature Fatigue: Properties and Prediction, Skelton, R., Editor, Applied Science Press, London, UK.

Miller, K. J., "Fatigue at Notches: A Review," Journal of Marine Design and Operations. Vol. B8, pp. 49-62, 2005.

Miller, M. P., McDowell, D. L., Oehmke, R. L. T., "A Life Prediction Model for Thermomechanical Fatigue Based on Microcrack Propagation", Thermomechanical Fatigue Behavior of Materials, ASTM STP 1186, pp. 35–49, 1993.

Mitchell, M.R., and Landgraf, R.W., Editors, 1993. Advances in Fatigue Lifetime Predictive Techniques: Second Volume, STP 1211, ASTM International, Philadelphia, PA.

Neu, R., and Sehitoglu, H., "Thermo-Mechanical Fatigue Oxidation, Creep, Part I: Experiments," Metallurgical Transactions A. Vol. 20A, pp. 1755-1767, 1989.

Neu, R., and Sehitoglu, H., "Thermo-Mechanical Fatigue Oxidation, Creep, Part II: Life Prediction," Metallurgical Transactions A. Vol. 20A, pp. 1769-1783, 1989.

Neuber, H., "Theory of Stress Concentration for Shear-Strained Prismatic Bodies with Arbitrary Nonlinear Stress-Strain Laws," ASME Journal of Applied Mechanics. Vol. 28, p. 544, 1961.

Neuber, H., 1937. Kerbspannungslehre: Theorie der Spannungskonzentration, Springer-Verlag, Berlin, Germany.

Nishino, S., and Yamada, K., "Surface and In-Depth Crack Propagation in High Temperature Low-Cycle Fatigue of SUS 316 Stainless Steel," Fatigue & Fracture of Engineering Materials & Structures. Vol. 17(11), pp. 1327-1334, 1994.

Ostergren, W. J., "Damage Function and Associated Failure Equations for Predicting Hold Time and Frequency Effects in Elevated Temperature, Low Cycle Fatigue," Journal of Testing and Evaluation. Vol. 4(5), pp. 327-339, 1976.

Ostergren, W. J., and Krempl, E., "Uniaxial Damage Accumulation Law for Time-Varying Loading Including Creep-Fatigue Interaction," Journal of Pressure Vessel Technology. Vol. 101(2), pp. 118-124, 1979.

Peckner, D. and Bernstein, I., Editors, 1977. Handbook of Stainless Steels, McGraw-Hill Book Company, New York, NY.

Peterson, R., 1953. Stress Concentration Design Factors, John Wiley and Sons, Inc., New York, NY.

Peterson, R., 1959. "Notch Sensitivity," Metal Fatigue, Sines, G. and Waisman, J., Editors. McGraw-Hill Companies, Inc., New York, NY.

Peterson, R., 1974. Stress Concentration Factors, John Wiley and Sons, Inc., New York, NY.

Qiu, J.H., "Effect of Ceramic Heat Insulating Paste on Degree of Sensitization of AISI Type 304 Stainless Steel," British Corrosion Journal. Vol. 33(4), pp. 318-320, 1998.

Rao, J., 2000. Turbine Blade Life Estimation, Alpha Science International, Oxford, UK.

Remy, L., Bernard, H., Malpertu, J. L., Rezai-Aria, F., "Fatigue Life Prediction under Thermo-Mechanical Loading in a Nickel-Base Superalloy," Thermomechanical Fatigue Behavior of Materials, ASTM STP 1186, pp. 3-16, 1993.

Reuchet, J., and Remy, L., "Fatigue Oxidation Interaction in a Superalloy-Application to Life Prediction in High Temperature Low Cycle Fatigue," Metallurgical Transactions A. Vol. 14A, pp. 141-149, 1983.

Riedler, M., Leitner, H., Prillhofer, B., Winter, G., and Eichlseder, W., "Lifetime Simulation of Thermo-Mechanically Loaded Components," Meccanica. Vol. 42(1), pp. 47-59, 2007.

Robinson, E.L., "Effect of Temperature Variation on the Creep Strength of Steel," Trans. ASME. Vol. 60, pp. 253-259, 1938.

Roessle, M.L., and Fatemi, A., "Strain-Controlled Fatigue Properties of Steels and Some Simple Approximations," International Journal of Fatigue. Vol. 22, pp. 495-511, 2000.

Rosa, U., Nagode, M., and Fajdiga, M., "Strain-Life Approach in Thermo-Mechanical Fatigue Evaluation of Complex Structures," Fatigue Fracture in Engineering Materials and Structures. Vol. 30, pp. 808-822, 2007.

Ruano, O.A., and Sherby, O.D., "Low Stress Creep of Fine-Grained Materials at Intermediate Temperatures: Diffusional Creep or Grain Boundary Sliding?," Material Science and Engineering. Vol. 56(2), pp. 167-75, 1982.

Sabioni, A., Ramos, R., Ji, V., and Jomard, F., "Oxygen diffusion study in oxidation films of the AISI 304 austenitic stainless steel," Defect and Diffusion Forum. Vol. 323-325, pp. 345-351, 2012.

Schwefel, H.P., Editor, 1981. Numerical Optimization of Computer Models, John Wiley & Sons, Chichester, UK.

Sehitoglu, H. and Boismier, D. A., "Thermo-Mechanical Fatigue of Mar-M247: Part 2- Life Prediction," Journal of Engineering Materials and Technology. Vol. 112(1), pp. 68-79, 1990.

Sehitoglu, H., "Thermo-Mechanical Fatigue Life Prediction Methods," Advances in Fatigue Lifetime Predictive Techniques, ASTM STP 1263, pp. 27-40, 1996.

Sehitoglu, H., "Thermo-Mechanical Fatigue Life Prediction Methods," Advances in Fatigue Lifetime Predictive Techniques, ASTM STP 1122, pp. 47–75, 1992.

Sehitoglu, H., 1996. "Thermal and Thermomechanical Fatigue of Structural Alloys," Handbook on Fatigue and Fracture, ASM International, Metals Park, OH.

Sehitoglu, H., 2006. "Overview of High Temperature and Thermo-Mechanical Fatigue (TMF)," Presentation given at University of Illinois Urbana-Champaign, Urbana, Ill.

Seifert, T., and Reidel, H., "Mechanism-based Thermomechanical Fatigue Life Prediction of Cast Iron," International Journal of Fatigue. Vol. 32(8), pp. 1358-1367, 2010.

Seifert, T., Schweizer, C., Schlesinger, M., Moser, M., and Eibl, M., "Thermomechanical Fatigue of 1.4849 Cast Steel - Experiments and Life Prediction using a Fracture

Mechanics Approach," International Journal of Materials Research. Vol. 101(8), pp. 942-950, 2010.

Šeruga, D., Fajdiga, M., and Nagode, M., "Creep Damage Calculation for Thermo Mechanical Fatigue," Strojniški vestnik – Journal of Mechanical Engineering. Vol. 57(5), pp. 371-378, 2011.

Sheffler, K. D., "Vacuum Thermal-Mechanical Fatigue Testing of Two Iron Base High Temperature Alloys," Thermal Fatigue of Materials and Components, ASTM STP 612, pp. 214-226, 1976.

Shi, H.-J., Wang, Z.-G., and Su, H.-H., "Thermomechanical Fatigue of a 316L Austenittic Steel at Two Different Temperature Intervals," Scripta Materialia. Vol. 35(9), pp. 1107-1113, 1996.

Siemens Energy, Inc., "Industrial Gas Turbines, The Comprehensive Product Range from 5 to 50 Megawatts," 2013. [Product Catalog]

Simmons, W.F., and Van Echo, J.A., 1965. Report on the Elevated-Temperature Properties of Stianless Steels, ASTM Data Series, Publicaton DS-5-S1, Philadelphia, PA.

Simoneau, R., & Roberge, R., "Cavitation-Corrosion Damage Mechanisms in Hydraulic Turbine Materials," Materials to Supply the Energy Demand. pp. 467-486, 1981.

Siow, K.S., Song, T.Y., and Qiu, J.H., "Pitting Corrosion of Duplex Stainless Steels," Anti-Corrosion Methods and Materials. Vol. 48(1), pp. 31-36, 2001.

Skelton, R., Webster, G., De Mestral, B., & Wang, C.-Y., "Modelling Thermo-mechanical Fatigue Hysteresis Loops from Isothermal Cyclic Data," ASTM Special Technical Publication, ASTM STP 1371, pp. 69–84, 2000.

Skelton, R.P., Editor, 1987. High Temperature Fatigue: Properties and Prediction, Elsevier Applied Science, Essex, UK.

Skrabski, L., 2011. "Sensitization of Stainless Steel," Presentation given at Pennsylvania State University, University Park, Pennsylvania.

Slavik, D., and Sehitoglu, H., "Constitutive Models Suitable for Thermal Loading," Journal of Engineering Materials Technology. Vol. 108(4), pp. 303-312, 1986.

Slavik, D., and Sehitoglu, H., 1987. "A Constitutive Model for High Temperature Loading," Thermal Stress, Material Deformation, and Thermo-Mechanical Fatigue, Sehitoglu, H. and Zamrik, S. Y., Editors, ASME, New York, NY.

Smith, C. A., "Stainless Steel in the Food Industry," Anti-Corrosion Methods and Materials. Vol. 31, pp. 7-8, 1984.

Smith, R. A., 1975. "Fatigue Crack Propagation from Notches," Ph.D. Thesis, University of Cambridge.

Smolik, G., Flinn, J., Miley, D.V., and Korth, G., "Isothermal oxidation behavior of FeMnAl alloys and comparisons with type 304 stainless steel," Metallurgical Society of AIME. Pp. 307-319, 1987.

Solomon, H. D., Amzallag, C., DeLair, R. E., and Vallee, A. J., "Comparison of the Fatigue Life of Type 304L SS as Measured in Load and Strain Controlled Tests," Proceedings of the 12th International Conference on Environmental Degradation of Materials in Nuclear Power System Water Reactors, 2005.

Sriraman, M.R., and Pidaparti, R.M., "Crack Initiation of Materials Under Combined Pitting Corrosion and Cyclic Loading," Journals of Materials Engineering and Performance. Vol. 19(1), pp. 7-12, 2010.

Stephens, R., Fatemi, A., Stephens, R., and Fuchs, H., 2000. Metal Fatigue in Engineering, John Wiley & Sons, New York, NY.

Swindeman, R.W., 1975. "Creep-Rupture Correlations for Type 304 Stainless Steel Heat 9T2796," Structural Materials for Service at Elevated Temperatures in Nuclear Power Generation, pp. 1-30, Schaefer, A.O. Editor. ASME Publication MPC-1, ASME, New York, NY.

Tahami, F.V., Daei-Sorkhabi, A.H., and Biglari, F.R., "Creep Constitutive Equations for Cold-drawn 304L Stainless Steel, " Materials Science & Engineering: A. Vol. 527(18-19), pp. 4993-4999, 2010.

Taira, S., "Lifetime of Structures Subjected to Varying Load and Temperature," Proceedings of the International Union of Theoretical and Applied Mechanics Colloquium on Creep in Structures, 1962.

Taira, S., "Relationship between Thermal Fatigue and Low-Cycle Fatigue at Elevated Temperature," Fatigue at Elevated Temperatures, ASTM STP 520, pp. 80-101, 1973.

Taira, S., and Ohnami, M., "Fracture and Deformation of Metals Subjected to Thermal Cycling Combined with Mechanical Stress," Proceedings of the Joint International Conference on Creep, 1963.

Taira, S., Fujino, M., and Marayuma, S., 1974."Effects of Temperature and the Phase between Temperature and Strain on Crack Propagation in a Low Carbon Steel during Thermal Fatigue," Mechanical Behavior of Materials, Society of Materials Science, Kyoto.

Taira, S., Fujino, M., and Ohtani, R., "Collaborative Study on Thermal Fatigue of Properties of High Temperature Alloys in Japan," Fatigue of Engineering Materials and Structures. Vol. 1, pp. 495-508, 1979.

Taira, S., Ohnami, M., and Kyogoku, T., "Thermal Fatigue under Pulsating Thermal Stress Cycling," Bulletin of the Japanese Society of Mechanical Engineering. Vol. 6, pp. 178-185, 1963.

Tang, Q.-X., Liu, J., and Han, J.-T., "High Temperature Oxidation Resistance of 309S Autenitic Stainless Steel," Journal of Iron and Steel Research. Vol. 21(10), pp. 43-47, 2009.

Ulbrich, A., Gobrecht, E., Siegel, M.R., Schmid, E., and Armitage, P.K., "High Steam Turbine Operating Flexibility Coupled with Service Interval Optimization," Proceedings of the 2003 International Joint Power Generation Conference. Pp. 451-459, 2003.

Vessel, A., Mozetic, M., Drenik, A., Hauptman, N., and Balat-Pichelin, M., "High Temperature Oxidation of Stainless Steel AISI316L in Air Plasma," Applied Surface Science. Vol. 255(5), pp. 1759-1765, 2008.

Visscher, C., 2006. "Parabolic Rate Law Derivation," from http://epsc.wustl.edu/~visscher/research/paraboliclaw.pdf.

Voce, E., "The Relationship Between Stress and Strain for Homogenous Deformation," Journal of the Institute of Metals. Vol. 74, pp. 536-562, 1948.

Wahi, R.P., Auerswald, J., Mukherji, D., Dudka, A., Fecht, H.-J., and Chen, W., "Damage and Fatigue Life of Superalloy IN738LC under Thermo-mechanical and Low Cycle Fatigue Loading," International Journal of Fatigue, Vol. 19(1), pp. S89-S94, 1987.

Wert, D.E., and DiSabella, R.P., "Strong, Corrosion-Resistant Stainless Steel," Advanced Materials & Processes. Vol. 164, pp. 34-36, 2006.

Westwood, H. J., 1978. "High Temperature Fatigue of 304 Stainless Steel under Isothermal and Thermal Cycling Conditions," Advances in the Research on the Strength and Fracture of Materials, Taplin, D. M. R., Editor, Pergamon Press, Oxford, UK.

Westwood, H.J., "Tensile Hold Time Effects on Isothermal and Thermal Low-Cycle Fatigue of 304 Stainless Steel," Proceedings of the Third International Conference on Mechnaical Behavior of Materials. Vol. 2, pp. 59-67, 1979.

Westwood, H.J., and Lee, W.K., "Creep Fatigue Crack Initiation ½ Cr-Mo-V Steel," Creep and Fracture of Engineering Materials and Structure, pp. 517-530, 1982.

Wetenkamp, H. R., Sidebottom, O. M., Schrader, H. J., "The Effect of Brake Shoe Action on Thermal Cracking and on Failure of Wrought Steel Railway Car Wheels," Engineering Experiment Station Bulletin, University of Illinois Bulletins. Vol. 47(77), 1950.

Wong, K., Photographer, 2008. "Rust Chain." Retrieved from http://commons.wikimedia.org/wiki/File:RustChain.JPG.

Yao, X., and Xu, Y., "Recent Advances in Evolutionary Computation," Journal of Computer Science and Technology. Vol. 21(1), pp. 1-18, 2006.

Yates, J. R., "A Simple Approximation for the Stress Intensity Factor of a Crack at a Notch," Journal of Strain Analysis. Vol. 26(1), pp. 9-13, 1991.

Yates, J. R., and Lüsebrink, O., "An Analysis of Notch Root Plasticity," Proceedings of the ASME Offshore Mechanical and Arctic Engineering Conference, 1994.

Yates, J. R., Kiew, H. T., and Goldthorpe, M. R., "Stress Intensity Factors for Cracks at the Root of Blunt Notches," Materials Engineering. Vol. III-B, pp. 855-861, 1993.

Yoshida, S., Kanazawa, K., Yamaguchi, K., Sasaki, M., Kobayashi, K., and Sato, M., "Elevated-Temperature Fatigue Properties of Engineering Materials," Transactions of National Research Institute for Metals (Tokyo). Vol. 19(5), pp.247-251, 1977.

Zamrik, S.Y., Davis, D.C., and Firth, L. C., Isothermal and Thermomechanical Fatigue of Type 316 Stainless Steel. Thermomechanical Fatigue Behavior of Materials, ASTM STP 1263, 1996, pp. 96-116.

Zauter, R., Petry, F., Christ, H. J., and Mughrabi, H., “Thermo-Mechanical Fatigue of the Austenitic Steel AISI 304L,” Thermomechanical Fatigue Behavior of Materials, ASTM STP 1186, pp. 70-90, 1993.